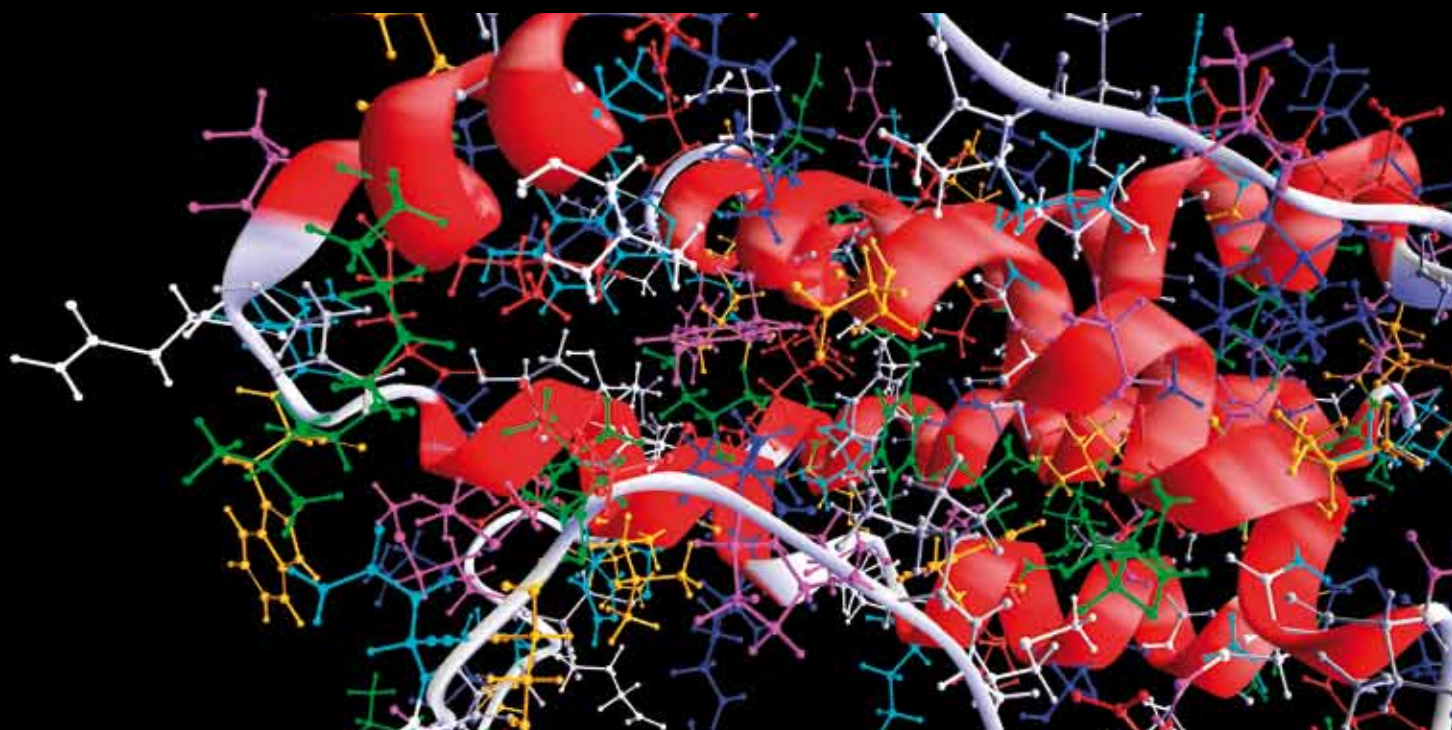


COMPUTER-AIDED DETECTION AND DIAGNOSIS IN MEDICAL IMAGING

GUEST EDITORS: CHUNG-MING CHEN, YI-HONG CHOU, NORIO TAGAWA, AND YOUNGHAEE DO





Computer-Aided Detection and Diagnosis in Medical Imaging

Computational and Mathematical Methods in Medicine

Computer-Aided Detection and Diagnosis in Medical Imaging

Guest Editors: Chung-Ming Chen, Yi-Hong Chou, Norio Tagawa,
and Younghae Do



Copyright © 2013 Hindawi Publishing Corporation. All rights reserved.

This is a special issue published in “Computational and Mathematical Methods in Medicine.” All articles are open access articles distributed under the Creative Commons Attribution License, which permits unrestricted use, distribution, and reproduction in any medium, provided the original work is properly cited.

Editorial Board

Zvia Agur, Israel
Emil Alexov, USA
Gary C. An, USA
Georgios Archontis, Cyprus
Pascal Auffinger, France
Facundo Ballester, Spain
Dimos Baltas, Germany
Chris Bauch, Canada
Maxim Bazhenov, USA
Philip Biggin, UK
Michael Breakspear, Australia
Thierry Busso, France
Carlo Cattani, Italy
William Crum, UK
Gustavo Deco, Spain
Carmen Domene, UK
Frank Emmert-Streib, UK
Ricardo Femat, Mexico
Alfonso T. Garca-Sosa, Estonia
Kannan Gunasekaran, USA
Damien R. Hall, Japan
William F. Harris, South Africa

Vassily Hatzimanikatis, USA
Volkhard Helms, Germany
J.-H. S. Hofmeyr, South Africa
Seiya Imoto, Japan
Bleddyn Jones, UK
Lawrence A. Kelley, UK
Lev Klebanov, Czech Republic
Ina Koch, Germany
David Liley, Australia
Quan Long, UK
Yoram Louzoun, Israel
Jianpeng Ma, USA
C.-M. C. Ma, USA
Reinoud Maex, France
Francois Major, Canada
Simeone Marino, USA
Ali Masoudi-Nejad, Iran
Seth Michelson, USA
Michele Migliore, Italy
Karol Miller, Australia
Ernst Niebur, USA
Kazuhisa Nishizawa, Japan

Martin Nowak, USA
Markus Owen, UK
Hugo Palmans, UK
Lech S. Papiez, USA
Jean Pierre Rospars, France
David James Sherman, France
S. Sivaloganathan, Canada
Elisabeth Tillier, Canada
Nestor V. Torres, Spain
Anna Tramontano, Italy
N. J. Trujillo-Barreto, Cuba
Gabriel Turinici, France
Kutlu O. Ulgen, Turkey
Nagarajan Vaidehi, USA
Edelmira Valero, Spain
Wim Van Drongelen, USA
Jinliang Wang, UK
Jacek Waniewski, Poland
Guang Wu, China
X. George Xu, USA
Henggui Zhang, UK

Contents

Computer-Aided Detection and Diagnosis in Medical Imaging, Chung-Ming Chen, Yi-Hong Chou, Norio Tagawa, and Younghae Do
Volume 2013, Article ID 790608, 2 pages

Statistical Texture Modeling for Medical Volume Using Linear Tensor Coding, Junping Deng, Xu Qiao, and Yen-Wei Chen
Volume 2013, Article ID 630902, 10 pages

Classification of Pulmonary Nodules by Using Hybrid Features, Ahmet Tartar, Niyazi Kilic, and Aydin Akan
Volume 2013, Article ID 148363, 11 pages

Segmentation of the Striatum from MR Brain Images to Calculate the ^{99m}Tc -TRODAT-1 Binding Ratio in SPECT Images, Ching-Fen Jiang, Chiung-Chih Chang, Shu-Hua Huang, and Chia-Hsiang Wu
Volume 2013, Article ID 593175, 8 pages

Customized First and Second Order Statistics Based Operators to Support Advanced Texture Analysis of MRI Images, Danilo Avola, Luigi Cinque, and Giuseppe Placidi
Volume 2013, Article ID 213901, 13 pages

Computer Aided Quantification of Pathological Features for Flexor Tendon Pulleys on Microscopic Images, Yung-Chun Liu, Hsin-Chen Chen, Hui-Hsuan Shih, Tai-Hua Yang, Hsiao-Bai Yang, Dee-Shan Yang, Fong-Chin Su, and Yung-Nien Sun
Volume 2013, Article ID 914124, 9 pages

Classification of Cerebral Lymphomas and Glioblastomas Featuring Luminance Distribution Analysis, Toshihiko Yamasaki, Tsuhan Chen, Toshinori Hirai, and Ryuji Murakami
Volume 2013, Article ID 619658, 10 pages

Particle System Based Adaptive Sampling on Spherical Parameter Space to Improve the MDL Method for Construction of Statistical Shape Models, Rui Xu, Xiangrong Zhou, Yasushi Hirano, Rie Tachibana, Takeshi Hara, Shoji Kido, and Hiroshi Fujita
Volume 2013, Article ID 196259, 9 pages

Artificial Neural Networks in Mammography Interpretation and Diagnostic Decision Making, Turgay Ayer, Qiushi Chen, and Elizabeth S. Burnside
Volume 2013, Article ID 832509, 10 pages

GND-PCA-Based Statistical Modeling of Diaphragm Motion Extracted from 4D MRI, Windra Swastika, Yoshitada Masuda, Rui Xu, Shoji Kido, Yen-Wei Chen, and Hideaki Haneishi
Volume 2013, Article ID 482941, 9 pages

Construction of Classifier Based on MPCA and QSA and Its Application on Classification of Pancreatic Diseases, Huiyan Jiang, Di Zhao, Tianjiao Feng, Shiyang Liao, and Yenwei Chen
Volume 2013, Article ID 713174, 7 pages

Volume-Rendering-Based Interactive 3D Measurement for Quantitative Analysis of 3D Medical Images, Yakang Dai, Jian Zheng, Yuetao Yang, Duoje Kuai, and Xiaodong Yang
Volume 2013, Article ID 804573, 9 pages

Segmentation and Morphometric Analysis of Cells from Fluorescence Microscopy Images of Cytoskeletons, Yoshihiro Ujihara, Masanori Nakamura, Hiroshi Miyazaki, and Shigeo Wada
Volume 2013, Article ID 381356, 11 pages

Discrimination between Alzheimer's Disease and Mild Cognitive Impairment Using SOM and PSO-SVM, Shih-Ting Yang, Jiann-Der Lee, Tzyh-Chyang Chang, Chung-Hsien Huang, Jiun-Jie Wang, Wen-Chuin Hsu, Hsiao-Lung Chan, Yau-Yau Wai, and Kuan-Yi Li
Volume 2013, Article ID 253670, 10 pages

Transfer Function Analysis of Respiratory and Cardiac Pulsations in Human Brain Observed on Dynamic Magnetic Resonance Images, Yi-Hsuan Kao, Wan-Yuo Guo, Adrain Jy-Kang Liou, Ting-Yi Chen, Chau-Chiun Huang, Chih-Che Chou, and Jiing-Feng Lirng
Volume 2013, Article ID 157040, 7 pages

Detection of Pulmonary Nodules in CT Images Based on Fuzzy Integrated Active Contour Model and Hybrid Parametric Mixture Model, Bin Li, Kan Chen, Lianfang Tian, Yao Yeboah, and Shanxing Ou
Volume 2013, Article ID 515386, 15 pages

Automatic Vertebral Column Extraction by Whole-Body Bone SPECT Scan, Sheng-Fang Huang, Hao-Yu Chao, Pan-Fu Kao, Wei-Chih Shen, Yu-Hsiang Chou, and Shu-Hsin Liu
Volume 2013, Article ID 647548, 11 pages

Editorial

Computer-Aided Detection and Diagnosis in Medical Imaging

Chung-Ming Chen,¹ Yi-Hong Chou,² Norio Tagawa,³ and Younghae Do⁴

¹ *Institute of Biomedical Engineering, National Taiwan University, Taipei, Taiwan*

² *Department of Radiology, Taipei Veterans General Hospital and National Yang Ming University, Taipei, Taiwan*

³ *Division of Information and Communication Systems, Tokyo Metropolitan University, Tokyo, Japan*

⁴ *Department of Mathematics, Kyungpook National University, Kyungpook, Republic of Korea*

Correspondence should be addressed to Chung-Ming Chen; chung@ntu.edu.tw

Received 28 July 2013; Accepted 28 July 2013

Copyright © 2013 Chung-Ming Chen et al. This is an open access article distributed under the Creative Commons Attribution License, which permits unrestricted use, distribution, and reproduction in any medium, provided the original work is properly cited.

Medical images nowadays play an essential role in detection and diagnosis of numerous diseases. Ranging from anatomical information, functional activities, to the molecular and cellular expressions, medical imaging provides direct visualization means to see through the human bodies and observe the minute anatomical changes and biological processes characterized by different physical and biological parameters. Informative as they are, medical imaging usually requires experienced medical doctors to best interpret the information revealed in the images. However, because of various subjective factors as well as limited analysis time and tools, it is quite common that different medical doctors may come up with diverse interpretations, leading to different diagnoses. Moreover, for the same set of medical imaging, a medical doctor may make different diagnosis results at different time.

To attain a more reliable and accurate diagnosis, recently, varieties of computer-aided detection (CAD) and diagnosis (CADx) approaches have been developed to assist interpretation of the medical images. At least four types, denoted as Types I–IV, of efforts may be identified among these CAD and CADx approaches. Type I is to assist visual detection, qualitative analysis, and interactive quantitative analysis of the objects of interest in the medical images by either enhancing the salient features of the objects or suppressing the background noises. Type II is to assist feature extraction of the objects of interest for further quantitative analyses by such techniques as boundary delineation, tree-structure reconstruction, fiber tracking, texture analysis, and so on.

Type III is to automatically detect and classify the objects of interest by integrating the data mining, medical image analysis, and signal processing technologies. Type IV is to estimate the anatomical and functional tissue properties not explicitly revealed in the medical images based on mathematical modeling, for example, physiology, biomechanics, heat transfer, and so forth.

This special issue presents one review paper and fifteen papers of latest research results on computer-aided detection and diagnosis in medical imaging covering all four types of works, including one paper of Type I, six papers of Type II, seven papers of Type III, and two papers of Type IV. The distribution of these four types of research works, though only with a limited number of papers, does reasonably account for the amount of research efforts in the various areas of CAD/CADx in medical imaging.

The Type I paper in this special issue, presented by Y. Dai et al., proposed a volume-rendering-based interactive 3D measurement framework for quantitative analysis of 3D medical images. The idea is to integrate 3D widgets and volume clipping into volume rendering, using 3D plane widgets, 3D line widgets, and 3D angle widgets to measure the areas, distances, and angles of interesting objects.

To assist feature extraction and quantitative analysis, the six papers of Type II in this special issue may be further divided into three groups, namely, registration, texture analysis, and segmentation, representing three essential tasks in CAD/CADx in medical imaging. The registration group has only one paper in which R. Xu et al. addressed one of the key

issues in medical image registration, that is, determination of corresponding points. A particle-system-based method was proposed to obtain adaptive sampling positions on the unit sphere for the construction of statistical shape models. In the group of texture analysis, D. Avola et al. presented a customizing approach to deriving a set of first- and second-order statistics-based operators for texture analysis of MRI images. J. Deng et al. proposed a robust statistical texture model for medical volumes based on a linear tensor coding (LTC) algorithm. Medical volumes are represented by a linear combination of mutually independent bases, from which distinctive bases may be selected for classification. To extract the morphological information, in the segmentation group, Y. Ujihara et al. developed a two-step region growing method to reconstruct cell geometry from confocal fluorescence microscopy images of the cytoskeleton. C.-F. Jiang et al. integrated the GVF-snake model and a hybrid registration technique to extract regions from MR T1-weighted images, mapping them into the corresponding SPECT images. To automatically recognize the vertebral column in a SPECT image, S.-F. Huang et al. formulated the bone segmentation problem as a graph clustering problem and proposed a “bone graph” image description method to facilitate manipulation of morphological relationships in the skeleton.

To assist nodule detection and/or differential diagnosis of various diseases, the seven papers of Type III in this special issue presented CAD/CADx approaches for six clinical applications. They are mammographic lesion detection and diagnosis, lung nodule detection, as well as differential diagnosis of Alzheimer disease (AD) versus mild cognitive impairment (MCI), cerebral lymphomas versus glioblastomas, pancreatic diseases, and trigger finger disease. As a review paper, T. Ayer et al. provided an informative overview of artificial neural networks-based mammography interpretation and diagnostic decision making. Both of B. Li et al. and A. Tartar et al. aimed to achieve computer-aided detection of lung nodules in CT images. Nevertheless, A. Tartar et al. focused on classification of a candidate nodule into true nodule or nonnodule by selecting the best features from three conventional methods. On the other hand, B. Li et al. proposed a complete framework for nodule detection based on a fuzzy integrated active contour model and a hybrid parametric mixture model of the juxtavascular nodules. For differential diagnosis, S.-T. Yang et al. proposed an MRI-based classification framework to distinguish the patients with AD and MCI from the normal participants, using particle swarm optimization for feature selection and support vector machine as the classifier. To differentiate cerebral lymphomas from glioblastomas, T. Yamasaki et al. presented a tumor classification system, classifying typical cases by luminance range thresholding and apparent diffusion coefficients thresholding and nontypical by a support vector machine (SVM). A. Jiang et al. developed a classification method for pancreatic diseases, using multilinear principal component analysis to extract the eigen tensors and SVM as the classifier with the parameter optimized by a quantum simulated annealing algorithm. Y.-C. Liu et al. proposed two parameters as the pathological progression indices for evaluation of trigger finger disease from the microscopic pulley images.

These two parameters are the size ratio of the abnormal tissue regions and the number ratio of the abnormal nuclei, derived from a color-based image segmentation system.

Both of the two Type IV papers in this special issue aimed to estimate the anatomical and functional tissue properties from MRI images. With dynamic MR images, Y.-H. Kao et al. investigated the respiratory and cardiac pulsations in the brain of normal subjects based on transfer function analysis. W. Swastika et al. analyzed two statistical models of diaphragm motion constructed by using regular principal component analysis (PCA) and generalized N-dimensional PCA (GND-PCA), the results of which showed that the GND-PCA model was superior to the PCA model.

*Chung-Ming Chen
Yi-Hong Chou
Norio Tagawa
Younghae Do*

Research Article

Statistical Texture Modeling for Medical Volume Using Linear Tensor Coding

Junping Deng,¹ Xu Qiao,^{1,2} and Yen-Wei Chen^{1,3}

¹ College of Information Science and Engineering, Ritsumeikan University, Kusatsu 5250072, Japan

² School of Control Science and Engineering, Shandong University, Jinan 250100, China

³ College of Computer Science and Information Technology, Central South University of Forestry and Technology, Hunan 410004, China

Correspondence should be addressed to Yen-Wei Chen; chen@is.ritsumei.ac.jp

Received 17 January 2013; Revised 9 May 2013; Accepted 27 May 2013

Academic Editor: Norio Tagawa

Copyright © 2013 Junping Deng et al. This is an open access article distributed under the Creative Commons Attribution License, which permits unrestricted use, distribution, and reproduction in any medium, provided the original work is properly cited.

We introduced a compact representation method named Linear Tensor Coding (LTC) for medical volume. With LTC, medical volumes can be represented by a linear combination of bases which are mutually independent. Furthermore, it is possible to choose the distinctive basis for classification. Before classification, correlations between category labels and the coefficients of LTC basis are used to choose the basis. Then we use the selected basis for classification. The classification accuracy can be significantly improved by the use of selected distinctive basis.

1. Introduction

In the recent years, the research of digital atlases is a popular and important topic in the medical volume processing [1, 2]. Many problems in medical volumes interpretation involve the need of a modeling to understand the volumes with which it is presented, and thus well representation of medical volumes is very important part of computer-assisted diagnosis (CAD). Due to much variability in biological structures, it makes medical volume interpretation to be a difficult task.

Currently the representation of medical volume can be mainly categorized as shape-based methods, in which a deformable model is represented or matched to, and appearance based methods, in which the model represents the volume region covered by the structures. Statistical shape model (SSM) can construct the generic structure (mean structure) and deformation for a shape ensemble [3]. Due to the deformation of the organ shape in some special disease, it is widely utilized in medical image processing, such as medical image registration and segmentation [4, 5]. Inspired by the work of active shape model (ASM), 3D ASM was proposed for construction of 3D statistical models for segmentation of the left ventricle of the heart [6]. The statistical shape models also show good performance for

distinguishing the abnormal liver from the normal one in [7]. Because many diseases change the texture (voxel value) of the organ significantly, we need to capture not only shape variations, but also texture (voxel value) variations. So the active appearance model (AAM) is proposed which can represent both shape and texture information. In [8], 3D active appearance model is used for segmentation of cardiac MR and ultrasound images. It is also possible to combine the two approaches together. For example, Mitchell et al. [9] used a combination of ASM and AAM to segment cardiac images. At each iteration, the two models ran independently to compute new estimates of the pose and shape parameters. For diagnosis assistance, making an accuracy diagnosis decision of liver is important for patient. Radiologists are mainly depending on the intensity variations (texture information) in livers on medical images to identify modules or tumors and make a diagnostic decision. However, there has been little research on applications of digital atlas to CAD.

Compared to statistical shape modeling, statistical texture modeling usually faces overfitting problems, and the statistical texture modeling for medical volumes is a challenging task because the dimensions of the medical volume are very high, while the training samples are fewer than the dimensions of the data. In [10], we have proposed generalized

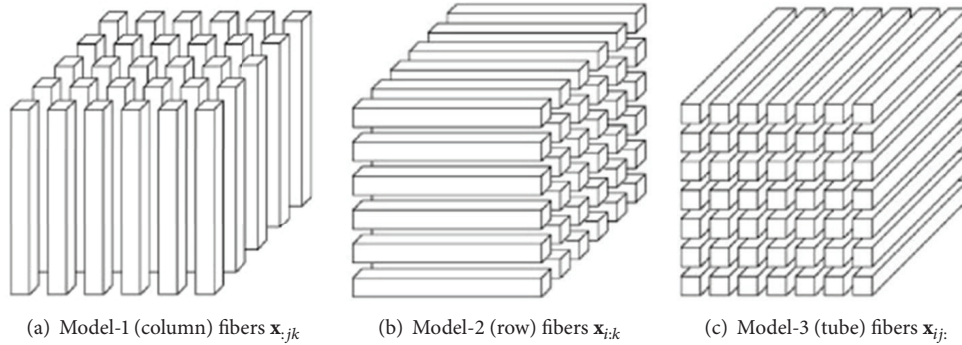


FIGURE 1: Fibers of a 3rd-order tensor.

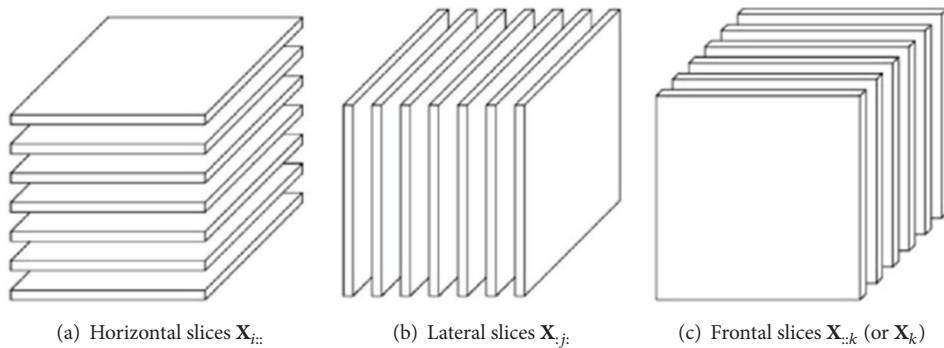


FIGURE 2: Slices of a 3rd-order tensor.

N -dimensional principal component analysis (GND-PCA) for the modeling of a series of medical volumes. It is able to achieve good performance on construction of statistical appearance models for medical volumes with few samples. The medical volume is treated as a 3rd-order tensor, and the optimal subspace on each mode is calculated simultaneously by minimizing the square error between the original volumes based on the subspace with an iteration algorithm. However, this method has some disadvantages, such as each basis of the GNDPCA not being independent and thus making the core tensor of the final result redundant. Also it is difficult to choose the distinctive basis for classification.

To resolve these problems, in our previous work, we proposed a linear tensor coding (LTC) algorithm, which can achieve more compact and meaningful tensor bases than GND-PCA [11, 12]. In this paper, we first apply it to statistical texture modeling of medical volumes. With LTC, medical volumes can be represented by a linear combination of bases, which are mutually independent. Furthermore, it is possible to choose the distinctive basis for classification. The proposed method was evaluated using a medical volume database. In the experiment, we compared both reconstructed results and classification results of LTC and GND-PCA. As for reconstruction results, the performance of LTC is superior to that of GND-PCA. Additionally, in the classification part, we first choose the distinctive basis based on the correlation between category labels and the coefficients of LTC basis, and then we use the selected basis for classification. The classification

accuracy can be significantly improved by the use of selected distinctive basis.

This paper is organized as follows. In Section 2, a brief review of basic theory of tensor and GND-PCA is made. LTC algorithm is introduced in Section 3, and analysis is given. Section 4 is the experimental part, and it illustrates the performance of LTC to be better than that of GND-PCA. Section 5 summarizes the key points of this paper.

2. Preliminaries

In this section, we provide a brief overview of tensor and multilinear algebra. In mathematics, multilinear algebra extends the methods of linear algebra. Just as linear algebra is built on the concept of a vector and develops the theory of vector spaces, multilinear algebra builds on the concepts of a tensor. A tensor is a multidimensional array. More formally, an N th-order tensor is an element of the tensor product of N vector spaces, each of which has its own coordinate system.

2.1. Tensor Definitions. As mentioned earlier, scalars are denoted by italic-shape letters, that is, (a, b, \dots) or (A, B, \dots) . Bold lower case letters, that is, $(\mathbf{a}, \mathbf{b}, \dots)$, are used to represent vectors. Matrices are denoted by bold upper case letters, that is, $(\mathbf{A}, \mathbf{B}, \dots)$, and higher-order tensors (more than third-order tensor) are denoted by calligraphic upper case letters, that is, $(\mathcal{A}, \mathcal{B}, \dots)$.

IN: a series of N th order tensors, $\mathcal{A}_i \in \mathbb{R}^{I_1 \times I_2 \times \dots \times I_N}$, $i = 1, 2, \dots, M$.
 OUT: N Matrices $\mathbf{U}_{\text{opt}}^{(n)} \in \mathbb{R}^{I_n \times J_n}$ ($J_n = 1, n = 1, 2, \dots, N$) with orthogonal column vectors.

(1) Initial values: $k = 0$ and $\mathbf{U}_0^{(n)}$ whose columns are determined as the first J_n leading eigenvectors of the matrices $\sum_{i=1}^M (\mathbf{A}_{i(n)} \cdot \mathbf{A}_{i(n)}^T)$.

(2) Iterate for k until convergence

(i) Maximize $S' = \sum_{i=1}^M \|\mathcal{C}_i \times_1 \mathbf{U}^{(1)T}\|^2$, $\mathcal{C}_i = \mathcal{A}_i \times_2 \mathbf{U}_k^{(2)T} \times \dots \times_N \mathbf{U}_k^{(N)T}$
 Solution: $\mathbf{U}^{(1)}$ whose columns are determined as the first J_1 leading eigenvectors of $\sum_{i=1}^M (\mathbf{C}_{i(1)} \cdot \mathbf{C}_{i(1)}^T)$
 Set $\mathbf{U}_{k+1}^{(1)} = \mathbf{U}^{(1)}$.

(ii) Maximize $S' = \sum_{i=1}^M \|\mathcal{C}_i \times_2 \mathbf{U}^{(2)T}\|^2$, $\mathcal{C}_i = \mathcal{A}_i \times_1 \mathbf{U}_{k+1}^{(1)T} \times_3 \mathbf{U}_k^{(3)T} \times \dots \times_N \mathbf{U}_k^{(N)T}$
 Solution: $\mathbf{U}^{(2)}$ whose columns are determined as the first J_2 leading eigenvectors of $\sum_{i=1}^M (\mathbf{C}_{i(2)} \cdot \mathbf{C}_{i(2)}^T)$
 Set $\mathbf{U}_{k+1}^{(2)} = \mathbf{U}^{(2)}$.
 ...

(iii) Maximize $S' = \sum_{i=1}^M \|\mathcal{C}_i \times_n \mathbf{U}^{(n)T}\|^2$,
 $\mathcal{C}_i = \mathcal{A}_i \times_1 \mathbf{U}_{k+1}^{(1)T} \times \dots \times_{n-1} \mathbf{U}_{k+1}^{(n-1)T} \times_{n+1} \mathbf{U}_k^{(n+1)T} \times \dots \times_N \mathbf{U}_k^{(N)T}$
 Solution: $\mathbf{U}^{(n)}$ whose columns are determined as the first J_n leading eigenvectors of $\sum_{i=1}^M (\mathbf{C}_{i(n)} \cdot \mathbf{C}_{i(n)}^T)$
 Set $\mathbf{U}_{k+1}^{(n)} = \mathbf{U}^{(n)}$.
 ...

(iv) Maximize $S' = \sum_{i=1}^M \|\mathcal{C}_i \times_N \mathbf{U}^{(N)T}\|^2$, $\mathcal{C}_i = \mathcal{A}_i \times_1 \mathbf{U}_{k+1}^{(1)T} \times \dots \times_{N-1} \mathbf{U}_{k+1}^{(N-1)T}$
 Solution: $\mathbf{U}^{(N)}$ whose columns are determined as the first J_N leading eigenvectors of $\sum_{i=1}^M (\mathbf{C}_{i(N)} \cdot \mathbf{C}_{i(N)}^T)$
 Set $\mathbf{U}_{k+1}^{(N)} = \mathbf{U}^{(N)}$.
 $k = k + 1$

(3) Set $\mathbf{U}_{\text{opt}}^{(1)} = \mathbf{U}_k^{(1)}$, $\mathbf{U}_{\text{opt}}^{(2)} = \mathbf{U}_k^{(2)}$, \dots , $\mathbf{U}_{\text{opt}}^{(N)} = \mathbf{U}_k^{(N)}$.

ALGORITHM 1: GND-PCA.

The order of a tensor is the number of dimensions, as known as ways or modes. An N th-order tensor \mathcal{A} is defined as a multiarray with N indices, where $\mathcal{A} \in \mathbb{R}^{I_1 \times I_2 \times \dots \times I_N}$ and \mathbb{R} is the real manifold. Elements of the tensor \mathcal{A} are denoted as $a_{i_1 \dots i_n \dots i_N}$, where $1 \leq i_n \leq I_n$. The space of the N th-order tensor is comprised by the N mode subspaces. From the perspective of \mathcal{A} , scalars, vectors, and matrices can be seen as zeroth-order, first-order, and second-order tensors, respectively.

The i th entry of a vector \mathbf{a} is denoted by a_i , element (i, j) of a matrix \mathbf{A} is denoted by a_{ij} , and element (i, j, k) of a 3rd-order tensor \mathcal{X} is denoted by x_{ijk} . Indices typically range from 1 to their capital version; for example, $i = 1, \dots, I$. The n th element in a sequence is denoted by a superscript in parentheses; for example, \mathbf{A}^n denotes the n th matrix in a sequence.

Subarrays are formed when a subset of the indices is fixed. For matrices, these are the rows and columns. A colon is used to indicate all elements of a mode. Thus, the j th column of \mathbf{A} is denoted by $\mathbf{a}_{:,j}$, and the i th row of \mathbf{A} is denoted by \mathbf{a}_i .

Fibers are the higher-order analogue of matrix rows and columns. A fiber is defined by fixing every index but one. A matrix column is a mode-1 fiber and a matrix row is a mode-2 fiber. Third-order tensors have column, row, and tube fibers, denoted as $\mathbf{x}_{:,jk}$, $\mathbf{x}_{i,jk}$, and \mathbf{x}_{ijk} , respectively. Fibers of a Third-order tensors are shown in Figure 1.

Slices are two-dimensional sections of a tensor, defined by fixing all but two indices. Figure 2 shows the horizontal, lateral, and frontal slices of a third-order tensor \mathcal{X} , denoted by $\mathbf{X}_{i,:}$, $\mathbf{X}_{:,j}$, and $\mathbf{X}_{::k}$, respectively.

The norm of a tensor $\mathcal{X} \in \mathbb{R}^{I_1 \times I_2 \times \dots \times I_N}$ is the square root of the sum of the squares of all its element; that is,

$$\|\mathcal{X}\| = \sqrt{\sum_{i_1=1}^{I_1} \sum_{i_2=1}^{I_2} \dots \sum_{i_N=1}^{I_N} x_{i_1 i_2 \dots i_N}^2}. \quad (1)$$

This is analogous to the matrix Frobenius norm, which is denoted as $\|\mathbf{A}\|$ for a matrix \mathbf{A} .

The inner product of two same-sized tensors $\mathcal{X}, \mathcal{Y} \in \mathbb{R}^{I_1 \times I_2 \times \dots \times I_N}$ is the sum of the products of their entries; that is,

$$\langle \mathcal{X}, \mathcal{Y} \rangle = \sum_{i_1=1}^{I_1} \sum_{i_2=1}^{I_2} \dots \sum_{i_N=1}^{I_N} x_{i_1 i_2 \dots i_N} y_{i_1 i_2 \dots i_N}. \quad (2)$$

It follows immediately that $\langle \mathcal{X}, \mathcal{X} \rangle = \|\mathcal{X}\|^2$.

A N -order tensor $\mathcal{X} \in \mathbb{R}^{I_1 \times I_2 \times \dots \times I_N}$ is rank one if it can be written as the outer product of N vectors; that is,

$$\mathcal{X} = \mathbf{a}^{(1)} \circ \mathbf{a}^{(2)} \circ \dots \circ \mathbf{a}^{(N)}. \quad (3)$$

IN: a series of N th order tensors, $\mathcal{A}_i \in \mathbb{R}^{I_1 \times I_2 \times \dots \times I_N}$, $i = 1, 2, \dots, M$. Define N Matrices

$\mathbf{U}_{\text{opt}}^{(n)} \in \mathbb{R}^{I_n \times J_n}$ ($J_n = 1, n = 1, 2, \dots, N$) with orthogonal column vectors.

OUT: S Rank-1 basis tensor \mathcal{B}_s , $s \leq S$ depends on convergence.

Iterate for s until convergence

(1) Initial values: $\mathcal{A}_i = \mathcal{A}_i - \mathcal{A}_i^{\text{Rec}_s}$, define $\mathcal{A}_i^{\text{Rec}_s} = 0$.

(2) (a) Initial values: $k = 0$ and $\mathbf{U}_0^{(n)}$ whose columns are determined as the first J_n leading eigenvectors of the matrices $\sum_{i=1}^M (\mathbf{A}_{i(n)} \cdot \mathbf{A}_{i(n)}^T)$.

(b) Iterate for k until convergence

(i) Maximize $S' = \sum_{i=1}^M \left\| \mathcal{E}_i \times_1 \mathbf{U}^{(1)T} \right\|^2$, $\mathcal{E}_i = \mathcal{A}_i \times_2 \mathbf{U}_k^{(2)T} \times \dots \times_N \mathbf{U}_k^{(N)T}$

Solution: $\mathbf{U}^{(1)}$ whose columns are determined as the first J_1 leading eigenvectors of $\sum_{i=1}^M (\mathbf{C}_{i(1)} \cdot \mathbf{C}_{i(1)}^T)$
Set $\mathbf{U}_{k+1}^{(1)} = \mathbf{U}^{(1)}$.

(ii) Maximize $S' = \sum_{i=1}^M \left\| \mathcal{E}_i \times_2 \mathbf{U}^{(2)T} \right\|^2$, $\mathcal{E}_i = \mathcal{A}_i \times_1 \mathbf{U}_{k+1}^{(1)T} \times_3 \mathbf{U}_k^{(3)T} \times \dots \times_N \mathbf{U}_k^{(N)T}$

Solution: $\mathbf{U}^{(2)}$ whose columns are determined as the first J_2 leading eigenvectors of $\sum_{i=1}^M (\mathbf{C}_{i(2)} \cdot \mathbf{C}_{i(2)}^T)$
Set $\mathbf{U}_{k+1}^{(2)} = \mathbf{U}^{(2)}$.

...

(iii) Maximize $S' = \sum_{i=1}^M \left\| \mathcal{E}_i \times_n \mathbf{U}^{(n)T} \right\|^2$,

$\mathcal{E}_i = \mathcal{A}_i \times_1 \mathbf{U}_{k+1}^{(1)T} \times \dots \times_{n-1} \mathbf{U}_{k+1}^{(n-1)T} \times_{n+1} \mathbf{U}_k^{(n+1)T} \times \dots \times_N \mathbf{U}_k^{(N)T}$

Solution: $\mathbf{U}^{(n)}$ whose columns are determined as the first J_n leading eigenvectors of $\sum_{i=1}^M (\mathbf{C}_{i(n)} \cdot \mathbf{C}_{i(n)}^T)$
Set $\mathbf{U}_{k+1}^{(n)} = \mathbf{U}^{(n)}$.

...

(iv) Maximize $S' = \sum_{i=1}^M \left\| \mathcal{E}_i \times_N \mathbf{U}^{(N)T} \right\|^2$, $\mathcal{E}_i = \mathcal{A}_i \times_1 \mathbf{U}_{k+1}^{(1)T} \times \dots \times_{N-1} \mathbf{U}_{k+1}^{(N-1)T}$

Solution: $\mathbf{U}^{(N)}$ whose columns are determined as the first J_N leading eigenvectors of $\sum_{i=1}^M (\mathbf{C}_{i(N)} \cdot \mathbf{C}_{i(N)}^T)$
Set $\mathbf{U}_{k+1}^{(N)} = \mathbf{U}^{(N)}$.

$k = k + 1$

(c) Set $\mathbf{U}_{\text{opt}}^{(1)} = \mathbf{U}_k^{(1)}$, $\mathbf{U}_{\text{opt}}^{(2)} = \mathbf{U}_k^{(2)}$, ..., $\mathbf{U}_{\text{opt}}^{(N)} = \mathbf{U}_k^{(N)}$.

(3) Size of $\mathbf{U}_{\text{opt}}^{(i)}$ is $I_i \times 1$, each basis $\mathcal{B}_s = \mathbf{U}_{\text{opt}}^{(1)} \otimes \mathbf{U}_{\text{opt}}^{(2)} \otimes \dots \otimes \mathbf{U}_{\text{opt}}^{(N)}$.

(4) For each data, coefficient on this basis $c_{i,s} = \mathcal{A}_i \times_1 \mathbf{U}_k^{(1)T} \times_2 \mathbf{U}_k^{(2)T} \times \dots \times_N \mathbf{U}_k^{(N)T}$.

(5) For each data $\mathcal{A}_i^{\text{Rec}_s} = c_{i,s} \cdot \mathcal{B}_s$.

ALGORITHM 2: Iteration algorithm of LTC.

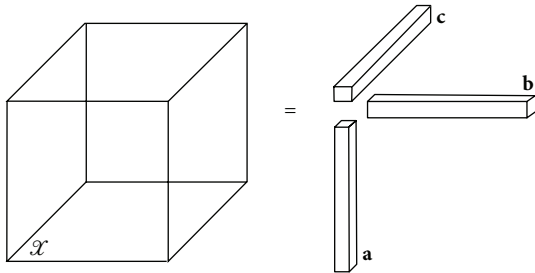


FIGURE 3: Rank-one 3rd-order tensor, $\mathcal{X} = \mathbf{a} \circ \mathbf{b} \circ \mathbf{c}$.

The symbol “ \circ ” represents the vector outer product. This means that each element of the tensor is the product of the corresponding vector elements: $x_{i_1 i_2 \dots i_N} = a^{(1)} a^{(2)} \dots a^{(N)}$, for all $1 \leq i_n \leq I_N$. Figure 3 illustrates $\mathcal{X} = \mathbf{a} \circ \mathbf{b} \circ \mathbf{c}$, a third-order rank-one tensor.

2.2. GND-PCA. GND-PCA was proposed by Xu and Chen for statistical appearance modeling of medical volumes with few samples [10]. The medical volume is treated as a 3rd-order tensor, and the optimal subspace on each mode is calculated simultaneously by minimizing the square error between the original volumes and reconstructed ones. In the following part of this section, we will briefly review the algorithm of GND-PCA.

Given a series of the N -order tensors with zero-means $\mathcal{A}_i \in \mathbb{R}^{I_1 \times I_2 \times \dots \times I_N}$, $i = 1, 2, \dots, M$, M is the number of samples. We aim to get another series of low rank $\{J_1, J_2, \dots, J_N\}$ tensors $\hat{\mathcal{A}}_i$ which accurately approximate the original tensors, where $J_n \leq I_n$. The new series is decomposed by the matrices $\mathbf{U}^{(n)} \in \mathbb{R}^{I_n \times J_n}$ with orthogonal columns according to the Tucker Model [13] which is shown by

$$\hat{\mathcal{A}}_i = \mathcal{B}_i \times_1 \mathbf{U}^{(1)} \times_2 \mathbf{U}^{(2)} \times \dots \times_n \mathbf{U}^{(n)} \times \dots \times_N \mathbf{U}^{(N)}, \quad (4)$$

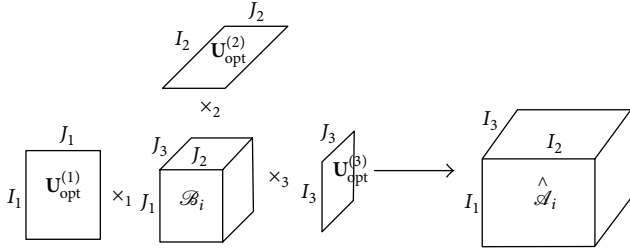


FIGURE 4: Illustration of reconstructing a third-order tensor by the principal component \mathcal{B}_i and the three orthogonal bases of mode subspaces $\mathbf{U}_{\text{opt}}^{(1)}$, $\mathbf{U}_{\text{opt}}^{(2)}$, $\mathbf{U}_{\text{opt}}^{(3)}$.

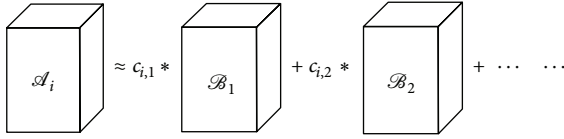


FIGURE 5: Example of representing the third-order tensor using a series of bases.

where $\mathcal{B}_i \in \mathbb{R}^{I_1 \times I_2 \times \dots \times I_N}$ are the core tensors. The product operator in (4) is matrix product. Tensor \mathcal{B}_i will unfold to matrix in each mode and then products with orthogonal matrix in each mode. The orthogonal matrices $\mathbf{U}^{(n)}$ can be determined by minimizing the cost function as

$$S = \sum_{i=1}^M \left\| \mathcal{A}_i - \mathcal{B}_i \times_1 \mathbf{U}^{(1)} \times_2 \mathbf{U}^{(2)} \times \dots \times_N \mathbf{U}^{(N)} \right\|^2. \quad (5)$$

The tensor \mathcal{B}_i is chosen as

$$\mathcal{B}_i = \mathcal{A}_i \times_1 \mathbf{U}^{(1)T} \times_2 \mathbf{U}^{(2)T} \times \dots \times_N \mathbf{U}^{(N)T}. \quad (6)$$

Minimization of (5) is equal to the maximization of the following equation:

$$S' = \sum_{i=1}^M \left\| \mathcal{A}_i \times_1 \mathbf{U}^{(1)T} \times_2 \mathbf{U}^{(2)T} \times \dots \times_N \mathbf{U}^{(N)T} \right\|^2. \quad (7)$$

There is no close-form solution to simultaneously resolve the matrices for (4); however, the explicit solution for one matrix can be obtained if the other matrices are fixed. This is expressed by Lemma 1 and is explained later.

Lemma 1. *Given the fixed matrices, $\mathbf{U}^{(1)}, \mathbf{U}^{(2)}, \dots, \mathbf{U}^{(n-1)}, \mathbf{U}^{(n+1)}, \dots, \mathbf{U}^{(N)}$, if the columns of the matrix $\mathbf{U}^{(n)}$ are selected as the first J_N leading eigenvectors of matrix $\sum_{i=1}^M (C_{i(n)} \cdot C_{i(n)}^T)$, where $C_{i(n)}$ is the mode- n matrix of the tensor $\mathcal{C}_i = \mathcal{A}_i \times_1 \mathbf{U}^{(1)} \times_2 \mathbf{U}^{(2)} \times \dots \times_{n-1} \mathbf{U}^{(n-1)} \times_{n+1} \mathbf{U}^{(n+1)} \times \dots \times_N \mathbf{U}^{(N)}$, the cost function S' can be maximized.*

The proof of Lemma 1 is given in [10], so here it will not be given again. According to Lemma 1 we can use an iteration algorithm to get the N optimal matrices, $\mathbf{U}_{\text{opt}}^{(1)}, \mathbf{U}_{\text{opt}}^{(2)}, \dots, \mathbf{U}_{\text{opt}}^{(N)}$, which are able to maximize the cost function S' . This algorithm is summarized by Algorithm 1.

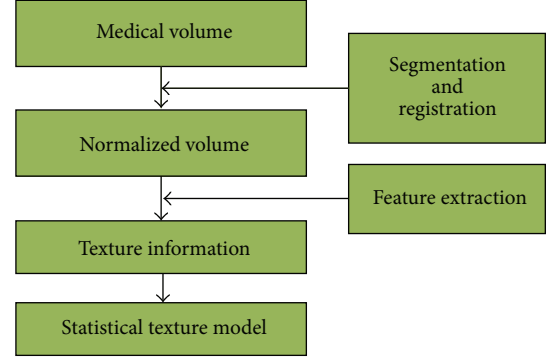


FIGURE 6: The flow chart of our experiment.

Using the calculated matrices $\mathbf{U}_{\text{opt}}^{(n)}$, $n = 1, 2, \dots, N$, each of the volume \mathcal{A}_i are represented with least errors $\hat{\mathcal{A}}_i$, where $\hat{\mathcal{A}}_i = \mathcal{B}_i \times_1 \mathbf{U}^{(1)} \times_2 \mathbf{U}^{(2)} \times \dots \times_n \mathbf{U}^{(n)} \times \dots \times_N \mathbf{U}^{(N)}$. The approximation can be illustrated by Figure 4 for the 3D case. The core tensors \mathcal{B}_i are the principle components.

3. Linear Tensor Coding

Although GND-PCA can achieve good performance on construction of statistical appearance models for medical volumes with few samples, it still has some disadvantages. Each basis of GND-PCA is not independent, so the core tensor of the final result is still redundant. And it is difficult to understand the meaning of each basis. Thus for given a series of the N -order tensors with zero-means $\mathcal{A}_i \in \mathbb{R}^{I_1 \times I_2 \times \dots \times I_N}$, $i = 1, 2, \dots, M$, we want to find another series of bases which have mutual independence and greater discrimination to represent the original tensors. Each tensor \mathcal{A}_i is represented by basis: $\mathcal{A}_i = \sum_{j=1} c_{i,j} \cdot \mathcal{B}_j$. Here the tensor \mathcal{B}_j is basis which has the same size as the input tensor, and the scalar $c_{i,j}$ is the coefficient of the tensor \mathcal{A}_i . Figure 5 illustrates the representation of one original tensor using a series of bases.

In mathematics, the problem of getting the compact representation can be formulated as the optimization equation

$$(\mathcal{B}_1, \mathcal{B}_2, \dots) = \arg \min \sum_{i=1}^M \left\| \mathcal{A}_i - \sum_{j=1} c_{i,j} \cdot \mathcal{B}_j \right\|. \quad (8)$$

Since the objective function is multiquadratic, there is no closed-form solution for this optimization. In addition, the number of bases is unfixed; hence, the optimization procedure is sensitive to initial estimation and easy to converge to local minima.

To address such problems, we have developed an algorithm: linear tensor coding algorithm (LTC) in our previous work [11, 12]. There are two important components in our algorithms; one is a local convergence to find optimized basis \mathcal{B}_j and the other is a global convergence to find the number of bases.

In the local parts, the GND-PCA method is applied for calculation of each basis. Inspired by (3), if we get N vectors,

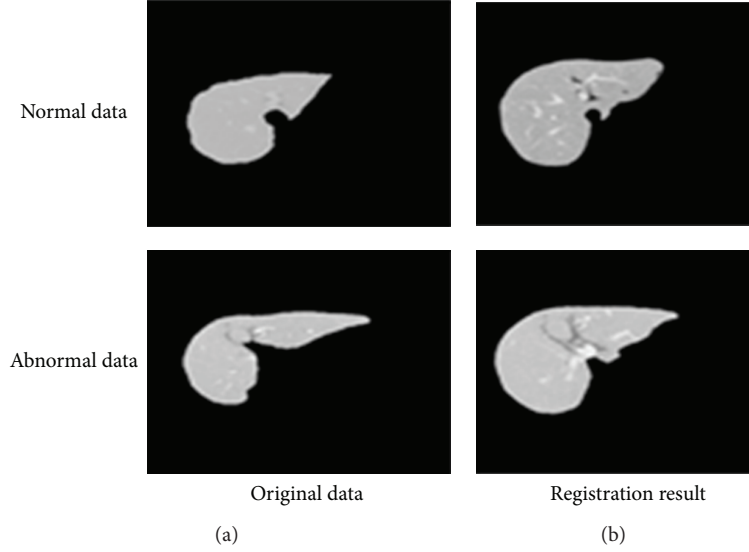


FIGURE 7: Original data and morphed data, respectively. The first column is original data and the second column is morphed data.

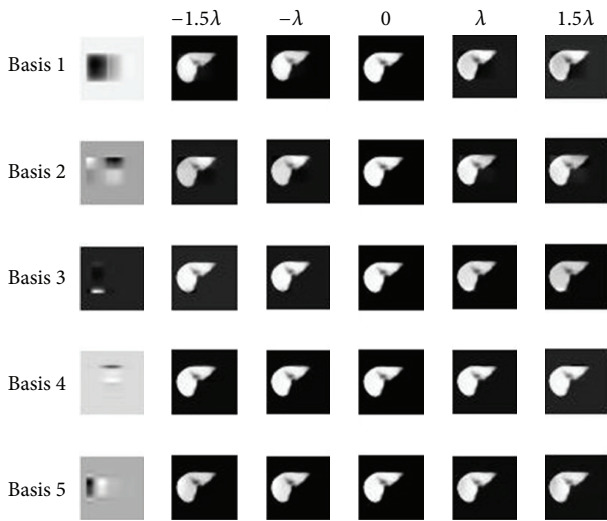


FIGURE 8: The slices of novel ensembles described by the first five bases, respectively. It changes the value of coefficients from $-1.5\lambda_1$ to $1.5\lambda_1$ of each basis.

we can generate an N -order tensor. Thus when we calculate the eigenspace on each mode, we only need the first vector $\mathbf{u}_1^{(i)}$ of each $\mathbf{U}^{(i)}$ which is the eigenvector with the largest eigenvalue in the corresponding mode. We choose $\mathbf{u}_1^{(i)}$, $1 \leq i \leq N$ as a set of initial estimations and the first tensor-formed base is calculated by

$$\mathcal{B}_1 = \mathbf{u}_1^{(1)} \circ \mathbf{u}_1^{(2)} \circ \dots \circ \mathbf{u}_1^{(N)}. \quad (9)$$

For each training tensor, the parameters corresponding to the first base are calculated by

$$c_{i,1} = \mathcal{A}_i \times_1 \mathbf{u}_1^{(1)T} \times_2 \mathbf{u}_1^{(2)T} \times \dots \times_N \mathbf{u}_1^{(N)T}. \quad (10)$$

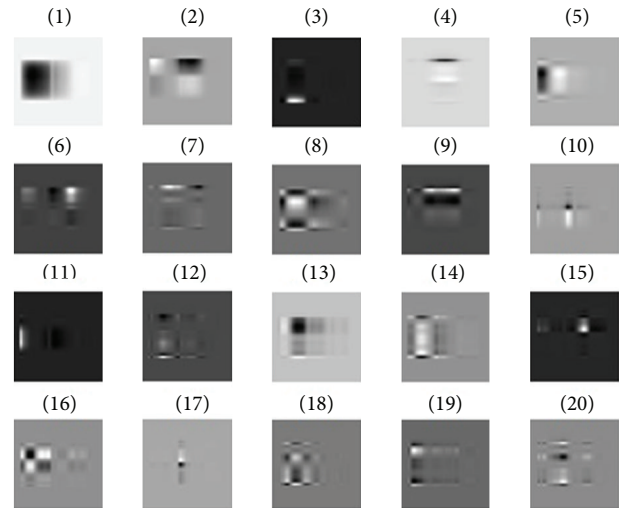


FIGURE 9: The first twenty bases. It illustrates that each basis can represent a local feature.

After getting the first base, we calculate the residual parts of each training tensor: $\overline{\mathcal{A}}_i = \mathcal{A}_i - c_{i,1} \cdot \mathcal{B}_1$. The residual parts $\overline{\mathcal{A}}_i$ are used instead of \mathcal{A}_i . Then the previous step was repeated, to calculate the basis one by one. The process to find a series of bases is a greedy approach to approximate the original tensors.

A global convergence is worked to find a number of bases. Recalling (8), we assign a threshold r . The process ends after finding the J basis, when the sum of norms of the residual tensors is below r , as shown in (11). Then each tensor data is represented with a group of coefficients with the benefit of the obtained basis. Consider

$$\text{norm} \left(\sum_{i=1}^M \left\| \mathcal{A}_i - \sum_{j=1}^J c_{i,j} * \mathcal{B}_j \right\| \right) \leq r. \quad (11)$$

The global process converges to a local minima, and thus there is no guarantee that there will be a global one. As this is a greedy approach, it suffers from the shortcoming that previous decisions are not reevaluated as the process unfolds. However, this specific greedy rule has a critical feature which makes it useful for tensor coding. Note that the optimization approach converges to a local minima in general, but in the case we just choose one base in LTC, one obtains GND-PCA for representing the data with a core tensor of which the rank of each mode is 1. So LTC can be considered as an extension of GND-PCA. The algorithm is shown in Algorithm 2.

4. Experimental Results

The proposed method is evaluated by using a liver database. In this database, there are 10 normal healthy ones and 10 abnormal ones. The size of each sample is $256 \times 256 \times 79$. The flow chart of our experiment is shown in Figure 6.

In order to remove shape variations, we apply a nonrigid transformation based on mathematical forms for morphing all the datasets to a same shape. Any nonrigid registration technique can be described by three components: a transformation which relates the target and source images, a similarity measure which measures the similarity between target and source image, and an optimization which determines the optimal transformation parameters as a function of the similarity. Additionally, we do not need to assume the physical parameters, which are difficult to guess in practice. Hence, we adopted the mathematical nonrigid transformation in our research. For the detailed process, please refer to [14].

The pretreated database is assigned as original database, and shape-normalized samples are assigned as morphed database. Figure 7 shows some original data and morphed data, respectively. The first column is original data and the second column is morphed data. The first row is one sample of the normal ones, and the second row is one sample of the abnormal ones. This illustrates that all the samples have familiar shapes, so the shape information does not effect experimental results.

Because we want to build a statistical texture model, each data can be represented by

$$\mathcal{A}_i = \mathcal{M} + \sum_{k=1}^K c_{i,k} * \mathcal{B}_k. \quad (12)$$

Here \mathcal{M} is the mean texture and $c_{i,k}$ are the coefficients. Supposing the coefficients $c_{i,k}$ to follow Gaussian distribution, we can estimate the mean m_k and derivation λ_k^2 .

By adjusting the parameter, we can construct a novel ensemble by

$$\widetilde{\mathcal{A}} = \mathcal{M} + \widetilde{c}_k * \mathcal{B}_k. \quad (13)$$

Here \widetilde{c}_k is adjusted coefficient, $-2\lambda_k \leq \widetilde{c}_k \leq 2\lambda_k$. Figure 8 illustrates the slices of novel ensembles described by the first five bases, respectively. They demonstrate that while changing the value of first coefficients from $-1.5\lambda_1$ to $1.5\lambda_1$, the intensity of left part has obviously changed, and the second basis mainly has effect on the right corner of

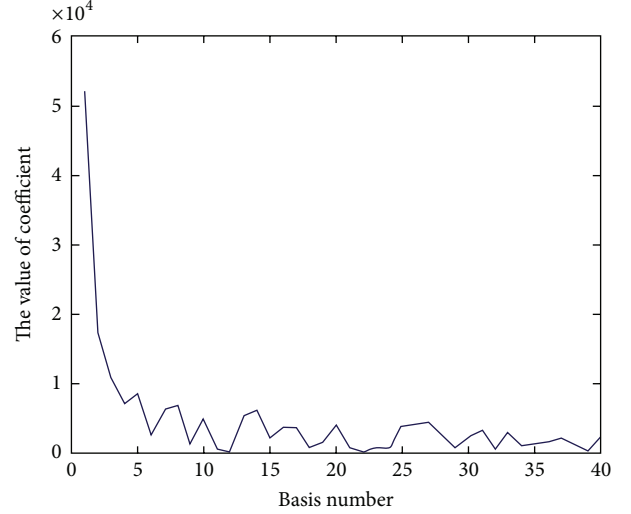


FIGURE 10: The coefficient of each basis for LTC.

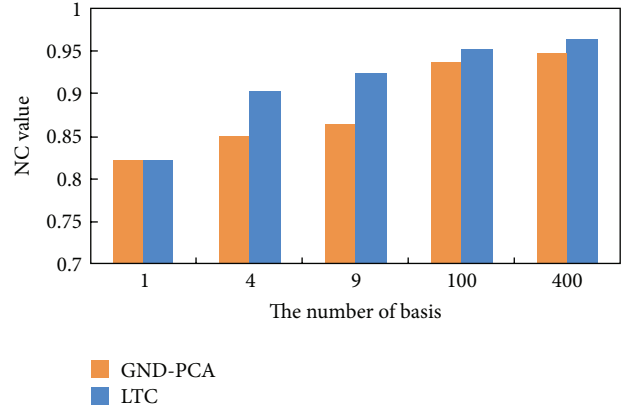


FIGURE 11: Reconstruction accuracy versus number of basis.

the slice. Furthermore, Figure 9 shows the first twenty bases; it illustrates that different bases can have effect on different parts. Thus we can change the local intensity of slice through change the coefficient of basis.

Figure 10 shows the values of coefficient when the number of bases is different for LTC. It illustrates that the first several values are obviously larger than the other ones. Because of this, the volume can be reconstructed by less bases than GND-PCA.

Figure 11 shows the graph of normalized correlation between original volume and reconstructed volume for different number of bases. The value of normalized correlation is between 0 and 1. The more similar the two volumes are, the larger its value is. The result in Figure 11 illustrates that the original volume can be better reconstructed by LTC when the number of bases is the same as GND-PCA.

For classification, the coefficients are used as the feature; SVM and KNN are utilized as classifiers, respectively. For LTC, we trained 1200 bases, and for GND-PCA, the size of core-tensor is $20 \times 20 \times 3$. And we used leave one out method to do the classification. Figure 12 shows the distribution of

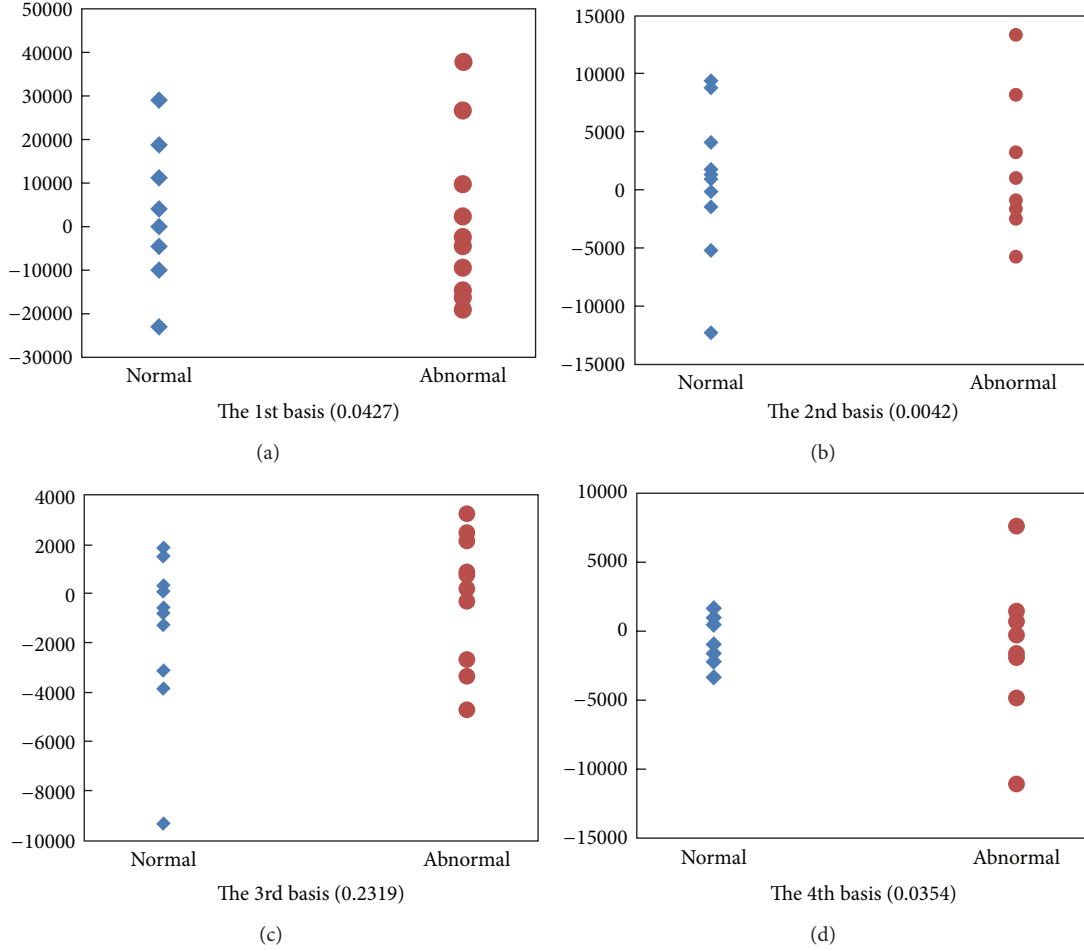


FIGURE 12: The distribution of coefficients of the first four bases. The blue one represents the normal liver and the red one represents the abnormal liver. The number in the brackets is the correlation coefficients.

coefficients of the first four bases of LTC. The blue ones are the normal livers, and the red ones are abnormal livers. The number in the brackets is the correlation coefficient which is calculated by

$$\text{correlation} = \frac{\sum_i^n (c_i - \bar{c})(l_i - \bar{l})}{\sqrt{\sum_i^n (c_i - \bar{c})^2 (l_i - \bar{l})^2}}. \quad (14)$$

Here, n is the number of samples, c_i is the coefficient of one fixed basis of LTC, and $l_i \in \{-1, 1\}$, $1 \leq i \leq n$, is the label of the samples. In our experiments, -1 represents normal liver, and 1 represents abnormal liver. For each basis, we can get a correlation coefficient. From the correlation coefficients in Figure 12, it illustrates that it is difficult for classification if using these basis because the correlation coefficients are so small. Thus, we firstly chose the basis using the correlation coefficients. But GND-PCA cannot choose basis because the core tensor is directly used for classification. Figure 13 shows the coefficients of the first four bases chosen through correlation coefficients. The blue ones are the normal livers, and the red ones are abnormal livers. The first number in the bracket is the position of basis in the original basis set and the

second number in the bracket is the correlation coefficient of corresponding basis.

Table 1 is the classification accuracy using different classifiers. Before choosing bases, we used all the basis for classification. We can see that the classification accuracies of LTC and GND-PCA are both bad. Then we choose the first one hundred bases which have greater correlation coefficients for classification. The classification accuracy is obviously improved.

5. Conclusion

In this paper, we describe a statistical texture modeling method for medical volumes which is known as LTC. LTC is an extension of GND-PCA. The medical volume such as the volume of the liver is represented by a linear combination of bases which have the same size as the tensor. Each basis is mutual independence and more discriminate than that of GND-PCA. In our experiments, we compared both reconstructed results and classification results of LTC and GND-PCA. As for reconstruction results, the performance of LTC is superior to that of GND-PCA. Additionally, in the classification part, we firstly chose the distinctive basis

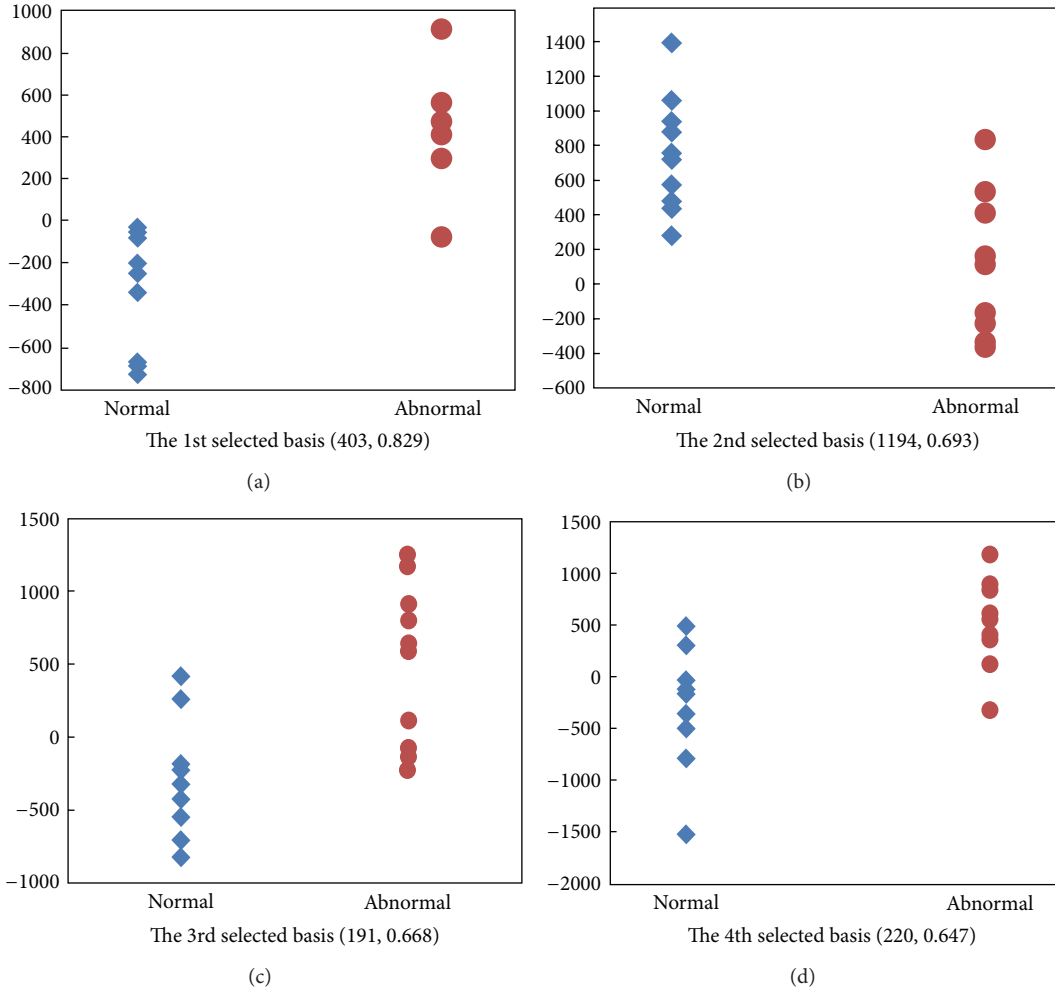


FIGURE 13: The distribution of coefficients of the first four basis chosen through correlation coefficients. The blue ones are the normal livers, and the red ones are abnormal livers. The first number in the bracket is the position of basis in the original basis set and the second number in the bracket is the correlation coefficient.

TABLE 1: The classification accuracy of GND-PCA and LTC.

	SVM	KNN
GND-PCA	7/20	10/20
LTC with all 1200 bases	7/20	9/20
LTC with 100 selected bases	19/20	19/20

through the correlation between category labels and the coefficients of basis of LTC. And then we use the selected basis for classification. The classification accuracy was significantly improved by the use of selected distinctive basis. Future work will involve testing our method with more data sets for classification and using our method in practical applications.

Acknowledgments

This work is supported in part by the Grant-in-Aid for Scientific Research from the Japanese Ministry for Education, Science, Culture and Sports under the Grant nos. 24300076,

24103710 and 24700179, as well as in part by the R-GIRO Research Fund from Ritsumeikan University.

References

- [1] F. H. Netterem, *Atlas of Human Anatomy*, WB Saunders, Philadelphia, Pa, USA, 2006.
- [2] K. H. Hohne, B. Pflesser, A. Pommert et al., “A new representation of knowledge concerning human anatomy and function,” *Nature Medicine*, vol. 1, no. 6, pp. 506–511, 1995.
- [3] T. F. Cootes, C. J. Taylor, D. H. Cooper, and J. Graham, “Active shape models-their training and application,” *Computer Vision and Image Understanding*, vol. 61, no. 1, pp. 38–59, 1995.
- [4] H. Huang, F. Makedon, and R. McColl, “High dimensional statistical shape model for medical image analysis,” in *Proceedings of the 5th IEEE International Symposium on Biomedical Imaging: From Nano to Macro (ISBI '08)*, pp. 1541–1544, Paris, France, May 2008.
- [5] H. C. van Assen, M. G. Danilouchkine, F. Behloul et al., “Cardiac LV segmentation using a 3D active shape model driven by fuzzy inference,” in *Proceedings of the 6th International Conference on*

- Medical Image Computing and Computer-Assisted Intervention (MICCAI '03)*, vol. 2878, pp. 533–540, 2003.
- [6] M. R. Kaus, J. von Berg, J. Weese, W. Niessen, and V. Pekar, “Automated segmentation of the left ventricle in cardiac MRI,” *Medical Image Analysis*, vol. 8, no. 3, pp. 245–254, 2004.
 - [7] S. Kohara, T. Tateyama, A. H. Foruzan et al., “Preliminary study on statistical shape model applied to diagnosis of liver cirrhosis,” in *Proceedings of the 18th IEEE International Conference on Image Processing (ICIP '11)*, pp. 2921–2924, Brussels, Belgium, September 2011.
 - [8] T. F. Cooles, G. J. Edwards, and C. J. Taylor, “Active appearance models,” *IEEE Transactions on Pattern Analysis and Machine Intelligence*, vol. 23, no. 6, pp. 681–685, 2001.
 - [9] S. C. Mitchell, B. P. F. Lelieveldt, R. van der Geest, J. Schaap, J. H. C. Reiber, and M. Sonka, “Segmentation of cardiac MR images: an active appearance model approach,” in *Medical Imaging 2000: Image Processing*, vol. 3979 of *Proceedings of SPIE*, San Diego, Calif, USA, February 2000.
 - [10] R. Xu and Y. Chen, “Generalized N-dimensional principal component analysis (GND-PCA) and its application on construction of statistical appearance models for medical volumes with fewer samples,” *Neurocomputing*, vol. 72, no. 10–12, pp. 2276–2287, 2009.
 - [11] X. Qiao, T. Lgarashi, K. Nakao, and Y. W. Chen, “Linear tensor coding for efficient representation of multi-dimensional data,” in *Proceedings of the MIRU 2010*, 2010.
 - [12] X. Qiao, X. T. Su, X. H. Han, and Y. W. Chen, “A new linear coding algorithm for efficient multi-dimensional data representation without data expansion,” in *Proceedings of the International Conference on New Trends in Information Science, Service Science and Data Mining (ISSDM '12)*, pp. 475–478, Taiwan, China, 2012.
 - [13] L. de Lathauwer, B. de Moor, and J. Vandewalle, “A multilinear singular value decomposition,” *SIAM Journal on Matrix Analysis and Applications*, vol. 21, no. 4, pp. 1253–1278, 2000.
 - [14] X. Qiao and Y. W. Chen, “A statistical texture model of the liver based on generalized N-dimensional principal component analysis (GND-PCA) and 3D shape normalization,” *International Journal of Biomedical Imaging*, vol. 2011, Article ID 601672, 8 pages, 2011.

Research Article

Classification of Pulmonary Nodules by Using Hybrid Features

Ahmet Tartar,¹ Niyazi Kilic,² and Aydin Akan²

¹ Department of Engineering Sciences, Istanbul University, 34320 Avcılar, Istanbul, Turkey

² Department of Electrical and Electronics Engineering, Istanbul University, 34320 Avcılar, Istanbul, Turkey

Correspondence should be addressed to Ahmet Tartar; atartar@istanbul.edu.tr

Received 28 March 2013; Revised 24 May 2013; Accepted 29 May 2013

Academic Editor: Chung-Ming Chen

Copyright © 2013 Ahmet Tartar et al. This is an open access article distributed under the Creative Commons Attribution License, which permits unrestricted use, distribution, and reproduction in any medium, provided the original work is properly cited.

Early detection of pulmonary nodules is extremely important for the diagnosis and treatment of lung cancer. In this study, a new classification approach for pulmonary nodules from CT imagery is presented by using hybrid features. Four different methods are introduced for the proposed system. The overall detection performance is evaluated using various classifiers. The results are compared to similar techniques in the literature by using standard measures. The proposed approach with the hybrid features results in 90.7% classification accuracy (89.6% sensitivity and 87.5% specificity).

1. Introduction

Computer aided detection (CAD) system is an extremely important task for the detection of pulmonary nodules in medical images. To attain a more reliable and accurate diagnosis, CAD systems have been recently developed to assist interpretation of the medical images. The systems that find true positive findings from the medical images are especially important in that they can also help radiologists in the identification of early stage pulmonary nodules. To best interpret the information revealed in the images, experienced physicians are required; however, such experts may reach different diagnosis results for the same set of medical imaging. Thus, CAD system is an intensive tool that can provide radiologists with a second opinion to improve the sensitivity of their diagnosis decision-making process [1]. The aim of a CAD system is to provide diagnosis information to improve clinical decision-making process; therefore, its success is related directly to its disease detection accuracy [2]. Today, CAD systems are frequently utilized to detect and diagnose numerous abnormalities in routine clinical work. CAD systems are usually specialized in anatomical regions such as the thorax, breast, or colon by using certain medical imaging technologies such as radiography, computed tomography (CT), or magnetic resonance imaging (MRI) [3].

Recently, lung cancer is still considered a major cause of deaths from cancer worldwide. In particular, it is one of the main public health issues in the developed industrial countries [4, 5]. This makes the treatment of lung cancer a very important task in the war against cancer. Early detection of potentially cancerous pulmonary nodules is highly important for improving the patient's chance of survival. Multidetector computed tomography system is a very sensitive imaging modality to detect small pulmonary nodules.

In previous studies, classification systems were developed by using the features of nodule candidate patterns with image-processing techniques [6–8], by classifying the shape of pulmonary nodule patterns [9, 10] and by using morphological features [11, 12]. To classify lung nodules, neural network approaches [13, 14] and Fisher linear discriminant classifier [15, 16] were proposed. In addition, several approaches have been proposed to detect pulmonary nodules in thin-slice helical computed tomography images [17, 18]. Similar techniques are introduced by using genetic algorithm with the random subspace method [19, 20], a single support vector machine [21], and random forest classifiers [22, 23]. Recently, the ensemble learning methods have been applied to classification problems [24, 25]. Especially, the ensemble learning algorithms such as bagging and adaboost are shown to be superior to a single classifier [26, 27].

In this study, a combination of four different methods was proposed for feature extraction from CT images.

Method 1. Two-dimensional principal component analysis (2D-PCA) applied to dataset.

Method 2. Statistical features obtained from 2D-PCA values.

Method 3. Geometric features obtained by using the regional descriptors of the 2D patterns based on the basic morphological shape information.

Method 4. Selecting the best features of the above three methods with mRMR (minimum Redundancy Maximum Relevance) method, hybrid features are obtained by combining the best features.

To perform a rigorous validation with the proposed system, completely independent training and testing datasets are utilized. All nodules in the dataset are first tuned/trained using a dataset provided as a courtesy of the University of Istanbul, Cerrahpasa Faculty of Medicine.

A classification task forms the backbone of a computer aided detection system. In this paper, we propose a new classification approach for pulmonary nodules using hybrid features to be used in such a CAD system. The objective of the proposed study is to analyze the effect of the hybrid features on classification of pulmonary nodules. The proposed classification approach has several novel potential roles.

- (i) To be used as an effective filtering method to reduce the number of false positives in a CAD system.
- (ii) To increase the diagnostic accuracy of the detection system.

The rest of this paper is organized as follows. The proposed classification approach for a CAD system and methods used in the algorithm are described in Section 2. This section includes the database information, feature extraction, feature selection, and classifier algorithms. Overall performance of the proposed system as well as comparisons with six other previously presented CAD systems is presented in Section 3. Conclusions are given in Section 4.

2. Materials and Methods

2.1. Pulmonary Nodule Database and Imaging Protocol. In the study, dataset containing 95 pulmonary nodules and 75 nonnodules patterns obtained from two-dimensional (2D) CT images from 63 patients was utilized. The 2D pulmonary nodule patterns are manually marked on CT image by radiologists. Then, the nodule pattern is extracted from the CT image as illustrated in Figure 1. Other patterns in the lung parenchyma similar to nodules but not marked as “nodule” by the radiologists are selected as the member patterns of nonnodule class. Images are collected from 39 male and 24 female patients whose ages are ranging from 25 to 78 years [mean = 55.4 ± 12.3 years]. The number of pulmonary nodules detected in the right and left lung parenchyma, as illustrated in Figure 2, is a total of 67 (20 in the upper part, 20 on the bottom part, and 27 pleural cases) and a total of 28

(12 in the upper part, 8 on the bottom part, 8 pleural case), respectively.

The average nodule diameter is 6.42 ± 3.00 mm. The diameter distribution of the nodules used in the database is shown in Figure 3. Also nodule and nonnodule pattern samples used in dataset are given in Figure 4. The age distribution of the patients is illustrated in Figure 5.

The dataset was obtained from chest CT images of patients scanned by using “Sensation 16” CT scanner (Siemens Medical Systems) between 2010 and 2012 at Radiology Department, Cerrahpasa Medicine Faculty, Istanbul University. CT scans were acquired at a tube potential voltage of 120 kVp. All CT images are in size of 512×512 pixels and stored as DICOM (Digital Imaging and Communications in Medicine) format files, directly from the CT modality.

2.2. Feature Extraction

2.2.1. Two-Dimensional Principal Component Analysis (2D-PCA). Principal component analysis (PCA) is defined as a classical dimension reduction method for feature extraction and data representation technique widely used in the areas of pattern recognition, computer vision, and signal processing [28]. Eigenvalue and eigenvector components are ranked according to their variance to the principal axes and ranked from having the most contribution to the least one. Number of the reduced dimension is based on summed contribution of the eigenvalues exceeding 99%. It provides a dimensionality reduction with an unsupervised learning algorithm [29]. Consider the following.

Let x be an n -dimensional column vector. The project image A is an $m \times n$ matrix, onto x by $y = Ax$. In order to determine the optimal projection vector x , the total scatter of the projected samples S_x is utilized to measure the optimality of x

$$S_x = x^T E \{ [A - E(A)]^T [A - E(A)] \} x = x^T S_A x, \quad (1)$$

where S_A depicts the image covariance matrix.

Suppose that there are M training samples A_i $\{i = 1, 2, 3, \dots, M\}$ and \bar{A} is the average image,

$$S_A = \frac{1}{M} \sum_{i=1}^M [A_i - \bar{A}]^T [A_i - \bar{A}]. \quad (2)$$

The optimal projection direction x_{opt} denotes the eigenvector of S_A corresponding to the largest eigenvalue. Usually a set of orthonormal projection directions, x_1, x_2, \dots, x_d , are chosen. These projection directions are the orthonormal eigenvectors of S_A corresponding to the first d largest eigenvalues.

For a given A , let $y_k = Ax_k$ $\{k = 1, 2, \dots, d\}$. A set of projected feature vector y_k and the principal components of A are found. The feature matrix of A is obtained as $B = [y_1, y_2, \dots, y_d]$. The nearest neighborhood classifier is

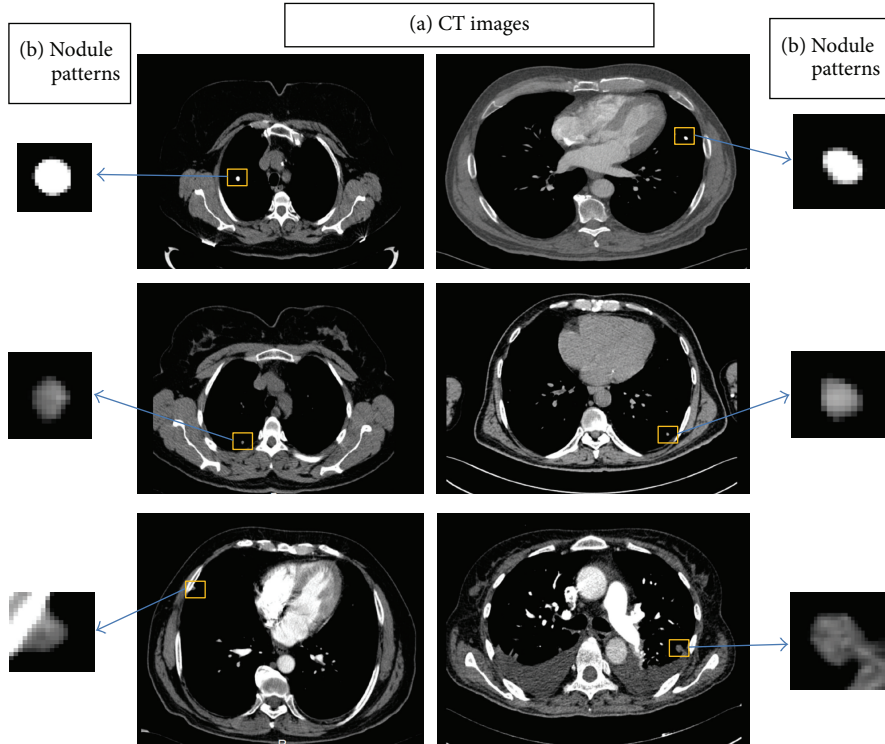


FIGURE 1: Two-dimensional image samples: (a) CT images and (b) pulmonary nodule patterns.

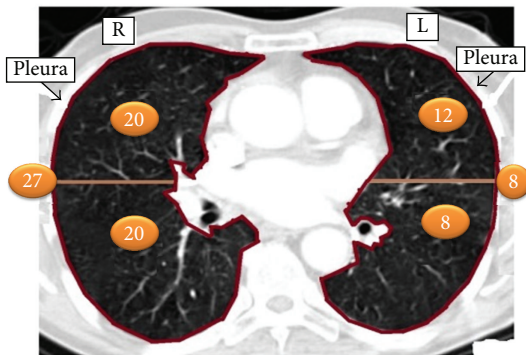


FIGURE 2: Representation of the number of pulmonary nodules in the right and left lung parenchyma.

adopted for classification. The distance between two arbitrary feature matrices, B_i and B_j , is given by

$$d(B_i, B_j) = \sum_{k=1}^d \|y_k^i - y_k^j\|_2, \quad (3)$$

where $\|y_k^i - y_k^j\|_2$ depicts the Euclidean distance between y_k^i and y_k^j [30].

A classification process is the basis of a computer aided detection system. The classification scheme proposed for a computer-aided detection algorithm used in this work is shown in Figure 6.

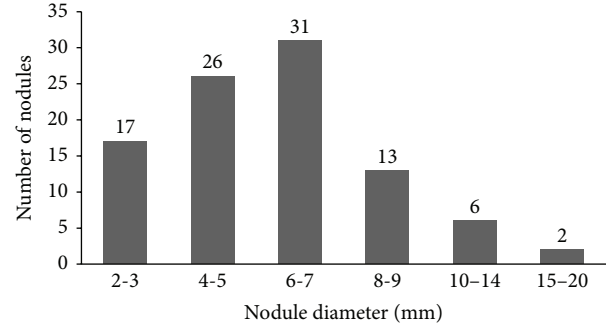


FIGURE 3: Histogram representing the distribution of the diameter for the 67 nodules of the database.

2.2.2. Morphological Image Processing. Morphology is a cornerstone of the mathematical set of tools underlying the development of techniques that extract the meaning features from an image [31]. To extract the features of pulmonary nodules, geometric features were obtained by using the regional descriptors of the 2D patterns based on the basic morphological shape information. The geometric features consist of the area, perimeter, diameter, solidity, eccentricity, aspect ratio, compactness, roundness, circularity, ellipticity of the patterns in this study.

These features are given by its definitions in Table 1. A total of 10 features are evaluated for extracting features of the patterns. From these features, *Solidity* denotes the proportion of the pixels in the convex hull that are also in the region. *Eccentricity* depicts the eccentricity of the ellipse that has the

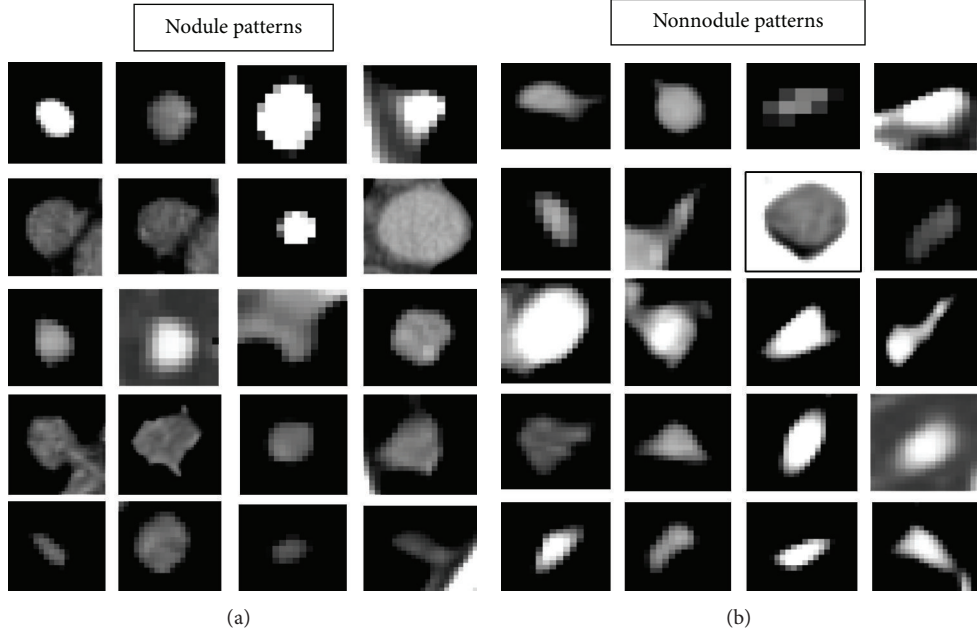


FIGURE 4: Nodule and nonnodule pattern samples used in dataset.

TABLE 1: Geometric features used for pulmonary nodule detection.

Measure	Definition
Area	A
Perimeter	P
Diameter	D
Solidity	S
Eccentricity	E
Aspect ratio	$\frac{\text{Min. diameter } (M)}{\text{Max. diameter } (L)}$
Compactness	$\frac{P^2}{4\pi A}$
Roundness	$\frac{4A}{\pi L^2}$
Circularity	$\frac{4\pi A}{P^2}$
Ellipticity	$\frac{\pi L^2}{2A}$

same second moments as the region. Also it is the ratio of the distance between the foci of the ellipse and its major axis length. The value of eccentricity is between 0 and 1. Measurements of compactness, roundness, circularity and ellipticity are computed by the definitions given in Table 1 [37].

2.3. Feature Selection

2.3.1. The mRMR Method. The mRMR (minimum Redundancy Maximum Relevance) method from the feature selection methods has been providing shorter calculation time and higher accuracy for the classifier. The mRMR method was

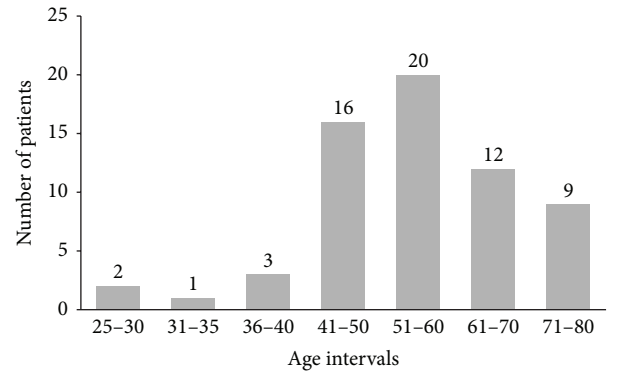


FIGURE 5: Histogram representing the age distribution of patients.

proposed by Peng et al. [38]. The mRMR method uses the mutual information between a feature and a class or a feature and another feature. The relevance of a feature set S for the class c is defined by the average of all mutual information values between individual feature x_i and class c ,

$$\max D(S, c), \quad D = \frac{1}{|S|} \sum_{x_i \in S} I(x_i; c), \quad (4)$$

where $I(x_i, c)$ denotes the mutual information between feature x_i and class c . The redundancy of all features in the set S is defined by the average of all mutual information values between the feature x_i and the feature x_j ,

$$\min R(S), \quad R = \frac{1}{|S|^2} \sum_{x_i, x_j \in S} I(x_i, x_j), \quad (5)$$

where $I(x_i, x_j)$ is the mutual information between features x_i and x_j . The mRMR criteria, that is, the combination of

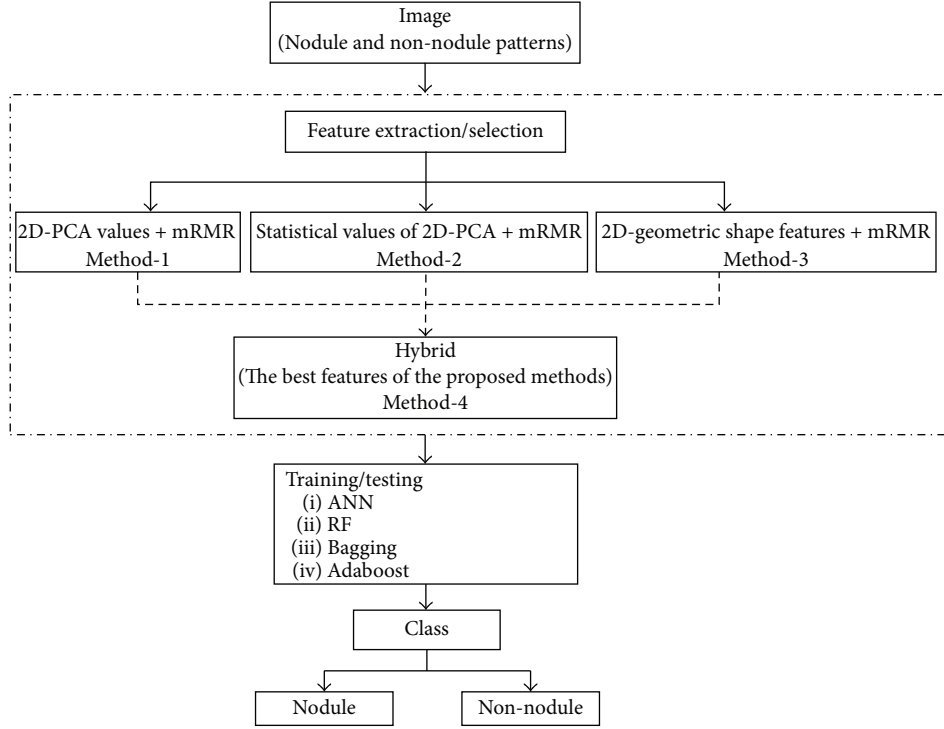


FIGURE 6: The classification scheme proposed for a CAD system.

two measures given in (4) and (5), are given by the following terms:

$$\text{the difference criterion: } \max(D - R), \quad (6)$$

$$\text{the quotient criterion: } \max\left(\frac{D}{R}\right). \quad (7)$$

As a result, the best feature set is obtained by optimizing expressions of (4) and (5) simultaneously according to (6) or (7).

2.4. Nodule Classification

2.4.1. Artificial Neural Network. An artificial neural network (ANN) is one of the tools of artificial intelligence intended to imitate the complex operation of organizing and processing information of the neurons in the human brain. ANN can recognize patterns correlating strongly with a set of data which correspond to a class by a learning process, in which interneuron connection weights are utilized to store knowledge about specific features identified within the data [39]. It is used for reducing experimental work and time losses. A common ANN is the multilayer perceptron (MLP) algorithm which is made up from three layers as shown in Figure 7. The ANN is trained by entering information from the input layer through the hidden and output layers of the network [40]. The ANN is performed by using the back-propagation algorithm based on the Levenberg-Marquardt rule [41].

The output signal for the l th neuron in the n th layer is given by the following expression:

$$y_l^n(t) = \varphi \left[\sum_{j=1}^p w_{lj}^n(t) y_j^{n-1}(t) + \Psi_l^n \right], \quad (8)$$

where $\varphi(\cdot)$ denotes the activation function, w_{lj}^n depicts the connection weight, t denotes the time index, and $\Psi_l^n = w_{l_0}^n(t)$ depicts the weights. The synaptic weight $w_{ji}^n(t)$ is defined by the following expression ($1 \leq n \leq N$):

$$\Delta w_{ji}^n(t+1) = w_{ji}^n(t) + \Delta w_{ji}^n(t). \quad (9)$$

And it is revised as the following:

$$\Delta w_{ji}^n(t) = \eta \lambda_j^n(t) y_i^{n-1}(t), \quad (10)$$

where η depicts the learning rate ($0 < \eta < 1$). Also the local error gradient is given by

$$\lambda_j^n(t) \equiv \frac{\partial E_t}{\partial u_j^n}. \quad (11)$$

To improve the performance of the back-propagation algorithm, a momentum term α is added as the following:

$$\Delta w_{ji}^n(t) = \eta \lambda_j^n(t) y_i^{n-1}(t) + \alpha \Delta w_{ji}^n(t-1), \quad (12)$$

where α is between 0 and 1. For the output layer, the local error gradient is defined by

$$\lambda_j^N(t) = [d_j(t) - y_j^N(t)] \varphi[u_j^N(t)] \equiv e_j(t) \varphi[u_j^N(t)], \quad (13)$$

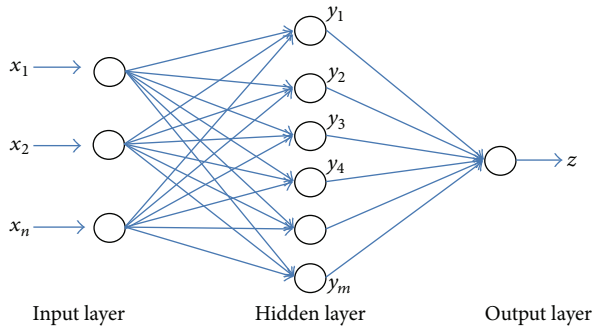


FIGURE 7: An artificial neural network structure.

where $d_j(t)$, $\varphi(\cdot)$ depict the goal output signal and the activation function, respectively.

2.4.2. Random Forest. Random forest was proposed by Breiman in 1999 [42]. It is a new development in tree based classifiers and fast proven to be one of the most important algorithms in the machine learning. It is defined as a combination of tree predictors depending on the values of a random vector sampled independently and with the same distribution for all trees in the forest. Random forest has given robust and improved results of classifications on standard data sets. It is providing very good competition to neural networks and ensemble techniques on different classification problems. Random forest is related to special type of ensembles using bagging and random splitting methods to grow multiple trees [42, 43].

There are several advantages for the Random forest method. Especially, Random forest can predict what features are important in the classification. It can process efficiently large data sets. Also it can be utilized as an effective method to estimate missing data.

2.4.3. Bagging. Bagging is unstable learning algorithm for small data set if small changes in the training data will generate very diverse classifiers. The use of bagging to improve performance by taking advantage of this effect was proposed by Breiman [44]. A single classifier could have a higher test error. The combination of classifiers can produce a lower test error than that of the single classifier because the diversity of classifiers usually compensates for errors of any single classifier [45]. A learning algorithm combination in those small changes in the training set leads to relatively large changes in accuracy.

2.4.4. Adaboost. Adaboost is one of the powerful methods for pattern recognition [46]. Adaboost classifier firstly introduced by Freund and Schapire [47, 48] is an ensemble classifier composed of many weak classifiers for the two-class classification problem. It generates strong classifier with weak classifiers. Adaboost makes a committee of member weak classifiers by adaptively adjusting the weights at each loop. While the weights of the training patterns classified correctly

by a weak classifier are decreased, the weights of the training patterns misclassified by the weak classifier are increased.

Adaboost algorithm shows good performance effect because of the ability to generate expanding diversity. In order to improve the performance result of the final ensemble, adaboost algorithms consist of diverse weak classifiers. Especially, the boosting algorithm adaboost.M1—the first directly—extends the original adaboost algorithm to the multiclass case without reducing it to multiple two-class problems.

Principal component analysis, mRMR method, and morphological image processing algorithms are performed by using the Matlab codes. Classification processes were provided by using data mining software called the Weka tool version 3.7.7 which is available from <http://www.cs.waikato.ac.nz/~ml/weka/>. Tests are done on a PC with Intel Core i7, 1.90 GHz CPU, and 4.00 GB RAM. For evaluating the classifiers, 5-fold cross-validation technique is used.

3. Results

Various classification methods are utilized for feature extraction and selection in medical pattern recognition. In this study, two-dimensional principal component analysis and geometric feature values were used for feature extraction. The mRMR method was applied for feature selection. The entire dataset is randomly partitioned into training and testing sets. The entire dataset is divided into approximately 50% training dataset and 50% test dataset. The training dataset consists of 47 pulmonary nodules and 37 nonodule patterns (total number of patterns is 84). The test dataset consists of 48 pulmonary nodules and 38 nonodule patterns (a total of 86 patterns). The best features for each method are determined using the mRMR feature selection only in the training dataset. Then, the classification accuracies of the methods are calculated using these features in the test dataset.

In the study, four different methods were proposed. For principal component analysis on method 1, the largest first seven values were selected for the first seven principal components because of highest variance value. So that, a 7×7 -dimensional matrix was formed for each pattern. Then, 1×49 -dimensional feature vector was obtained. In this way, at least 99% value of the total variance for each pattern was taken into account. To select the best features that contribute to the performance of classification system in the training set, the mRMR method was utilized. The number of best features performed with the mRMR method was determined as 20.

In method 2, the statistical features, *minimum* (min), *maximum* (max), *mean*, *standard deviation* (std), *variance* (var), and *3rd moment* values, are calculated in the training dataset. Thus, a 1×6 -dimensional feature vector was obtained. The best feature ranking that performed with the mRMR method is *3rd moment*, *min*, *mean*, *std*, *max*, and *var*. The number of best features performed with the mRMR method was the first 5 features which are *3rd moment*, *min*, *mean*, *std*, and *max*.

TABLE 2: Overall performance results of the proposed classification approach.

	Sensitivity (%)	TCA (%)	Specificity (%)	AUROC	Kappa	RMSE
Method 1						
ANN	87.5	84.9	83.8	0.928	0.693	0.356
RF	87.5	80.2	81.8	0.889	0.594	0.375
Bagging (ANN)	100	61.6	100	0.599	0.145	0.557
Bagging (RF)	87.5	86.0	84.2	0.911	0.717	0.339
Adaboost (ANN)	87.5	81.4	82.4	0.920	0.619	0.416
Adaboost (RF)	83.3	75.6	75.8	0.880	0.498	0.384
Method 2						
ANN	85.4	83.7	81.6	0.913	0.670	0.327
RF	83.3	83.7	80.0	0.890	0.672	0.356
Bagging (ANN)	100	60.5	100	0.616	0.116	0.522
Bagging (RF)	83.3	81.4	78.9	0.912	0.623	0.346
Adaboost (ANN)	81.3	80.2	76.9	0.869	0.600	0.385
Adaboost (RF)	83.3	80.2	78.4	0.901	0.598	0.351
Method 3						
ANN	83.3	83.7	80.0	0.893	0.672	0.358
RF	81.3	77.9	75.7	0.869	0.551	0.383
Bagging (ANN)	39.6	59.3	52.5	0.738	0.224	0.482
Bagging (RF)	83.3	84.9	80.5	0.912	0.696	0.344
Adaboost (ANN)	83.3	83.7	80.0	0.867	0.672	0.378
Adaboost (RF)	85.4	83.7	81.6	0.906	0.670	0.348
Method 4						
ANN	89.6	90.7	87.5	0.940	0.812	0.307
RF	85.4	83.7	81.6	0.908	0.670	0.335
Bagging (ANN)	60.4	66.3	59.6	0.770	0.333	0.463
Bagging (RF)	87.5	86.0	84.2	0.922	0.717	0.325
Adaboost (ANN)	87.5	86.0	84.2	0.921	0.717	0.334
Adaboost (RF)	85.4	80.2	80.0	0.911	0.596	0.343

In method 3, geometric features based on the basic morphological shape information were utilized for the 2D patterns in the training dataset. The geometric features include the area, perimeter, diameter, solidity, eccentricity, aspect ratio, compactness, roundness, circularity, and ellipticity of the patterns. The number of best features performed with the mRMR method was 5 features consisting of *compactness*, *aspect ratio*, *area*, *solidity* and *ellipticity*.

A new hybrid approach for classification was introduced on method 4. A new feature vector was created by combining the best features of the above three methods, aiming at increasing the sensitivity of the proposed classification approach. A total of 30 features selected by the three methods were now applied to the test dataset.

Random forest, artificial neural networks, ensemble bagging with RF, ensemble bagging with ANN, ensemble adaboost with RF, and ensemble adaboost with ANN classifiers were separately applied in all of the methods.

The classifiers were compared, and overall performance results of the proposed classification approach were given in Table 2. The performance measurements are given by

$$\text{sensitivity} = \frac{TP}{TP + FN}, \quad (14)$$

$$\text{specificity} = \frac{TN}{TN + FP}, \quad (15)$$

$$\text{TCA} = \frac{TP + TN}{TP + FP + TN + FN}, \quad (16)$$

$$\text{RMSE} = \sqrt{\frac{\sum (y' - y)^2}{n}}, \quad (17)$$

$$\text{FPR} = \frac{FP}{FP + TP}, \quad (18)$$

where TP, TN, FP, and FN denote the number of nodules classified as true positive, true negative, false positive, and false negative, respectively. FPR is false positive rate per image.

Sensitivity is the number of correctly predicted positives divided by the total number of positive cases. Specificity is the number of correctly predicted negatives divided by

TABLE 3: Confusion matrixes classified by the proposed methods.

	TP	FP	FN	TN
Method 1				
ANN	42	6	7	31
RF	42	6	11	27
Bagging (ANN)	48	0	33	5
Bagging (RF)	42	6	6	32
Adaboost (ANN)	42	6	10	28
Adaboost (RF)	40	8	13	25
Method 2				
ANN	41	7	7	31
RF	40	8	6	32
Bagging (ANN)	48	0	34	4
Bagging (RF)	40	8	8	30
Adaboost (ANN)	39	9	8	30
Adaboost (RF)	40	8	9	29
Method 3				
ANN	40	8	6	32
RF	39	9	10	28
Bagging (ANN)	19	29	6	32
Bagging (RF)	40	8	5	33
Adaboost (ANN)	40	8	6	32
Adaboost (RF)	41	7	7	31
Method 4				
ANN	43	5	3	35
RF	41	7	7	31
Bagging (ANN)	29	19	10	28
Bagging (RF)	42	6	6	32
Adaboost (ANN)	42	6	6	32
Adaboost (RF)	41	7	10	28

the total number of negative cases. TCA (*total classification accuracy*) represents the probability of correctly classified patterns. For RMSE (*root mean squared error*), y , y' , and n depict actual value, predicted value, and number of data patterns, respectively. In order to measure the performance of the classification system, AUROC is often used as well as sensitivity and specificity [49]. AUROC represents the area under the receiver operating characteristic curve. Kappa statistics is a chance-corrected measure of agreement between the classifications and the true classes. If Kappa is equal to 1, it indicates perfect agreement. If Kappa is equal to 0, it represents chance agreement.

Confusion matrixes of the classifiers in the proposed methods were shown in Table 3.

A ROC curve is usually used as a technique to visualize the performance of classifiers and is extremely useful to compare the performance of different classifiers in medical decision-making systems. The curve indicates the tradeoff between the true positive and false positive rates.

The area under ROC (*AUROC*) used here is largely adopted to represent the expected performance of a classifier. The AUROC of a classifier is equivalent to the probability that the classifier ranks a randomly chosen positive instance

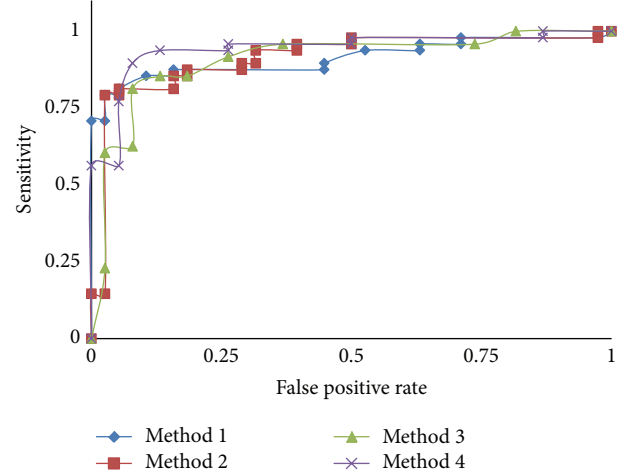


FIGURE 8: ROC curves showing CAD performance with the methods proposed.

higher than a randomly chosen negative instance [50]. For our proposed methods, ROC curves are illustrated in Figure 8.

3.1. Performance Comparison. To evaluate the performance of the classification approach, the results of this study were compared with previously reported CAD systems. It is highly difficult task to make comparison between previously published CAD systems due to different datasets, nodule size or type, and nodule or nonnodule patterns. It is still important to make a relative comparison. It is obviously shown that the performance results of a CAD system can differ significantly depending on those variables.

A single 2D slice is selected for each 3D object as seen in Figure 1. Pulmonary nodules are observed on a several slice range of the whole CT scan. Radiologists inspect these slices for the 2D patterns then select and label the pulmonary nodule pattern which has the largest dimension (i.e., area, diameter). Thus, when any physician detects a pulmonary nodule on the CT slices, he/she chooses the largest 2D pattern which is labeled and used in the dataset.

For comparative analysis, it is examined recently and reported that CAD systems have utilized the LIDC (Lung Image Database Consortium) database to evaluate detection systems [32–34]. Opfer and Wiemker [32] utilized the dataset comprised of 93 cases (2–3 mm slice thickness) with 127 nodules. Sahiner et al. used the dataset having a total of 73 nodules by combining 28 CT scans from the LIDC and 20 scans from another database [34]. Rubin et al. used a total of 84 CT scans with a total of 143 nodules in the range of 3–30 mm in nodule size [33]. Other papers utilized their own databases for the performance analysis of CAD system [35, 36, 51]. Suzuki et al. used the dataset of 20 CT scans (1.25 mm slice thickness and 0.6 mm pixel interval) containing 195 noncalcified nodule patterns (≥ 3 mm) [35]. Tartar et al. utilized low-dose CT images scanned from 71 different patients with a total of 121 nodules (8–20 mm nodule size interval), totaling 101 CT scans (10 mm slice thickness

TABLE 4: Comparison of the classification performance of reported CAD systems.

CAD system	Nodule size used (mm)	Reported sensitivity (%)
Opfer and Wiemker [32]	≥ 4	74.0
Rubin et al. [33]	≥ 3	76.0
Sahiner et al. [34]	3–36.4	79.0
Suzuki et al. [35]	8–20	80.3
Tartar et al. [36]	2–20	82.1
Messay et al. [15]	3–30	82.66
Proposed approach	2–20	89.6

and 0.586–0.684 pixel interval) [36]. Shiraishi et al. used the dataset containing 67 pulmonary nodules and 67 nonnodules obtained from 46 patients in our previous study [51].

In this study, a dataset containing 95 pulmonary nodules and 75 nonnodules patterns obtained from two-dimensional CT images from 63 patients is used. All of our CT scans are scanned by using the standard imagery protocol. A comparison of the performance of reported CAD systems was shown in Table 4. As seen from the table, the proposed classification approach achieved a sensitivity of 89.6% and an accuracy of 90.7% in the range of 2–20 mm nodule size. All other CAD systems have reasonable sensitivity values in classification of pulmonary nodules. It is extremely important to consider the small nodule size in the classification of a CAD system. This increases the probability of early detection of nodules. Considering these results, it can be seen that the proposed study represents a relatively high sensitivity. In addition, the overall false positive rate per image is calculated as 0.079 by using the expression of (18) for the hybrid approach.

4. Conclusions

In this paper, a new classification approach of pulmonary nodules for a CAD system from CT imagery is presented. An important feature of a CAD system desired by radiologists is that it is able to detect and classify small nodule patterns. The dataset in our study is composed of nodules with relatively smaller diameters (>2 mm), as shown in Figure 3 and Table 4.

In the literature, various classification algorithms for CAD systems have been extensively studied. In order to reduce the complexity of the algorithm and the computational load, the use of fewer features is extremely important, while maintaining an acceptable detection performance. For example, the CAD system in Messay et al. [15] uses 40 features selected from a set of 245 features with sensitivity of 82.66%, Hardie et al. [16] uses a subset of 46 features selected from a set of 114 features by sensitivity of 78.1%, and Shiraishi et al. [51] utilizes 71 features by sensitivity of 70.4%, respectively. In this study, in order to choose the best set of image features characterizing the patterns, various feature extraction/selection methods such as 2D-PCA, statistical features of 2D-PCA, morphological image processing based

on geometric features, and mRMR feature selection method were implemented.

The performances of the proposed approaches are evaluated by using different classifiers and performance metrics such as accuracy, sensitivity, specificity, AUROC, Kappa statistic, and RMSE. The proposed classification approach utilizes 30 features combined by the hybrid approach with sensitivity of 89.6%, accuracy of 90.7, and specificity of 87.5%.

Considering the test results in Table 2, ensemble learning algorithms yield the best performances on the features suggested in methods 1 and 3. However, especially, in the hybrid approach (method 4) combining the best features of the three methods, nonlinear multilayered ANN is shown to be superior to the other classifiers. Our approach uses ANN classifier with fewer features to avoid generalization problems, high complexity, and computational burden that can be caused by using an ANN with very large number of (potentially irrelevant) features. In addition, as shown in Table 3, false positive (FP) rate is shown to decline in the hybrid approach which provides higher detection performance by using fewer features.

Conflict of Interests

The authors have no conflict of interests with the trademarks included in the paper.

Acknowledgment

This work was supported by Scientific Research Projects Coordination Unit of Istanbul University, Project Numbers: 24014, 14381, 31474, and 35119.

References

- [1] K. Doi, "Computer-aided diagnosis in medical imaging: historical review, current status and future potential," *Computerized Medical Imaging and Graphics*, vol. 31, no. 4-5, pp. 198–211, 2007.
- [2] M. L. Giger, H.-P. Chan, and J. Boone, "Anniversary paper: history and status of CAD and quantitative image analysis: the role of Medical Physics and AAPM," *Medical Physics*, vol. 35, no. 12, pp. 5799–5820, 2008.
- [3] R. M. Summers, "Road maps for advancement of radiologic computer-aided detection in the 21st century," *Radiology*, vol. 229, no. 1, pp. 11–13, 2003.
- [4] "Cancer facts and figs," The American Cancer Society, 2009.
- [5] A. Jemal, R. Siegel, E. Ward, Y. Hao, J. Xu, and M. J. Thun, "Cancer statistics, 2009," *CA Cancer Journal for Clinicians*, vol. 59, no. 4, pp. 225–249, 2009.
- [6] K. Kanazawa, Y. Kawata, N. Niki et al., "Computer-aided diagnosis for pulmonary nodules based on helical CT images," *Computerized Medical Imaging and Graphics*, vol. 22, no. 2, pp. 157–167, 1998.
- [7] U. Bağcı, M. Bray, J. Caban, J. Yao, and D. J. Mollura, "Computer-assisted detection of infectious lung diseases: a review," *Computerized Medical Imaging and Graphics*, vol. 36, no. 1, pp. 72–84, 2012.
- [8] K. Murphy, B. van Ginneken, A. M. R. Schilham, B. J. de Hoop, H. A. Gietema, and M. Prokop, "A large-scale evaluation of

- automatic pulmonary nodule detection in chest CT using local image features and k-nearest-neighbour classification,” *Medical Image Analysis*, vol. 13, no. 5, pp. 757–770, 2009.
- [9] S. Iwano, T. Nakamura, Y. Kamioka, and T. Ishigaki, “Computer-aided diagnosis: a shape classification of pulmonary nodules imaged by high-resolution CT,” *Computerized Medical Imaging and Graphics*, vol. 29, no. 7, pp. 565–570, 2005.
- [10] S. Iwano, T. Nakamura, Y. Kamioka, M. Ikeda, and T. Ishigaki, “Computer-aided differentiation of malignant from benign solitary pulmonary nodules imaged by high-resolution CT,” *Computerized Medical Imaging and Graphics*, vol. 32, no. 5, pp. 416–422, 2008.
- [11] H. Chen, J. Zhang, Y. Xu, B. Chen, and K. Zhang, “Performance comparison of artificial neural network and logistic regression model for differentiating lung nodules on CT scans,” *Expert Systems with Applications*, vol. 39, pp. 11503–11509, 2012.
- [12] T. Kubota, A. K. Jerebko, M. Dewan, M. Salganicoff, and A. Krishnan, “Segmentation of pulmonary nodules of various densities with morphological approaches and convexity models,” *Medical Image Analysis*, vol. 15, no. 1, pp. 133–154, 2011.
- [13] D.-T. Lin, C.-R. Yan, and W.-T. Chen, “Autonomous detection of pulmonary nodules on CT images with a neural network-based fuzzy system,” *Computerized Medical Imaging and Graphics*, vol. 29, no. 6, pp. 447–458, 2005.
- [14] A. Retico, P. Delogu, M. E. Fantacci, I. Gori, and A. Preite Martinez, “Lung nodule detection in low-dose and thin-slice computed tomography,” *Computers in Biology and Medicine*, vol. 38, no. 4, pp. 525–534, 2008.
- [15] T. Messay, R. C. Hardie, and S. K. Rogers, “A new computationally efficient CAD system for pulmonary nodule detection in CT imagery,” *Medical Image Analysis*, vol. 14, no. 3, pp. 390–406, 2010.
- [16] R. C. Hardie, S. K. Rogers, T. Wilson, and A. Rogers, “Performance analysis of a new computer aided detection system for identifying lung nodules on chest radiographs,” *Medical Image Analysis*, vol. 12, no. 3, pp. 240–258, 2008.
- [17] J. J. Suárez-Cuenca, P. G. Tahoces, M. Souto et al., “Application of the iris filter for automatic detection of pulmonary nodules on computed tomography images,” *Computers in Biology and Medicine*, vol. 39, no. 10, pp. 921–933, 2009.
- [18] M. Hanamiya, T. Aoki, Y. Yamashita, S. Kawanami, and Y. Korogi, “Frequency and significance of pulmonary nodules on thin-section CT in patients with extrapulmonary malignant neoplasms,” *European Journal of Radiology*, vol. 81, no. 1, pp. 152–157, 2012.
- [19] M. C. Lee, L. Boroczky, K. Sungur-Stasik et al., “Computer-aided diagnosis of pulmonary nodules using a two-step approach for feature selection and classifier ensemble construction,” *Artificial Intelligence in Medicine*, vol. 50, no. 1, pp. 43–53, 2010.
- [20] W.-J. Choi and T.-S. Choi, “Genetic programming-based feature transform and classification for the automatic detection of pulmonary nodules on computed tomography images,” *Information Sciences*, vol. 212, pp. 57–78, 2012.
- [21] Q. Wang, W. Kang, C. Wu, and B. Wang, “Computer-aided detection of lung nodules by SVM based on 3D matrix patterns,” *Clinical Imaging*, vol. 37, no. 1, pp. 62–69, 2013.
- [22] S. L. A. Lee, A. Z. Kouzani, and E. J. Hu, “Random forest based lung nodule classification aided by clustering,” *Computerized Medical Imaging and Graphics*, vol. 34, no. 7, pp. 535–542, 2010.
- [23] A. Bosch, A. Zisserman, and X. Muñoz, “Image classification using random forests and ferns,” in *Proceedings of the IEEE 11th International Conference on Computer Vision (ICCV ’07)*, Rio de Janeiro, Brazil, October 2007.
- [24] E. Bauer and R. Kohavi, “An empirical comparison of voting classification algorithms: bagging, boosting, and variants,” *Machine Learning*, vol. 36, no. 1-2, pp. 105–139, 1999.
- [25] R. Maclin and D. Opitz, “Empirical evaluation of bagging and boosting,” in *Proceedings of the 14th National Conference on Artificial Intelligence (AAAI ’97)*, pp. 546–551, July 1997.
- [26] T.-K. An and M.-H. Kim, “A new diverse AdaBoost classifier,” in *Proceedings of the International Conference on Artificial Intelligence and Computational Intelligence (AICI ’10)*, pp. 359–363, Sanya, China, October 2010.
- [27] Z. Zhang and X. Xie, “Research on AdaBoost.M1 with random forest,” in *Proceedings of the 2nd International Conference on Computer Engineering and Technology (ICCET ’10)*, vol. 1, pp. 647–652, Chengdu, China, April 2010.
- [28] A. K. Jain, R. P. W. Duin, and J. Mao, “Statistical pattern recognition: a review,” *IEEE Transactions on Pattern Analysis and Machine Intelligence*, vol. 22, no. 1, pp. 4–37, 2000.
- [29] L. J. Hargrove, G. Li, K. B. Englehart, and B. S. Hudgins, “Principal components analysis preprocessing for improved classification accuracies in pattern-recognition-based myoelectric control,” *IEEE Transactions on Biomedical Engineering*, vol. 56, no. 5, pp. 1407–1414, 2009.
- [30] H. Kong, L. Wang, E. K. Teoh, X. Li, J.-G. Wang, and R. Venkateswarlu, “Generalized 2D principal component analysis for face image representation and recognition,” *Neural Networks*, vol. 18, no. 5-6, pp. 585–594, 2005.
- [31] R. Gonzales and R. Woods, *Image Processing*, Prentice Hall, New York, NY, USA, 2007.
- [32] R. Opfer and R. Wiemker, “Performance analysis for computer-aided lung nodule detection on LIDC data,” in *Medical Imaging 2007: Image Perception, Observer Performance, and Technology Assessment*, vol. 6515 of *Proceedings of the SPIE*, San Diego, Calif, USA, 2007.
- [33] G. D. Rubin, J. K. Lyo, D. S. Paik et al., “Pulmonary nodules on multi-detector row CT scans: performance comparison of radiologists and computer-aided detection,” *Radiology*, vol. 234, no. 1, pp. 274–283, 2005.
- [34] B. Sahiner, L. M. Hadjiiski, H.-P. Chan et al., “Effect of CAD on radiologists’ detection of lung nodules on thoracic CT scans: observer performance study,” in *Medical Imaging 2007: Image Perception, Observer Performance, and Technology Assessment*, vol. 6515 of *Proceedings of SPIE*, San Diego, Calif, USA, 2007.
- [35] K. Suzuki, S. G. Armato III, F. Li, S. Sone, and K. Doi, “Massive training artificial neural network (MTANN) for reduction of false positives in computerized detection of lung nodules in low-dose computed tomography,” *Medical Physics*, vol. 30, no. 7, pp. 1602–1617, 2003.
- [36] A. Tartar, N. Kılıç, and A. Akan, “Bagging support vector machine approaches for pulmonary nodule detection,” in *Proceedings of the International Conference on Control, Decision and Information Technologies*, Tunisia, May 2013.
- [37] C. Solomon and T. Breckon, *Fundamentals of Digital Image Processing: A Practical Approach With Examples in Matlab*, Wiley-Blackwell, 2011.
- [38] H. Peng, F. Long, and C. Ding, “Feature selection based on mutual information: criteria of max-dependency, max-relevance, and min-redundancy,” *IEEE Transactions on Pattern Analysis and Machine Intelligence*, vol. 27, no. 8, pp. 1226–1238, 2005.

- [39] L. Lancashire, S. Ugurel, C. Creaser, D. Schadendorf, R. Rees, and G. Ball, "Utilizing artificial neural networks to elucidate serum biomarker patterns which discriminate between clinical stages in melanoma," in *Proceedings of the IEEE Symposium on Computational Intelligence in Bioinformatics and Computational Biology (CIBCB '05)*, La Jolla, Calif, USA, November 2005.
- [40] H. I. Erdal, O. Karakurt, and E. Namli, "High performance concrete compressive strength forecasting using ensemble models based on discrete wavelet transform," *Engineering Applications of Artificial Intelligence*, vol. 26, no. 4, pp. 1246–1254, 2013.
- [41] I. Mukherjee and S. Routroy, "Comparing the performance of neural networks developed by using Levenberg-Marquardt and Quasi-Newton with the gradient descent algorithm for modelling a multiple response grinding process," *Expert Systems with Applications*, vol. 39, no. 3, pp. 2397–2407, 2012.
- [42] L. Breiman, "Random forests," Tech. Rep., Statistics Department, University of California, Berkeley, Calif, USA, 1999.
- [43] L. Breiman, "Random forests," *Machine Learning*, vol. 45, no. 1, pp. 5–32, 2001.
- [44] L. Breiman, "Bagging predictors," *Machine Learning*, vol. 24, no. 2, pp. 123–140, 1996.
- [45] D. Opitz and R. Maclin, "Popular ensemble methods: an empirical study," *Journal of Artificial Intelligence Research*, vol. 11, pp. 169–198, 1999.
- [46] H. Fan and H. Wang, "Predicting protein subcellular location by AdaBoost.M1 algorithm," in *Proceedings of the 2nd International Conference on Artificial Intelligence, Management Science and Electronic Commerce (AIMSEC '11)*, pp. 3168–3171, Deng Leng, China, August 2011.
- [47] Y. Freund and R. E. Schapire, "Experiments with a new boosting algorithm," in *Proceedings of the 13th Conference on Machine Learning*, pp. 148–156, 1996.
- [48] Y. Freund and R. E. Schapire, "A decision-theoretic generalization of on-line learning and an application to boosting," *Journal of Computer and System Sciences*, vol. 55, no. 1, pp. 119–139, 1997.
- [49] B. Li, K. Chen, L. Tian, Y. Yeboah, and S. Ou, "Detection of pulmonary nodules in CT images based on fuzzy integrated active contour model and hybrid parametric mixture model," *Computational and Mathematical Methods in Medicine*, vol. 2013, Article ID 515386, 15 pages, 2013.
- [50] T. Fawcett, "ROC graphs: notes and practical considerations for data mining researches," Tech. Rep. HPL-2003-4, HP Labs, 2003.
- [51] J. Shiraishi, Q. Li, K. Suzuki, R. Engelmann, and K. Doi, "Computer-aided diagnostic scheme for the detection of lung nodules on chest radiographs: localized search method based on anatomical classification," *Medical Physics*, vol. 33, no. 7, pp. 2642–2653, 2006.

Research Article

Segmentation of the Striatum from MR Brain Images to Calculate the ^{99m}Tc -TRODAT-1 Binding Ratio in SPECT Images

Ching-Fen Jiang,¹ Chiung-Chih Chang,² Shu-Hua Huang,³ and Chia-Hsiang Wu¹

¹ Department of Biomedical Engineering, I-Shou University, Kaohsiung 82445, Taiwan

² Department of Neurology, Chang Gung Memorial Hospital, Kaohsiung Medical Center, Chang Gung University College of Medicine, Kaohsiung 83301, Taiwan

³ Department of Nuclear Medicine, Chang Gung Memorial Hospital, Kaohsiung Medical Center, Chang Gung University College of Medicine, Kaohsiung 83301, Taiwan

Correspondence should be addressed to Ching-Fen Jiang; cfjiang@isu.edu.tw

Received 18 January 2013; Revised 3 June 2013; Accepted 4 June 2013

Academic Editor: Norio Tagawa

Copyright © 2013 Ching-Fen Jiang et al. This is an open access article distributed under the Creative Commons Attribution License, which permits unrestricted use, distribution, and reproduction in any medium, provided the original work is properly cited.

Quantification of regional ^{99m}Tc -TRODAT-1 binding ratio in the striatum regions in SPECT images is essential for differential diagnosis between Alzheimer's and Parkinson's diseases. Defining the region of the striatum in the SPECT image is the first step toward success in the quantification of the TRODAT-1 binding ratio. However, because SPECT images reveal insufficient information regarding the anatomical structure of the brain, correct delineation of the striatum directly from the SPECT image is almost impossible. We present a method integrating the active contour model and the hybrid registration technique to extract regions from MR T1-weighted images and map them into the corresponding SPECT images. Results from three normal subjects suggest that the segmentation accuracy using the proposed method was compatible with the expert decision but has a higher efficiency and reproducibility than manual delineation. The binding ratio derived by this method correlated well ($R^2 = 0.76$) with those values calculated by commercial software, suggesting the feasibility of the proposed method.

1. Introduction

Alzheimer's and Parkinson's diseases are two common neurodegenerative diseases associated with the aging process. The induced intellectual and functional deterioration of patients with these diseases can not only bring a heavy load to his/her family but also has an economic impact on society. Early diagnosis with appropriate treatment within a reasonable time frame can prevent abrupt degeneration of these diseases and distressing symptoms.

The current trend in the early diagnosis of such diseases is usually to adopt a combination of functional images and structural images to inspect the functional and structural changes in specific brain regions. However, qualitative observation alone limits early detection of neurodegenerative diseases, because the associated functional/structural changes are slowly progressive in the early stage and can be too subtle to be detected by human vision. Therefore,

quantification of these changes can facilitate early detection of neurodegenerative diseases.

SPECT imaging of dopamine transporter with ^{99m}Tc -TRODAT-1 (TRODAT-1) has been proposed to be a valuable and feasible means for the diagnosis of Parkinson's disease and dementia with Lewy bodies (DLB) [1–5]. The specific tracer, TRODAT-1, a radiolabeled tropane that binds dopamine transporters, allows *in vivo* assessment of the presynaptic dopaminergic neuron activity inside the striatum [3, 6]. SPECT images from patients with these diseases reveal a decrease in specific striatal uptake of TRODAT-1 in terms of a dull contrast of radioactivity between the striatum and adjacent brain tissue due to a selective loss of dopamine in the striatum. Even though several approaches show the feasibility of using TRODAT-1 SPECT in the evaluation of patients in the early stages of these neurodegenerative diseases, visual inspection or semi-auto quantification cannot avoid high intra- or interobserver variability and thus hampers

the associated diagnostic accuracy [7, 8]. A reliable automatic method could considerably speed up the procedure and make it more reproducible.

Even though some commercialized software packages provide automatic calculation of the TRODAT-1 binding ratio (BR), definition of the striatum in the SPECT image still relies on manual delineation. However, the brain structure is poorly-defined in SPECT images, which reveal more functional information than anatomical structural information. Therefore, demarcation of the region of interest (ROI) in the SPECT image is usually carried out by overlapping the SPECT images with the corresponding MR images, such that physicians can map the ROI delineated in the MR images to the SPECT images. Within this process, there are two key components of determining the accuracy of the TRODAT-1 binding quantification. First, the striatum should be correctly defined. Second, the MR images must be precisely registered with the corresponding SPECT images. However, even a well-trained physician can hardly guarantee obtaining accurate and repeatable results at these two stages. Therefore, this study aims to develop a robust method to fulfill the shortages in the current approaches.

Regarding the segmentation task for subcortical brain structures, several semiautomatic methods have been proposed. Worth et al. proposed the regional thresholding method to segment the caudate from the adjacent tissue [9]. A box was manually located to cover these three tissues, including the ventricles, the caudate, and some white matter, to derive a bimodal histogram, and then the threshold was determined as the mean of the two peaks of the histogram. However, the box location required human determination, and the vague boundaries of the caudate tail surrounded by gray matter still require manual drawing. Barra and Boire proposed a fuzzy-logic-based method to segment subcortical brain structures in MR images by integrating the numerical information derived from the wavelet features and structural information containing symbolized distance and relative direction coding [10]. More recently, Xia et al. took advantage of the high-contrast lateral ventricle as the reference to localize the upper and lower bonds of the caudate nucleus for region growing [11]. Fine-tuning according to the topological and morphological information was still required to smooth the initial segmentation. In view of these methods, as several factors, such as the complex anatomic brain structure, the connection of different tissues of a similar intensity, the heterogeneous intensity within the same class of tissue, and the partial volume effect, limit the performance of fully automatic segmentation of the striatum; therefore, using expert knowledge to refine the initial ROI derived by running the computer program was inevitable. However, visual confirmation and manual correction are conducted slice by slice and thus may still be labor intensive and time consuming.

Instead of applying expert knowledge in the last step to refine the segmentation in the previous studies, we propose a new approach using an active contour model to reverse the process of segmentation, that is, to let the expert determine the rough location of the striatum and allow the computer to perform the refinement, such that human intervention can be

minimized and the segmentation efficiency can be enhanced. The segmented regions were then mapped into the corresponding SPECT images via a hybrid registration method for BR calculation. These methods associated with the imaging protocol are described in detail in Section 2. To verify the reliability of the proposed method, the segmentation results and the derivative BRs were compared with those of experts assisted by commercial software. The results are presented and discussed, following which a brief conclusion is made.

2. Methods

We used hybrid SPECT/CT and 3D T1-weighted images to achieve the goal. Each volume played a distinct role in the overall process. The registration of the MR and the SPECT volume pairs was first conducted using the corresponding CT volume as a medium. After that, the striatum was segmented from the registered MR images. Once the MR images were adjusted to the same size under the same coordinates with the SPECT images through registration, the ROIs obtained by applying the active contour model to the registered MR images could be directly mapped into the SPECT images to calculate the binding potential. The overall process is summarized in Figure 1 and described in detail below.

2.1. Imaging Protocol. For this examination, all the patients were injected intravenously with a single bolus dose of 740 MBq (20 mCi) of ^{99m}Tc -TRODAT-1. Brain SPECT/CT (Symbia T; Siemens, Erlangen, Germany) images were obtained 4 hours later. The SPECT/CT scanner was equipped with low-energy high-resolution collimators and a dual-slice spiral CT. Acquisition parameters for SPECT were a 128×128 matrix, 500 mm FOV with 60 frames (40 s/frame). The scan parameters for the CT were 130 kV, 17 mAs, 5 mm slices, and image reconstruction with a medium-smooth kernel. The SPECT images were attenuation-corrected based on the CT images and scatter-corrected with Flash 3DR algorithm (ordered subsets expectation and 3D maximization with resolution correction) with 8 subsets and 8 iterations.

MR images were acquired using a 3.0 T MRI scanner (Excite, GE Medical Systems, Milwaukee, WI, USA). Structural images were acquired for an anatomical reference using a T1-weighted, inversion-recovery-prepared, three-dimensional, spoiled, and gradient-recalled acquisition in a steady-state sequence with repetition time/inversion time = 8,600 ms/450 ms, a 240×240 mm field of view and a 1 mm slice thickness.

2.2. Image Registration. To precisely map the ROI delineated from the MR into a corresponding position in the SPECT image, registration of the MR volume with the SPECT-CT volume was required. Even though several automatic registration methods have been proposed, their success is only guaranteed when the two scanning data to be registered contain consistent volumes. However, the clinical volume sets from different image modalities are usually truncated unevenly, lending additional difficulties to the application of conventional registration methods, such as principal axes

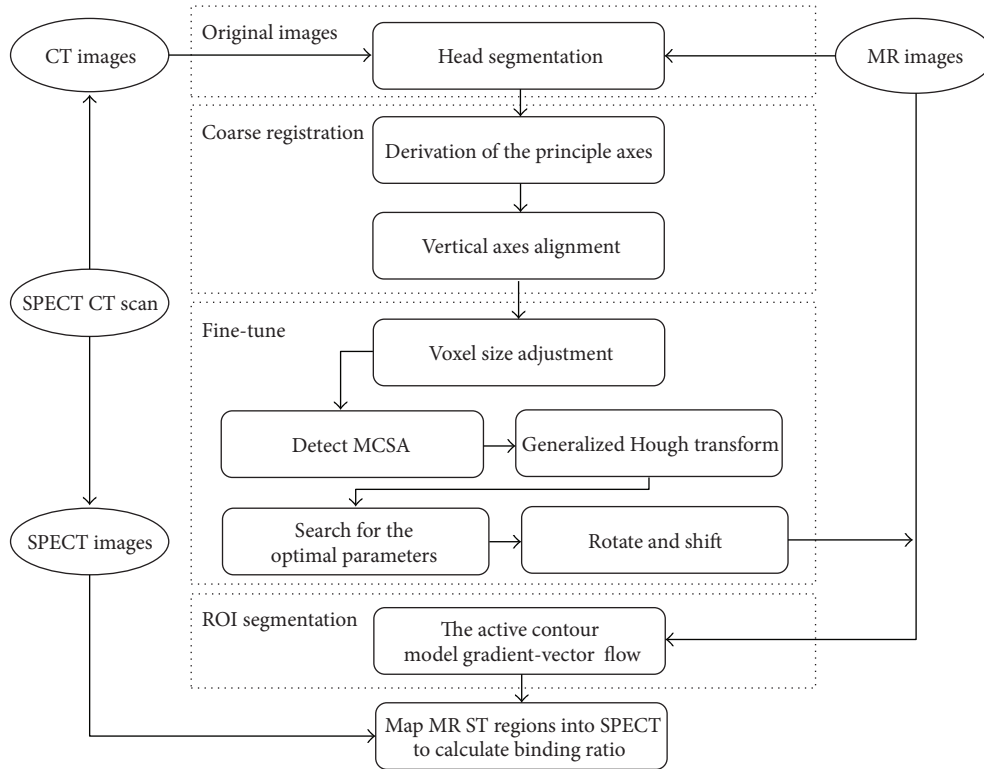


FIGURE 1: The overall process to derive the BRs in SPECT images via registration of the images from SPECT-CT and MR with ROI segmentation from the registered MR images.

registration (PAR) or mutual information (MI). To alleviate this problem, we developed a hybrid registration method combining principal axes registration with the general Hough transform [12]. In addition, we took advantage of SPECT-CT, which can acquire SPECT and CT images simultaneously, while the patient maintains his/her position on the same couch. Registration used the CT image as the registration medium to increase the registration accuracy between the SPECT and the MR image volumes. The registration process is fully automatic. The essential idea of the design is briefly described below.

The voxel size was adjusted to a 1mm^3 cube through bicubic interpolation prior to the following registration process. The 3D head was segmented as an entity to derive its three principal axes prior to registration. In this two-stage registration scheme, principal axes registration was first applied for coarse registration followed by fine-tuning via applying the general Hough transform to the contour of the maximal cross-sectional area (MCSA). The original concept of principal axes registration (PAR) is to superimpose the two volumes by aligning the corresponding three principal axes from both head volumes [13]. However, the registration accuracy of PAR is restricted by the degree of correspondence between the two sets of principal axes [14]. As the scanning range of one image modality is usually not the same as the other, the centroids of the two different volume sets would not be identical. In consequence, the two sets of principal axes derived from the different centroids do not coincide with each other. Therefore, in the coarse-registration stage,

we only adopted PAR to adjust the orientations of the long axis of the head to be parallel with the z -axis of the system coordinates. After this stage, the long axis from both head volumes coincided with each other, but the horizontal planes with the two short axes from the two volumes were still mismatched.

In the second stage, the registration error in the horizontal plane was then fine-tuned. We then turned the 3D registration task into a 2D one by searching for the slices containing the (MCSA) in both volumes, in that we had proved the reliability of using the MCSA as the anatomical feature for registration [15]. The vertical shift was first corrected by aligning these two slices; then the detected contour of the MCSA was used to derive the registration parameters via the generalized Hough transform (GHT). The process of the GHT algorithm in this approach included two steps. First, an R -table was built by calculating the vector set, $\{\vec{a}_i\}$, between each contour point (x_i, y_i) and the center of the contour, $P_c(x_c, y_c)$, in the CT image. Then, the corresponding center point (P'_c) was derived by searching for the maximal intersection via remapping the vector information to each contour point $\mathbf{X}_i(x_i, y_i)$ in the MR image. In this study, as there was no scale for reference and the voxel size had been adjusted to be the same, we adapted a robust search only for the rotation angle β in (1), when the optimal match between P_c and P'_c was achieved

$$\begin{aligned} x_c &= x_i + \gamma \cos(\theta + \beta), \\ y_c &= y_i + \gamma \sin(\theta + \beta), \end{aligned} \quad (1)$$

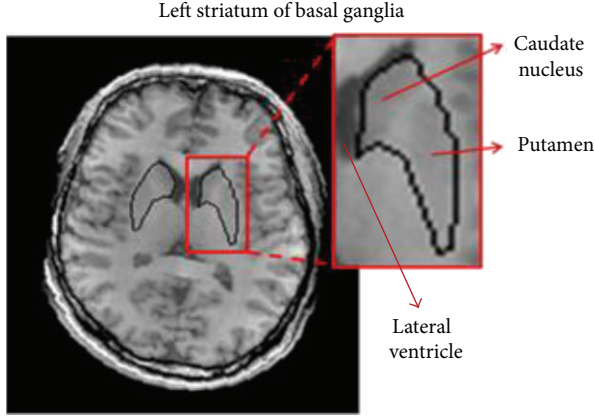


FIGURE 2: Anatomical structure of the striatum from the axial view of an MR T1-weighted image.

where θ is the angle between the directional vector \vec{a}_i and the positive direction of the x -axis and γ is the length of the \vec{a}_i .

The registration parameters of the rigid transform derived above were then applied to the MR volumes to match with the SPECT images.

2.3. ROI Segmentation from MR T1-Weighted Images. The registered MR T1-weighted images obtained from the previous stage were then used as the reference to demarcate the striatum on the corresponding SPECT images. As the assessment of TRODAT-1 BR is usually carried out from the axial view of SPECT images, the segmentation of the striatum was performed in the axial planes of the MR images. Figure 2 shows the structure of the striatum from the axial view of the MR image. It can be seen that the left and right sides of striatum of the basal ganglia are located beside the ventricle. Each side of the striatum can be further divided into the caudate nucleus and putamen. We named the two pairs of caudate nucleus and putamen the ST regions. However, the division of the ST regions is not obvious because they usually fuse with other brain structures. The unclear cut between the caudate nucleus and putamen and the surrounding brain structure brings up difficulties in isolating the ST regions solely using automatic image segmentation techniques without any expert intervention.

To segment these four ROIs, we adopted a modified active contour model. In this way, an initial contour of the first slice can be determined by an expert according to the topological and morphological characteristics of the ST. Once the location and shape of the ST regions are confined into the bond of the initial contour, then refinement can be carried out by the computer according to the intensity information. In addition, assuming smooth variation of the 3D ST region contour, the final contour of the present slice can be directly used as the initial contour for the next slice. To achieve this goal, the active contour model is a suitable choice.

The basis of the active contour model, named snake, is to represent an initial contour in the parametric form of

$v(s) = [x(s), y(s)]$, $s \in [0, 1]$ that deforms to the optimal shape by minimizing the energy functional

$$\begin{aligned} E_{\text{snake}} &= \int_0^1 [E_{\text{int}}(v(s)) + E_{\text{ext}}(v(s))] ds \\ &= \int_0^1 \frac{1}{2} [\alpha |v'(s)|^2 + \beta |v''(s)|^2 + E_{\text{ext}}(v(s))] ds, \end{aligned} \quad (2)$$

where α and β are the parameters to weight the influence on the curve deformation from the curve's tension $v'(s)$ and the rigidity $v''(s)$, respectively.

Theoretically, at the minima of the energy functional, the snake must satisfy the Euler equation

$$\alpha v''(s) - \beta v''''(s) - \nabla E_{\text{ext}}(v(s)) = 0. \quad (3)$$

As the first derivative of energy gives the force, the above equation can be interpreted as a force balance equation

$$F_{\text{int}}(v) + F_{\text{ext}}(v) = 0. \quad (4)$$

The internal force, $F_{\text{int}}(v) = \alpha v''(s) - \beta v''''(s)$, restricts the curve to stretch and bend, while the external force, $F_{\text{ext}}(v) = -\nabla E_{\text{ext}}(v)$, pulls the curve toward the desired image edges.

The snake is an active rather than a salient model due to the dynamic deformation process by treating the force balance equation as function of time t . Therefore, the solution of (3) can be approximated by iteratively searching for the steady state of the following equation, where the $v(s, t) = [x(s, t), y(s, t)]$ denotes $v(s)$ at the t th iteration

$$\frac{\partial v(s, t)}{\partial t} = \alpha v''(s, t) - \beta v''''(s, t) - \nabla E_{\text{ext}}(v(s, t)). \quad (5)$$

In practice, a numerical solution to (5) can be achieved by discretizing s iteratively using a finite difference method [16], as per

$$\begin{aligned} \mathbf{x}_t &= (\mathbf{A} + \gamma \mathbf{I})^{-1} (\mathbf{x}_{t-1} - \mathbf{p}_{x,t-1}), \\ \mathbf{y}_t &= (\mathbf{A} + \gamma \mathbf{I})^{-1} (\mathbf{y}_{t-1} - \mathbf{p}_{y,t-1}), \end{aligned} \quad (6)$$

where \mathbf{A} is a pentadiagonal matrix containing the constants α and β . The parameter of γ is the step size to control the degree of the contour deformation between iterations. \mathbf{I} is the unit matrix. \mathbf{x}_t and \mathbf{y}_t are the vectors consisting of the x - and y -coordinates of the contour $v(s, t)$, respectively. $\mathbf{p}_{x,t-1}$ and $\mathbf{p}_{y,t-1}$ are the vectors containing $\partial E_{\text{ext}}(x(s, t-1), y(s, t-1))/\partial x$, and $\partial E_{\text{ext}}(x(s, t-1), y(s, t-1))/\partial y$ as their elements for all s , respectively.

The external force (∇E_{ext}) in the active model can usually be classified into two types: static and dynamic. Static forces are derived from the image gradients, which do not change throughout the deformation process, while dynamic forces vary as the snake deforms. Using the image gradient as the external force makes the conventional snake difficult to move into a concave edge, because the null image gradients within a homogenous region inside the contour fail to attract the contour, and as a result, the contour is only affected by

the internal forces. Even though several dynamic external forces have been proposed to alleviate such a limitation of the static external forces, they also raised other problems, increasing the calculation complexity or leading to uncontrollable deformation [17, 18]. A new static external force, called *gradient-vector flow* (GVF), adding the directional property into the original image gradient map, was proposed by Xu and Prince to improve the performance of the static snake in concave edge detection [19]. Several reports have demonstrated the success of applying the GVF snake to medical image segmentation [20–23], including brain MRI [24]. This encouraged us to apply the GVF to segment the ST regions in our study.

The gradient-vector-flow field is defined as $\mathbf{v}(x, y) = [u(x, y), v(x, y)]$ such that the external energy function becomes

$$E_{\text{gvf}} = \iint [\mu (|\nabla u|^2 + |\nabla v|^2) + |\nabla f|^2 |\mathbf{v} - \nabla f|^2] dx dy, \quad (7)$$

where μ is a parameter to control the degree of smoothness of the gradient-vector-flow field and ∇f is an edge map derived from the original image $f(x, y)$.

To solve the equation numerically by discretization and iteration, let n indicate the times of iteration, and the increments in x , y , and t are all equal to 1. The relation of vector flows from the current to the next position can be derived as

$$\begin{aligned} u^{n+1}(x, y) &= (1 - |\nabla f|^2) u^n(x, y) \\ &+ \mu [u^n(x+1, y) + u^n(x, y+1) \\ &+ u^n(x-1, y) + u^n(x, y-1) \\ &- 4u^n(x, y)] + |\nabla f| f_x(x, y), \\ v^{n+1}(x, y) &= (1 - |\nabla f|^2) v^n(x, y) \\ &+ \mu [v^n(x+1, y) + v^n(x, y+1) \\ &+ v^n(x-1, y) + v^n(x, y-1) \\ &- 4v^n(x, y)] + |\nabla f| f_y(x, y). \end{aligned} \quad (8)$$

There are 4 parameters determined empirically to obtain the optimal results in the approach. The elasticity parameter (α) and the rigidity parameter (β) in (2) were set to be 0.1 and 0.2, respectively. The parameter (γ) in (6) was set to be 1. The external force weight (μ) in (7) was set to be 0.5.

3. Results and Discussion

3.1. Registration Results. An example is given in Figure 3 to illustrate the use of our developed interface to detect the slices containing the MCSA from the CT and MR volumes and register these two images through the GHT. Once the rigid transform with the registration parameters had been applied to the MR image volume, it can directly match the SPECT volume, as shown in Figure 4. The registration accuracy reached 96.48%. Our previous study quantitatively evaluated

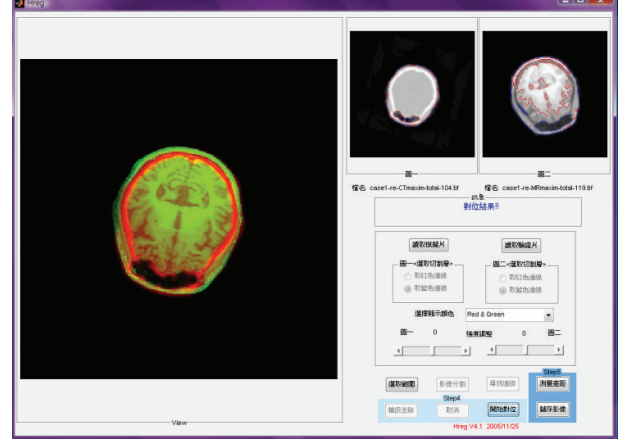


FIGURE 3: An example of registration of the CT image (middle small panel) and the MR image (right small panel) to render the final fused image (left large panel). The red and blue lines in the small panels are the detected boundaries and the contour of the head.

TABLE 1: Correspondence of the manual delineation between the observers.

JI (%)	Rater A-Rater B	Rater B-Rater C	Rater A-Rater C
Case 1	60.4 ± 4.8	62.1 ± 1.1	75.6 ± 2.1
Case 2	54.3 ± 4.5	54.7 ± 5.6	71.8 ± 5.2
Case 3	58.0 ± 4.7	58.1 ± 5.4	76.6 ± 5.2

the registration accuracy of the proposed method better than the results obtained solely using the PAR method or directly registering SPECT with MR images [12].

3.2. Segmentation Results. The expert delineation and the GVF segmentation of the ST regions containing two pairs of the caudate nucleus and putamen are given in Figure 5. A quantitative comparison of these two methods is given below.

We used the Jaccard index (JI) to quantify the degree of match between the two corresponding ROIs. The JI is defined as the ratio of the intersection of two volumes Ω_1 and Ω_2 by the union of them. If the two volumes completely overlap, the JI value is equal to 100%

$$JI = \frac{|\Omega_1 \cap \Omega_2|}{|\Omega_1 \cup \Omega_2|} \times 100\%. \quad (9)$$

The five sequential axial slices containing the ST from three normal cases were recruited in the comparative evaluation. Three neurologists first manually delineated the ST regions, including the caudate nucleus and putamen, on two lateral sides of the brain. The intrarater correspondences in terms of the mean and standard deviation of the JI values from the five slices are listed in Table 1, suggesting great differences between observers. It was found that Raters A and C had the highest correspondence, with a JI value greater than 70%.

The JI values were also derived by mapping the manually defined contours by each rater into the GVF segmented results. The initial contour of the first slice in each case was

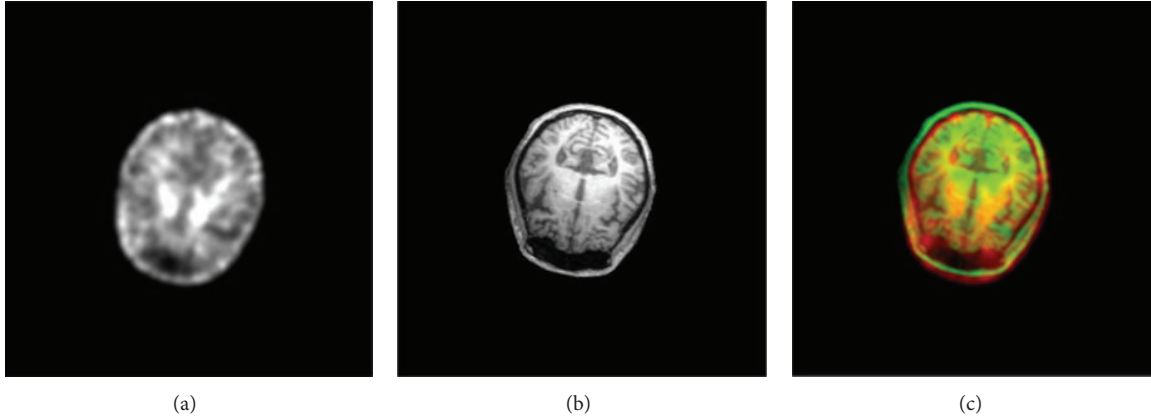


FIGURE 4: Registration between (a) SPECT and (b) MR to give the final overlaid image in (c).

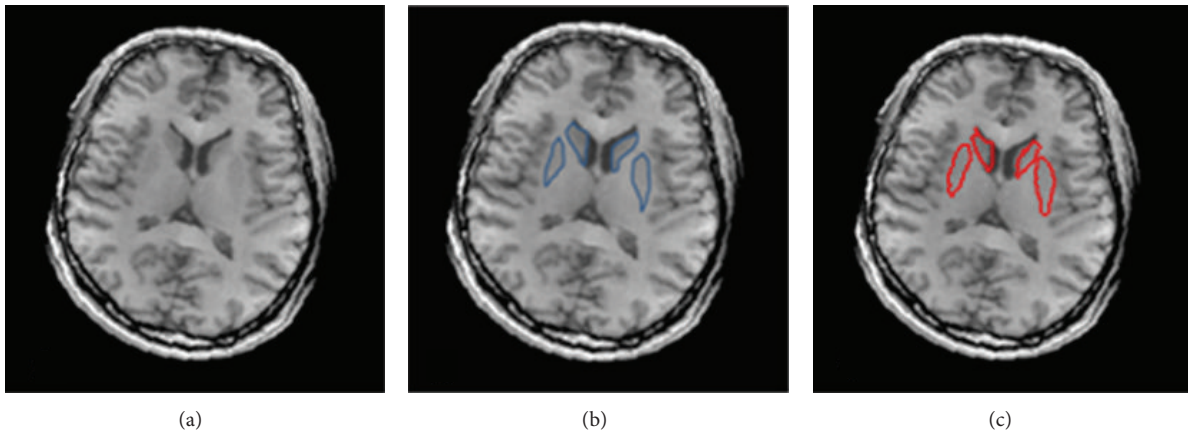


FIGURE 5: The ST regions in (a) the original MR T1-weighted image and the corresponding segmentation results by (b) manual delineation and (c) the GVF snake.

TABLE 2: Correspondence between manual delineation and the GVF snake result for each observer.

Jl (%)	Rater A-GVF snake	Rater B-GVF snake	Rater C-GVF snake
Case 1	64.4 ± 9.0	56.2 ± 5.5	65.3 ± 4.8
Case 2	68.6 ± 1.6	57.7 ± 5.1	65.4 ± 6.5
Case 3	61.1 ± 3.8	51.5 ± 3.1	59.9 ± 3.7

defined by the same specialist in the GVF snake process. Table 2 shows the correspondence with GVF segmentation. We used the paired t -test to evaluate the significance level between the JIs derived from the interrater comparison and those from the rater-GVF comparison for each slice in each case. The insignificant differences ($P = 0.124$ under a 95% confidence interval) suggest that the segmentation accuracy using the GVF snake is compatible with the level of manual drawing.

Rater A, the chief neurologist, was required to conduct the manual drawing twice. The JI values of the two delineations are listed in the middle column of Table 3, showing

TABLE 3: Correspondence between two repeated conductions of each method.

Slice no.	Jl (%)	
	Manual drawing	GVF deformation
1	66.3	77.05
2	61.2	73.31
3	53.34	78.3
4	51.3	71.46
5	45.57	78.44
Mean ± std	55.5 ± 8.2	75.7 ± 3.2

std: standard deviation.

that the correspondence declined along with the slice number. Instead of segmentation solely by hand, the GVF snake was also applied twice to the same set of images. Only the first slice required an initial contour manually defined by the rater each time. The JI values of repeated conduction of the GVF snake are also listed in the third column of Table 3, suggesting more stable results than those from slice-by-slice manual drawing.

In comparison with the index of overlap (similar to JI) between hand-drawing and computer-aided segmentation reported in the literature [9–11], the JI values obtained in our study were relatively low. This could be due to the extra region, that is, the putamen, involved in our study. The segmentation target of the previous reports is focused on the caudate nucleuses that are next to ventricles with greater contrast (Figure 1) and therefore more easily identified. In comparison with the caudate nucleuses, the low contrast of the putamen to the surrounding tissue increases the difficulty of extraction. Using expert hand drawing as the comparison basis seems to be the only choice in current studies, since there is no gold standard to determine the absolute accuracy of segmentation of the ST regions due to individual-dependent variation in the brain structure. However, we demonstrated that significant interobserver and intraobserver variability in such a decision exists even among the well-trained neurologists participating in our study, which was overlooked in previous studies. The inconsistency in decision-making could be incurred by the small size (in the order of 100 pixels) of the structures as compared with the imaging resolution and image noise. Under a compatible level of precision as shown in Tables 1 and 2, we demonstrated that the reproducibility and consistency improved when using the GVF snake segmentation method. In addition to stability, the GVF snake can save labor and provide a more efficient way than previous studies to define the ST regions contours in consecutive slices, as it only requires an initial contour drawn by hand in the first slice.

3.3. Binding Ratio Calculation. In the final stage of evaluation of the reliability of the proposed method, after completing the MR and SPECT image registration, the BRs were also derived from the segmented ST regions in the SPECT images using the proposed method to compare with those obtained using commercial software (Siemens Medical Systems, Knoxville, TN, USA), in which the ST regions were manually outlined by an expert. The BR was calculated by normalizing the mean intensity in the ST regions by the mean intensity in the occipital cortices. Linear regression analysis (Figure 6) revealed a close correlation ($CC = 0.874$, under 95% confidence interval) between the BRs derived by the two systems.

4. Conclusions

To calculate the regional TRODAT-1 binding ratio in SPECT studies, accurate and repeatable extraction of the ST regions from MR images is required to indirectly define the corresponding regions in the SPECT images. Segmentation directly on the SPECT image is not applicable in this case, because it distorts the ST regions. Clinical routine tends to apply manual delineation of the ST regions, which is prone to errors incurred through interobserver and intraobserver variability. Previous researchers have developed several segmentation algorithms to complete similar tasks, where expert decisions for anatomical and morphological information were still necessary to refine the results. As the localization

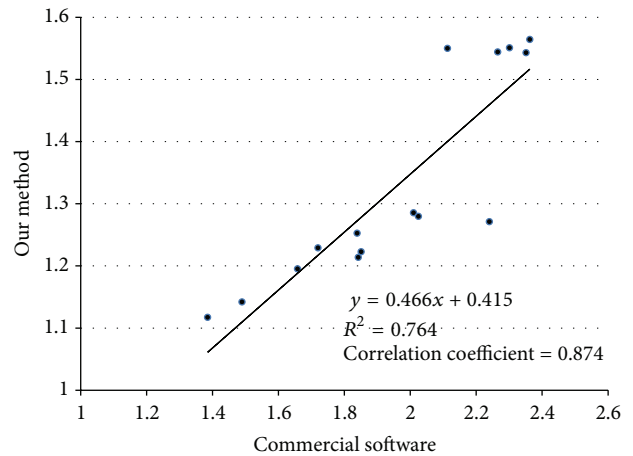


FIGURE 6: Linear regression analysis between the BRs derived by our method and those by the commercial software.

of the ST regions is a knowledge-driven task, the proposed method allowed the expert to assign the initial contour in the proper location and applied the gradient-vector-flow snake to approach the real contours. In such a way, the complexity of the algorithm can be reduced and the efficiency of segmentation can be increased. Results from three normal subjects showed a higher reproducibility of the proposed method than manual segmentation under compatible segmentation accuracy. The MR images with segmented ST regions were overlaid on the SPECT images using our previously developed registration algorithm to calculate the TRODAT-1 BR. The derived BRs correlated well with those derived using commercial software, suggesting a good reliability of the proposed method.

Acknowledgments

The authors would like to thank Dr. Chen Nai-Ching and Dr. Chi-Wei Huang from the Department of Neurology, Chang Gung Memorial Hospital, Kaohsiung Medical Center, Kaohsiung, Taiwan, for their kind assistance in the task of manual drawing of the ST regions in this study.

References

- [1] S. Asenbaum, “Nuclear medicine in neurodegenerative disorders,” *Imaging Decisions MRI*, vol. 6, pp. 19–28, 2002.
- [2] K. L. Chou, H. I. Hurtig, M. B. Stern et al., “Diagnostic accuracy of [^{99m}Tc]TRODAT-1 SPECT imaging in early Parkinson’s disease,” *Parkinsonism and Related Disorders*, vol. 10, no. 6, pp. 375–379, 2004.
- [3] J. L. Cummings, C. Henchcliffe, S. Schaiyer, T. Simuni, A. Waxman, and P. Kemp, “The role of dopaminergic imaging in patients with symptoms of dopaminergic system neurodegeneration,” *Brain*, vol. 134, no. 11, pp. 3146–3166, 2011.
- [4] A. Siderowf, A. Newberg, K. L. Chou et al., “[^{99m}Tc]TRODAT-1 SPECT imaging correlates with odor identification in early Parkinson disease,” *Neurology*, vol. 64, no. 10, pp. 1716–1720, 2005.

- [5] Y.-H. Weng, T.-C. Yen, M.-C. Chen et al., "Sensitivity and specificity of ^{99m}Tc -TRODAT-1 SPECT imaging in differentiating patients with idiopathic Parkinson's disease from healthy subjects," *Journal of Nuclear Medicine*, vol. 45, no. 3, pp. 393–401, 2004.
- [6] W.-S. Huang, S.-Z. Lin, J.-C. Lin, S.-P. Wey, G. Ting, and R.-S. Liu, "Evaluation of early-stage Parkinson's disease with ^{99m}Tc -TRODAT-1 imaging," *Journal of Nuclear Medicine*, vol. 42, no. 9, pp. 1303–1308, 2001.
- [7] P. D. Acton, P. T. Meyer, P. D. Mozley, K. Plossl, and H. F. Kung, "Simplified quantification of dopamine transporters in humans using [^{99m}Tc]TRODAT-1 and single-photon emission tomography," *European Journal of Nuclear Medicine and Molecular Imaging*, vol. 27, no. 11, pp. 1714–1718, 2000.
- [8] P. D. Acton, P. D. Mozley, and H. F. Kung, "Logistic discriminant parametric mapping: a novel method for the pixel-based differential diagnosis of Parkinson's disease," *European Journal of Nuclear Medicine and Molecular Imaging*, vol. 26, no. 11, pp. 1413–1423, 1999.
- [9] A. J. Worth, N. Makris, M. R. Patti et al., "Precise segmentation of the lateral ventricles and caudate nucleus in mr brain images using anatomically driven histograms," *IEEE Transactions on Medical Imaging*, vol. 17, no. 2, pp. 303–310, 1998.
- [10] V. Barra and J.-Y. Boire, "Automatic segmentation of subcortical brain structures in MR images using information fusion," *IEEE Transactions on Medical Imaging*, vol. 20, no. 7, pp. 549–558, 2001.
- [11] Y. Xia, K. Bettinger, L. Shen, and A. L. Reiss, "Automatic segmentation of the caudate nucleus from human brain MR images," *IEEE Transactions on Medical Imaging*, vol. 26, no. 4, pp. 509–517, 2007.
- [12] C.-F. Jiang, C.-C. Chang, and S.-H. Huang, "Regions of interest extraction from SPECT images for neural degeneration assessment using multimodality image fusion," *Multidimensional Systems and Signal Processing*, vol. 23, pp. 437–449, 2012.
- [13] A. P. Dhawan, "Image registration," in *Medical Image Analysis*, M. A. Kay, Ed., pp. 251–276, IEEE Press, Piscataway, NJ, USA, 2003.
- [14] A. P. Dhawan, L. K. Arata, A. V. Levy, and J. Mantil, "Iterative principal axes registration method for analysis of MR-PET brain images," *IEEE Transactions on Biomedical Engineering*, vol. 42, no. 11, pp. 1079–1087, 1995.
- [15] C.-F. Jiang, C.-H. Huang, and S.-T. Yang, "Using maximal cross-section detection for the registration of 3D image data of the head," *Journal of Medical and Biological Engineering*, vol. 31, no. 3, pp. 217–226, 2011.
- [16] M. Kass, A. Witkin, and D. Terzopoulos, "Snakes: active contour models," *International Journal of Computer Vision*, vol. 1, no. 4, pp. 321–331, 1988.
- [17] L. D. Cohen and I. Cohen, "Finite-element methods for active contour models and balloons for 2-D and 3-D images," *IEEE Transactions on Pattern Analysis and Machine Intelligence*, vol. 15, no. 11, pp. 1131–1147, 1993.
- [18] B. Leroy, I. Herlin, and L. Cohen, "Multi-resolution algorithms for active contour models," in *Proceedings of the 12th International Conference on Analysis and Optimization of Systems Images (ICAOS '96)*, pp. 58–65, 1996.
- [19] C. Xu and J. L. Prince, "Snakes, shapes, and gradient vector flow," *IEEE Transactions on Image Processing*, vol. 7, no. 3, pp. 359–369, 1998.
- [20] B. Erkol, R. H. Moss, R. J. Stanley, W. V. Stoecker, and E. Hvatum, "Automatic lesion boundary detection in dermoscopy images using gradient vector flow snakes," *Skin Research and Technology*, vol. 11, no. 1, pp. 17–26, 2005.
- [21] J. Tang and S. T. Acton, "Vessel boundary tracking for intravital microscopy via multiscale gradient vector flow snakes," *IEEE Transactions on Biomedical Engineering*, vol. 51, no. 2, pp. 316–324, 2004.
- [22] J. Tang, S. Millington, S. T. Acton, J. Crandall, and S. Hurwitz, "Surface extraction and thickness measurement of the articular cartilage from MR images using directional gradient vector flow snakes," *IEEE Transactions on Biomedical Engineering*, vol. 53, no. 5, pp. 896–907, 2006.
- [23] N. Tanki, K. Murase, M. Kumashiro et al., "Quantification of left ventricular volumes from cardiac cine MRI using active contour model combined with gradient vector flow," *Magnetic Resonance in Medical Sciences*, vol. 4, no. 4, pp. 191–196, 2005.
- [24] C. Xu and J. L. Prince, "Gradient vector flow deformable models," in *Handbook of Medical Imaging*, pp. 159–169, Academic Press, 2000.

Research Article

Customized First and Second Order Statistics Based Operators to Support Advanced Texture Analysis of MRI Images

Danilo Avola,¹ Luigi Cinque,² and Giuseppe Placidi¹

¹ Department of Life, Health and Environmental Sciences, University of L'Aquila, Via Vetoio Coppito 2, 67100 L'Aquila, Italy

² Department of Computer Science, Sapienza University of Rome, Via Salaria 113, 00198 Rome, Italy

Correspondence should be addressed to Danilo Avola; danilo.avola@univaq.it

Received 26 February 2013; Revised 1 May 2013; Accepted 8 May 2013

Academic Editor: Younghae Do

Copyright © 2013 Danilo Avola et al. This is an open access article distributed under the Creative Commons Attribution License, which permits unrestricted use, distribution, and reproduction in any medium, provided the original work is properly cited.

Texture analysis is the process of highlighting key characteristics thus providing an exhaustive and unambiguous mathematical description of any object represented in a digital image. Each characteristic is connected to a specific property of the object. In some cases the mentioned properties represent aspects visually perceptible which can be detected by developing operators based on Computer Vision techniques. In other cases these properties are not visually perceptible and their computation is obtained by developing operators based on Image Understanding approaches. Pixels composing high quality medical images can be considered the result of a stochastic process since they represent morphological or physiological processes. Empirical observations have shown that these images have visually perceptible and hidden significant aspects. For these reasons, the operators can be developed by means of a statistical approach. In this paper we present a set of customized first and second order statistics based operators to perform advanced texture analysis of Magnetic Resonance Imaging (MRI) images. In particular, we specify the main rules defining the role of an operator and its relationship with other operators. Extensive experiments carried out on a wide dataset of MRI images of different body regions demonstrating usefulness and accuracy of the proposed approach are also reported.

1. Introduction

As it is well known, there is no univocal definition of texture [1–3]. This is due to the various and heterogeneous aspects involving the texture analysis process. In particular, two aspects influence more than other textural detection and recognition approaches: *image classification* and *target definition*. The first is used to classify images as belonging to the natural domain (e.g., cell movement) or artificial domain (e.g., gear movement) [4, 5]. Although this discrimination may seem obvious, it can present ambiguities due to both kind of image and acquisition method. The second aspect regards type and detail of the extracted key characteristics to define different textures. In some cases it could be sufficient to extract coarse information to highlight macroscopic textural aspects (i.e., macrottextures) of studied objects. In other cases it could be necessary to extract more detailed information to describe microscopic textural aspects (i.e., microtextures) [6–10]. In our context, we have analyzed MRI images of organs and tissues (e.g., brain). These images represent the

morphological aspects of biological entities and they belong to the natural domain [11, 12]. In MRI, the pixels composing an image can be considered a reliable representation of water distribution in the body [13, 14], and the obtained images can be seen as the result of a stochastic process. This last assumption influences the choice of the reference model to be used for supporting the feature extraction method of the texture elements. The model is usually implemented by one of the following three descriptive approaches: *statistical*, *structural*, or *hybrid* [15–19]. It also includes the theoretical guidelines to develop the textural operators. The latter represents the core of the paper that will be detailed in the next section where the window based top-down image browsing method and the implementation of the customized first and second order statistics based operators will be described.

The operators applied on a wide dataset containing *in vivo* MRI images were conceived to detect macroscopic and microscopic textural features supporting a complete and unambiguous mathematical description. Artifacts in the treated images could make the texture analysis process

qualitatively ineffective since macro- and microvariations of the textural structures are linked to the spatial and contrast resolution of these images. Fortunately the current MRI scanners provide high quality images reasonably free from serious artifacts [20, 21].

Different works in the literature concerning the description of the natural domain by texture analysis processes [22–28], as well as our preliminary intuitions supported by some preparatory experimental observations on pixel arrangement of the MRI images, led us to focus on CV and IU based statistical operators. These included some operators to estimate the human visual perception of well-known textural features (e.g., *contrast*) and some operators to detect significant hidden textural features (e.g., *entropy*). Subsequently, our approach was refined by studying some remarkable works in texture analysis of MRI images. In a first set of works, detailed in [29–31], the authors described a method to model the objects contained in the layout of MRI images. After a training phase on a given image dataset to distinguish different target objects (e.g., brain mass, background), the approach was customized to achieve established tasks (e.g., layout segmentation) supporting a set of suitable Computer Aided Diagnosis (CAD) functionalities (e.g., mass identification). Their system architecture was composed of three main modules. The first (i.e., recognition) performed a feature extraction process on a set of template images to define numerical classes able to describe the different target objects composing the image layout. The second (i.e., classification) analyzed the source images, using the numerical classes defined in the previous module, to provide a classification of the different image zones. Finally, the last (i.e., segmentation) defined the boundaries between heterogeneous zones and merged homogeneous ones. Although their method included a set of statistical operators similar to those used in the present work, the authors did not produce any adequate explanation about operator potentiality, limits, and functional characteristics. Moreover, they neither showed any relationship between operators nor explained rules for their use. All these last aspects that make possible the reutilization of the operators to define new tasks on new target objects are addressed in the present work. Another reference work is [32], where the ability of the texture analysis in detecting micro- and macrovariations of the pixel distribution was described. The authors introduced an approach to classify multiple sclerosis lesions. Three imaging sequences were compared in quantitative analyses, including a comparison of anatomical levels of interest, variance between sequential slices, and two methods of region of interest drawing. They focused on the classification of white matter and multiple sclerosis lesions in determining the discriminatory power of textural parameters, thus providing high accuracy and reliable segmentation results. A work in the same direction is [33]: the concept, strategies, and considerations of MRI texture analysis were presented. The work summarized applications of texture analysis in multiple sclerosis as a measure of tissue integrity and its clinical relevance. The reported results showed that texture based approaches can be profitably used as tools of evaluating treatment benefits for patients suffering from this type of pathology. Another basic

work showing the importance of the texture analysis applied on the brain is [34], where the authors focused their efforts on characterizing healthy and pathologic human brain tissues: white matter, gray matter, cerebrospinal fluid, tumors, and edema. In their approach each selected brain region of interest was characterized with both its mean gray level values and several texture parameters. Multivariate statistical analyses were then applied to discriminate each brain tissue type represented by its own set of texture parameters. Thanks to its rich morphological aspects, not only brain can be widely studied through texture analysis approaches but also other organs and tissues where they can appear less noticeable. In [35] the feasibility of texture analysis for the classification of liver cysts and hemangiomas on MRI images was shown. Texture features were derived by gray level histogram, cooccurrence and run-length matrix, gradient, autoregressive model, and wavelet transform obtaining results encouraging enough to plan further studies to investigate the value of texture based classification of other liver lesions (e.g., hepatocellular and cholangiocellular carcinoma). Another work following the same topic is [36], where a quantitative texture feature analysis of double contrast-enhanced MRI images to classify fibrosis was introduced. The approach, based on well-known analysis software (MaZda, [37]), was implemented to compute a large set of texture parameters for each image. A statistical regularization technique, generalized linear model path, was used to define an effective model based on texture features for dichotomous classification of fibrosis category. Different texture analysis approaches for liver segmentation and classification are reported in [38]. The work treated images coming from MRI as well as other imaging modalities (e.g., ultrasound) to support complete liver description to allow specific algorithms development to solve different diagnostic tasks. Studies similar to those carried out on brain and liver are increasingly performed on the heart to investigate its patterns and structures. For example, in [39] a method for automating the myocardial contours identification to optimize the detection and the tracking of the grid of tags within myocardium was presented. Endocardial and epicardial contours detection was based on the use of texture analysis and active contours models. In particular, the authors adopted the texture analysis to define energy maps supporting the whole segmentation process, and the results were very promising. A similar work was proposed in [40], where the authors described a dynamic texture based motion segmentation approach to address the challenging problem of heart localization and segmentation in 4D spatiotemporal cardiac images. The method introduced time-dependent dynamic constraints into model based segmentation, with the advantage of producing segmentation results both spatially and temporally consistent. Another interesting method focused on heart characteristics was described in [41], where an automatic segmentation of the left ventricle in 2D tagged MRI images based on contrast enhancement was presented. The method applied histogram modification and local contrast enhancement for improving contrast between tagged lines and nontagged tissue. The ventricular blood filled and tagged regions were isolated by subtracting gray minimum from maximum within a small window. In this context,

wide feature values represented textured regions, and small values highlighted homogeneous ones, respectively. Finally, boundaries of the left ventricle were extracted. A last case study is focused on bone structures that more than others seem to present hidden and weak textural patterns. In [42] an approach to assess the ability of specific texture parameters to detect exercise load-associated differences in MRI images representing the neck cross-section was presented. In particular, the femoral neck trabecular bone at the level of the insertion of articular capsule was divided manually into regions of interest representing four anatomical sectors: anterior, posterior, superior, and inferior. Selected cooccurrence matrix based texture parameters were used to evaluate differences in apparent trabecular structure between the exercise loading groups and anatomical sectors of the femoral neck. The reported results showed qualitative and quantitative evaluations in detecting and classifying structural differences in trabecular bone associated with specific exercise loading. Another remarkable work was [43], where the authors described a unified framework for automatic segmentation of intervertebral disks of scoliotic spines from different types of magnetic resonance image sequences. Their method exploited a combination of statistical and spectral texture features to discriminate closed regions representing intervertebral disks from background in acquired images of the spine. A set of texture features were extracted from every closed region obtained from an automatic segmentation procedure based on the watershed approach. The authors validated their approach by using a supervised k -nearest-neighbor classifier on a wide number of images. A final work on this topic was [44], where a method for automatic segmentation of the tibia and femur in clinical magnetic resonance images of knees was presented. The texture information was incorporated into an active contours framework through the use of vector-valued geodesic snakes with local variance as a second value at each pixel, in addition to intensity. The use of this additional information allowed to develop a system to better handle noise and nonuniform intensities found within the structures to be segmented. Besides those mentioned, other works [45–49] were focused on the texture analysis on medical images to accomplish heterogeneous tasks; among these we considered only approaches related to four specific anatomical regions (*brain, heart, liver, and bones*) since they represented the images on which we used the customized first and second order statistics based operators. Unlike the works cited above that adopted texture analysis to achieve specific targets (e.g., lesion detection, mass classification, and 3D reconstruction), our intent was to provide a set of customized first and second order statistics based operators to support the definition of any new task. We designed a general purpose texture analysis approach to evaluate the behavior of each operator on the established medical domains. In addition, having each operator a different numerical feedback when applied on images belonging to a specific domain, we defined some main rules specifying the role of an operator and its relationship with others in distinguishing different textural aspects. For all these reasons, our approach is not directly comparable with others since any work regarding roles and rules of operators is given. Moreover, our method to extract

textural features can be considered novel with respect to the current state of the art.

The paper is structured as follows. Section 2 details the proposed texture analysis process, including the first and second order statistics based operators. Information about their potentiality, limits, and functional characteristics are also reported. Section 3 summarizes and discusses the extensive experimental results showing the application of each operator on MRI images of brain, heart, liver, and bones. Finally, Section 4 concludes the paper.

2. Materials and Methods

This section details the designed texture analysis process. The mentioned process is the same on each established type of image (i.e., brain, heart, liver, and bones), where only the definition of some parameters has to be adjusted depending on both the specific type of image (e.g., brain or heart) and the fixed targets (e.g., brain mass or heart lesions identification). Being different targets heterogeneous and hugely numerous, our purpose is to provide a guideline on *why* and *how* to adopt the developed method and related operators without a specific case study. In the rest of the paper, we suppose that every image (e.g., brain) is analyzed by our approach in a supervised way in order to study the numerical feedback of each operator according to different constitutive parts of the image (e.g., background, cerebral tissue, on skull). This step is fundamental since it leads the segmentation activity, the basic process to support each complex task in biomedical image analysis [50, 51].

Each image is entirely browsed by a window (recognition window, RW) of fixed size (i.e., $n_a \times n_b$, $n_a, n_b \in N$), in top-to-down and left-to-right way without overlapping. It is important to note that any other non-overlapping browser strategy would give the same results. The size of the window can change depending on the specific target, the type of the image, and its spatial resolution. The first aspect points out that the patterns associated to different textural analysis processes (e.g., ventricular lesion discovery, semilunar valve identification) on a given dataset of images (e.g., heart) can be detected by a suitable set of operators trained to identify different pixel configurations. The second highlights that the study of the micro- and macrotectural components depends on the specific organ or tissue. Finally, the last aspect draws attention to the relationship between the scanning window and the image spatial resolution. Our approach is conceived to face the first two aspects, while in the experimental section (Section 3) we show the image technical characteristics and the related assumptions for the browsing window size.

Each RW contains a set of pixels (i.e., p_i) elaborated from the whole set of functions (i.e., operators: f_i) to provide a corresponding set of numerical values (i.e., Q_{j,f_i}), each one representing a characterization of the mentioned pixels depending on the adopted operator (see the next subsection). Formally, we can summarize the general operation of the developed functions as follows:

$$Q_{j,f_i} = f_i(p_0, p_1, p_2, \dots, p_n), \quad (1)$$

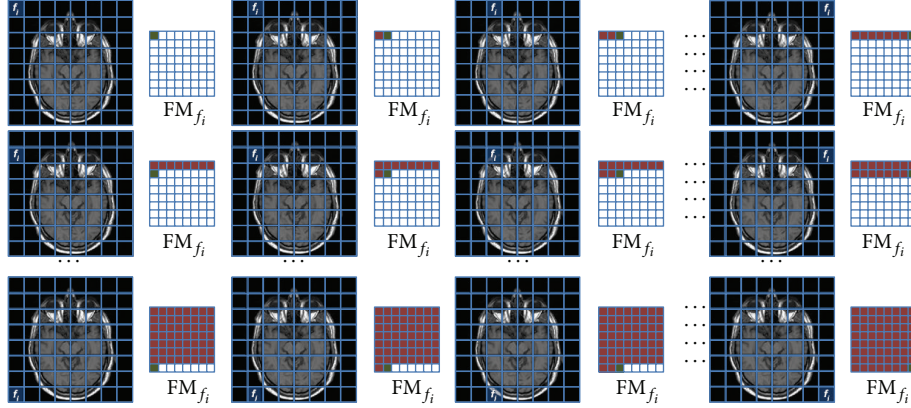


FIGURE 1: The source image is browsed by the operator f_i to obtain the related feature map FM_{f_i} . The map is subsampled as each RW provides a pixel as result. In the example the source image is analyzed by 64 RW thus providing a subsampled 8×8 image.

where $Q_{j,f_i} \in N^3$ represents the new pixel $j \in N$ of the new image (i.e., feature map, FM_{f_i}) depending on the function f_i . The pixel is structured in $(x, y, z) \in N^3$ where $(x, y) \in N^2$ sets the spatial position of the pixel, while $z \in N$ sets the amplitude value. $f_i : N^n \times N$ represents the operator $i \in N$ with domain in N^n and codomain N , and $n \in N$ represents the number of elaborated pixels (i.e., pixels contained in RW). $p_i \in N^3$ represents a pixel contained in the RW having the same structure of Q_{j,f_i} .

As shown in Figure 1, the elaboration of each source image provides a subsampled FM_{f_i} . The numerical values contained in this new map represent the behavior of the operator f_i in processing the different pixel configurations belonging to the different constitutive parts of the image. By performing this operation on the whole dataset of images, we obtain an equal number of subsampled images (i.e., feature space, FS_{f_i}) related to the operator f_i ; furthermore, following the same method, we can obtain the feature space related to each specific operator ($FS_{f_1}, FS_{f_2}, \dots, FS_{f_m}, m \in N$). These spaces suitably managed and interpreted represent the basic statistical information to implement an ad hoc mathematical model to achieve different targets (e.g., brain mass identification). We adopt the pyramid based texture analysis approach [52, 53] (i.e., subsampling strategy) to avoid redundant values in modeling definition. Despite this, the proposed approach is fully parametric thus allowing RW shape and size modification, image browsing process setting (i.e., with and without overlap), and number of the pyramidal levels choice. In Section 3 we detail and fix the whole set of parameters.

2.1. Operator Implementation. This section shows the CV and IU textural operators customized after our investigative experience regarding the established domains: brain, heart, liver, and bones. Since the browsing process determines the $(x, y) \in N^2$ position of the new pixel within the related feature map, in the following formalization we can omit it. Finally, we highlight that the observations related to the numerical feedback of the operators have to be considered tied to the established natural domains without general implications on different kinds of images.

The first two operators we consider are based on the first order statistic, specifically, N -order moment (M_{n_1}) and N -order central moment (C_{n_2}):

$$M_{(n_1)} = \sum_{i=0}^{L-1} i^{n_1} \cdot p(i), \quad C_{(n_2)} = \sum_{i=0}^{L-1} (i - M_{(n_1)})^{n_2} \cdot p(i), \quad (2)$$

where $p(i)$ represents the probability that the gray level $i \in [0 \dots L - 1]$ appears within the RW, L represents the number of levels of color in the source image, and n_1, n_2 represent the orders of the $M_{(n_1)}$ and $C_{(n_2)}$, respectively.

The following constraints must hold:

$$\forall i \in [0 \dots L - 1] \subset N, \quad 0 \leq p(i) \leq 1, \quad (3)$$

$$\sum_{i=0}^{L-1} p(i) = 1; \quad n_1, n_2 \in N.$$

Actually, they are not properly textural operators, since their task is only to measure the informative content of different image zones. In particular, the first operator ($M_{(n_1)}$) calculates the average of the levels of color related to the pixels contained within the RW; the second operator ($C_{(n_2)}$) measures the amplitude dispersion that the pixels contained within the RW have compared to their average (i.e., $M_{(n_1)}$). The order of the two operators leads the dynamic and the detail of the obtained numerical values. In our context, these operators are mainly used to distinguish the background of an image from the rest of image. In fact, the background image zones are usually characterized by very low $M_{(n_1)}$ values and low $C_{(n_2)}$ values. Moreover, these operators are also used to support the discrimination of regions of interest (ROIs) which present high $M_{(n_1)}$ and very high $C_{(n_2)}$. A last use of these operators regards the detection of zones belonging to ROIs and not to background; this generally occurs in those areas across two different textural zones (e.g., cerebral tissue and skull) which present low $M_{(n_1)}$ and high $C_{(n_2)}$.

The rest of the operators introduced in this section are fully texture based since they work both on spatial disposition and amplitude value of the pixels contained within the RW.

They are based on the Haralick et al. studies [54, 55] which were oriented to discriminate different meaningful textural features through the utilization of co-occurrence matrices. Currently, there are more advanced methods to discover textural features on natural images [56, 57]; despite this, our preliminary studies on the established domains have led us in using the proposed approach which seems completely suitable and profitable. Experimental results supported our efforts. Actually, we have adopted a variation of the classical approach which is designed to detect textural features by considering only four fixed directions (i.e., 0° , 45° , 90° , and 135°). As shown in Figure 2, our method considers each pixel contained within the RW as the center of a discrete circumference whose radius (d) can be freely defined (in Figure 2: $d = 2$). Each pair of points formed by the current central point and the one located on the perimeter of the circumference will increase the related position within the cooccurrence matrix. A careful analysis of the numerical results obtained by this approach allows for obtaining both textural aspects related to the pixels contained within the RW and contextual information of the pixels positioned around the RW. In this way, changing the parameter d of the RW, we can analyze the dynamic of the textural variations in a significant neighborhood of the RW.

The first two textural operators belonging to the second order statistic are customized to emulate two main visual perceptions related to the CV field [58], specifically, *homogeneity* ($HG(d)_{(n_3)}$) and *contrast* ($CT(d)_{(n_4, n_5)}$):

$$\begin{aligned} HG(d)_{(n_3)} &= \sum_{i=0}^{L-1} \sum_{j=0}^{L-1} [p_d(i, j)]^{n_3}, \\ CT(d)_{(n_4, n_5)} &= \sum_{i=0}^{L-1} \sum_{j=0}^{L-1} |i - j|^{n_4} \cdot [p_d(i, j)]^{n_5}, \end{aligned} \quad (4)$$

where $p_d(i, j)$ represents the probability that two pixels, with distance d , have, respectively, $i \in [0 \cdots L-1]$ and $j \in [0 \cdots L-1]$ amplitude values. n_3 , n_4 , and n_5 represent the parameters of the generalized $HG(d)_{(n_3)}$ and $CT(d)_{(n_4, n_5)}$.

The following constraints must hold:

$$\forall (i, j) \in [0 \cdots L-1] \times [0 \cdots L-1] \subset N^2, \quad 0 \leq p_d(i, j) \leq 1,$$

$$\sum_{i=0}^{L-1} p_d(i, j) = 1, \quad n_3, n_4, n_5 \in N. \quad (5)$$

$HG(d)_{(n_3)}$ measures the degree of uniformity associated to the different image zones. It provides high values on those zones having a high homogeneity level, while low values denote zones highly disconnected, as well as zones containing different textures. By comparing numerical values of adjacent image zones, the operator can measure the changing of textural structures covering a portion of an image. In particular high or low variations of the analyzed image zones reflect light or wide changes in textural structures, respectively. The results obtained from the described operator are highly dependent on the setting of the radius d since in natural

domains, including the established ones, the uniformity is a characteristic with rapid changes depending on the local pixel distribution. Finally, the parameter n_3 serves to define the dynamic of the obtained results: it has to be customized according to both image kind and specific target.

$CT(d)_{(n_4, n_5)}$ measures the amplitude variation between different image zones. When applied to textures composed of pixels with constant intensities (i.e., similar amplitude values), it provides very low values ($CT(d)_{(n_4, n_5)} \approx 0$). On the contrary, the operator provides high numerical values on image zones having high variations of the pixel intensities, thus reflecting amplitude changes and density transitions. From a different point of view, this operator can be seen as a measure of how textural components are structured on different image zones. In fact, the passage between very high and very low values belonging to different zones reflects a definite structured pattern while constant values do not show any significant modification. Also in this case, the value of the radius d influences the result of the operator. This is due to the possible amplitude variations of the texture. However, the operator shows significant diversifications only considering distant radius values. Finally, the parameters n_4 and n_5 have to be experimentally investigated to define the sensibility of the operator in discovering the structural variations of the involved patterns.

In our context, $HG(d)_{(n_3)}$ and $CT(d)_{(n_4, n_5)}$ can be seen as the measure of macrotextural aspects of the MRI images tied to the visual perception to immediately identify the basic components contained within the layout of the treated images.

The other two textural operators belonging to the second order statistics are customized to determine two hidden significant features useful to identify both the period and the size of the involved patterns, specifically, *inverse difference* ($ID(d)_{(n_6, n_7)}$) and *entropy* ($ET(d)_{(n_8, n_9)}$):

$$\begin{aligned} ID(d)_{(n_6, n_7)} &= \sum_{i=0}^{L-1} \sum_{j=0}^{L-1} \frac{[p_d(i, j)]^{n_6}}{1 + (i - j)^{n_7}}, \\ ET(d)_{(n_8, n_9)} &= - \sum_{i=0}^{L-1} \sum_{j=0}^{L-1} [p_d(i, j)]^{n_8} \cdot [\log_{k_1}(p_d(i, j))]^{n_9}, \end{aligned} \quad (6)$$

where $n_6, n_7, n_8, n_9, k_1 \in N$ represent the parameters of the generalized $ID(d)_{(n_6, n_7)}$ and $ET(d)_{(n_8, n_9)}$. The other terms are defined as in (5).

$ID(d)_{(n_6, n_7)}$ measures and characterizes the local distribution of pixels within an image zone. The set of numerical values it provides can be used to define a specific pixel configuration and its repetitions. In this operator the parameters n_6 , n_7 , and d are adopted to fix experimentally one or more patterns within the source image by considering their scale, sizes, and rotations. This operator is conceived to catch high level of details. For this reason it is suitable to define microtextural aspects of the analyzed zones.

$ET(d)_{(n_8, n_9)}$ measures the degree of disorder related to different image zones. Its values are directly proportional to the randomness level detected within the analyzed zones. Also in this case the parameters n_8 , n_9 , k_1 , and d have to be

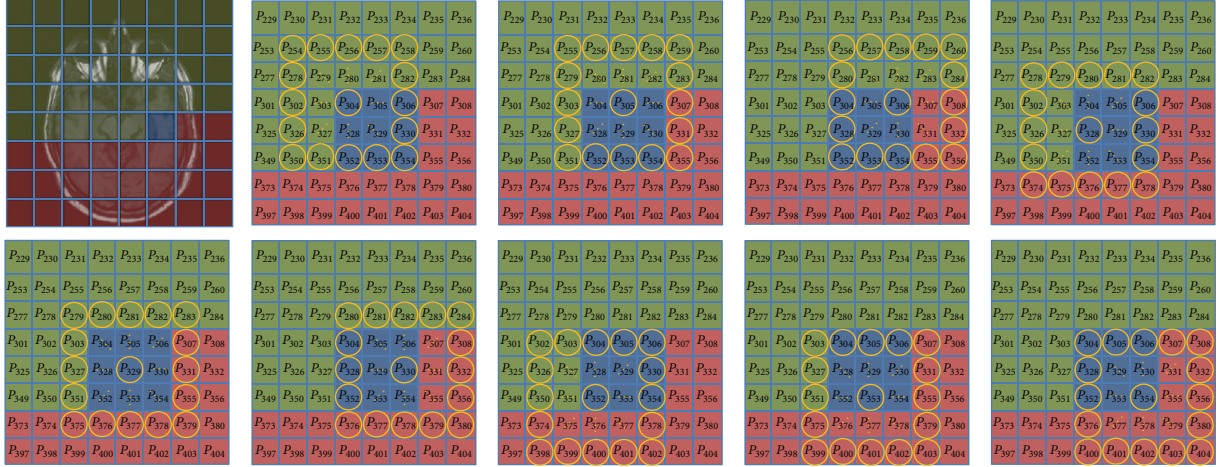


FIGURE 2: Variation of the Haralick et al. approach which considers all the possible directions and not only the cardinal ones. In the example the RW contains 9 pixels; each circumference provides 16 pair of pixels; therefore the current RW provides 144 values to the co-occurrence matrix.

empirically fixed to support the pattern definition. In particular, the following strategy provided profitable results to support the identification of the pixel configuration: starting from image zones having high homogeneity levels ($HG(d)_{(n_3)}$), the behavior of this operator can be analyzed according to the progressive increments of d ; in this way we can provide the structural changes of the distribution composing the identified patterns.

In our context, $ID(d)_{(n_6, n_7)}$ and $ET(d)_{(n_8, n_9)}$ are used to define the basic features of the microtextural aspects of the image zones, in particular, to distinguish different significant textural structures composing the given images (according to the fixed tasks).

Empirical experiences have allowed us to consider two other textural operators to support the working of the previous ones. These operators do not have a specific meaning: they are utilized to increase the detail and the reliability of the proposed second order statistics based operators, specifically, *correlation* ($CR(d)_{(n_{10}, n_{11})}$) and *difference entropy* ($DE(d)_{(n_{12}, n_{13})}$):

$$CR(d)_{(n_{10}, n_{11})} = \sum_{i=0}^{L-1} \sum_{j=0}^{L-1} \frac{(i - \mu_x) \cdot (j - \mu_y) \cdot [p_d(i, j)]^{n_{10}}}{[\sigma_x \cdot \sigma_y]^{n_{11}}},$$

$$DE(d)_{(n_{12}, n_{13})} = - \sum_{i=0}^{L-1} [p_{x-y}(i)]^{n_{12}} \cdot [\log_{k_2}(p_{x-y}(i))]^{n_{13}},$$
(7)

where $n_{10}, n_{11}, n_{12}, n_{13}, k_2 \in N$ represent the parameters of the generalized $CR(d)_{(n_{10}, n_{11})}$ and $DE(d)_{(n_{12}, n_{13})}$. The other terms are defined as in (5). Moreover

$$\mu_x = \sum_{i=0}^{L-1} \sum_{j=0}^{L-1} [i \cdot (p_d(i, j))],$$

$$\sigma_x = \sqrt{\sum_{i=0}^{L-1} \sum_{j=0}^{L-1} [(i - \mu_x)^2 \cdot (p_d(i, j))]},$$

$$\mu_y = \sum_{i=0}^{L-1} \sum_{j=0}^{L-1} [j \cdot (p_d(i, j))],$$

$$\sigma_y = \sqrt{\sum_{i=0}^{L-1} \sum_{j=0}^{L-1} [(j - \mu_y)^2 \cdot (p_d(i, j))]},$$

$$p_{x-y}(k) = \sum_{i=0}^L \sum_{j=0}^L [p_d(i, j)]^q, \quad \text{where } |i - j| = k.$$
(8)

$CR(d)_{(n_{10}, n_{11})}$ and $DE(d)_{(n_{12}, n_{13})}$ are mainly used to recognize relationships between near RWs and different discovered patterns, respectively. In other words, the first can be used to identify spatial constraints of RWs composing the same pattern, while the second can be adopted to determine the spatial constraints of different textural patterns.

In this context, it is important to note that the whole set of operators have different degrees of dependence. This means that the results of each operator have to be considered jointly with those provided from the others. A single operator is only able to describe the general features of a complex texture. To identify more patterns, different textural aspects have to be adopted within the same mathematical model. Table 1 shows the dependence between operators which can be considered as a general guideline to adopt the customized set of textural operators to implement specific tasks related to the established domains. With reference to the first row of Table 1, we can observe that the operator $M_{(n_1)}$ is strongly joint to the operator $C_{(n_2)}$; this means that they have to be jointly evaluated to provide a reliable numerical result. Subsequently, the other dependent levels highlight the order by which the values coming from $M_{(n_1)}$ have to be compared with those provided from the other operators. This approach is aimed at refining the obtained results. When two or more operators have similar dependent level, the choice is empirically performed according to the specific task. The other rows can be interpreted in the same way. Finally, we highlight that

TABLE 1: Relationship between the customized first and second order statistics based operators. The value from 1 (low) to 4 (high) points out the dependence level between two operators.

Operators	$M_{(n_1)}$	$C_{(n_2)}$	$HG(d)_{(n_3)}$	$CT(d)_{(n_4, n_5)}$	$ID(d)_{(n_6, n_7)}$	$ET(d)_{(n_8, n_9)}$	$CR(d)_{(n_{10}, n_{11})}$	$DE(d)_{(n_{12}, n_{13})}$
$M_{(n_1)}$...	4	3	3	2	2	1	2
$C_{(n_2)}$	4	...	2	3	2	3	2	2
$HG(d)_{(n_3)}$	3	2	...	4	3	3	1	1
$CT(d)_{(n_4, n_5)}$	3	3	4	...	3	2	2	2
$ID(d)_{(n_6, n_7)}$	2	2	3	3	...	4	3	2
$ET(d)_{(n_8, n_9)}$	2	3	3	2	4	...	3	3
$CR(d)_{(n_{10}, n_{11})}$	1	2	1	2	3	3	...	4
$DE(d)_{(n_{12}, n_{13})}$	2	2	1	2	2	3	4	...

the results summarized in Table 1 are derived by analyzing the behavior of the operators on the established domains according to the segmentation task. For this reason, they can be adopted as general guidelines on each defined new task.

3. Results and Discussion

In order to define qualitative and technical aspects of the proposed approach, experimental results were obtained from a wide dataset containing images of brain, heart, liver, and bones. In particular, the experimental phase was divided into three sessions: basic parameter definition, model parameter definition, and qualitative response. The first served to identify the basic parameters through which the source images had to be browsed; the second focused on the parameter definition of each first and second order statistics based operator according to a specific natural domain; finally, the third focused on the qualitative aspects of the approach with respect to a specific basic task (i.e., segmentation). All the experimental sessions were performed using MRI transversal T_1 weighted, T_2 weighted, and proton density (PD) images having 8 bit (i.e., $L = 256$) and 512×512 pixels.

3.1. Basic Parameter Definition. Table 2 summarizes the preliminary analysis which supported the definition of several critical parameters of the proposed approach. We used 110 images, collected by 41 different patients suitably subdivided within the four natural domains. As previously mentioned, we have focused on the segmentation task since it represents the basic step of the image processing. Dimension and shape of the RW represent crucial aspects. An RW too wide causes the loss of textural details; an RW too small is unable to detect textural features. On each image both variance (i.e., C_2) and basic entropy (i.e., $ET(2)_{(2,3)}$) values of the pixel distribution were empirically evaluated with the aim of maximizing them and at the same time minimizing the RW. These observations have shown that a square RW sized 6×6 pixels can provide the best solution to catch the micro- and macrotextural aspects from all studied domains. In some cases, when noise and low information occur within specific image zones, it can be useful to enlarge or decrease (of one unit) the RW size. Moreover, these observations have also highlighted that the image browsing can be performed in conventional mode (i.e., top-to-down and left-to-right)

without overlapping, while maintaining the integrity of the extracted textural information content. Only in some cases, regarding bones (in particular, the hand) it can be necessary to browse the image with an overlapping strategy to infer information about structures and patterns. For the same reasons, overlapping strategy can be applied on images having very low textural variations. In this experimental session we obtained both base (L_0) and first (L_1) pyramidal levels. The base level was considered to analyze variance and entropy values, while the first level was exploited to support the definition of image zones having low information content. Finally, we have also deduced that the usefulness of the first level is directly proportional to dynamical aspects of the involved textures. In fact, in brain and heart images which have high variation of the textural structures, the first level of the pyramid can provide distinguishing information than liver and bone images which have textural structures less complex and heterogeneous.

3.2. Model Parameter Definition. Table 3 summarizes the parametric definition of the first and second statistics based operators which define our statistical model. We used 380 images, collected by 160 different patients. Also in this case, the images were suitably subdivided within the four natural domains. In this session we analyzed different patients (and related images) from the previous ones with the aim of obtaining a more objective investigation. Moreover, this session was implemented by developing an ad hoc machine-learning supervised algorithm [59] able to highlight the differences of the numerical feedbacks provided by the set of operators during the analysis process. Initially, each parameter of each operator was fixed to 1 in order to obtain an initial state of the algorithm. Subsequently, a skilled user modified variance (i.e., C_2) and basic entropy (i.e., $ET(2)_{(2,3)}$) values to identify the different image zones having the highest numerical feedbacks. Starting from these values the skilled user implemented a feature vector composed of all operators. The parameters contained within the vector were methodically increased or decreased to produce different feature spaces useful to perform the current task (in this case, segmentation). In other words, the skilled user modified, in a supervised way, the parameters contained within the vector taking into account the role and dependence table (Table 1) of each operator. The main aim of the parameter variation

TABLE 2: 1° experimental session: basic parameter definition.

Body regions	Training patients	Training images	Task	Basic parameter definition				Image scanning process	Type	Pyramid level Levels	Pyramid level L_1 usefulness
				Recognition window (RW) Shape	Size	Mode	Levels				
Brain	15	35	Segmentation	Square	$n_a \times n_b = 6 \times 6$	Top-to-down Left-to-right	Without overlapping	L_0 and L_1	Very high		
Heart	10	30	Segmentation	Square	$n_a \times n_b = 6 \times 6$ $n_a \times n_b = 7 \times 7$	Top-to-down Left-to-right	Without overlapping	L_0 and L_1	High		
Liver	8	25	Segmentation	Square	$n_a \times n_b = 6 \times 6$ $n_a \times n_b = 5 \times 5$	Top-to-down Left-to-right	Without overlapping	L_0 and L_1	Middle		
Bone	8	20	Segmentation	Square	$n_a \times n_b = 6 \times 6$ $n_a \times n_b = 5 \times 5$	Top-to-down Left-to-right	With and without overlapping	L_0 and L_1	Low		

TABLE 3: II° experimental session: model parameter definition.

Body regions	Training patients	Training images	$M_{(n_1)}$	Model parameter definition							CR(d) _(n_{10}, n_{11})	DE(d) _(n_{12}, n_{13})
				$C_{(n_2)}$	HG(d) _(n_3)	CT(d) _(n_4, n_5)	ID(d) _(n_6, n_7)	ET(d) _(n_8, n_9)				
Brain	55	135	$n_1 = 1, 2$	$n_2 = 2, 3$	$n_3 = 2, 3$ $d = 1, 2, 3, 4$	$n_4 = 2, 3$ $n_5 = 1, 2$ $d = 1, 2, 3, 4$	$n_6 = 1, 2, 3$ $n_7 = 2$ $d = 1, 2, 3, 4$	$n_8 = 1, 2$ $n_9 = 1, 2$ $k_1 = 2$ $d = 1, 2, 3, 4$	$n_{10} = 1, 2, 3$ $n_{11} = 1, 3$ $d = 1, 3$	$n_{12} = 2, 3, 4$ $n_{13} = 2, 4$ $k_2 = 2$ $d = 2, 4$		
Heart	45	105	$n_1 = 1, 2$	$n_2 = 2, 3$	$n_3 = 2, 3$ $d = 1, 2, 3, 4$	$n_4 = 2, 3$ $n_5 = 1, 2$ $d = 1, 2, 3, 4$	$n_6 = 2, 3$ $n_7 = 2$ $d = 2, 4$	$n_8 = 2, 3$ $n_9 = 2$ $k_1 = 2$ $d = 2, 4$	$n_{10} = 1, 3$ $n_{11} = 2, 3$ $d = 1, 2, 4$	$n_{12} = 1, 4$ $n_{13} = 2, 4$ $k_2 = 2$ $d = 1, 2, 4$		
Liver	35	85	$n_1 = 1, 2$	$n_2 = 2, 3$	$n_3 = 2, 3, 4$ $d = 1, 2, 3, 4$	$n_4 = 2, 3$ $n_5 = 1, 2$ $d = 1, 2, 3, 4$	$n_6 = 1, 3$ $n_7 = 3$ $d = 1, 2, 3, 4$	$n_8 = 1, 2, 3$ $n_9 = 3$ $k_1 = 2$ $d = 2, 3, 4$	$n_{10} = 2, 4$ $n_{11} = 3$ $d = 1, 2, 4, 6$	$n_{12} = 1, 4$ $n_{13} = 2$ $k_2 = 2$ $d = 1, 2, 3, 4$		
Bone	25	55	$n_1 = 1, 2$	$n_2 = 2, 3, 4$	$n_3 = 2, 3, 4$ $d = 2, 4, 6$	$n_4 = 2, 3$ $n_5 = 2$ $d = 2, 3, 4$	$n_6 = 1, 3$ $n_7 = 2$ $d = 2, 3, 4$	$n_8 = 2, 3, 4$ $n_9 = 3$ $k_1 = 2$ $d = 2, 4$	$n_{10} = 2, 4$ $n_{11} = 2, 4, 6$ $d = 2, 4$	$n_{12} = 3$ $n_{13} = 3$ $k_2 = 2$ $d = 2, 4$		

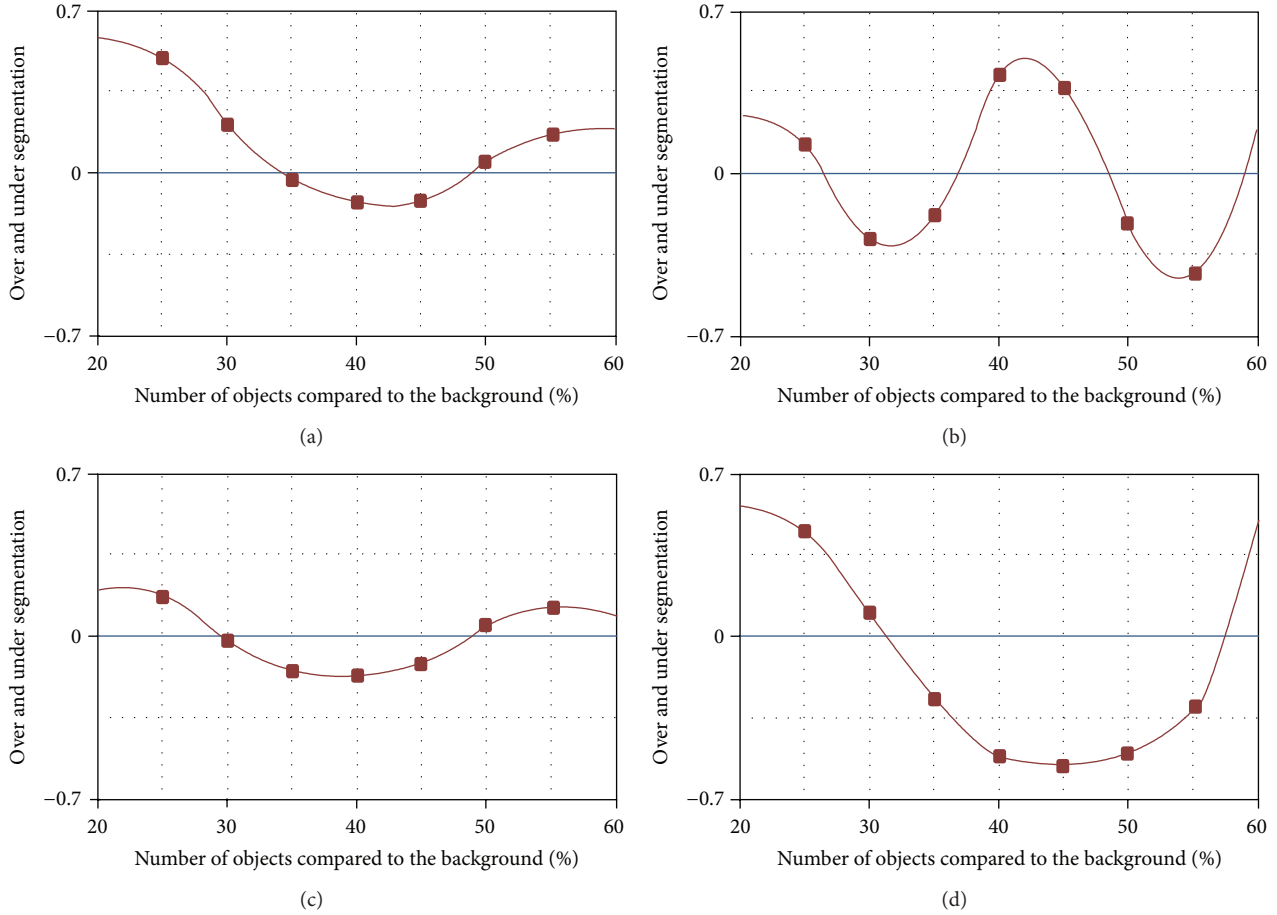


FIGURE 3: Qualitative response on (a) brain, (b) heart, (c) liver, and (d) bone.

was to increase the numerical feedback of the textural operators decreasing the variation among “independent” (or less dependent) operators. Once several feature spaces were computed (i.e., states of the algorithm), the approach provided a final set of numerical intervals. These intervals can be considered as the mathematical model describing the fixed task. In particular, each object contained within the layout of an image can be defined by a specific set of numerical values obtained by considering the whole set of operators and related variations due to the different parameters. Despite the large amount of parameters shown in Table 3, just a minor part of them with a restricted set of values define the main features of the objects. For example, the discrimination of the background from the informative content is almost always performed by using $M_{(n_1)}$ and $C_{(n_2)}$ with $n_1 = 1$ and $n_2 = 2$, respectively. The other values are used to solve particular cases due to noise or artifacts. Similarly, the radius adopted to the different operators to describe the related textural features is almost always fixed on $d = 2$ and $d = 3$; the other values are used to solve particular issues tied to the boundary detection of two different textural zones. However, the whole set of parameters shown in the Table 3 can be considered as a guideline to implement and customize multipurpose operators. Finally, we observe that when a skilled

user defines a new task (e.g., mass detection) on a well-established domain, (e.g., brain) a new training stage has to be performed to define the new reference mathematical model.

3.3. Qualitative Response. Figure 3 summarizes the qualitative response of the proposed approach in relation to the assigned basic task: the segmentation. In order to obtain comparable results independently of the specific natural domain, the set of images was chosen according to some simple morphological rules: (a) high stationarity of the texture, (b) substantial availability of the target objects, and (c) avoiding ambiguities related to the transition of different objects. All these aspects can be reasonably satisfied considering images belonging to “middle” transversal scanner planes where organs and tissues represent a wide portion of the whole image (not less than 20%). We report four graphics (Figure 3) representing the qualitative ratio between the pixels belonging to the real objects and the ones belonging to the segmented objects. In particular, Figures 3(a), 3(b), 3(c), and 3(d) represent the qualitative measurements of the brain, heart, liver, and bones, respectively. Note that while the abscissa in the first three cases represents the increasing amount of objects due to the transversal scanning plan, in the last case it represents the amount of objects due to a supervised choice

of the images. The four figures show that the segmentation error (over and/or under segmentation) is less than 8% on the whole set of images by using the same set of operators.

4. Conclusion

Texture analysis of MRI images supports their exhaustive and unambiguous mathematical description. The base of this process is composed of a set of feature extractors to detect the key characteristics related to the objects contained within the image layout. These characteristics change depending on the established task (e.g., volume evaluation, lesions identification); despite this, our parametric approach designed for specific MRI images (i.e., brain, heart, liver, and bones) and the developed set of customizable textural operators can jointly provide a numerical interpretation of the images according to the specific task. This numerical interpretation represents a tool to describe different models to implement heterogeneous CAD functionalities (e.g., mass identification). To prove the usefulness and the accuracy of the proposed approach, we have fixed and tested the segmentation task on the analyzed domains; these experimental sessions allowed providing a set of information (i.e., roles, rules, and dependences) on the developed operators which can be used as guidelines to implement new tasks and CAD functionalities.

Acknowledgment

The authors are grateful to Mrs. Carmelita Marinelli for the technical assistance.

References

- [1] M. Tuceryan and A. K. Jain, "Texture analysis," in *Handbook of Pattern Recognition & Computer Vision*, pp. 235–276, World Scientific Publishing, River Edge, NJ, USA, 1993.
- [2] N. Sebe and M. S. Lew, "Texture features for content-based retrieval," in *Principles of Visual Information Retrieval*, pp. 51–85, Springer, London, UK, 2000.
- [3] P. Maillard, "Comparing texture analysis methods through classification," *Photogrammetric Engineering and Remote Sensing*, vol. 69, no. 4, pp. 357–367, 2003.
- [4] J. Chen, T. N. Pappas, A. Mojsilović, and B. E. Rogowitz, "Adaptive perceptual color-texture image segmentation," *IEEE Transactions on Image Processing*, vol. 14, no. 10, pp. 1524–1536, 2005.
- [5] A. K. Jain and F. Farrokhnia, "Unsupervised texture segmentation using Gabor filters," in *Proceedings of the IEEE International Conference on Systems, Man, and Cybernetics*, pp. 14–19, November 1990.
- [6] J. C. Russ, *The Image Processing Handbook*, CRC Press, Taylor & Francis Group, 2007.
- [7] P. Soille, *Morphological Image Analysis: Principles and Applications*, Springer, New York, NY, USA, 2010.
- [8] V. Randle and O. Engler, *Introduction to Texture Analysis: Macrotexture, Microtexture and Orientation Mapping*, CRC Press, Taylor & Francis Group, Amsterdam, The Netherlands, 2000.
- [9] M. E. Mavroforakis, H. V. Georgiou, N. Dimitropoulos, D. Cavouras, and S. Theodoridis, "Mammographic masses characterization based on localized texture and dataset fractal analysis using linear, neural and support vector machine classifiers," *Artificial Intelligence in Medicine*, vol. 37, no. 2, pp. 145–162, 2006.
- [10] T. Hofmann, J. Puzicha, and J. M. Buhmann, "Unsupervised texture segmentation in a deterministic annealing framework," *IEEE Transactions on Pattern Analysis and Machine Intelligence*, vol. 20, no. 8, pp. 803–818, 1998.
- [11] G. K. von Schulthess, *Morphology and Function in MRI*, Springer, London, UK, 2012.
- [12] P. V. Prasad, *Magnetic Resonance Imaging: Methods and Biologic Applications*, Humana Press Inc., Totowa, NJ, USA, 2006.
- [13] D. Weishaupt, V. D. Koechli, and B. Marincek, *How Does MRI Work? An Introduction to the Physics and Function of Magnetic Resonance Imaging*, Springer, New York, NY, USA, 2006.
- [14] G. Placidi, *MRI: Essentials for Innovative Technologies*, CRC Press, Taylor & Francis Group, 2012.
- [15] R. M. Haralick, "Statistical and structural approaches to texture," *Proceedings of the IEEE*, vol. 67, no. 5, pp. 786–804, 1979.
- [16] S. W. Zucker, "Toward a model of texture," *Computer Graphics and Image Processing*, vol. 5, no. 2, pp. 190–202, 1976.
- [17] J. Zhang and T. Tan, "Brief review of invariant texture analysis methods," *Pattern Recognition*, vol. 35, no. 3, pp. 735–747, 2002.
- [18] A. R. Rao, *A Taxonomy for Texture Description and Identification*, Springer, Berlin, Germany, 1990.
- [19] N. V. Lobo, T. Kasparis, F. Roli, J. T. Kwok, M. Georgiopoulos, and M. Loog, *Structural, Syntactic and Statistical Pattern Recognition*, Springer, Berlin, Germany, 2008.
- [20] M. A. Brown and R. C. Semelka, *MRI: Basic Principles and Applications*, Wiley-Blackwell, 2010.
- [21] W. I. Mangrum, K. L. Christianson, S. M. Duncan, P. B. Hoang, A. W. Song, and E. M. Merkle, *Duke Review of MRI Principles*, Elsevier Mosby, 2012.
- [22] H. Mobahi, S. R. Rao, A. Y. Yang, Y. Allen, S. S. Sastry, and Y. Ma, "Segmentation of natural images by texture and boundary compression," *International Journal of Computer Vision*, vol. 95, no. 1, pp. 86–98, 2011.
- [23] T. V. Pappathomas, R. S. Kashi, and A. Gorea, "A human vision based computational model for chromatic texture segregation," *IEEE Transactions on Systems, Man, and Cybernetics, Part B: Cybernetics*, vol. 27, no. 3, pp. 428–440, 1997.
- [24] C. Zheng, Q. Qin, G. Liu, and Y. Hu, "Image segmentation based on multiresolution Markov random field with fuzzy constraint in wavelet domain," *IET Image Processing*, vol. 6, no. 3, pp. 213–221, 2012.
- [25] J. Malik, S. Belongie, T. Leung, and J. Shi, "Contour and texture analysis for image segmentation," *International Journal of Computer Vision*, vol. 43, no. 1, pp. 7–27, 2001.
- [26] Q. Xu, J. Yang, and S. Ding, "Color texture analysis using the wavelet-based hidden Markov model," *Pattern Recognition Letters*, vol. 26, no. 11, pp. 1710–1719, 2005.
- [27] M. Madanian, A. Vafaei, and A. H. Monadjemi, "Segmentation and classification of texture images inspired by natural vision system and HMAX algorithm," *International Journal of Research and Reviews in Computer Science*, vol. 3, no. 1, pp. 1467–1472, 2012.

- [28] G. F. McLean, "Vector quantization for texture classification," *IEEE Transactions on Systems, Man and Cybernetics*, vol. 23, no. 3, pp. 637–649, 1993.
- [29] D. Avola, L. Cinque, and G. Placidi, "Medical image analysis through a texture based computer aided diagnosis framework," *International Journal of Biometrics and Bioinformatics*, vol. 6, no. 5, pp. 144–152, 2012.
- [30] D. Avola, L. Cinque, and M. Di Girolamo, "A novel T-CAD framework to support medical image analysis and reconstruction," in *Proceeding of the 16th International Conference on Image Analysis and Processing (ICIAP '11)*, vol. 6979, pp. 414–423, Springer, 2011.
- [31] D. Avola and L. Cinque, "Encephalic NMR image analysis by textural interpretation," in *Proceedings of the 23rd Annual ACM Symposium on Applied Computing (SAC '08)*, pp. 1338–1342, ACM, March 2008.
- [32] L. C. V. Harrison, M. Raunio, K. K. Holli et al., "MRI texture analysis in multiple sclerosis: toward a clinical analysis protocol," *Academic Radiology*, vol. 17, no. 6, pp. 696–707, 2010.
- [33] Y. Zhang, "MRI texture analysis in multiple sclerosis," *International Journal of Biomedical Imaging*, vol. 2012, Article ID 762804, 7 pages, 2012.
- [34] S. Herlidou-Même, J. M. Constans, B. Carsin et al., "MRI texture analysis on texture test objects, normal brain and intracranial tumors," *Magnetic Resonance Imaging*, vol. 21, no. 9, pp. 989–993, 2003.
- [35] M. E. Mayerhoefer, W. Schima, S. Trattnig, K. Pinker, V. Berger-Kulemann, and A. Ba-Ssalamah, "Texture-based classification of focal liver lesions on MRI at 3.0 Tesla: a feasibility study in cysts and hemangiomas," *Journal of Magnetic Resonance Imaging*, vol. 32, no. 2, pp. 352–359, 2010.
- [36] G. Bahl, I. Cruite, T. Wolfson et al., "Noninvasive classification of hepatic fibrosis based on texture parameters from double contrast-enhanced magnetic resonance images," *Journal of Magnetic Resonance Imaging*, vol. 36, no. 5, pp. 1154–1161, 2012.
- [37] MaZda software, 2013, <http://www.eletel.p.lodz.pl/programy/mazda/>.
- [38] S. Rathore, M. A. Iftikhar, M. Hussain, and A. Jalil, "Texture analysis for liver segmentation and classification: a survey," in *Proceedings of the 9th International Conference on Frontiers of Information Technology (FIT '11)*, pp. 121–126, December 2011.
- [39] A. Histace, B. Matuszewski, and Y. Zhang, "Segmentation of myocardial boundaries in tagged cardiac MRI using active contours: a gradient-based approach integrating texture analysis," *International Journal of Biomedical Imaging*, vol. 2009, Article ID 983794, 8 pages, 2009.
- [40] J. Huang, X. Huang, D. Metaxas, and L. Axel, "Dynamic texture based heart localization and segmentation in 4-D cardiac images," in *Proceedings of the 4th IEEE International Symposium on Biomedical Imaging: From Nano to Macro (ISBI '07)*, pp. 852–855, April 2007.
- [41] X. Yang and K. Murase, "Tagged cardiac MR image segmentation by contrast enhancement and texture analysis," in *Proceedings of the 9th International Conference on Electronic Measurement and Instruments (ICEMI '09)*, pp. 4210–4214, August 2009.
- [42] L. C. V. Harrison, R. Nikander, M. Sikiö et al., "MRI texture analysis of femoral neck: detection of exercise load-associated differences in trabecular bone," *Journal of Magnetic Resonance Imaging*, vol. 34, no. 6, pp. 1359–1366, 2011.
- [43] C. Chevretil, F. Cheriet, C. Aubin, and G. Grimard, "Texture analysis for automatic segmentation of intervertebral disks of scoliotic spines from MR images," *IEEE Transactions on Information Technology in Biomedicine*, vol. 13, no. 4, pp. 608–620, 2009.
- [44] L. M. Lorigo, O. Faugeras, W. E. L. Grimson, R. Keriven, and R. Kikinis, "Segmentation of bone in clinical knee MRI using texture-based geodesic active contours," in *Proceeding of the International Conference on Medical Image Computing and Computer-Assisted Intervention (MICCAI '98)*, vol. 1496, pp. 1195–1204, Springer, 1998.
- [45] M. C. de Oliveira and R. I. Kitney, "Texture analysis for discrimination of tissues in MRI data," in *Proceedings of the 18th Annual Conference on Computers in Cardiology*, pp. 481–484, September 1991.
- [46] V. A. Kovalev, F. Kruggel, H. Gertz, and D. Y. Von Cramon, "Three-dimensional texture analysis of MRI brain datasets," *IEEE Transactions on Medical Imaging*, vol. 20, no. 5, pp. 424–433, 2001.
- [47] K. Wu, C. Garnier, J. Coatrieux, and H. Shu, "A preliminary study of moment-based texture analysis for medical images," *Proceedings of the Annual International Conference of the IEEE Engineering in Medicine and Biology Society. IEEE Engineering in Medicine and Biology Society*, vol. 2010, pp. 5581–5584, 2010.
- [48] S. Nagaraj, G. N. Rao, and K. Koteswararao, "The role of pattern recognition in computer-aided diagnosis and computer-aided detection in medical imaging: a clinical validation," *International Journal of Computer Applications*, vol. 8, no. 5, pp. 18–22, 2010.
- [49] K. Somkantha, N. Theera-Umpon, and S. Auephanwiriyakul, "Boundary detection in medical images using edge following algorithm based on intensity gradient and texture gradient features," *IEEE Transactions on Biomedical Engineering*, vol. 58, no. 3, pp. 567–573, 2011.
- [50] N. Alamgir, K. Myeongsu, K. Yung-Keun, K. Cheol-Hong, and K. Jong-Myon, "A hybrid technique for medical image segmentation," *Journal of Biomedicine and Biotechnology*, vol. 2012, Article ID 830252, 7 pages, 2012.
- [51] N. Sharma, A. Ray, S. Sharma, K. Shukla, S. Pradhan, and L. Aggarwal, "Segmentation and classification of medical images using texture-primitive features: application of BAM-type artificial neural network," *Journal of Medical Physics*, vol. 33, no. 3, pp. 119–126, 2008.
- [52] J. S. De Bonet, "Multiresolution sampling procedure for analysis and synthesis of texture images," in *Proceedings of the Conference on Computer Graphics (SIGGRAPH '97)*, pp. 361–368, ACM, August 1997.
- [53] D. J. Heeger and J. R. Bergen, "Pyramid-based texture analysis/synthesis," in *Proceedings of the 22nd Annual ACM Conference on Computer Graphics and Interactive Techniques (SIGGRAPH '95)*, pp. 229–238, ACM, August 1995.
- [54] R. M. Haralick, K. Shanmugam, and I. Dinstein, "Textural features for image classification," *IEEE Transactions on Systems, Man and Cybernetics*, vol. 3, no. 6, pp. 610–621, 1973.
- [55] B. Sebastian, A. Unnikrishnan, and K. Balakrishnan, "Grey level co-occurrence matrices: generalization and some new features," *International Journal of Computer Science, Engineering and Information Technology*, vol. 2, no. 2, pp. 151–157, 2012.

- [56] A. R. Backes, A. S. Martinez, and O. M. Bruno, "Texture analysis using graphs generated by deterministic partially self-avoiding walks," *Pattern Recognition*, vol. 44, no. 8, pp. 1684–1689, 2011.
- [57] R. Suguna and P. Anandhakumar, "A novel feature extraction technique for texture discrimination using orthogonal polynomial operators," *European Journal of Scientific Research*, vol. 51, no. 4, pp. 550–563, 2011.
- [58] H. Tamura, S. Mori, and T. Yamawaki, "Textural features corresponding to visual perception," *IEEE Transactions on Systems, Man and Cybernetics*, vol. 8, no. 6, pp. 460–473, 1978.
- [59] E. Alpaydini, *Introduction to Machine Learning*, MIT Press, 2nd edition, 2010.

Research Article

Computer Aided Quantification of Pathological Features for Flexor Tendon Pulleys on Microscopic Images

**Yung-Chun Liu,^{1,2} Hsin-Chen Chen,^{1,3} Hui-Hsuan Shih,^{1,2} Tai-Hua Yang,^{4,5}
Hsiao-Bai Yang,^{6,7} Dee-Shan Yang,⁸ Fong-Chin Su,^{2,4} and Yung-Nien Sun^{1,2}**

¹ Department of Computer Science & Information Engineering, National Cheng Kung University, Tainan 701, Taiwan

² Medical Device Innovation Center, National Cheng Kung University, Tainan 701, Taiwan

³ Department of Neurosurgery, University of Pittsburgh, Pittsburgh, PA 15213, USA

⁴ Department of Biomedical Engineering, National Cheng Kung University, Tainan 701, Taiwan

⁵ Orthopedic Biomechanics Laboratory, Division of Orthopedic Research, Mayo Clinic Rochester, Rochester, MN 55905, USA

⁶ Department of Pathology, Medical College, National Cheng Kung University, Tainan 701, Taiwan

⁷ Department of Pathology, Ton-Yen General Hospital, Hsinchu 302, Taiwan

⁸ Department of Orthopedic Surgery, Ton-Yen General Hospital, Hsinchu 302, Taiwan

Correspondence should be addressed to Yung-Nien Sun; yunsun@mail.ncku.edu.tw

Received 18 January 2013; Revised 22 May 2013; Accepted 26 May 2013

Academic Editor: Norio Tagawa

Copyright © 2013 Yung-Chun Liu et al. This is an open access article distributed under the Creative Commons Attribution License, which permits unrestricted use, distribution, and reproduction in any medium, provided the original work is properly cited.

Quantifying the pathological features of flexor tendon pulleys is essential for grading the trigger finger since it provides clinicians with objective evidence derived from microscopic images. Although manual grading is time consuming and dependent on the observer experience, there is a lack of image processing methods for automatically extracting pulley pathological features. In this paper, we design and develop a color-based image segmentation system to extract the color and shape features from pulley microscopic images. Two parameters which are the size ratio of abnormal tissue regions and the number ratio of abnormal nuclei are estimated as the pathological progression indices. The automatic quantification results show clear discrimination among different levels of diseased pulley specimens which are prone to misjudgments for human visual inspection. The proposed system provides a reliable and automatic way to obtain pathological parameters instead of manual evaluation which is with intra- and interoperator variability. Experiments with 290 microscopic images from 29 pulley specimens show good correspondence with pathologist expectations. Hence, the proposed system has great potential for assisting clinical experts in routine histopathological examinations.

1. Introduction

Trigger finger is a common medical condition which occurs when the sheath of finger flexor tendon thickens, causing unsmooth glide of the tendon. The affected finger usually yields pains, intermittent snapping (triggering), or actual locking (during flexion or extension) resulting in patient difficulty [1]. Although more than one potential cause has been described, the etiology of the trigger finger remains idiopathic [2]. In order to understand the real causes and risk factors of trigger finger, microscopic evaluation for various degrees of pathological change hence becomes a critical issue.

The pathological mechanism in the flexor sheath has been reported as the fibrocartilaginous metaplasia (or chondroid

metaplasia) of its “A1” pulley based on the histopathological analysis [3]. In a normal pulley, there is a dense, regular, and connective tissue that is composed of collagenous fibers in compact and parallel bundles. Generally, histopathological specimens of collagenous fibers appear eosinophilic and pink in color under hematoxylin and eosin (H&E) stain. Moreover, it can be observed from microscopic images that the fibroblasts of a normal pulley possess long rod-like nuclei between the longitudinal bundles. On the other hand, the pulley of a trigger finger usually demonstrates the phenomenon of fibrocartilaginous metaplasia (or chondroid metaplasia), which is characterized by the presence of chondrocytes (cartilage cells). The affected fibers thus contain round nuclei and sulfate

proteoglycans appearing in blue/purple color under the H&E stain [4].

A good interpretation of microscopic image depends on the level of abnormality observed from a combination of good visual evaluation and theoretical knowledge by pathologists [5]. Such qualitative evaluation of pathological changes remains the most common approach to grade trigger finger. However, due to intra- and interobserver variability, the accuracy of the grading results is decreased and the reproducibility of the experiment is difficult to ensure. Moreover, some quantities, such as the amount of nuclei, are impractical to obtain by visually examining the entire microslide. These limitations increase the probability of making an inappropriate decision for follow-up therapy. The aim of this paper is to define two parameters that reflect the above-mentioned color and shape features of pulley specimens and develop an image analysis system for automatic and objective microscopic evaluation of the pulley pathological changes.

Microscopic image analysis methods have been actively investigated because they provide the most direct information for evaluating morphological or functional changes of tissues of interest at the microscopic level. Tabesh et al. [6] proposed an automatic prostate cancer classification system to analyze the microscopy of the prostate cancer tissues with color features in the R, G, and B channels of the acquired images. However, as the acquired images are nonuniformly illuminated, their simple thresholding method is not directly applicable in our case. Wu et al. [7] proposed a live cell image segmentation method to directly segment the cell regions using gray level. However, in our case, the pink areas which represent the normal tissues and the purple areas which represent the diseased tissues show very close gray level in the acquired images. Only using the gray level information in separating the abnormal from normal tissues on the pulley microscopic image would likely give erroneous results. The Canny edge detector is also a popular way to detect the border of cells [8]. However, in our case, the Canny operator detects not only the borders of nuclei but also the borders of dark blue and noise areas. As we are only interested in the borders of nuclei, too many irrelevant edges detected by the Canny operator tend to make the postprocessing process tedious and increase the likelihood of detection errors.

In this paper, we propose an image analysis system to automatically quantify the pathological features of pulleys with trigger finger on microscopic images. Two parameters, which are the size ratio of abnormal tissue regions (parameter 1) and the number ratio of abnormal nuclei (parameter 2), are designed to reflect the severity of diseased tissues based on the pathologist suggestions. Figure 1 shows the flowchart of the proposed method. First, the proposed system applies a color normalization to efficiently reduce the influence of nonuniform color distribution among the captured images. Then, the system adopts a three-stepped color segmentation process to extract normal and abnormal tissue regions from the hue-saturation-intensity (HSI) color space of the color-normalized image in order to calculate parameter 1. In addition, we design an active double thresholding algorithm to segment the nuclei and utilize a rule-based classifier based

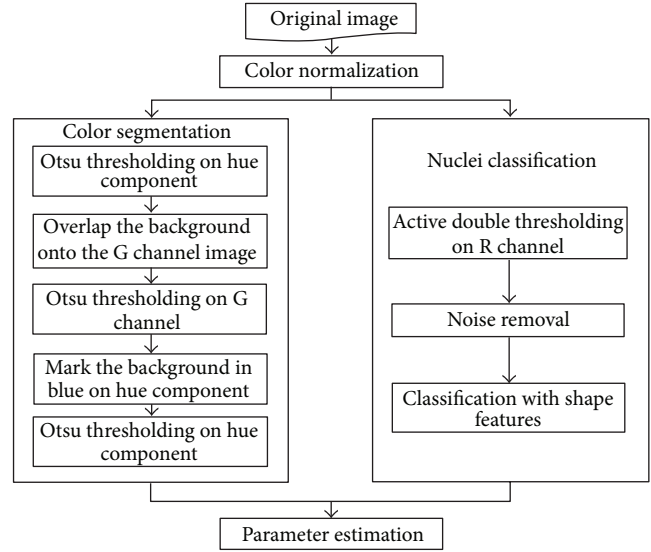


FIGURE 1: Flowchart of the proposed system.

on nuclei shape properties to identify normal and abnormal nuclei for calculating parameter 2. Experiments demonstrate high correspondence between the automatically estimated parameters and the qualitative judgments of a pathologist.

2. Materials

The microscopic images of specimens in this study were provided by the laboratories in National Cheng Kung University Hospital and in Ton Yen General Hospital. The pathological pulley tissue specimens were obtained from the patients who were clinically diagnosed with trigger finger disease by orthopedists D. S. Yang and T. H. Yang. For pathological examination, all of the specimens followed the procedures of fixation in formalin, procession in graded alcohols and xylene, embedding in paraffin, cutting of sections with a microtome, and being stained with hematoxyline-eosin (H&E). The microtome was preset for a $5\ \mu\text{m}$ in thickness.

In these specimens, the normal pulley showed a dense regular fibrotic tissue. The collagenous fibers were arranged in compact, parallel bundles. Between the bundles were rows of modified fibroblasts with elongated spindle-shaped nuclei. The pathologic pulley tissue presented fibrocartilage metaplasia. It was composed of irregular connective tissue with fibrocartilaginous metaplasia (or chondroid metaplasia). In the H&E stained slides, the nuclei were dark blue in color and the collagenous fibers were pink in color. The fibrocartilaginous metaplastic (or chondroid metaplastic) tissue demonstrated more chondromyxoid materials (including hyaluronic acid, chondroitin sulfate, and proteoglycan) and showed blue or purple colors. Furthermore, nuclei of cartilage-like cells were round in shape. The prepared slides were first observed and graded according to the severity of myxoid metaplasia by pathologist H. B. Yang under a light microscope (Olympus, BX50). These specimens were also analyzed by the proposed system based on the above-mentioned color and shape

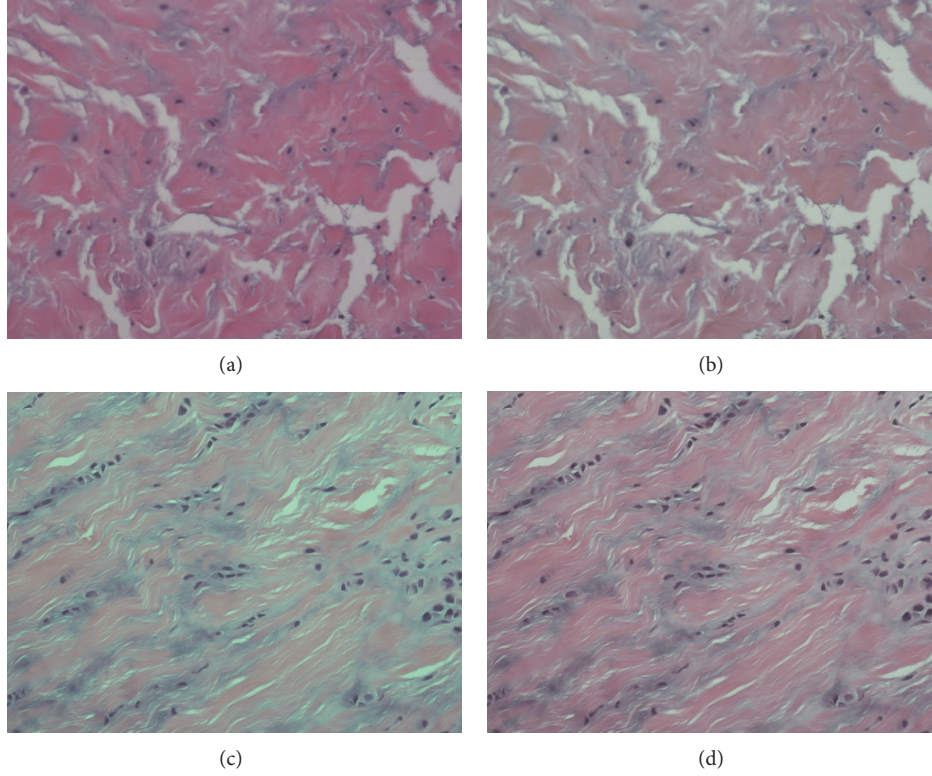


FIGURE 2: Color normalization. (a) and (c) are two original images from different specimens; (b) and (d) are results of (a) and (c) after performing color normalization, respectively.

features. The automatic evaluation results were then compared with the manually graded results.

3. Methods

3.1. Color Normalization. The color normalization method is used to resolve the problem of nonuniform distribution in color and illumination of the acquired images, which are caused by the different staining and imaging conditions of the microscopic slices. As shown in Figures 2(a) and 2(c), color distributions of the two acquired images are quite different from each other. Color normalization will help to map these different microscopic images to a common image type with similar color distribution.

The color normalization method provided by Reinhard et al. [9] is adopted in this study. Initially, we must choose some standard images (target images) from the source image dataset with the following characteristics: the contrast ratio is high and the color of nuclei is dark blue. In other words, these standard images can show high contrast and can be used to categorize the various tissue types. We then normalize the input (or source) image to the color distribution of target images.

We transform the images from RGB color space into LMS color space by the following equation:

$$\begin{bmatrix} L \\ M \\ S \end{bmatrix} = \begin{bmatrix} 0.3811 & 0.5783 & 0.0402 \\ 0.1967 & 0.7244 & 0.0782 \\ 0.0241 & 0.1288 & 0.8444 \end{bmatrix} \begin{bmatrix} R \\ G \\ B \end{bmatrix}. \quad (1)$$

Because the data in this color space are often quite skewed, Reinhard et al. reduced skew error by converting the data to a logarithmic space by using (2):

$$L' = \log L, \quad M' = \log M, \quad S' = \log S. \quad (2)$$

Moreover, Ruderman et al. [10] suggested a transformation from $L'M'S'$ to $l\alpha\beta$ through (3). It is because $l\alpha\beta$ are the three orthogonal axes decomposed from $L'M'S'$ by using principle component analysis into the three most maximal directions ($l\alpha\beta$) decorrelating the $L'M'S'$ axes. In the experiments, the resulting color distribution of different tissues is more widely separated in $l\alpha\beta$ color space than in the original RGB color space:

$$\begin{bmatrix} l \\ \alpha \\ \beta \end{bmatrix} = \begin{bmatrix} \frac{1}{\sqrt{3}} & 0 & 0 \\ 0 & \frac{1}{\sqrt{6}} & 0 \\ 0 & 0 & \frac{1}{\sqrt{2}} \end{bmatrix} \begin{bmatrix} 1 & 1 & 1 \\ 1 & 1 & -2 \\ 1 & -1 & 0 \end{bmatrix} \begin{bmatrix} L' \\ M' \\ S' \end{bmatrix}. \quad (3)$$

We then calculate the mean and the standard deviation values of l , α and β for all target images and obtain the averaged mean and averaged standard deviation which are denoted as μ_t^l , μ_t^α , and μ_t^β , and σ_t^l , σ_t^α , and σ_t^β , respectively. These average mean and standard deviation values are calculated once and then used for the normalization of every input image. For each input image, we have to calculate the mean

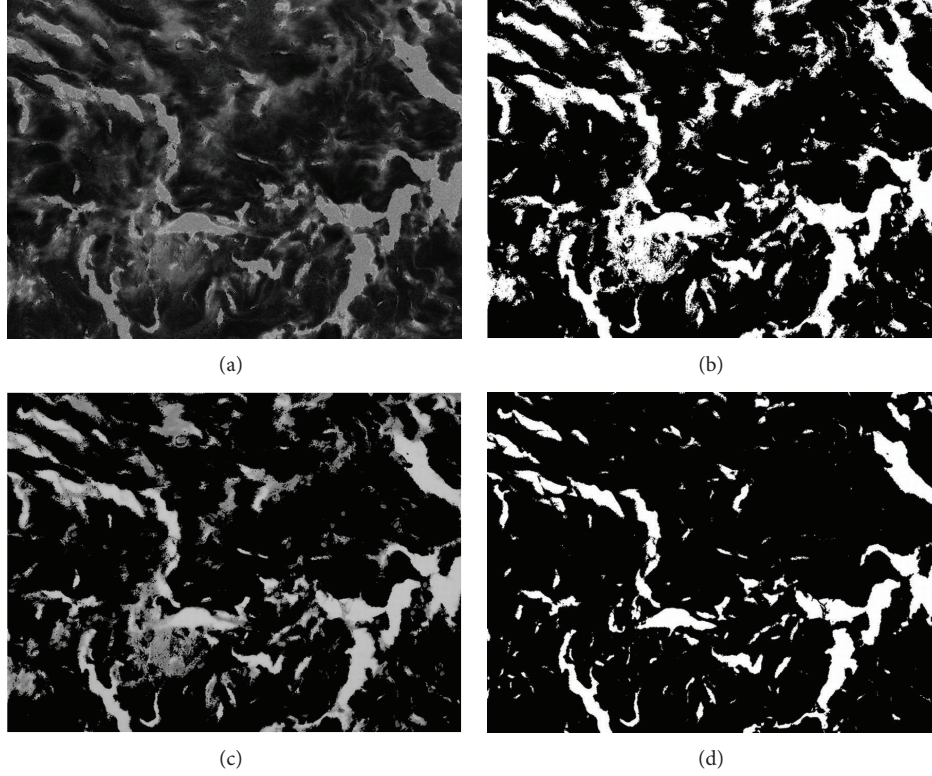


FIGURE 3: Color segmentation for Figure 2(a) (part 1). (a) The hue component of Figure 2(b); (b) the Otsu thresholding result of (a); (c) overlap the G channel to the white areas of (b); (d) the result of segmentation on (c), where white areas represent empty background and black areas represent tissue foreground.

and standard deviation values denoted as $\mu_s^l, \mu_s^\alpha,$ and $\mu_s^\beta,$ and $\sigma_s^l, \sigma_s^\alpha, \sigma_s^\beta,$ respectively.

The normalization of an input image is performed by calculating the new color values l'', α'' and β'' for each pixel by the following equations:

$$\begin{aligned} l^* &= l - \mu_s^l, & \alpha^* &= \alpha - \mu_s^\alpha, & \beta^* &= \beta - \mu_s^\beta, \\ l' &= \frac{\sigma_t^l}{\sigma_s^l} l^*, & \alpha' &= \frac{\sigma_t^\alpha}{\sigma_s^\alpha} \alpha^*, & \beta' &= \frac{\sigma_t^\beta}{\sigma_s^\beta} \beta^*, \\ l'' &= l' + \mu_t^l, & \alpha'' &= \alpha' + \mu_t^\alpha, & \beta'' &= \beta' + \mu_t^\beta. \end{aligned} \quad (4)$$

Finally, we transform the resulting image in $\alpha\beta$ color space back to RGB color space by using (5):

$$\begin{bmatrix} R \\ G \\ B \end{bmatrix} = \begin{bmatrix} 4.4679 & -3.5873 & 0.1193 \\ -1.2186 & 2.3809 & -0.1624 \\ 0.0497 & -0.2439 & 1.2045 \end{bmatrix} \times \begin{bmatrix} \exp\left(\frac{\sqrt{3}}{3}l'' + \frac{\sqrt{6}}{6}\alpha'' + \frac{\sqrt{2}}{2}\beta''\right) \\ \exp\left(\frac{\sqrt{3}}{3}l'' + \frac{\sqrt{6}}{6}\alpha'' - \frac{\sqrt{2}}{2}\beta''\right) \\ \exp\left(\frac{\sqrt{3}}{3}l'' - \frac{\sqrt{6}}{3}\alpha'' + 0\beta''\right) \end{bmatrix}. \quad (5)$$

Figures 2(b) and 2(d) show the normalization results of Figures 2(a) and 2(c), respectively. The color distributions of the normalized images are comparable to those of the target images. All input images from different batches of specimens can be processed by this procedure for color normalization.

3.2. HSI Model Transformation and Three-Stepped Color Segmentation.

Before color segmentation, we transform the normalized image into the HSI color space by using (6) [11, 12]. Currently, the pink part and major part of the purple areas in the normalized image are lower in hue value, and the background and some small parts of the purple areas in the normalized image have higher hue values. Figure 3(a) shows the hue component of Figure 2(b):

$$H = \begin{cases} \theta & \text{if } B \leq G \\ 360 - \theta & \text{if } B > G, \end{cases} \quad (6)$$

$$\theta = \cos^{-1} \left\{ \frac{(1/2)[(R-G) + (R-B)]}{[(R-G)^2 + (R-B)(G-B)]^{1/2}} \right\}.$$

Based on the hue distribution, we apply the automatic thresholding method proposed by Otsu [13] to obtain the first binary image as shown in Figure 3(b), which is roughly divided into foreground and background. In Otsu's

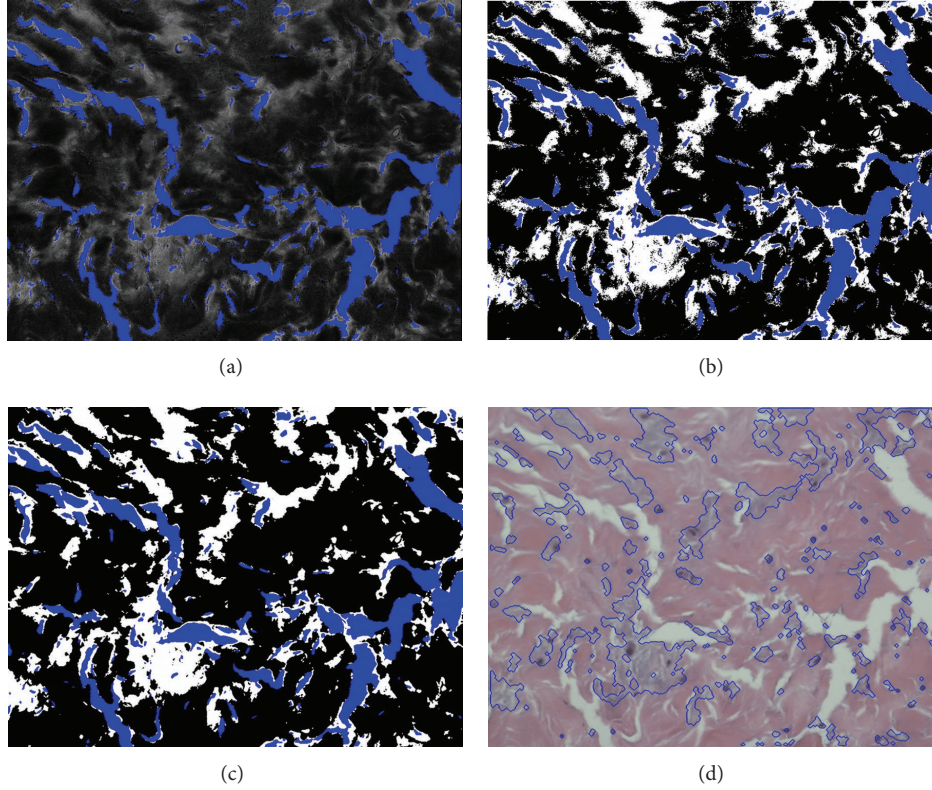


FIGURE 4: Color segmentation for Figure 2(a) (part 2). (a) Blue is the empty background and the other hue component areas are tissue foreground; (b) the segmented result, where blue represents background, white represents abnormal tissue, and black represents normal tissue; (c) rank filtering result; (d) boundaries of abnormal tissue regions mapped onto the normalized image.

thresholding, the optimal threshold k^* , which separates two classes, is obtained by using optimization:

$$\arg \max_{k^*} \{ \sigma_B^2(k), 0 \leq k \leq 255 \}, \quad (7)$$

where $\sigma_B^2 = \omega_0 \omega_1 (\mu_0 - \mu_1)^2$ is the interclass variance and $\omega_0, \omega_1, \mu_0$, and μ_1 are the probabilities of class occurrences and the mean levels of the two classes, respectively. The black areas represent the pink and most of the purple tissue areas as the foreground and the white areas cover some small parts of the purple tissue areas and the empty background. In other words, some purple areas may be faultily classified into the background. To make the foreground include all the purple tissues, we have to extract the remaining purple part from the background areas. The obtained background areas are used as the mask to map onto the G channel of normalized image, which is shown in Figure 3(c), and the second Otsu thresholding on the G channel is then applied to obtain the remaining purple areas. We then get the second binary image as in Figure 3(d), where the white area represents the real background and the black area represents the complete foreground of pink and purple tissue areas.

After obtaining the foreground, we then have to separate the abnormal tissue from the normal tissue areas. In Figure 4(a), we label the background areas obtained in the previous step in blue and overlap onto the original hue

component image in Figure 3(a). As mentioned before, the normal tissue areas show lower hue values and the abnormal areas have higher hue, so we can use the Otsu thresholding again to divide these two areas. The segmented result is shown in Figure 4(b), where the blue areas represent the background, the black areas represent the normal tissues, and the white areas represent the abnormal tissues. As the segmentation results are fragmented in the boundaries, we apply the rank filter to remove fragmented regions. We calculate the pixel numbers of each color in Figure 4(b) with a 9×9 mask and then assign the color with the highest count to the central pixel of mask; the result is shown in Figure 4(c). Figure 4(d) shows the boundaries of abnormal tissues mapped onto the normalized image.

3.3. Active Double Thresholding and Nuclei Classification.

Another characteristic to evaluate the level of pathological change is the ratio of round nuclei which belongs to the abnormal cells. We can use this ratio, instead of the area ratio, to characterize tissue condition when the staining colors are faded or if specimens are degraded after a long preservation time.

After color normalization, we find that the R channel of the normalized image is more suitable for nuclei segmentation due to its high contrast of nuclei as in Figure 5(a). (In this section, we demonstrate the procedures of nuclei

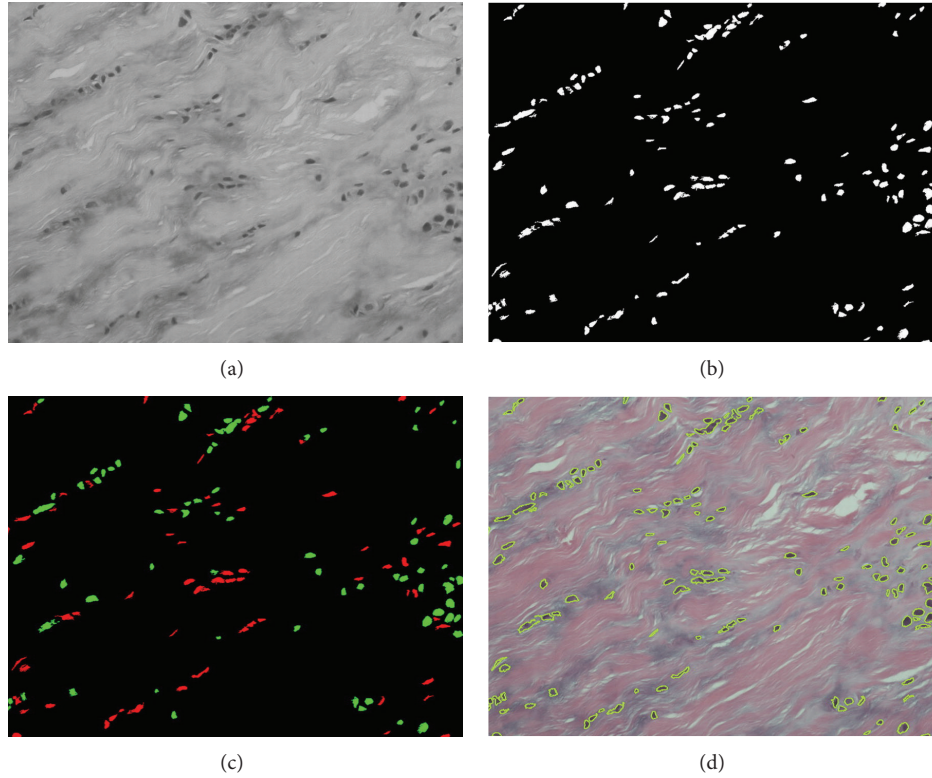


FIGURE 5: Nuclei classification for Figure 2(d). (a) The R channel of Figure 2(d); (b) the result after double thresholding; (c) the classification result, where red represents the normal nuclei and green represents the abnormal nuclei; (d) overlap the nucleus edges onto the original image.

classification with another normalized image shown in Figure 2(d).) Therefore, we use the double thresholding scheme [14] to segment the nucleus areas. The intensity of nuclei is nearly the darkest of the whole R channel image. As the intensity distributions of images are different, we thus apply an active thresholding scheme to satisfy all images. First, for each input R channel image, we take the average of the ten lowest intensity values as the lowest intensity value of the image. Second, we add two empirical values 30 and 45 to this lowest value and use them as the two values for double thresholding. The lower threshold value is used as the seed and the higher threshold value is the restriction of region growing. After we apply the double thresholding scheme, the white areas of the resulting image represent the segmentation of nuclei and the segmentation result of nuclei is shown in Figure 5(b).

Now we can classify the segmented nuclei into three categories according to their shapes. The normal nuclei are usually long and rod-like, and the abnormal nuclei are usually round in shape. However, the connected area with multinuclei, which is regarded as the third category, is irregular in shape and classified as abnormal because only the abnormal nuclei will grow and connect each other into a cluster.

To classify these nuclei, we then calculate the area size, the circularity index, and the maximum and the minimum distances between the centroid and boundary points for each nucleus area. We then classify the nucleus as normal and

rod-like if the circularity index is less than 0.95, the ratio of maximum to minimum distance is greater than 3, and the area is less than 2,000 pixels. All other areas are then classified as abnormal nuclei. In addition, we also define the area as a single abnormal round nucleus if the area is less than 2,000 pixels.

After defining all the single abnormal round nuclei, we then calculate the average area of these nuclei. The average area is then used to calculate how many nuclei are in a connected multinuclei area. Figure 5(c) shows the classification results where red presents the normal nuclei, green presents the abnormal nuclei. The nucleus edges were overlapped onto the original image as shown in Figure 5(d).

4. Results and Discussion

4.1. Specimen Preparation. In this study, we collected abnormal and normal specimens from trigger finger patients and nondiseased cadavers, respectively. All the specimens used in the experiments were graded into four severity stages as H (High), M (Middle), L (Low), and N (Normal) in trigger finger disease by the pathologist (Dr. Hsiao-Bai Yang). The numbers of collected specimens were 10 with H stage, 10 with M stage, 6 with L stage, and 3 with N stage, respectively (29 specimens in total). From each specimen, 49 images in the size of 2560×1920 were acquired by using our previously developed autofocusing system [15]. As some of the 49 images

TABLE 1: The size ratio of abnormal tissue regions (parameter 1).

Specimen no.	Normal (pixel ²)	Abnormal (pixel ²)	Ratio
H-1	31791895	12495997	0.282
H-2	30894213	10986876	0.262
H-3	31869804	11038359	0.257
H-4	32511973	11026116	0.253
H-5	33797170	10267132	0.233
H-6	31635397	11474053	0.266
H-7	31451368	11224479	0.263
H-8	32950410	11695269	0.262
H-9	34067450	10887277	0.242
H-10	27747278	10290969	0.271
Mean ± SD			0.259 ± 0.014
M-1	35698059	7946874	0.182
M-2	34326147	8515580	0.199
M-3	35324719	8461582	0.193
M-4	33284256	7671304	0.187
M-5	34422738	9418395	0.215
M-6	34315916	9170559	0.211
M-7	33027627	9072248	0.215
M-8	34051300	7529957	0.181
M-9	35167293	8706583	0.198
M-10	32745438	8083811	0.198
Mean ± SD			0.198 ± 0.013
L-1	40491940	5972857	0.129
L-2	43877544	2773360	0.059
L-3	36923582	6077911	0.141
L-4	37539086	4417329	0.105
L-5	34975123	7460192	0.176
L-6	36623101	5244448	0.125
Mean ± SD			0.123 ± 0.039
N-1	40904631	5482052	0.118
N-2	32792539	3323970	0.092
N-3	32724101	4340358	0.117
Mean ± SD			0.109 ± 0.054

contained a large area of background and irrelevant tissues (e.g., microvasculature), such images provided less image evidence of pulley tissues and were not suitable for evaluating the proposed pathological parameters. Consequently, the same pathologist of our research group was asked to exclude the unsuitable images based on her expertise on tissue pathology. Then, a random selection process was performed to acquire 10 images from the remaining images for the subsequent quantitative analysis.

4.2. Pathological Indices. The proposed microscopic image analysis system was designed to obtain two pathological parameters. The size ratio of abnormal tissue regions is parameter 1 which can be calculated by using (8). In (8), the area of normal tissue regions represents the sum of pink (or blue for abnormal) areas from the 10 selected images of each specimen. Table 1 presents the resulting parameter 1s for different specimens obtained by using the proposed color segmentation procedure. The number ratio of abnormal

TABLE 2: The number ratio of abnormal nuclei (parameter 2).

Specimen no.	Normal	Abnormal	Ratio
H-1	271	660	0.709
H-2	481	1088	0.693
H-3	244	529	0.684
H-4	117	385	0.767
H-5	289	1098	0.792
H-6	721	1653	0.696
H-7	292	655	0.692
H-8	165	817	0.832
H-9	446	1013	0.694
H-10	59	151	0.719
Mean ± SD			0.728 ± 0.051
M-1	382	687	0.643
M-2	318	591	0.650
M-3	192	360	0.652
M-4	131	187	0.588
M-5	308	652	0.679
M-6	173	343	0.665
M-7	335	456	0.576
M-8	726	1311	0.644
M-9	382	647	0.629
M-10	379	795	0.677
Mean ± SD			0.640 ± 0.034
L-1	824	771	0.483
L-2	1080	1210	0.528
L-3	520	636	0.550
L-4	404	477	0.541
L-5	862	1165	0.575
L-6	123	259	0.678
Mean ± SD			0.559 ± 0.066
N-1	473	247	0.343
N-2	310	205	0.398
N-3	292	308	0.513
Mean ± SD			0.418 ± 0.074

nuclei is parameter 2 and can be calculated by using (9). In (9), the number of normal (or abnormal) nuclei is the total number of normal (or abnormal) nuclei obtained from the 10 selected images of each specimen by using the rule-based classifier. Table 2 shows the resulting parameter 2s for different specimens:

The size ratio of abnormal tissue regions

$$= \frac{\text{Area of abnormal tissue regions}}{\text{Area of abnormal tissue regions} + \text{Area of normal tissue regions}} \quad (8)$$

The number ratio of abnormal nuclei

$$= \frac{\text{Number of abnormal nuclei}}{\text{Number of abnormal nuclei} + \text{Number of normal nuclei}} \quad (9)$$

Based on the pathological staging, the resulting parameters in Table 1 show clear deviations among the three

TABLE 3: P values between different serious stages.

Group pair	Parameter 1	Parameter 2
High versus middle	0.000	0.000
Middle versus low	0.004	0.028

(H, M, and L) stages. There are significant differences between the mean values of adjacent stages. Using the average of two mean values for two adjacent stages, we can obtain two threshold values to perform simple discrimination between the three severity stages. Consequently, there are no errors in H and M stages and only one misclassification from L to M stage from all the collected specimens of our experiments. In Table 2, the number ratio of abnormal nuclei also shows similar characteristics with good deviations among the three stages. Simple discrimination among the three severity stages is performed the same way as in Table 1. There are no classification errors in the H stage, 2 misclassifications from M to L stage, and 1 misclassification from L to M stage. However, the three misclassifications with parameter 2 have no intersections with the one with parameter 1. This implies that the discrimination between three severity stages can be correctly performed with the weighted combination of parameters 1 and 2. Since we only have a limited number of specimens presently, a more complicated classification mechanism is left for research with more sufficient specimens in the future. The pathological parameters of N stage are measured with only 3 specimens and also presented in Tables 1 and 2. The mean values of the two parameters are all smaller than the ones of L stage. Because stages L and N are less severe, the resulting measurements reflect the clinical expectation. Figures 6 and 7 show the boxplots [16] for the three severity stages with parameter 1 and parameter 2, respectively. For each box in the figure, the central mark is the median, the edges of box are the 25th and 75th percentiles, the whiskers extend to the most extreme data points, and outliers are plotted individually. The boxplots also reflect the clustering ability of the two parameters similar to the above-mentioned simple discrimination examples.

In addition, statistical analysis was performed by Student's t -test and the P values between different severity stages were calculated (as shown in Table 3). If the P value is less than 0.05, the two groups are considered to have significant differences and can be easily divided. For parameter 1, the P values for group pairs H versus M and M versus L are 0.000 and 0.004, respectively. For parameter 2, the P values for group pairs H versus M and M versus L are 0.000 and 0.028, respectively. As all statistical tests are significant (less than 0.05), it is suggested that both parameters can be used as pathological indices for grading the severity stages effectively.

4.3. System Performance

4.3.1. Parameter Setting. The values of the system parameters used in active double thresholding (in Section 3.3) could be a factor influencing the stability of automated image

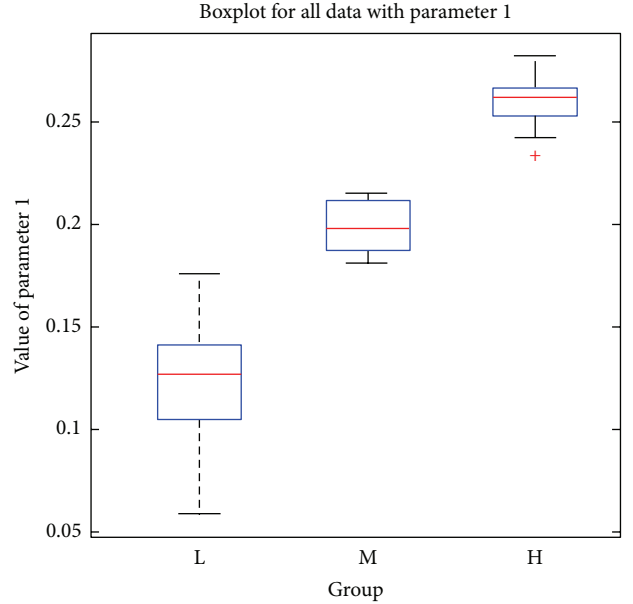


FIGURE 6: Boxplot for the three severity stages with parameter 1.

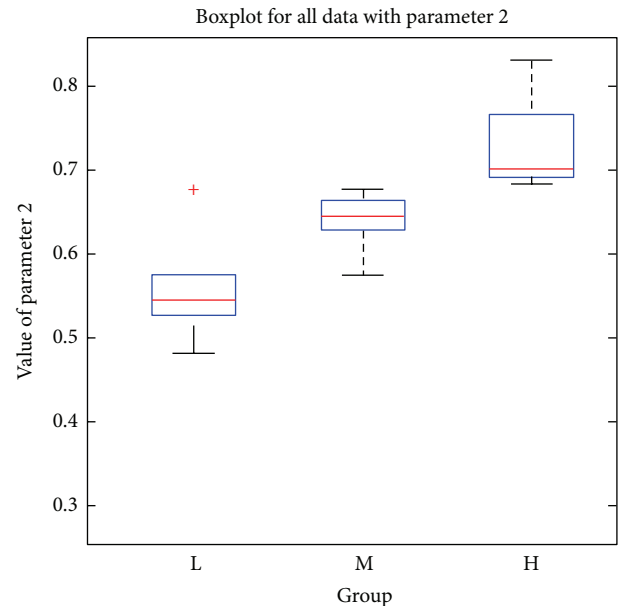


FIGURE 7: Boxplot for the three severity stages with parameter 2.

analysis. Thus, we employed the color normalization step to effectively reduce the influences caused by different imaging and staining conditions. After color normalization, the system parameters can be determined based on the intensity contrast between pulley tissue and surrounding regions on the normalized images. When applying the same parameter values throughout the entire experiment with 290 images, the proposed system was capable of achieving accurate measurement results.

On the other hand, the system parameters used in nuclei classification were determined and tuned by the pathologists

based on their pathological knowledge and clinical experiences. Our experimental results showed that the system is capable of making correct discriminations between the disease stages based on the ratio of abnormal nuclei by using the same set of system parameters. All the 290 images from the 29 specimens were analyzed consistently. If some more complicated parameters are designed for tissue measurement in the future, more complex classifiers can be helpful to determine these system parameters.

4.3.2. Computational Time. The system was developed on an Intel Core i5 2.8 GHz PC with 3.5 GB memory. For an image of 2560×1920 pixels, the average computational time of color normalization, color segmentation, and nuclei classification was approximately 5, 12, and 10 seconds, respectively.

5. Conclusions

In this paper, we have developed an automatic image analysis system to evaluate the severity of trigger finger disease from the microscopic pulley images. Two pathological parameters are designed and can be computed automatically and efficiently. The quantitative measurements are stable and without intra- and interoperator variability of manual measurements. Twenty-nine pulley specimens are evaluated with the same image analysis setting in the experiments. The experimental results show that the two parameter measures have good deviations among the three pathological stages and can be used to discriminate the severity stages with simple discrimination mechanism. Thus, the proposed image analysis system clearly provides an efficient and reliable way in measuring the pathological progression of trigger finger disease. The quantitative parameters are objective and can also be extended for other kinds of pathological specimens. In the future, we will recruit more cases in the validation of trigger finger disease and also explore new opportunities for other clinic applications.

Acknowledgment

The authors would like to express their appreciation for the Grant under Contract NSC 100-2627-B-006-008 from the National Science Council, Taiwan. This work also utilized the shared facilities supported by the Medical Device Innovation Center, National Cheng Kung University, Tainan, Taiwan.

References

- [1] K. Drossos, M. Remmelink, N. Nagy, V. de Maertelaer, J. L. Pasteels, and F. Schuind, "Correlations between clinical presentations of adult trigger digits and histologic aspects of the A1 pulley," *Journal of Hand Surgery*, vol. 34, no. 8, pp. 1429–1435, 2009.
- [2] A. H. Makkouk, M. E. Oetgen, C. R. Swigart, and S. D. Dodds, "Trigger finger: etiology, evaluation, and treatment," *Current Reviews in Musculoskeletal Medicine*, vol. 1, no. 2, pp. 92–96, 2008.
- [3] S. P. Sampson, M. A. Badalamente, L. C. Hurst, and J. Seidman, "Pathobiology of the human A1 pulley in trigger finger," *Journal of Hand Surgery*, vol. 16, no. 4, pp. 714–721, 1991.
- [4] M. C. Sbernardori and P. Bandiera, "Histopathology of the A1 pulley in adult trigger fingers," *Journal of Hand Surgery*, vol. 32, no. 5, pp. 556–559, 2007.
- [5] M. A. Marchevsky and P. H. Bartels, *Image Analysis—A Primer of Pathologists*, Raven Press, 1994.
- [6] A. Tabesh, V. P. Kumar, H.-Y. Pang et al., "Automated prostate cancer diagnosis and gleason grading of tissue microarrays," in *Medical Imaging 2005: Image Processing*, Proceedings of SPIE, pp. 58–70, February 2005.
- [7] K. Wu, D. Gauthier, and M. D. Levine, "Live cell image segmentation," *IEEE Transactions on Biomedical Engineering*, vol. 42, no. 1, pp. 1–12, 1995.
- [8] J. Canny, "A computational approach to edge detection," *IEEE Transactions on Pattern Analysis and Machine Intelligence*, vol. 8, no. 6, pp. 679–698, 1986.
- [9] E. Reinhard, M. Ashikhmin, B. Gooch, and P. Shirley, "Color transfer between images," *IEEE Computer Graphics and Applications*, vol. 21, no. 5, pp. 34–41, 2001.
- [10] D. L. Ruderman, T. W. Cronin, and C.-C. Chiao, "Statistics of cone responses to natural images: implications for visual coding," *Journal of the Optical Society of America A*, vol. 15, no. 8, pp. 2036–2045, 1998.
- [11] R. C. Gonzalez and R. E. Woods, *Digital Image Processing*, Prentice Hall, Upper Saddle River, NJ, USA, 3rd edition, 2008.
- [12] H. D. Cheng, X. H. Jiang, Y. Sun, and J. L. Wang, "Color image segmentation: advances and prospects," *Pattern Recognition*, vol. 34, no. 12, pp. 2259–2281, 2001.
- [13] N. Otsu, "A threshold selection method from gray-level histograms," *IEEE Transactions on Systems, Man, and Cybernetics*, vol. 9, no. 1, pp. 62–66, 1979.
- [14] Q. Chen, Q.-S. Sun, P. A. Heng, and D.-S. Xia, "A double-threshold image binarization method based on edge detector," *Pattern Recognition*, vol. 41, no. 4, pp. 1254–1267, 2008.
- [15] Y.-C. Liu, F.-Y. Hsu, H.-C. Chen, Y.-N. Sun, and Y.-Y. Wang, "A coarse-to-fine auto-focusing algorithm for microscopic image," in *Proceedings of the International Conference on System Science and Engineering (ICSSE '11)*, pp. 416–419, 2011.
- [16] R. McGill, J. W. Tukey, and W. A. Larsen, "Variations of box-plots," *The American Statistician*, vol. 32, no. 1, pp. 12–16, 1978.

Research Article

Classification of Cerebral Lymphomas and Glioblastomas Featuring Luminance Distribution Analysis

Toshihiko Yamasaki,^{1,2} Tsuhan Chen,¹ Toshinori Hirai,³ and Ryuji Murakami⁴

¹ School of Electrical and Computer Engineering, Cornell University, Phillips Hall, Ithaca, NY 14853-5401, USA

² Department of Information and Communications Engineering, The University of Tokyo, 7-3-1 Hongo, Bunkyo-ku, Tokyo 113-8656, Japan

³ Department of Diagnostic Radiology, Kumamoto University, 1-1-1 Honjo, Kumamoto City, Kumamoto 860-8556, Japan

⁴ Department of Medical Imaging, Kumamoto University, 4-24-1 Kuhonji, Kumamoto City, Kumamoto 862-0976, Japan

Correspondence should be addressed to Toshihiko Yamasaki; yamasaki@hal.t.u-tokyo.ac.jp

Received 17 January 2013; Accepted 20 May 2013

Academic Editor: Yi-Hong Chou

Copyright © 2013 Toshihiko Yamasaki et al. This is an open access article distributed under the Creative Commons Attribution License, which permits unrestricted use, distribution, and reproduction in any medium, provided the original work is properly cited.

Differentiating lymphomas and glioblastomas is important for proper treatment planning. A number of works have been proposed but there are still some problems. For example, many works depend on thresholding a single feature value, which is susceptible to noise. In other cases, experienced observers are required to extract the feature values or to provide some interactions with the system. Even if experts are involved, interobserver variance becomes another problem. In addition, most of the works use only one or a few slice(s) because 3D tumor segmentation is time consuming. In this paper, we propose a tumor classification system that analyzes the luminance distribution of the whole tumor region. Typical cases are classified by the luminance range thresholding and the apparent diffusion coefficients (ADC) thresholding. Nontypical cases are classified by a support vector machine (SVM). Most of the processing elements are semiautomatic. Therefore, even novice users can use the system easily and get the same results as experts. The experiments were conducted using 40 MRI datasets. The classification accuracy of the proposed method was 91.1% without the ADC thresholding and 95.4% with the ADC thresholding. On the other hand, the baseline method, the conventional ADC thresholding, yielded only 67.5% accuracy.

1. Introduction

The purpose of this study is to present an objective and accurate tumor classification system that considers the luminance distribution of the whole 3D tumor region. Differentiating lymphomas and glioblastoma by noninvasive ways is an important problem because they require different chemotherapy regimens. For example, if the tumor is highly suspected to be lymphomas, stereotactic biopsy is usually recommended to confirm the diagnosis. If the tumor is highly suspected to be glioblastoma, craniotomy would be chosen. Chemotherapy regimens are different for the two tumors, as well.

Therefore, a number of works have been proposed. For instance, Toh et al. [1] proposed the ADC thresholding and the ADC ratio thresholding. The distribution of the ADC

values was also discussed in [2]. Makino et al. [3] proposed standard uptake value (SUV) thresholding. In [4], a relative regional cerebral blood volume ratio was proposed. Calli et al. [5], on the other hand, used perfusion and diffusion MR imaging and introduced four parameters to differentiate the tumors. In [6], histogram analysis of the normalized cerebral blood volume in enhancing and perienhancing lesions was presented. Note that [1–6] do not include any image processing. Certain feature values are extracted from input MRIs by hand by experts [1–5] or regions of interest were specified by experts to generate the histograms [6]. Tumors were simply classified by thresholding using predefined static threshold values in [1–6]. An image-processing-based system can be found in [7]. In [7], texture analysis using Gabor wavelet coefficient thresholding was proposed, but this technique also relied on simple thresholding. Thresholding

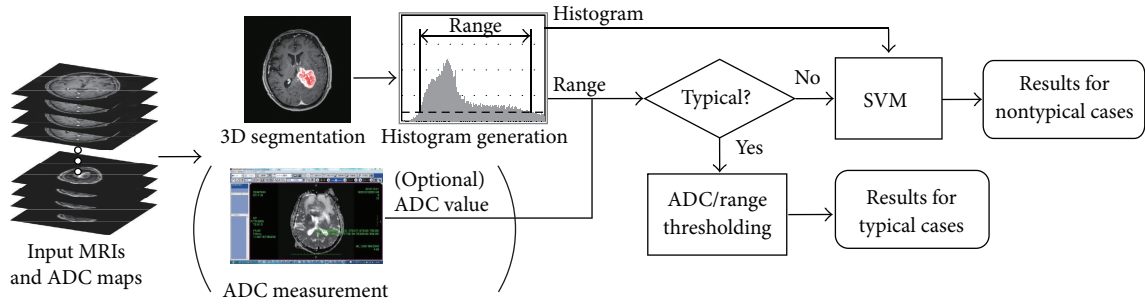


FIGURE 1: Flowchart of the proposed algorithm.

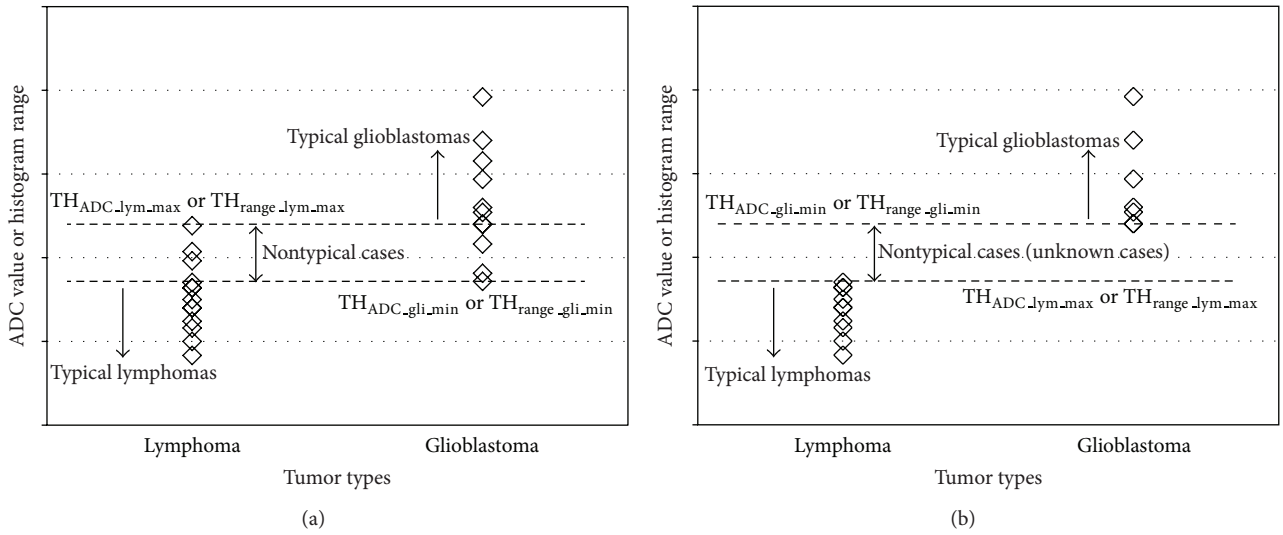


FIGURE 2: Concept of ADC and luminance range thresholding.

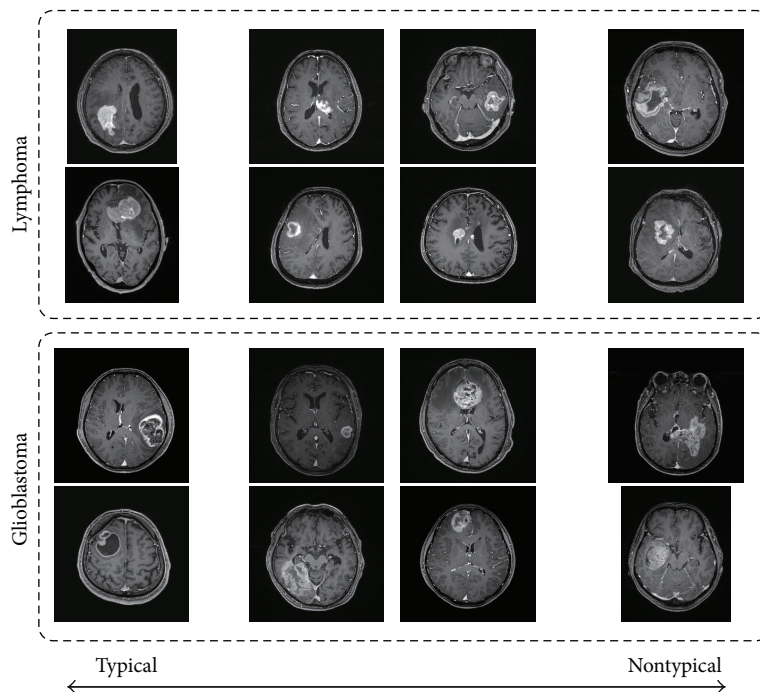


FIGURE 3: Sample MRIs of lymphomas and glioblastomas.

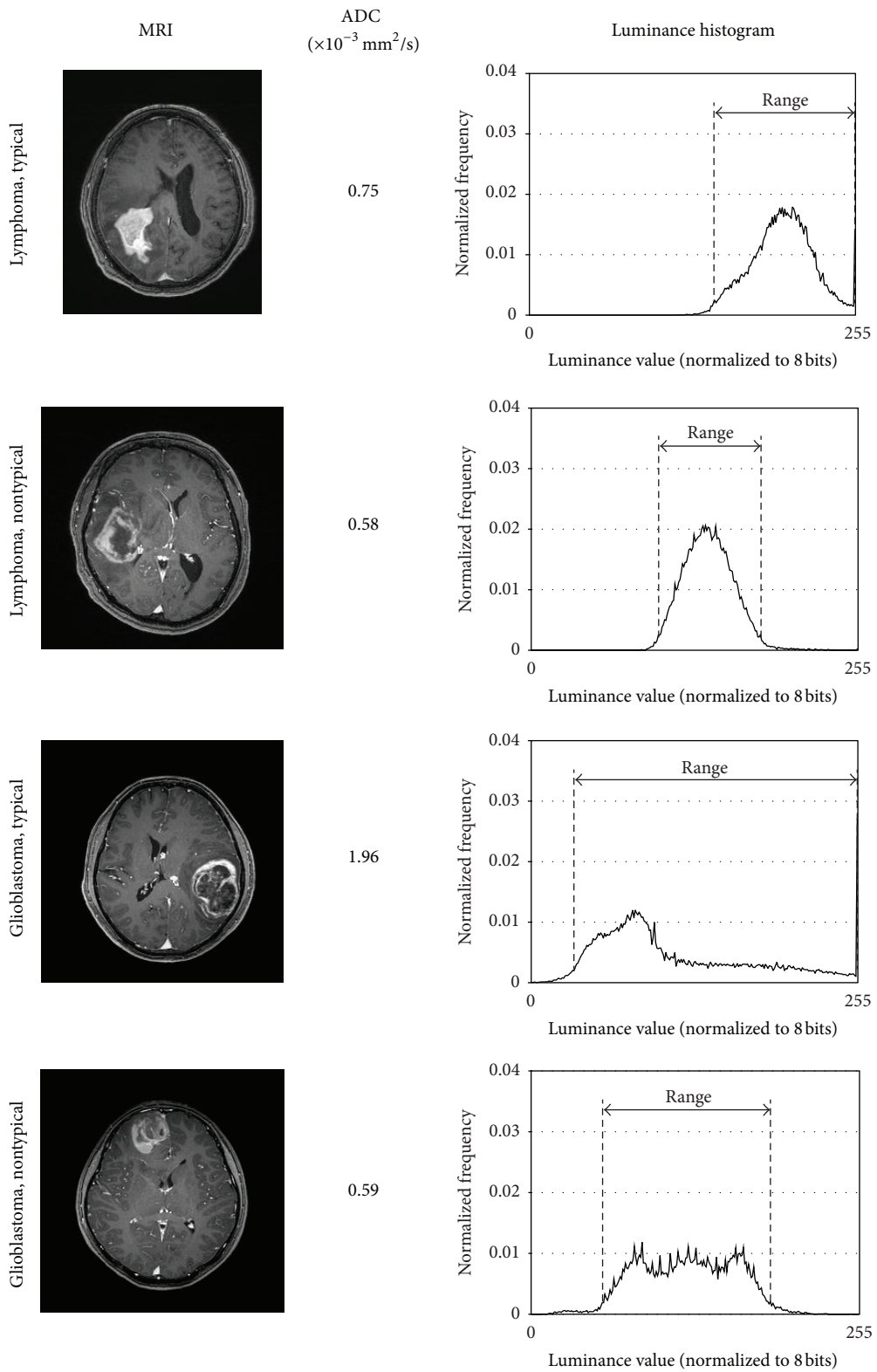


FIGURE 4: Sample images and extracted luminance histograms of typical/nontypical lymphomas/glioblastomas.

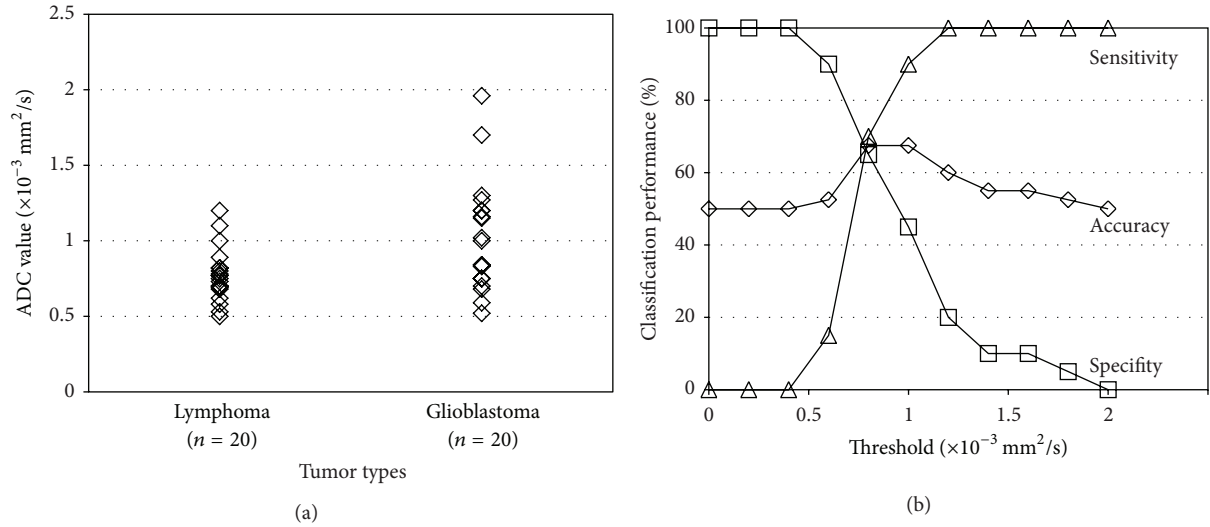


FIGURE 5: (a) Distribution of the ADC values. (b) Classification performance when ADC thresholding [1] is used. In the sensitivity/specificity calculation, lymphomas were considered as “positive” and glioblastomas were considered as “negative.”

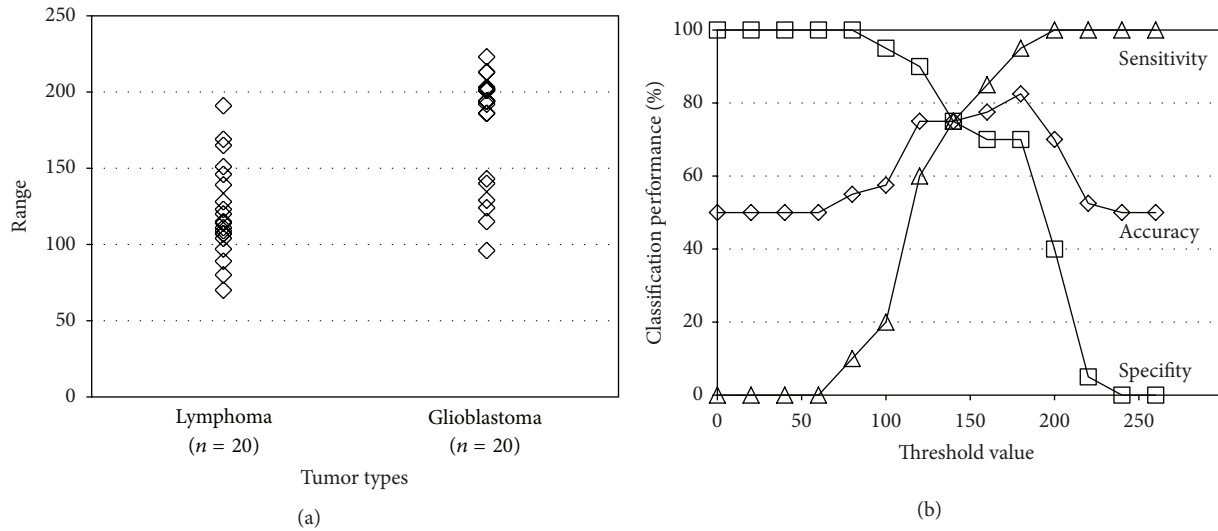


FIGURE 6: (a) Distribution of the luminance range values. (b) Classification performance when range thresholding is used. In the sensitivity/specificity calculation, lymphomas were considered as “positive” and glioblastomas were considered as “negative.”

feature values is sensitive to noise. It is very easy to find exceptional cases for such simple thresholding. In addition, extracting parameters subjectively by the observers induces an interobserver variance problem. For instance, the ADC values extracted by experts differ from observers to observers. From this point of view, even the learning-based approaches which employ a lot of subjective parameters such as [8] would not become a solution to the aforementioned thresholding-based approaches. In addition, the analysis is done by using only a single or a few slices of the MRIs in most cases because segmenting the whole tumor region needs labor-intensive user interactions and takes a lot of time. For more robust and accurate tumor classification, analysis of the whole tumor region would be desired. For this purpose, we proposed a system that employed luminance distribution learning using

the whole tumor region [9]. In the system, the classification accuracy was up to 87%.

The method proposed in this work is (1) objective because the input from users is as small as possible, (2) accurate by the combination of the luminance distribution analysis of the whole tumor region and the two thresholding methods, and (3) semiautomatic facilitating novice users to use the system easily. The 3D tumor segmentation and its luminance distribution analysis within a reasonable processing time have been made possible by our previous fast segmentation algorithm [10]. As a result, even novice users can classify the tumors accurately.

The system without the ADC thresholding is free of interobserver variances and achieves 91.1% accuracy. When the subjectively measured ADC value is included,

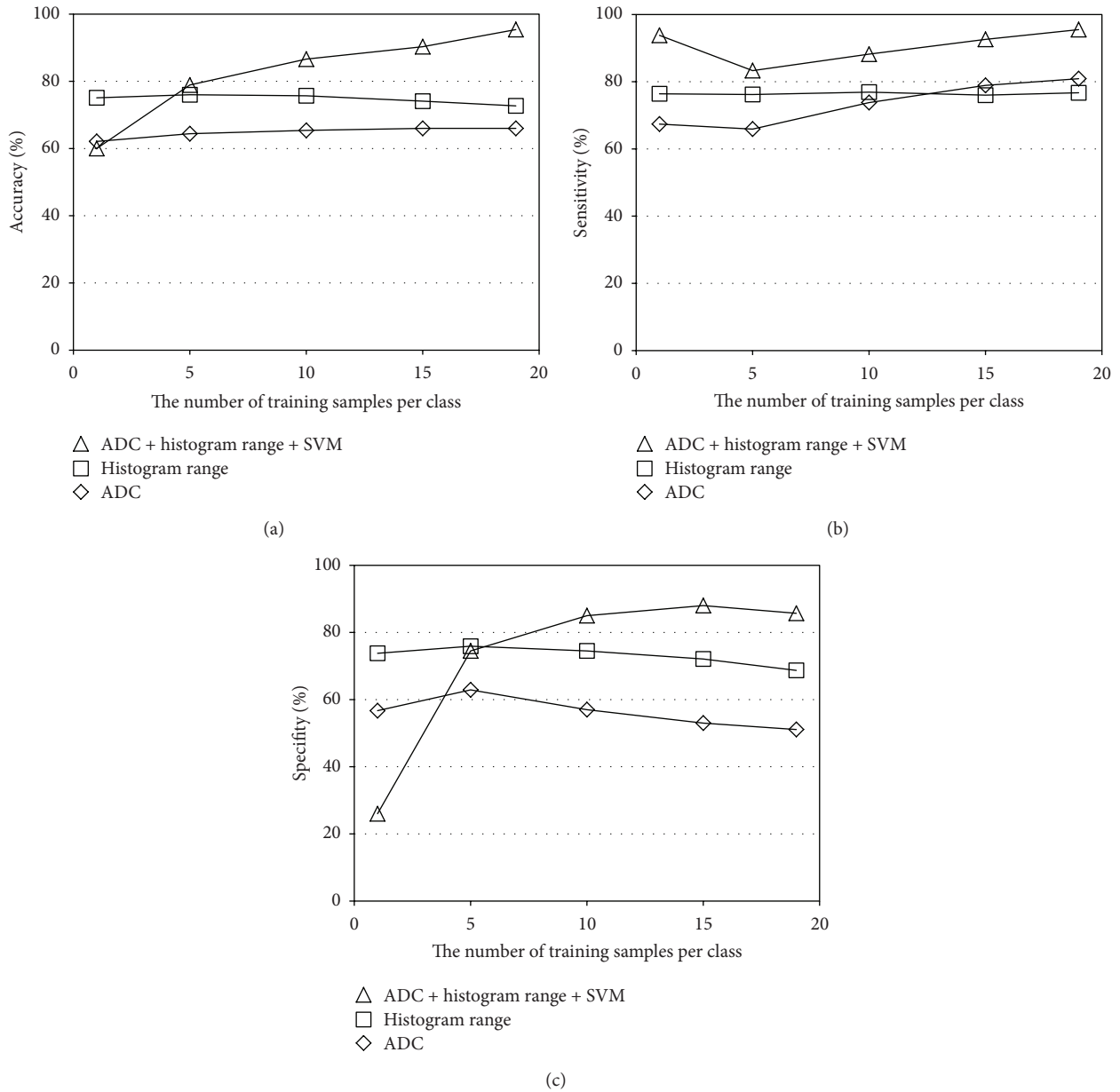


FIGURE 7: Classification performance of the proposed method and the two thresholding-based methods: (a) accuracy, (b) sensitivity, and (c) specificity.

the classification accuracy can be improved up to 95.4%. The main concept of our proposed algorithm has already been presented in [11]. In this paper, more detailed analysis and comparison are conducted to show the validity of the proposed method.

The rest of this paper is organized as follows. In Section 2, the proposed algorithm is described in detail. The experimental results are demonstrated in Section 3, followed by concluding remarks in Section 4.

2. Proposed Algorithm

It is often reported that the morphological appearance of the tumor does not allow direct judgments. However, it is also

often observed that the lymphomas tend to have flatter and lower luminance as compared to glioblastomas and glioblastomas are brighter on the edge and darker in the center [6]. Therefore, glioblastomas have wider dynamic range in their luminance value. We use these different characteristics in two ways: one for thresholding using the luminance dynamic range and the other for the luminance distribution learning using SVM.

The flow chart of the proposed algorithm is shown in Figure 1. Firstly, the tumor region is segmented by using our fast 3D segmentation algorithm [10]. The required interaction is only tumor/nontumor seed setting, which does not require any expert knowledge. The processing time is about a few tens of seconds. Though the fast 3D tumor segmentation is

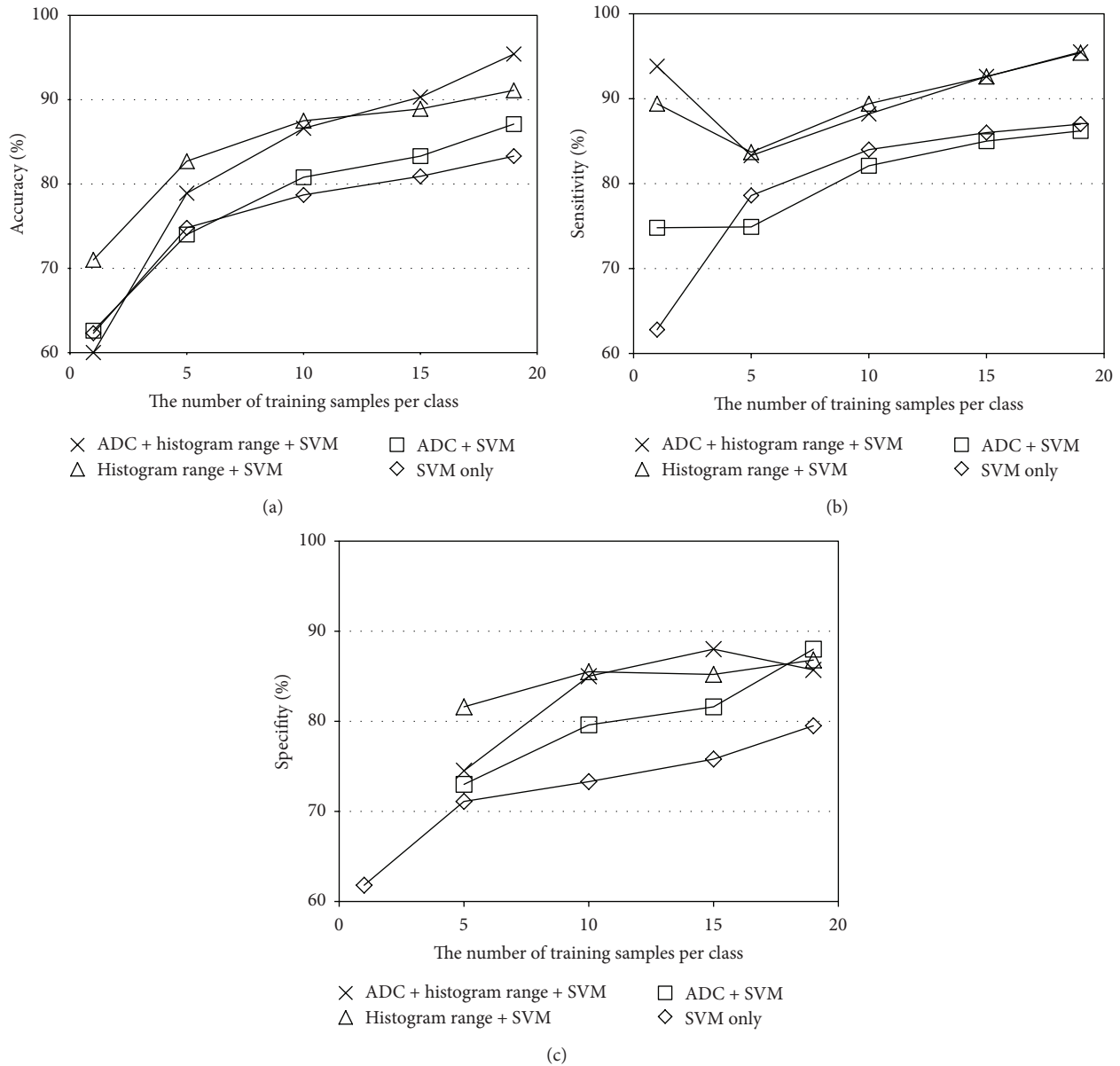


FIGURE 8: Classification performance comparison between the subsets of the proposed system: (a) accuracy, (b) sensitivity, and (c) specificity.

not the scope of this paper, we would like to emphasize that the system was made reasonable because of the quick segmentation. In this stage, moderately accurate segmentation is enough because the segmentation results are used only for generating the luminance histograms, not for treatment design.

Then, the normalized histogram of the luminance of the tumor is generated automatically using the whole tumor region. In this paper, the voxel value range was quantized from 12 bits (4,096 levels) to 8 bits (256 levels) to make the histograms less sparse. By using the generated luminance histogram, the luminance range whose normalized frequency is larger than a predefined threshold (0.002 in our study) is detected.

At the same time, if experts are available, the average ADC value is measured. The region of interest (ROI), whose area is set about 50 mm^2 , is decided by the experts. This ADC value measurement is optional.

According to [1], the ADC values tend to be smaller for lymphomas and large for glioblastomas. In the same manner, we found in our investigation that the luminance ranges are narrower for lymphomas and wider for glioblastomas. Although there are many exceptions as shown in our experiments, the tumors with very low ADC value can be regarded as lymphomas and those with very high ADC value can be regarded as glioblastomas. Therefore, we separate the typical cases and nontypical cases by using both the ADC value and the luminance range. Namely, we

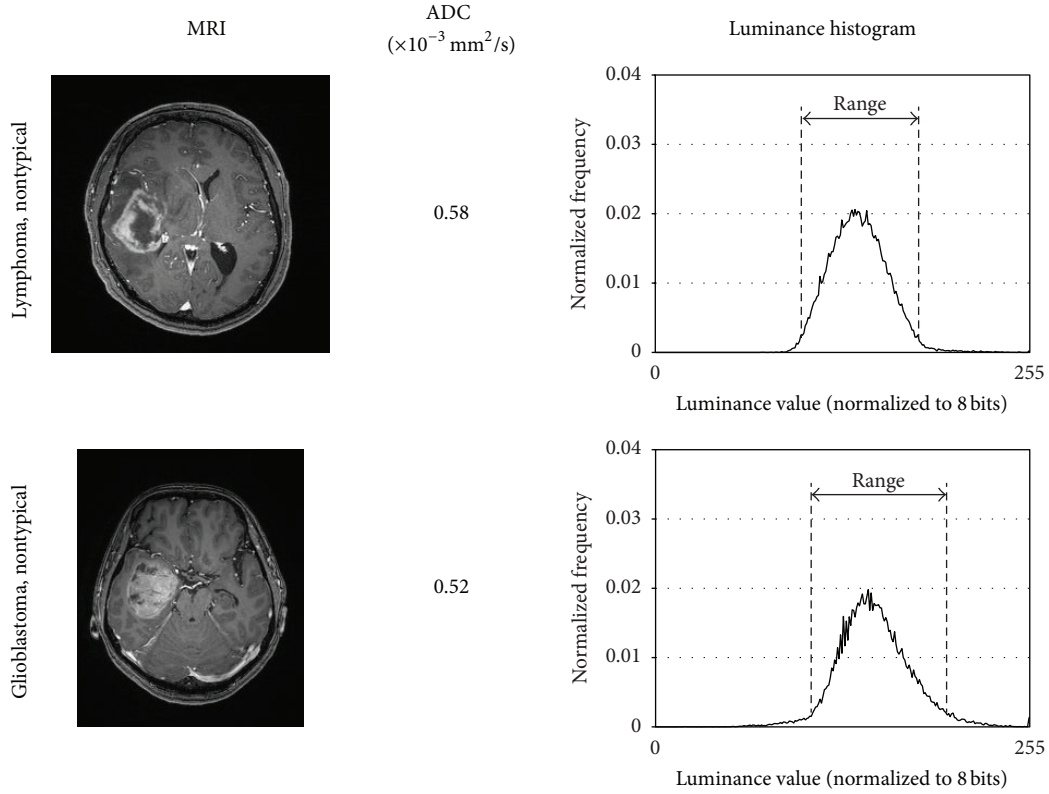


FIGURE 9: Examples of misclassified cases.

extract the four threshold values from the training data: the maximum ADC value and the maximum luminance range of the lymphomas ($TH_{ADC.lym.max}$ and $TH_{range.lym.max}$), and the minimum ADC value and the minimum luminance range of the glioblastomas ($TH_{ADC.gli.min}$ and $TH_{range.gli.min}$). There are two cases to consider.

$$(1) TH_{ADC.gli.min} \leq TH_{ADC.lym.max} \text{ or } TH_{range.gli.min} \leq TH_{range.lym.max} \text{ (Figure 2(a)).}$$

If the ADC value is smaller than $TH_{ADC.gli.min}$ or the luminance range is narrower than $TH_{range.gli.min}$, the tumor is regarded as a typical lymphoma. On the other hand, if the ADC value is larger than $TH_{ADC.lym.max}$ or the luminance range is wider than $TH_{range.lym.max}$, the tumor is regarded as a typical glioblastoma. Otherwise, the tumor is regarded as a nontypical case and classified by SVM, which is trained by the luminance histograms in the training dataset.

$$(2) TH_{ADC.gli.min} > TH_{ADC.lym.max} \text{ and } TH_{range.gli.min} > TH_{range.lym.max} \text{ (Figure 2(b)).}$$

If the ADC value is smaller than $TH_{ADC.lym.max}$ or the luminance range is narrower than $TH_{range.lym.max}$, the tumor is regarded as a typical lymphoma. On the other hand, if the ADC value is larger than $TH_{ADC.gli.min}$ or the luminance range is wider than $TH_{range.gli.min}$, the tumor is regarded as a typical glioblastoma. Those between $TH_{ADC.gli.min}$ and $TH_{ADC.lym.max}$ and between $TH_{range.gli.min}$ and $TH_{range.lym.max}$ are regarded as nontypical (unknown)

cases and classified by SVM. This case rarely happens when the number of training data is large enough.

Note that the thresholding is used to extract typical cases. Therefore, the problem of thresholding-based method pointed out in Section I does not arise in this case. In addition, the four threshold values are decided automatically from the training dataset. Preliminary experiments to set proper threshold values are not needed.

The advantage of the proposed system is that the ADC measurement can be omitted if experienced observers are not available. In this case, the required interaction from the users is only seed setting for the segmentation. The histogram generation, range thresholding, and classification using SVM can be done automatically. Therefore, anyone can reproduce the same results. Though a histogram-based approach was proposed in [6], the histograms were generated only from ROIs specified by the observers, not from the whole tumor region. And the classification was still based on thresholding a single parameter that was extracted from the histograms.

3. Experimental Results

3.1. Experimental Setup. We retrospectively reviewed the MR images of 40 patients with histologically proved glioblastomas ($n = 20$) and lymphomas ($n = 20$). All tumors were pathologically proved. The resolutions of structural MRIs and ADC maps were $256 \times 256 \times 160$ and $128 \times 128 \times 22$, respectively. There were 22 male and 18 female

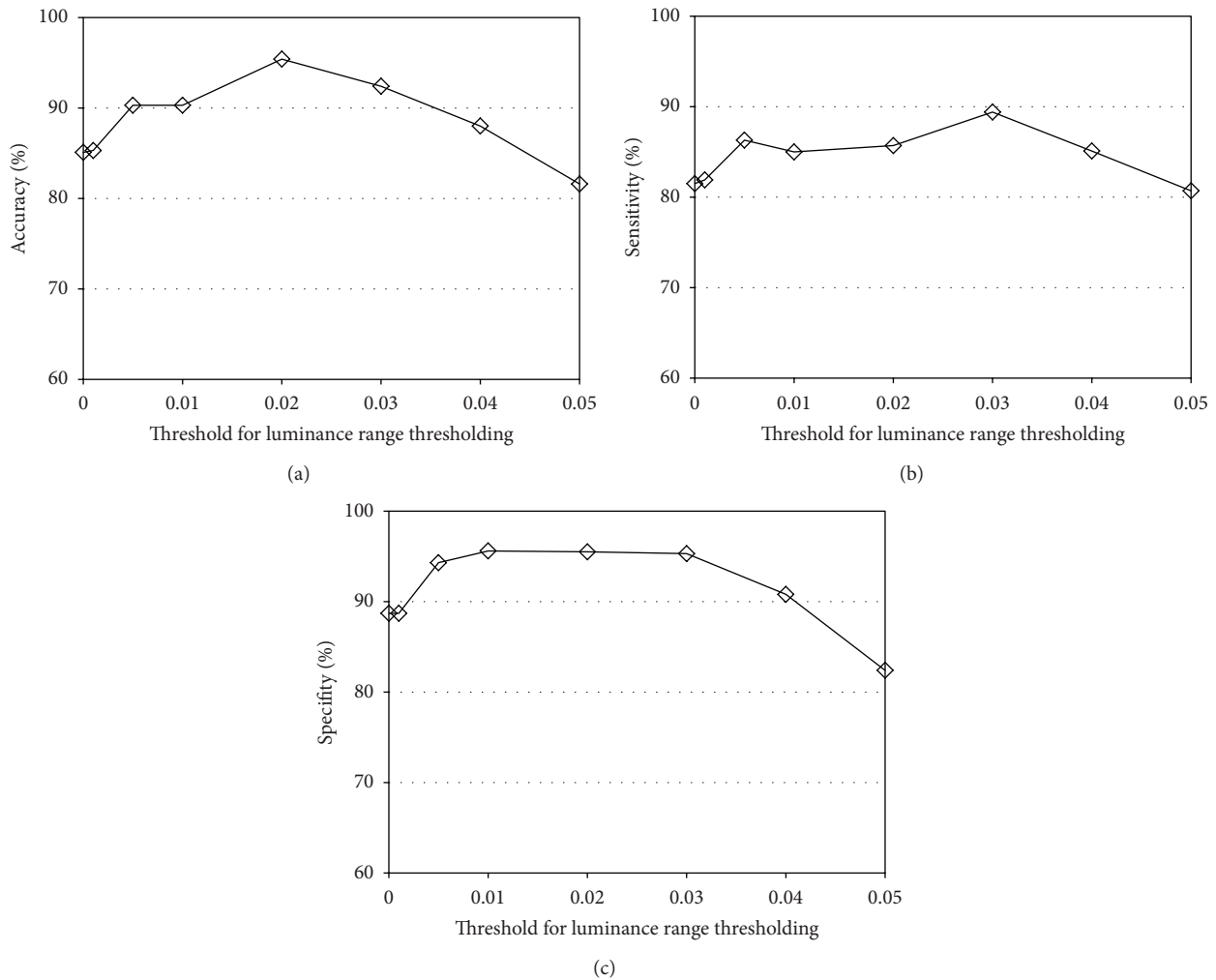


FIGURE 10: Classification performance as a function of the luminance range threshold: (a) accuracy, (b) sensitivity, and (c) specificity.

patients, and their ages ranged from 12 to 91 years, with a mean of 65 years and a median of 69 years. Typical and nontypical cases are included in the dataset. The number of typical/nontypical cases is not listed here because it is hard to define typicalness/nontypicalness. Some example images are shown in Figure 3. As shown in the figure, some of the lymphomas and glioblastomas look very similar to each other and hard to differentiate just by looking at the MRIs. The ADC values were measured by a neuroradiologist with 19 years' experience (T. Hirai). A linear kernel [12] was used if not mentioned otherwise.

In Figure 4, typical and nontypical cases of lymphoma and glioblastoma and their luminance histograms are shown. As discussed in Section 3, the luminance histograms of lymphoma tend to have narrower luminance range and those of glioblastomas tend to have wider luminance range.

3.2. Classification Performance of Conventional Single Value Thresholding. Figure 5 demonstrates the distribution of the ADC values of lymphomas and glioblastomas (Figure 5(a)) and the differentiation performance as a function of the threshold value (Figure 5(b)). It is observed that the ADC values of the lymphoma and those of the glioblastomas

overlap each other and therefore the ADC thresholding [1] does not work well. The best accuracy was only 67.5% when the threshold was $0.8\text{--}1.0 \times 10^{-3} \text{ mm}^2/\text{s}$, which is slightly better than the chance level (50%).

The distribution of the luminance range values and classification accuracy by simple thresholding are shown in Figure 6. It is shown that the luminance range thresholding can classify lymphomas and glioblastomas better than the ADC thresholding [1]. The best classification accuracy is 82.5%. However, this is the result of fine tuning of the two parameters: the threshold value for the range extraction and the threshold value for classification (luminance range thresholding). The classification performance is sensitive to these threshold values and therefore this approach is not practical.

3.3. Classification Performance of Our Proposed Algorithm. In the experiments in this subsection, $k(k = 1\text{--}19)$ samples per class were randomly selected for the training and the rest were used for the testing. The histograms of the typical tumors were also included in the training. This procedure was repeated 1,000 times and the average performance is presented. This

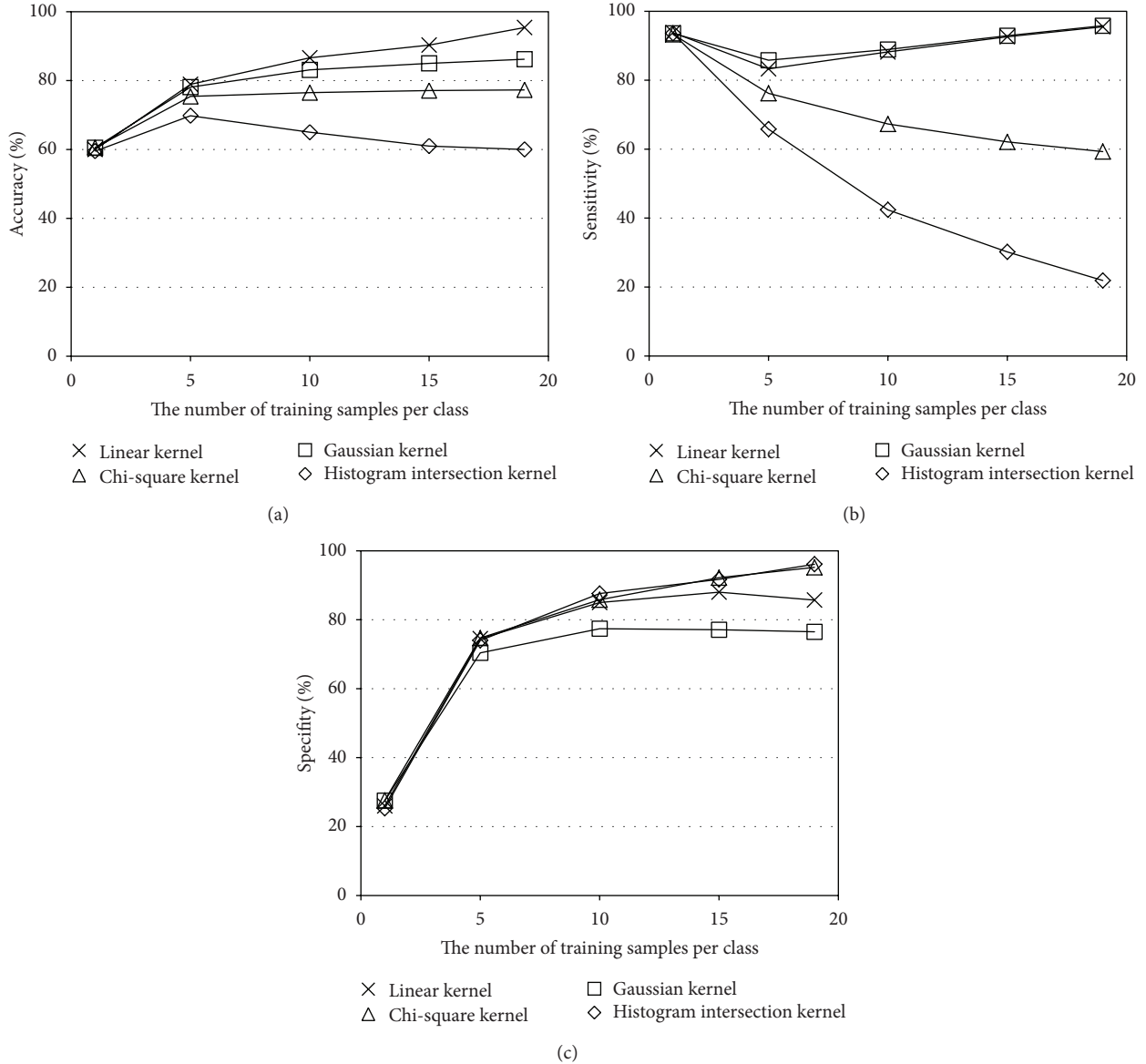


FIGURE 11: Performance comparison between four kernels: (a) accuracy, (b) sensitivity, and (c) specificity.

random-sampling-based evaluation was employed because the threshold values depend on the training samples.

The classification performance of our proposed method is shown in Figure 7 and it is compared with those by naïve ADC thresholding and luminance range thresholding. When the luminance distribution learning using SVM is not used, nontypical (or unknown) cases cannot be handled. Therefore, the threshold values for the ADC thresholding (TH_{ADC}) and the luminance range thresholding (TH_{range}) were set as follows:

$$\begin{aligned}
 TH_{ADC} &= \frac{TH_{ADC_gli_min} + TH_{ADC_lym_max}}{2}, \\
 TH_{range} &= \frac{TH_{range_gli_min} + TH_{range_lym_max}}{2}.
 \end{aligned} \tag{1}$$

It is observed that the classification accuracy of the ADC thresholding is up to 66% and that of the luminance range thresholding is 72%–76%. On the other hand, the proposed method achieves 95.4% when $k = 19$. Besides, our proposed method outperforms the other two methods when k is equal to or larger than 5.

Figure 8 shows the classification performance when the subset of our proposed method is used. It is interesting to note that even the SVM-only approach (i.e., only the SVM trained with the luminance histograms was used) can achieve 83.3% accuracy when $k = 19$. This is significantly better than the ADC thresholding [1]. The luminance range thresholding + SVM method yields 91.1% accuracy. Since this method does not require any experiences or knowledge of the tumors, no interobserver variance exists and even novice users can get the same performance. It is also observed

that the luminance range thresholding outperforms the other approaches when the training samples are less. The best performance (95.4%) was achieved when all the features are used. Namely, the typical cases were classified by using both the ADC thresholding and the luminance range thresholding and the nontypical cases were classified by the SVM using the luminance histogram. The performance of the ADC thresholding + SVM [9] was 87.1%.

The example images which were misclassified are shown in Figure 9. The neuroradiologist could not classify them correctly just by looking at the images and ADC values. Therefore, these mistakes are reasonable and show the limitation of our proposed method.

The dependence on the luminance range threshold is demonstrated in Figure 10. The best classification performance is observed at $th = 0.002$. As the threshold value shifts from its optimal value, the classification performance is degraded gradually. However, the classification accuracy is over 90% even when $th = 0.001$ or $th = 0.003$, showing the robustness of the proposed method.

It is well known that SVMs using a Chi-square kernel or histogram intersection kernel work better than Gaussian or linear kernel when the feature vector is histogram based. Therefore, the four kernels are compared in Figure 11. In our framework, the linear kernel was the best. It should also be noted that the linear kernel was the fastest in training.

4. Conclusions

Luminance distribution analysis using the whole tumor region has been developed for differentiating lymphomas and glioblastomas. The typical tumors were classified by the luminance range thresholding. And the nontypical cases were learned and classified by SVM using the luminance histogram. Since subjective measurement of the parameters was not needed, the system was easy to use even for novice users and there was no interobserver variance. The combination of the luminance range thresholding and the SVM-based classification achieved 91.1% accuracy. Besides, when the ADC value measured by an expert was added in the thresholding, the accuracy was improved up to 95.4%.

Acknowledgment

The authors would like to thank Professor Masakazu Yagi of Osaka University for fruitful discussions.

References

- [1] C. Toh, M. Castillo, A. M.-C. Wong et al., "Primary cerebral lymphoma and glioblastoma multiforme: differences in diffusion characteristics evaluated with diffusion tensor imaging," *American Journal of Neuroradiology*, vol. 29, no. 3, pp. 471–475, 2008.
- [2] A. Doskaliyev, F. Yamasaki, M. Ohtaki et al., "Lymphomas and glioblastomas: differences in the apparent diffusion coefficient evaluated with high b-value diffusion-weighted magnetic resonance imaging at 3T," *European Journal of Radiology*, vol. 81, no. 2, pp. 339–344, 2012.
- [3] K. Makino, T. Hirai, H. Nakamura et al., "Does adding FDG-PET to MRI improve the differentiation between primary cerebral lymphoma and glioblastoma? Observer performance study," *Annals of Nuclear Medicine*, vol. 25, no. 6, pp. 432–438, 2011.
- [4] M. Hartmann, S. Heiland, I. Harting et al., "Distinguishing of primary cerebral lymphoma from high-grade glioma with perfusion-weighted magnetic resonance imaging," *Neuroscience Letters*, vol. 338, no. 2, pp. 119–122, 2003.
- [5] C. Calli, O. Kitis, N. Yunten, T. Yurtseven, S. Islekel, and T. Akalin, "Perfusion and diffusion MR imaging in enhancing malignant cerebral tumors," *European Journal of Radiology*, vol. 58, no. 3, pp. 394–403, 2006.
- [6] J. H. Ma, H. S. Kim, N.-J. Rim, S.-H. Kim, and K.-G. Cho, "Differentiation among glioblastoma multiforme, solitary metastatic tumor, and lymphoma using whole-tumor histogram analysis of the normalized cerebral blood volume in enhancing and perienhancing lesions," *American Journal of Neuroradiology*, vol. 31, no. 9, pp. 1699–1706, 2010.
- [7] Y. Liu, M. Muftah, T. Das, L. Bai, K. Robson, and D. Auer, "Classification of MR tumor images based on Gabor wavelet analysis," *Journal of Medical and Biological Engineering*, vol. 32, no. 1, pp. 22–28, 2012.
- [8] K. Yamashita, T. Yoshiura, H. Arimura et al., "Performance evaluation of radiologists with artificial neural network for differential diagnosis of intra-axial cerebral tumors on MR images," *American Journal of Neuroradiology*, vol. 29, no. 6, pp. 1153–1158, 2008.
- [9] T. Yamasaki, T. Chen, T. Hirai, and R. Murakami, "Classification of cerebral lymphoma and glioblastoma by the combination of ADC thresholding and luminance distribution learning," in *Proceedings of the International Workshop on Pattern Recognition for Healthcare Analytics (IWPRHA '12)*, WEB Proceedings, #1, July 2012.
- [10] T. Yamasaki, T. Chen, M. Yagi, T. Hirai, and R. Murakami, "GrowCut-based fast tumor segmentation for 3D magnetic resonance images," in *Medical Imaging 2012: Image Processing*, vol. 8314 of *Proceedings of SPIE, Paper #831434*, San Diego, Calif, USA, February 2012.
- [11] T. Yamasaki, T. Chen, T. Hirai, and R. Murakami, "Differentiating cerebral lymphomas and GBMs featuring luminance distribution analysis," in *Medical Imaging 2013: Computer-Aided Diagnosis*, vol. 8670 of *Proceedings of SPIE, Paper 8670-35*, Lake Buena Vista, Fla, USA, February 2013.
- [12] R. Fan, K. Chang, C. Hsieh, X. Wang, and C. Lin, "LIBLINEAR: a library for large linear classification," *Journal of Machine Learning Research*, vol. 9, pp. 1871–1874, 2008.

Research Article

Particle System Based Adaptive Sampling on Spherical Parameter Space to Improve the MDL Method for Construction of Statistical Shape Models

Rui Xu,¹ Xiangrong Zhou,² Yasushi Hirano,¹ Rie Tachibana,³ Takeshi Hara,² Shoji Kido,¹ and Hiroshi Fujita²

¹ Graduate School of Medicine, Yamaguchi University, Tokiwadai 2-16-1, Ube, Yamaguchi 755-8611, Japan

² Graduate School of Medicine, Gifu University, Yanagito 1-1, Gifu 501-1194, Japan

³ Information Science and Technology Department, Oshima National College of Maritime Technology, Komatsu 1091-1, Oshimagun Suooshimacho, Yamaguchi 742-2193, Japan

Correspondence should be addressed to Rui Xu; qdruixu@gmail.com

Received 16 January 2013; Revised 1 May 2013; Accepted 20 May 2013

Academic Editor: Yi-Hong Chou

Copyright © 2013 Rui Xu et al. This is an open access article distributed under the Creative Commons Attribution License, which permits unrestricted use, distribution, and reproduction in any medium, provided the original work is properly cited.

Minimum description length (MDL) based group-wise registration was a state-of-the-art method to determine the corresponding points of 3D shapes for the construction of statistical shape models (SSMs). However, it suffered from the problem that determined corresponding points did not uniformly spread on original shapes, since corresponding points were obtained by uniformly sampling the aligned shape on the parameterized space of unit sphere. We proposed a particle-system based method to obtain adaptive sampling positions on the unit sphere to resolve this problem. Here, a set of particles was placed on the unit sphere to construct a particle system whose energy was related to the distortions of parameterized meshes. By minimizing this energy, each particle was moved on the unit sphere. When the system became steady, particles were treated as vertices to build a spherical mesh, which was then relaxed to slightly adjust vertices to obtain optimal sampling-positions. We used 47 cases of (left and right) lungs and 50 cases of livers, (left and right) kidneys, and spleens for evaluations. Experiments showed that the proposed method was able to resolve the problem of the original MDL method, and the proposed method performed better in the generalization and specificity tests.

1. Introduction

Statistical shape models (SSMs) are an efficient method which considers statistical information of a set of training shapes to improve the robustness of medical image processing algorithms. It has been widely used in the task of segmentation and achieved good results [1]. It is reported that the best three ranked segmentation algorithms on livers are based on SSMs in the contest held in 2007 [2]. According to our knowledge, several SSMs have been proposed, which are point distribution models (PDMs) [3], m-rep [4], SPHARMS [5, 6], and so on. We focus on PDMs in this paper since it is the most widely used SSMs.

The main problem of the construction of SSMs is how to determine corresponding points on each shape. For simple 2D shapes, that is, faces, corresponding points can be determined manually by placing a set of landmarks on shapes;

however obvious disadvantages are both large manual labors and the inevitably subjects' bias. Especially for complex 3D shapes of clinical data, manual determination of hundreds or thousands of landmarks is not practical. Therefore, lots of researches have focused on automatic ways to find corresponding points [1]. The determination of shapes' correspondence can be generalized as a shape registration problem. A group-wise based method is proposed to align a group of shapes according to an information-based theory, called minimal description length (MDL) [7], in order to get the simplest description of constructed SSMs [8]. It is reported that the MDL based method is the state-of-the-art method according to exhaustive evaluations [9]. At first, the MDL method can only find the corresponding points of 2D shapes [8, 10, 11]. Recently, it is generalized to deal with the problems of 3D shapes [12–14]. We follow the pilot study [12], since the open source codes helped us to understand its essence [15].

In the following context, we call the pilot study [12] the original MDL method.

The original MDL method can be divided into three steps. First, each original surface mesh of genus-0 topology is initially mapped onto a parameter space of a unit sphere by a conformal mapping [16]. Each vertex of an original surface mesh is transformed onto the unit sphere, and a new spherical mesh built by transformed vertices according to their original linked relationships is called a parameterized mesh in this paper. Second, these parameterized meshes are aligned by manipulating their vertices simultaneously on the unit sphere in order to minimize the MDL measure. Finally, each of the aligned parameterized meshes is sampled by a set of uniformly distributed points on the unit sphere, and the sampled points are mapped back by the corresponding inverse conformal mapping onto each original shape surface to obtain corresponding points. Mapping surfaces onto a unit sphere makes shapes' registration become easier, since the freedoms of translation and scale can be eliminated and only the freedoms of rotation and subjects' differences are left. However, the manipulation of parameterized meshes makes them to be distorted during MDL registration. Some triangles of parameterized meshes are shrunk while others are expanded. This makes the predetermined conformal mapping become poor. If uniformly distributed positions are sampled on the unit sphere for each parameterized mesh, less sampling points are obtained in the shrunk regions and more sampling points are obtained in expanded regions. Therefore, this method has suffered from the problem that determined corresponding points are usually densely located in some parts and coarsely in other parts on original surfaces.

This problem may be resolved by either redetermining a new conformal mapping for each shape to replace the poor one or finding adaptive sampling positions on the unit sphere instead of the uniformly distributed sampling method. In this paper, we use the latter method to resolve the problem of the original MDL method. Here, we propose a method to obtain adaptive sampling positions on the unit sphere by considering distortions of parameterized meshes. The proposed method is based on a particle system which is originally adopted for modeling isosurfaces of shapes in [17].

2. Materials and Methods

The proposed particle-system based method is operated when the original MDL registration is finished. Therefore, the proposed method can be seen as a postprocessing of the pilot study [12]. The flowchart of the proposed method is given by Figure 1. The input is a set of parameterized meshes aligned by the original MDL method [12] on the unit sphere. Vertices of these meshes are used to generate a probability distribution to show the frequency of vertices existing at a position on the unit sphere. This probability distribution can reflect how parameterized meshes are distorted in the MDL registration. Next, a set of particles are uniformly placed on the unit sphere. A particle can be seen as a dot or a sampling position. Each particle gives repulsive forces to push its surrounding particles away from itself. The value of the force for a pair

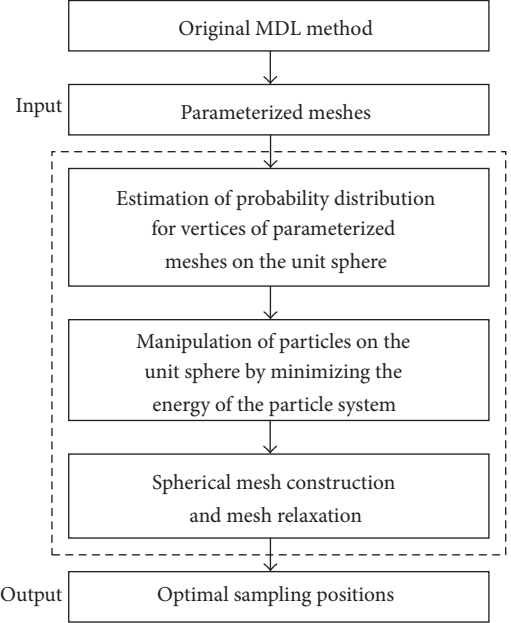


FIGURE 1: The flowchart of the particle system based adaptive sampling on spherical parameter space to improve the MDL method. The main steps of the proposed method are surrounded by the dash rectangle.

of particles is related to both of their distance and the probability of vertices at which the particles are located. An energy function can be calculated by adding the forces of all particles. By minimizing this energy, particles are manipulated on the unit sphere until the energy becomes steady. The final particles are treated as vertices to build a spherical mesh. Finally, this mesh is relaxed to slightly adjust vertices' positions on the spherical surface, and the optimal sampling points are the vertices of the relaxed mesh. When the proposed method is finished, each parameterized mesh is sampled at these sampling points on the unit sphere, and then the sampled points are transformed back to each surface of organs by its corresponding inverse conformal mapping to get corresponding points of each shape. The details are described in the following subsections.

2.1. Probability Distribution for Vertices of Parameterized Meshes. We adopt the probability distribution for vertices of parameterized meshes located on the unit sphere to describe how these parameterized meshes are distorted in the original MDL registration. If triangles of parameterized meshes are shrunk in a region, there will be more vertices in that part. Therefore, vertices have a high probability to exist there. Conversely, the probability is low in regions where triangles are expanded. We adopt a parzen window [18] based method to estimate this probability distribution. Given \mathbf{v}_{ij} denoted by the j th vertex of the i th parameterized mesh, the probability of vertices existing in a location \mathbf{x} on the unit sphere $p(\mathbf{x})$ can be calculated by

$$p(\mathbf{x}) = \alpha \sum_i \sum_j \varphi(\|\mathbf{x} - \mathbf{v}_{ij}\|), \quad (1)$$

where α is a coefficient to ensure $\int p(\mathbf{x})d\mathbf{x} = 1$ and $\|\mathbf{x} - \mathbf{v}_{ij}\|$ is the Euclidian distance of the two points \mathbf{x} and \mathbf{v}_{ij} . $\varphi(d)$ is a truncated Gaussian kernel whose definition is given by

$$\varphi(d) = \frac{1}{\sqrt{2\pi}\sigma} \exp\left(-\frac{d^2}{2\sigma^2}\right) \quad d \leq 3\sigma, \quad (2)$$

$$\varphi(d) = 0 \quad d > 3\sigma,$$

where σ is set to be 0.033 in this paper.

In implementation, we discretize the unit sphere by a 5-time recursively-refined icosahedron mesh which contains 10242 vertices uniformly distributed on the unit sphere. An example of the estimated probability distribution is shown by Figure 2.

2.2. Energy of the Particle-System. The energy of the particle-system is defined by

$$E(\mathbf{x}_1, \dots, \mathbf{x}_N) = \sum_{i=1}^N \sum_{i \neq j} \omega(\mathbf{x}_i, \mathbf{x}_j) \cdot F(\mathbf{x}_i, \mathbf{x}_j), \quad (3)$$

where $\mathbf{x}_1, \dots, \mathbf{x}_N$ are all N particles and their energy is denoted as $E(\mathbf{x}_1, \dots, \mathbf{x}_N)$. $F(\mathbf{x}_i, \mathbf{x}_j)$ is the force term of i th and j th particles and $\omega(\mathbf{x}_i, \mathbf{x}_j)$ is the weight associated for them. We adopt the force term suggested in [17]. Its definition is given by

$$F(\mathbf{x}_i, \mathbf{x}_j) = \begin{cases} \cot\left(\frac{\|\mathbf{r}_{ij}\|}{\sigma} \cdot \frac{\pi}{2}\right) + \frac{\|\mathbf{r}_{ij}\|}{\sigma} \cdot \frac{\pi}{2} - \frac{\pi}{2} & \|\mathbf{r}_{ij}\| \leq \sigma, \\ 0 & \|\mathbf{r}_{ij}\| > \sigma, \end{cases} \quad (4)$$

where $\|\mathbf{r}_{ij}\|$ is the Euclidean distance of the pair of particles which are \mathbf{x}_i and \mathbf{x}_j . σ is a parameter. Larger value of σ means that a particle has taken forces from more surrounding particles in a larger region, so more computation costs are required. But the value should be large enough to make particles move. In our system, we choose it to be 0.25 for trade-offs between performances and computation costs.

It is important to design suitable weight terms $\omega(\mathbf{x}_i, \mathbf{x}_j)$ to make the particle system work properly. If all weight terms are set to be equal, particles finally spread uniformly on the unit sphere when the energy is minimized. Here, we make use of the estimated probability distribution of vertices to design suitable weight terms in order to obtain the optimal sampling positions which are adaptive to distortions of parameterized meshes. The definition of the weight terms $\omega(\mathbf{x}_i, \mathbf{x}_j)$ is given by

$$\omega(\mathbf{x}_i, \mathbf{x}_j) = \frac{D(\mathbf{x}_i) + D(\mathbf{x}_j)}{2},$$

$$D(\mathbf{x}_i) = \begin{cases} \frac{a}{(p(\mathbf{x}_i))^{\gamma}}, & p(\mathbf{x}_i) > b, \\ \frac{a}{b}, & p(\mathbf{x}_i) \leq b, \end{cases} \quad (5)$$

where \mathbf{x}_i is the position on which the i th particle is located. $p(\mathbf{x}_i)$ is the estimated probability of vertices at the location

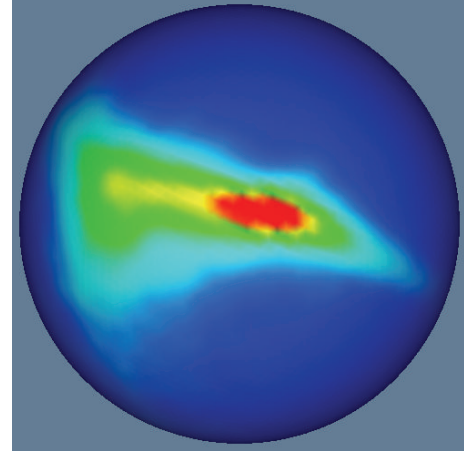


FIGURE 2: An example of the estimated probability distribution for vertices of parameterized meshes on the unit sphere. The red regions show where probabilities of vertices existing in those regions are high, and the blue regions show where the probabilities of vertices existing in those regions are low. The estimated probability distribution is able to reflect how triangles of parameterized meshes are distorted. For example, high probability (red color) means that triangles in those regions are shrunk, and low probability (blue color) means that triangles in those regions are expanded.

of \mathbf{x}_i . a, b, γ are parameters whose values are set to be $1e - 5$, $1e - 5$ and 2.2, respectively in experiments.

2.3. Minimization of the Energy of the Particle-System. The optimal positions of particles are obtained by minimizing the energy defined in (3). This can be generalized as an optimization problem. Considering the number of particles is large, we adopt an iterative gradient descent based method to make it converge faster to a local minimum. Here, we only update one particle's position along the opposite gradient direction at one time, and this procedure is operated for each particle in turns. One iteration is called when the iterative updating for all particles is finished. The pseudocode is given by Algorithm 1. Its initialization requires a set of uniformly-distributed particles on the unit sphere (\mathbf{x}_i^0 ($i = 1, 2, \dots, N$)), the same maximal step length associated for each particle for gradient descent ($\lambda_i = \lambda_{\text{Max}}$ ($i = 1, 2, \dots, N$)), the minimal step length (λ_{Min}), and the total iteration times (T). When we update the i th particle's position in the t th iteration, we firstly calculate a position \mathbf{y}' using the current step length λ_i for the i th particle along the opposite gradient direction. By using the condition of $\|\mathbf{y}'\| = 1$, we ensure that the new position \mathbf{y} is on the surface of unit sphere. Then, we calculate the new energy E_{new} , by replacing \mathbf{x}_i^t with the new position \mathbf{y} . If E_{new} is smaller than the former energy E_{old} , we accept \mathbf{y} as the new position for the i th particle in the t th iteration, update E_{old} by E_{new} and end the loop. If not, we halve the step length of the i th particle and try a new position to see whether it can minimize the energy. However, the step length should not be smaller than λ_{Min} . In such a case, we give up updating the position of the i th particle in the t -iteration and only let the step length of the i th particle to be equal to λ_{Min} .

```

Initialization:  $\mathbf{x}_i^0$  ( $i = 1, 2, \dots, N$ ),  $\lambda_i = \lambda_{\text{Max}}$  ( $i = 1, 2, \dots, N$ ),  $\lambda_{\text{Min}}$ ,  $T$ .
 $E_{\text{old}} = E(\mathbf{x}_1^0, \mathbf{x}_2^0, \dots, \mathbf{x}_N^0)$ 
FOR  $t = 0 \rightarrow T$  DO
  FOR  $i = 1 \rightarrow N$  DO
    LOOP
       $\mathbf{y}' \leftarrow \mathbf{x}_i^t - \lambda_i \frac{\partial E}{\partial \mathbf{x}_i}$ 
       $\mathbf{y} \leftarrow \|\mathbf{y}'\| = 1$ 
       $E_{\text{new}} = E(\dots, \mathbf{x}_{i-1}^t, \mathbf{y}, \mathbf{x}_{i+1}^t, \dots)$ 
      IF  $E_{\text{new}} < E_{\text{old}}$  THEN
         $\mathbf{x}_i^t \leftarrow \mathbf{y}$ 
         $E_{\text{old}} \leftarrow E_{\text{new}}$ 
        BREAK LOOP
      ELSE
         $\lambda_i \leftarrow \lambda_i/2$ 
      END IF
      IF  $\lambda_i < \lambda_{\text{Min}}$  THEN
         $\lambda_i \leftarrow \lambda_{\text{Min}}$ 
        BREAK LOOP
      END IF
    END LOOP
  END FOR
END FOR

```

ALGORITHM 1: An iterative gradient descent based method to minimize the energy of the particle system defined in (3).

In our experiments, we set the iteration times T to be 15. λ_{Max} and λ_{Min} are determined as follows. Before Algorithm 1 begins, we randomly choose 10 percent of particles and calculate the mean value of the norms (or lengths) of their gradients. This mean value is denoted by \bar{g}_{norm} . λ_{Max} is set to be $10.0/\bar{g}_{\text{norm}}$, and λ_{Min} is set to be $1e - 4/\bar{g}_{\text{norm}}$.

2.4. Construction of Sampling Mesh and Relaxation. When the Algorithm 1 is finished, the obtained particles' positions are treated as vertices to be linked by Delaunay triangles to build a spherical mesh. This mesh gives how sampling points (particles) are linked with each other, and this linked information is required in SSMs. Additionally, we require this information to slightly adjust particles on the spherical surface to obtain optimal sampling positions. According to [19], Delaunay triangles of a surface can be obtained by constructing convex hulls for a set of 3D points. Constructing triangles directly by this way lead to a locally ununiform mesh. This can be improved by the technique of mesh relaxation, which slightly adjusts vertices' positions according to their linked information. Here, we adopt the method suggested by [20] to optimize the constructed mesh. Finally, the positions for the vertices of the relaxed mesh are the optimal sampling positions on the unit sphere.

3. Results and Discussion

3.1. Data. We evaluate the proposed method by 6 kinds of human organs, which are livers, left and right lungs, left and right kidneys, and spleens. We collect 47 cases of lungs and 50 cases of other organs from different subjects by a practical clinical protocol using high-resolution CT (HRCT) with

the slice thickness of 1 mm and in-plane resolution around 0.6 mm. The organs' regions are manually labeled on original scans and then resampled to be saved as binary masks with the resolution of $1 \text{ mm} \times 1 \text{ mm} \times 1 \text{ mm}$. Finally, marching cubes followed by mesh decimation using the visualization toolkit (VTK) [21] is adopted to get a triangles' mesh for each organ. The number of vertices for each mesh is related to organ's sizes. There are about 3000–5000 vertices for livers and lungs and 1000–2000 vertices for kidneys and spleens. These meshes are used as inputs for evaluations.

3.2. Optimal Sampling Positions Obtained by the Proposed Method. Algorithm 1 requires a given number of uniformly distributed points (particles) on the unit sphere for its initialization. It looks like a strict and difficult condition; however, we can obtain these points with any given number if we make a little change on Algorithm 1 by setting the terms of $\omega(\mathbf{x}_i, \mathbf{x}_j)$ in (3) to be an equal value (i.e., $\omega(\mathbf{x}_i, \mathbf{x}_j) = 1$). For example, we can get 1000 points uniformly distributed on the unit sphere as follows. Here, we make use of a 4-time iteratively refined icosahedron mesh which contains 2562 uniformly distributed vertices on the unit sphere. First, we break the mesh and randomly select 1000 vertices as initialized positions for particles. Then we set the terms $\omega(\mathbf{x}_i, \mathbf{x}_j)$ to be 1 and run Algorithm 1. When the iterative procedure is finished, we can obtain 1000 points uniformly distributed on the unit sphere. This procedure is illustrated by Figure 3. Actually other methods could also be used for the initialization, such as random selection 1000 points on the unit sphere.

The uniformly distributed points are treated as initial positions for the particle system to get optimal sampling

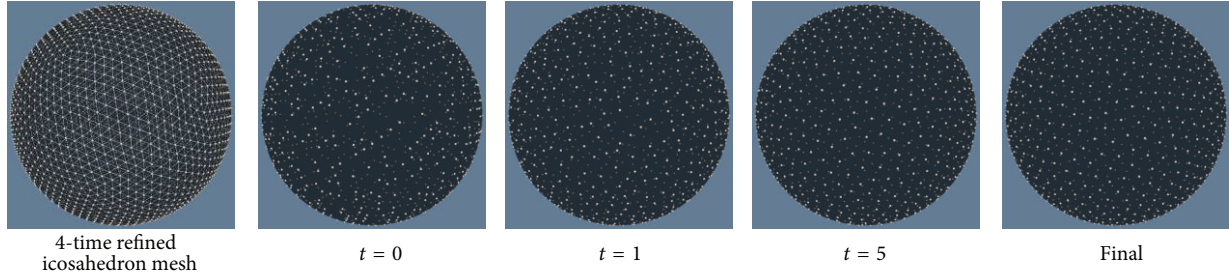


FIGURE 3: Example to obtain 1000 uniformly distributed points on the unit sphere by the iterative procedure of Algorithm 1. Here, we set the term $\omega(\mathbf{x}_i, \mathbf{x}_j) = 1$ in (3). We randomly choose 1000 vertices of a 4-time iteratively refined icosahedron mesh as initial points ($t = 0$). Particles' positions are given after the 1st ($t = 1$) and 5th ($t = 5$) iterations are finished. The final result is shown at last.

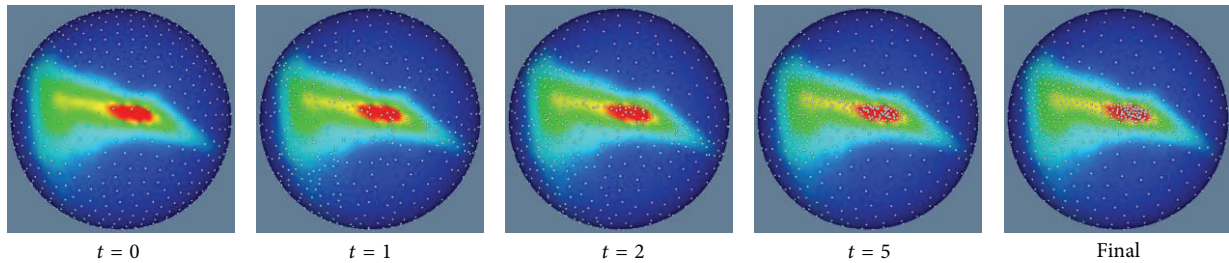


FIGURE 4: Iterative procedure to manipulate 1000 particles on the unit sphere according to Algorithm 1, where the weight terms of $\omega(\mathbf{x}_i, \mathbf{x}_j)$ in (3) are set to be (5). The probability distribution for vertices of parameterized meshes is shown with colors on the unit sphere. Red parts show where the probability is high, and blue parts show where the probability is low. The figure ($t = 0$) shows initialized particles which are uniformly distributed on the unit sphere. Particles' positions are shown after the 1st ($t = 1$), 2nd ($t = 2$), and 5th ($t = 5$) iterations are finished, respectively. Final positions of particles are shown by the most right figure from which it can be seen that more particles are located in red regions and less particles are located in blue regions.

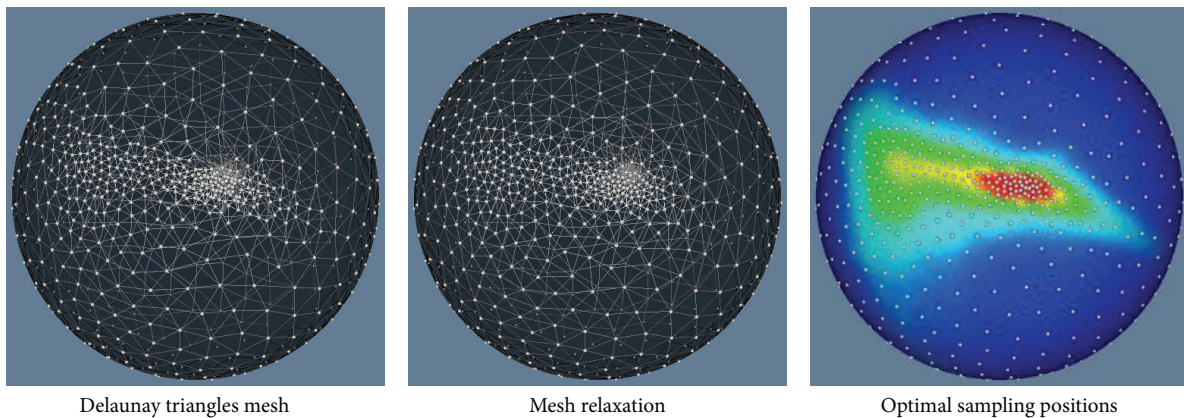


FIGURE 5: Results of constructed Delaunay triangles mesh, mesh relaxation, and the obtained 1000 optimal sampling positions on the unit sphere.

positions. By setting the weight terms $\omega(\mathbf{x}_i, \mathbf{x}_j)$ in (3) to be (5), Algorithm 1 is able to make the final particles' locations to be adaptive to the probability of vertices of parameterized meshes. Figure 4 gives examples to show the iterative procedure to manipulate 1000 particles on the unit sphere according to Algorithm 1.

When the iterative procedure is finished, the obtained particles are treated as vertices to build a spherical mesh by Delaunay triangles. The left figure in Figure 5 gives the constructed Delaunay triangles mesh on the unit sphere. It can be

seen that triangles in local regions are not uniform. The mesh is improved by mesh relaxation, shown in the middle figure in Figure 5. The final optimal sampling positions overlaid on the probability distribution of vertices are shown in the right figure of Figure 5.

3.3. *Corresponding Points and Evaluations on SSMs.* We evaluate the performances of the proposed method and the original MDL method by using six kinds of human organs. Examples of corresponding points determined by the two methods

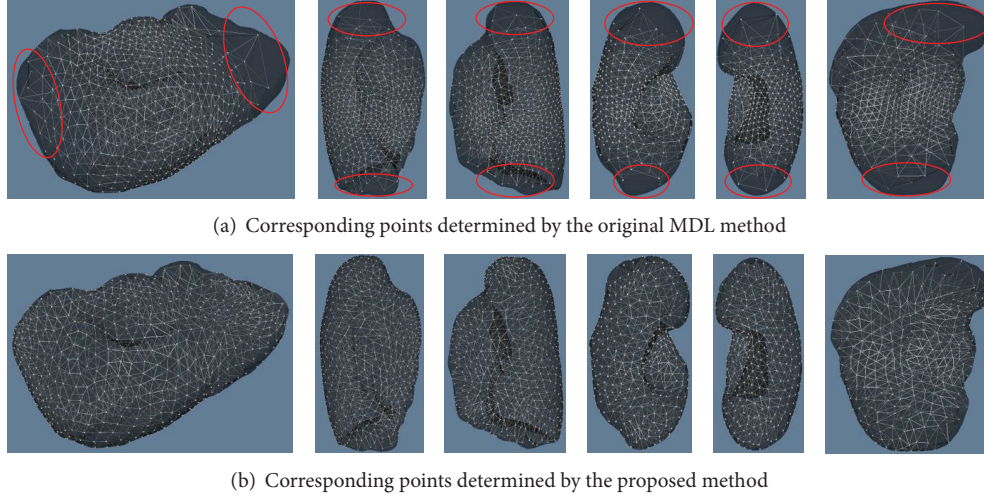


FIGURE 6: Corresponding points determined by the original MDL method [12] and the proposed method. The organs from left to right are livers, right lungs, left lungs, right kidneys, left kidneys, and spleens. Red circles illustrate the regions where there are fewer corresponding points.

are given by Figure 6. It can be seen that corresponding points are gathered in partial regions on the surfaces of organs for the results of the original MDL method. Especially, there are nearly no corresponding points in the regions indicated by red circles. This problem is able to be corrected by the proposed method. It can be seen that corresponding points are almost uniformly located on the surfaces of organs.

We build two SSMs based on the corresponding points determined by the two methods and compare their performances by the generalization and specificity tests, which are the most widely used method to evaluate SSMs suggested by [22]. Generalization tests are based on leave-one-out experiments, where $N - 1$ shapes are used for training SSMs and the remaining one is used to test whether it can be represented by the trained SSMs. The distance between the untrained shape and the reconstructed shape by SSMs is calculated to show how much difference exists. Low values indicate that the constructed SSMs have good generalization performances on untrained shapes. The measure of generalization is defined by

$$G(M) = \frac{1}{N} \sum_{i=1}^N \text{Dis}(\mathbf{X}_i, \mathbf{X}'_i), \quad (6)$$

where N is the total number of shapes, \mathbf{X}_i is the i th untrained shape, \mathbf{X}'_i is the corresponding reconstructed shape by SSMs using the largest M eigen-vectors, and $\text{Dis}(\mathbf{X}_i, \mathbf{X}'_i)$ is the distance of the two shapes, \mathbf{X}_i and \mathbf{X}'_i .

In specificity tests, the constructed SSMs are used to synthesize a large number of shapes. Each synthesized shape is compared with training shapes and finds the closest one. The mean value of distances between synthesized shapes and their corresponding closest training shapes is used as the measure of specificity tests. Low values indicate that the trained SSMs have good specificity on training shapes. The measure of specificity is defined by

$$S(M) = \frac{1}{L} \sum_{i=1}^L \min_{\mathbf{X}_j \in \Omega_{\mathbf{X}}} \text{Dis}(\mathbf{Y}_i, \mathbf{X}_j), \quad (7)$$

where L is the number of synthesize shapes by SSMs using M largest eigen vectors, \mathbf{Y}_i is the i th synthesize shape, $\Omega_{\mathbf{X}}$ is the set of training shapes to build SSMs, and $\text{Dis}(\mathbf{Y}_i, \mathbf{X}_j)$ is the distance of the two shapes, \mathbf{Y}_i and \mathbf{X}_j . In experiments, we synthesize 10000 shapes for the specificity test.

Shape distances in generalization and specificity tests are calculated by (8), in order to make the comparison of two shapes not to be concentrated on corresponding points [23].

$$\text{Dis}(\mathbf{X}, \mathbf{Y}) = \frac{1}{2} \left[\frac{1}{U} \sum_{\mathbf{x} \in \mathbf{X}} \min_{\mathbf{y} \in \mathbf{Y}} d(\mathbf{x}, \mathbf{y}) + \frac{1}{V} \sum_{\mathbf{y} \in \mathbf{Y}} \min_{\mathbf{x} \in \mathbf{X}} d(\mathbf{x}, \mathbf{y}) \right], \quad (8)$$

where \mathbf{x} and \mathbf{y} are vertices of the two shape \mathbf{X} and \mathbf{Y} , respectively, $d(\mathbf{x}, \mathbf{y})$ is the Euclidian distance of two vertices, and U and V are the number of vertices for the two shapes.

Since livers and lungs are larger than kidneys and spleens, we use 1000 corresponding points to build SSMs of livers and lungs and 500 corresponding points to build SSMs of kidneys and spleens. Additionally, we adopt general-purpose computing on graphics processing units (GPGPU) to deal with the large computation costs on (8).

Results on generalization and specification tests are given in Figure 7. We calculate the mean values and the standard deviations for generalization and specificity measures to compare the two methods. It can be seen that the proposed method gives smaller measures of generalization and specificity for all the six kinds of organs, which means that the proposed method performs better than the original MDL method.

3.4. Discussion. Although it is a good idea to conformally transform each shape onto a unit sphere to eliminate variations on translations and scales before the MDL registration is performed [12], the conformal mappings become poor because manipulation of parameterized meshes makes them to be distorted in shape alignment. Therefore, a uniform

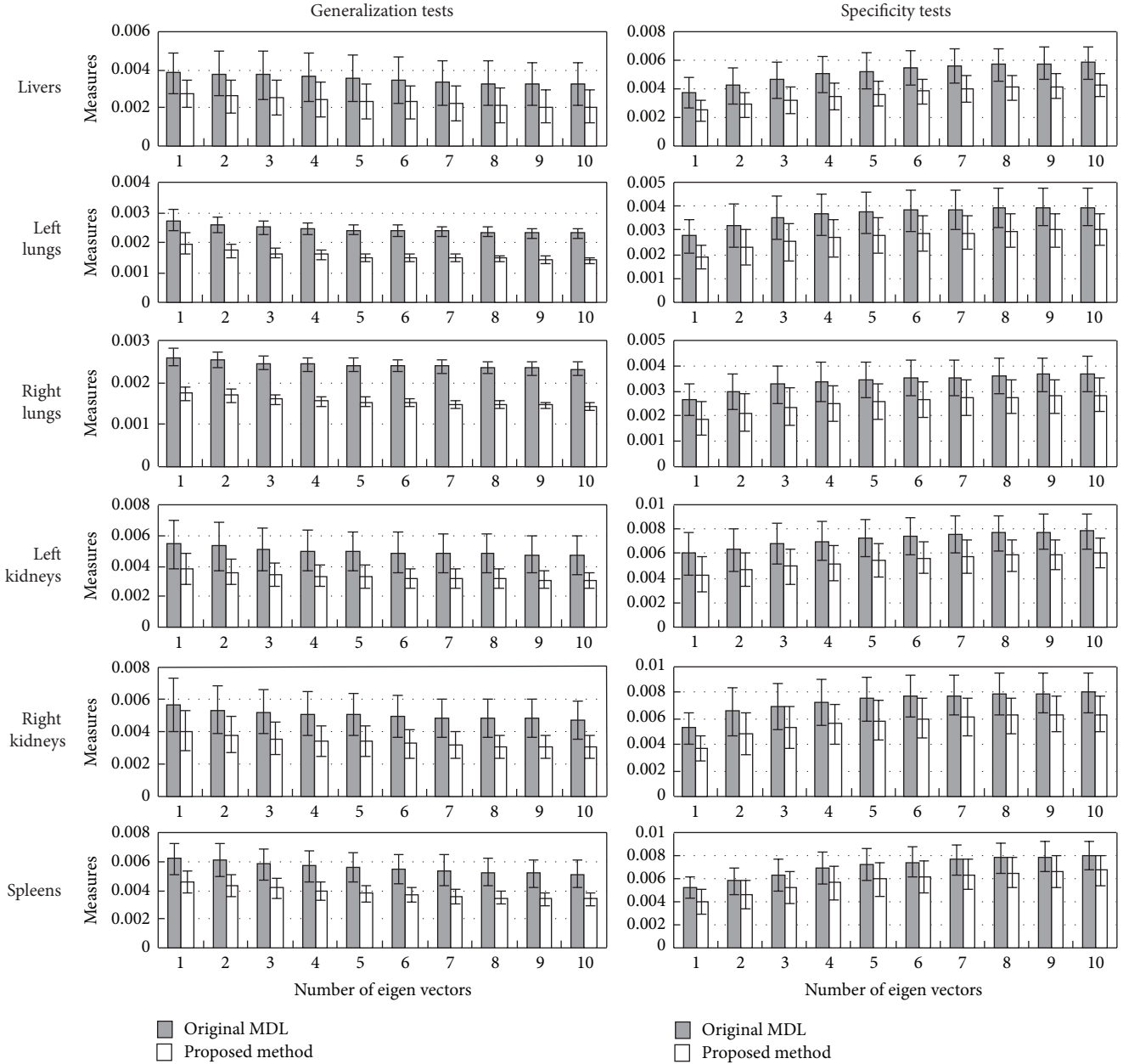


FIGURE 7: Two SSMs constructed by both the original MDL method [12] and the proposed method are compared in the generalization and specificity tests on the human organs of livers, left and right lungs, left and right kidneys, and spleens. We compare the two SSMs when the largest M (1~10) eigen vectors are used. The bars give the mean values, and the positive and negative steps give the standard deviations.

distributed sampling on the parameterized meshes after the MDL registration causes the determined corresponding points to be densely located in some parts and coarsely in other parts. An example of uniform sampling adopted in the original MDL method is shown by the most left figure in Figure 4 (with subtitle “ $t = 0$ ”). It can be seen that there are a few sampling positions located in regions where triangles of parameterized meshes are shrunk (red regions) and relatively more sampling positions in regions where triangles are expanded (blue regions). This causes the problem that determined corresponding points are not uniformly distributed on the original surfaces of organs.

In the proposed method, the obtained optimal sampling positions are adaptive to the distortions of parameterized meshes. The most right figure (with the subtitle “Final”) in Figure 4 gives such an example. It can be seen that there are a lot of sampling positions in the red regions where triangles are shrunk and relatively few positions in the blue regions where triangles are expanded. Therefore, determined corresponding points can spread uniformly on the original surfaces of organs even though conformal mappings become poor after MDL registration.

In the generalization and specificity tests, it can be seen that SSMs built by corresponding points determined by

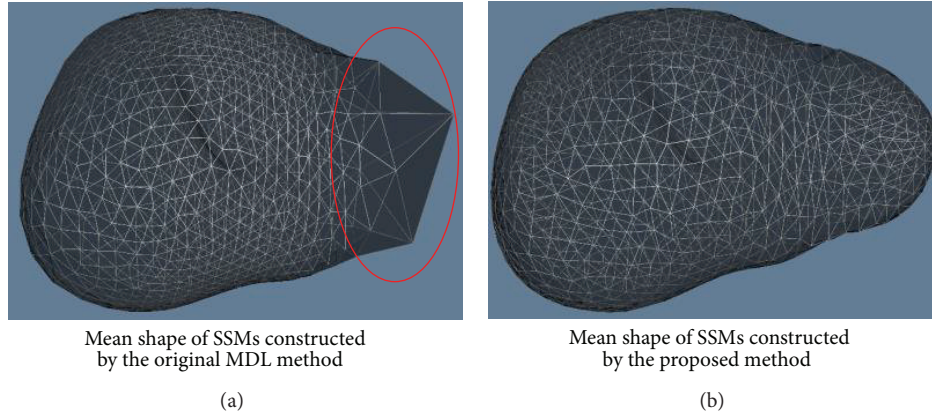


FIGURE 8: Mean shapes of SSMs constructed by the corresponding points determined by the original MDL method [12] and the proposed method for livers. It can be seen that the part indicated by the red circle cannot represent detailed shapes of livers.

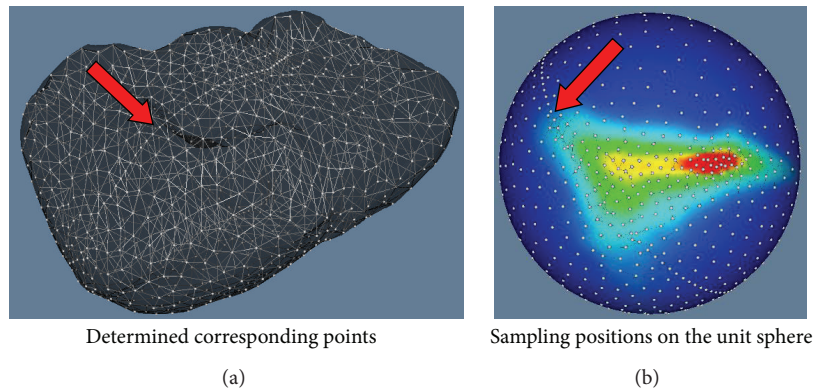


FIGURE 9: An example to show the dense-line artifact we encountered when we reimplemented the work [24]. (a) The determined corresponding points for a case of livers. The dense line artifact is indicated by the red arrow. (b) The adaptive sampling positions on the unit sphere. The line artifact exists in the reconnected part (indicated by the red arrow) through which two half-spherical sampling meshes are united.

the proposed method perform better. Here, we give an example to show the reason. Figure 8 gives the mean shapes of SSMs built by the corresponding points determined by the original MDL method and the proposed method for livers. It can be seen that the mean shape built by the original MDL method loses detailed information of livers' shapes. In particular, the mean shape decays in the part indicated by the red circle. However, the mean shape contains more details for the livers' shapes by using the proposed method. Therefore, SSMs built by the proposed method performs better than SSMs built by the original MDL method.

It seems that there is another work to resolve the same problem of original MDL in [24], where a 2D-dithering based remeshing method was adopted [20, 25]. We reimplement it; however we encounter a dense-line problem. An example of this problem is shown by Figure 9. In methodology, the method [24] has to firstly get two adaptive half-spherical meshes separately and then unit them to construct a whole spherical mesh whose vertices are the optimal sampling positions. If the densities of vertices on the two meshes' margins (through which the two meshes are connected) are different, this artifact problem will happen. We refer to all the related literature [20, 23, 24], and we find no descriptions of how to keep the two densities equal while ensuring the required

condition of the MDL method that the number of sampling positions should be unchanged. Although it seems that there is no such a line artifact problem in [24], we do not know how to avoid this problem. In the proposed method, since we manipulate a set of particles to find optimal sampling positions directly on the unit sphere, the connection of two meshes is not required. Therefore, the proposed method is able to avoid the line artifact problem in methodology. Additionally, we feel that it could not be fair to compare the performances of the proposed method and the reimplemented version with dense-line artifacts. Therefore, we only state the fact that we encounter in the reimplementing of [24] and do not give the compared results.

Additionally, we note that there is a particle and entropy based method for SSMs [26]. The difference is that we apply the particle-based method as the postprocessing step of MDL method in order to obtain optimal sampling positions on the unit sphere.

4. Conclusion

MDL based shape registration method proposed in [12] was a state-of-the-art method to determine the corresponding points on surfaces of 3D organs. Since uniformly distributed

points on the unit sphere were used to sample the shapes registered in the parameter space, the obtained corresponding points were not uniformly distributed on the original surfaces of organs. In this paper, we proposed a particle system based method to find the optimal sampling positions on the unit sphere to resolve this problem. In our method, a set of particles was manipulated on the unit sphere to find the optimal sampling positions by minimizing a carefully designed energy function. We evaluated the proposed method on six kinds of human abdominal and chest organs, which were livers, left and right lungs, left and right kidneys, and spleens. We collected 47 cases of lungs and 50 cases of other organs from different subjects to evaluate the proposed method. Experiments showed that the proposed method was able to find optimal sampling positions on the unit sphere and resolve the problem of the original MDL method. Additionally, we compared the proposed method with the original MDL method in the generalization and specificity tests. Experimental results showed that SSMs built by the proposed method performed better than SSMs built by the original MDL method. In future, we will apply the built SSMs in some segmentation tasks of human organs.

Acknowledgment

This research was supported by MEXT KAKENHI Grant no. 21103008.

References

- [1] T. Heimann and H. P. Meinzer, "Statistical shape models for 3D medical image segmentation: a review," *Medical Image Analysis*, vol. 13, no. 4, pp. 543–563, 2009.
- [2] T. Heimann, B. V. Ginneken, M. A. Styner et al., "Comparison and evaluation of methods for liver segmentation from CT datasets," *IEEE Transactions on Medical Imaging*, vol. 28, pp. 1251–1265, 2009.
- [3] T. F. Cootes, C. J. Taylor, D. H. Cooper, and J. Graham, "Active shape models—their training and application," *Computer Vision and Image Understanding*, vol. 61, no. 1, pp. 38–59, 1995.
- [4] S. M. Pizer, P. T. Fletcher et al., "Deformable m-reps for 3D medical image segmentation," *International Journal of Computer Vision*, vol. 55, pp. 85–106, 2003.
- [5] G. Székely, A. Kelemen, C. Brechbühler, and G. Gerig, "Segmentation of 2-D and 3-D objects from MRI volume data using constrained elastic deformations of flexible Fourier contour and surface models," *Medical Image Analysis*, vol. 1, no. 1, pp. 19–34, 1996.
- [6] A. Kelemen, G. Székely et al., "Elastic model-based segmentation of 3D neuroradiological datasets," *IEEE Transactions on Medical Imaging*, vol. 18, pp. 828–839, 1999.
- [7] J. Rissanen, *Stochastic Complexity in Statistical Inquiry*, World Science, Singapore, 1989.
- [8] R. H. Davies, C. J. Twining, T. F. Cootes, J. C. Waterton, and C. J. Taylor, "A minimum description length approach to statistical shape modeling," *IEEE Transactions on Medical Imaging*, vol. 21, no. 5, pp. 525–537, 2002.
- [9] M. A. Styner, J. A. Rajamani, L.-P. Nolte et al., "Evaluation of 3D correspondence methods for model building," in *Information Processing in Medical Imaging*, vol. 2732 of *Lecture Notes in Computer Science*, pp. 63–75, 2003.
- [10] H. H. Thodberg, "Minimum description length shape and appearance models," in *Image Processing Medical Imaging*, vol. 2732 of *Lecture Notes in Computer Science*, pp. 51–62.
- [11] A. Ericsson and K. Astrom, "Minimizing the description length using steepest descent," in *Proceedings of the British Machine Vision Conference*, pp. 93–102, 2003.
- [12] T. Heimann, I. Wolf, T. Williams, and H. Meinzer, "3D Active Shape Models using gradient descent optimization of description length," in *Information Processing in Medical Imaging*, *Lecture Notes in Computer Science*, pp. 566–577, 2005.
- [13] R. H. Davies, C. J. Twining, T. F. Cootes, and C. J. Taylor, "Building 3-D statistical shape models by direct optimization," *IEEE Transactions on Medical Imaging*, vol. 29, no. 4, pp. 961–981, 2010.
- [14] R. H. Davies, C. J. Twining, T. F. Cootes, J. C. Waterton, and C. J. Taylor, "3D statistical shape models using direct optimization of description length," in *Proceedings of the 7th European Conference on Computer Vision (ECCV '02)*, pp. 3–21, 2002.
- [15] T. Heimann, I. Oguz, I. Wolf, M. Styner, and H. Meinzer, "Implementing the automatic generation of 3D statistical shape models with ITK," *The Insight Journal MICCAI Open Science Workshop*, 2006, <http://hdl.handle.net/1926/224>.
- [16] X. F. Gu, Y. Wang, T. F. Chan, P. M. Thompson, and S. T. Yau, "Genus zero surface conformal mapping and its application to brain surface mapping," *IEEE Transactions on Medical Imaging*, vol. 23, no. 8, pp. 949–958, 2004.
- [17] M. D. Meyer, P. Georgel, and R. T. Whitaker, "Robust particle systems for curvature dependent sampling of implicit surfaces," in *Proceedings of the International Conference on Shape Modeling and Applications (SMI '05)*, pp. 124–133, June 2005.
- [18] R. O. Duta, P. E. Hart, and D. G. Stork, *Pattern Classification*, Wiley-Interscience, 2nd edition, 2000.
- [19] J. O'Rourke, *Computational Geometry in Csecond Edition*, Cambridge University Press, 2001.
- [20] P. Alliez, M. Meyer et al., "Interactive geometry remeshing," *ACM Transactions on Graphics*, vol. 21, pp. 347–354, 2002.
- [21] The Visualization Toolkit (VTK), <http://www.vtk.org/>.
- [22] R. H. Davies, C. J. Twining, and C. J. Taylor, *Statistical Models of Shape: Optimization and Evaluation*, Springer, 1st edition, 2008.
- [23] T. Heimann, *Statistical Shape Models for 3D Medical Image Segmentation*, VDM, 2008.
- [24] T. Heimann, I. Wolf, and H.-P. Meinzer, "Automatic generation of 3D statistical shape models with optimal landmark distributions," *Methods of Information in Medicine*, vol. 46, no. 3, pp. 275–281, 2007.
- [25] V. Ostromoukhov, "A simple and efficient error-diffusion algorithm," in *Proceedings of the Computer Graphics Annual Conference (SIGGRAPH '01)*, pp. 567–572, August 2001.
- [26] J. Cates, P. T. Fletcher, M. Styner, M. Shenton, and R. Whitaker, "Shape modeling and analysis with entropy-based particle systems," in *Information Processing in Medical Imaging*, vol. 4584 of *Lecture Notes in Computer Science*, pp. 333–345, 2007.

Review Article

Artificial Neural Networks in Mammography Interpretation and Diagnostic Decision Making

Turgay Ayer,¹ Qiushi Chen,¹ and Elizabeth S. Burnside²

¹ H. Milton Stewart School of Industrial and Systems Engineering, Georgia Institute of Technology,
765 Ferst Dr., Atlanta, GA 30332, USA

² Department of Radiology, University of Wisconsin Medical School, E3/311, 600 Highland Avenue, Madison, WI 53792-3252, USA

Correspondence should be addressed to Turgay Ayer; ayer@isye.gatech.edu

Received 18 January 2013; Accepted 22 April 2013

Academic Editor: Yi-Hong Chou

Copyright © 2013 Turgay Ayer et al. This is an open access article distributed under the Creative Commons Attribution License, which permits unrestricted use, distribution, and reproduction in any medium, provided the original work is properly cited.

Screening mammography is the most effective means for early detection of breast cancer. Although general rules for discriminating malignant and benign lesions exist, radiologists are unable to perfectly detect and classify all lesions as malignant and benign, for many reasons which include, but are not limited to, overlap of features that distinguish malignancy, difficulty in estimating disease risk, and variability in recommended management. When predictive variables are numerous and interact, ad hoc decision making strategies based on experience and memory may lead to systematic errors and variability in practice. The integration of computer models to help radiologists increase the accuracy of mammography examinations in diagnostic decision making has gained increasing attention in the last two decades. In this study, we provide an overview of one of the most commonly used models, artificial neural networks (ANNs), in mammography interpretation and diagnostic decision making and discuss important features in mammography interpretation. We conclude by discussing several common limitations of existing research on ANN-based detection and diagnostic models and provide possible future research directions.

1. Introduction

Breast cancer is the most common nonskin cancer and the second leading cause of cancer deaths among American women [1]. About one in eight American women are projected to develop breast cancer in their lives [2]. The American Cancer Society (ACS) estimates that 288,130 women were diagnosed with breast cancer and 39,520 died from this disease in 2011 [3].

Unfortunately, there is no foolproof method to prevent breast cancer. However, when detected early, the disease is often effectively curable. For example, 5-year survival rate increases from 27% to 98% when breast cancer is detected in an early stage [3]. That is why there is an intense interest in screening modalities for early detection.

Mammography, a low-dose X-ray procedure for visualizing the internal structure of the breast, is the most effective means to date for early detection of breast cancer [4]. Mammograms can detect masses, tiny deposits of calcium referred

to as microcalcifications, and other subtle changes that may indicate cancer. Early diagnosis through screening mammography is the most effective means of decreasing the death rate from breast cancer. Randomized trials have shown that the use of screening mammography in the general population reduces breast cancer mortality by at least 24 percent [5]. It is estimated that more than 20 million mammograms are performed in the US annually and approximately 70% of women over age 40 have had a mammogram in the last two years [6, 7].

All mammograms are overseen and interpreted by radiologists. Subspecialty radiologists who are experts in the field often have fellowship training in mammography and read these studies exclusively. Community radiologists, who read the majority of mammograms in the context of a diverse general practice, on the other hand, have lower rates of cancer detection and higher rates of biopsy [8]. It is reported that in the US, only about 20% of women who have biopsies turn out to have cancer [9]. While only about 3.5% of abnormal

screening mammograms interpreted by community radiologists reveal cancer, subspecialty radiologists have a significantly higher positive predictive value (PPV) [8]. Community radiologists also have a lower sensitivity resulting in missed breast cancers. While community radiologists detect about 3.0 breast cancers per 1,000 screening mammograms, subspecialty radiologists detect significantly more: about 5.3 cancers per 1,000 mammograms [10]. Furthermore, the US as a whole appears to have different decision thresholds than other countries. Smith-Bindman et al. [11] report that although cancer detection rates are identical in the US and in the UK, radiologists in the US declared many more mammogram results uncertain or suspicious compared with their British counterparts. As a result, American women with and without cancer underwent at least double the number of followup tests, like biopsies.

The American College of Radiology (ACR) has been working on addressing these issues by attempting to standardize mammography reporting, reduce confusion in breast imaging interpretations, and facilitate outcome monitoring. For example, the ACR has developed a lexicon, the breast imaging reporting and data system (BI-RADS), which standardizes mammogram feature distinctions and the terminology used to describe them [12]. The BI-RADS lexicon, which includes the descriptors that can predict benign or malignant disease, is intended to guide radiologists and physicians in the breast cancer decision making process to facilitate patient management. Furthermore, the results can be compiled in a standard format that permits the collection, maintenance, and analysis of demographic, mammographic, and outcomes data.

Although general rules for discriminating malignant and benign lesions exist, radiologists are unable to classify all lesions as malignant and benign, as the successful diagnosis requires systematic search patterns using numerous factors in the presence of noise in images [13]. When predictive variables are numerous and interact, ad hoc decision making strategies based on experience and memory, the only viable method for radiologists, may lead to errors [14] and variability in practice [11, 15]. That is why there is intense interest in developing tools that can calculate an accurate probability of breast cancer to aid in decision making [16–18].

To improve the accuracy of mammography interpretation and aid in detection and diagnosis of abnormalities, several computer-aided detection (CAD) and computer-aided diagnostic (CADx) tools have been developed. The integration of computer models to help radiologists increase the accuracy of mammography examinations in diagnosis [19–23] has gained increasing attention since the last two decades. CAD and CADx models may help radiologists in the detection and discrimination of lesions as benign and malignant by providing objective information, such as the risk of breast cancer [24]. In this paper, we provide an overview of one of the most commonly used models, artificial neural networks (ANNs), in CAD and CADx for mammography interpretation and biopsy decision making and discuss important features in breast cancer diagnosis. We present a list of the articles described in this study in Table 1.

2. ANN Models in Breast Cancer Detection and Diagnosis

ANNs are computer models that have the ability to duplicate aspects of human intelligence while incorporating the processing power of computers and are thus capable of processing a large amount of information simultaneously by learning from previous cases [25]. ANNs have many desirable properties that make them well suited for medical decision making. ANNs are capable of “learning” complicated patterns from data that are difficult for humans to identify [26]. They can also often overcome ambiguous and missing data [27] and provide accurate predications [28, 29]. The structure of a generic ANN model built for aiding in mammography interpretation is presented in Figure 1. The ANN models built for aiding in mammography interpretation typically take patients demographic risk factors (such as age and a family history) and mammographic findings (such as mass or calcification variables) as inputs and estimate the corresponding breast cancer risk to aid in biopsy decision.

Microcalcifications are one of the major indicators of breast cancer. A large proportion, 30%–50%, of breast cancers demonstrate microcalcifications on mammography, and 60%–80% of cancers exhibit microcalcifications on histologic examination [30, 31]. Identifying microcalcifications, which range in size between 0.1 and 1 mm, is a difficult detection task for radiologists [31, 32]. Furthermore, distinguishing between malignant and commonly occurring benign microcalcifications is challenging.

There are two different ways of using ANNs to aid in mammography interpretation. The first approach is to apply the classifier directly to the region of interest (ROI) image data. As a second approach, ANNs can also learn from the features extracted from the preprocessed image signals. Below, we summarize some of the noteworthy studies that took the first approach.

Stafford et al. [33] developed a committee of three-layer ANNs to examine digital mammograms after image preprocessing. These ANNs were trained and tested on 256 mammograms and transformed the original ROI images into output images such that each pixel was assigned a value between 0 and 1. The committee consisted of four ANNs, each with expertise on identifying microcalcifications within a certain size range. In particular, the four ANNs were built by using the microcalcification samples with size ranges of 50–250 μm , 100–500 μm , 200–1,000 μm , and 400–2,000 μm , respectively. The committee took the highest output among these four ANNs (the winner-take-all rule) as the output for each pixel. The full system was tested on microcalcifications of size ranging from 50–2,000 μm . The committee reached 84% sensitivity at 75% specificity.

Zhang et al. [30] developed a novel neural network to identify whether an ROI included more than a pre-specified number of microcalcifications. In this proposed neural network model, a subsequent layer did not depend on the location patterns in the preceding layer, a special structure called the shift-invariant property. Therefore, the result of the shift-invariant ANN (SI-ANN) did not depend on the location information in the input ROI images. If a

TABLE 1: Summary of ANN studies in mammography interpretation and diagnostic decision making.

Study	Type	ANN structure	Input	Dataset and training/testing strategy	Results and findings
Stafford et al. (1993) [33]	CADe	A committee of four three-layer BP-ANNs	Pixel information	167 mammograms with pathologies and 89 without pathologies. 50% for training and 50% for testing.	Test on 20 out of 128 mammograms covering microcalcification size-range of 50–250 μm : 0.9% FP at 85% TP, 2.4% FP at 100% TP. 50–2,000 μm : 25% FP at 84% TP, 40% FP at 100% TP.
Zhang et al. (1994) [30]	CADe	The Shift-Invariant ANN (SI-ANN)	Pixel information	168 ROIs from 34 digitized mammograms. 50%-50% cross-validation. 52 mammograms	ROC index: $A_z = 0.91 \pm 0.02$, 45% FP at 100% TP. ROC index: $A_z = 0.9$.
Chan et al. (1995) [35]	CADe	The Convolution Neural Network (CNN)	Pixel information	Group 1: 110 TP and 116 FP. Group 2: 108 TP and 116 FP. Two-fold cross-validation.	FP rate: 0.1 cluster per image at 100% TP (for obvious cases), 1.5 cluster per image at 90% TP (for average and subtle cases).
Nagel et al. (1998) [36]	CADe	SI-ANN	Features extracted from image	196 TPs and 1,252 FPs. Leave-one-out cross-validation.	The number of FPs per image at 83% TP: 1.6 for ANN, 0.8 for ANN and rule-based method. Average ROC index: $A_z = 0.85$ (stdev = 0.04) for ANN, $A_z = 0.64$ (stdev = 0.07) for ANN + rule-based method ($P = 0.014$).
Wu et al. (1992) [34]	CADe	BP-ANN	Pixel information	56 positive, 56 negative, and 56 FP ROIs, respectively. 50%-50% cross-validation.	For individual microcalcifications: $A_z = 0.71$. For clustered microcalcifications: $A_z = 0.85$; 50% FP at 95% TP.
Jiang et al. (1996) [45]	CADx	BP-ANN	Computer-extracted morphological features	40 malignant and 67 benign cases from 100 images. Leave-one-out cross-validation.	Identified 100% malignant and 82% of the benign cases. Significantly better than radiologists without computer aid ($P = 0.03$).
Jiang et al. (1999) [46]	CADx	BP-ANN	Computer-extracted morphological features	46 malignant and 58 benign cases. Leave-one-out cross-validation.	By 10 radiologists: $A_z = 0.61$, sensitivity = 73.5%, specificity = 31.6%. With aid of ANN: $A_z = 0.75$ ($P < 0.0001$), sensitivity = 87.4%, specificity = 41.9%.
Huo et al. (1998) [47]	CADx	BP-ANN	Morphological features characterizing margin and density	38 benign and 57 malignant cases from 65 patients. Leave-one-out cross-validation.	ANN: $A_z = 0.90$, 19.2% specificity at 100% sensitivity. Hybrid method (rule-based + ANN): $A_z = 0.94$, 69.2% specificity at 100% sensitivity.
Kallergi (2004) [22]	CADx	BP-ANN	Morphological and distributional descriptors	50 benign and 50 malignant cases. Leave-one-out cross-validation.	$A_z = 0.98 \pm 0.01$, 85% specificity at 100% sensitivity.

TABLE 1: Continued.

Study	Type	ANN structure	Input	Dataset and training/testing strategy	Results and findings
Chan et al. (1997) [48]	CADx	BP-ANN	Texture features SGLD matrices	41 malignant and 45 benign cases from 54 patients. Leave-one-out cross-validation.	With best subset of features: <i>Mammogram-by-mammogram</i> : $A_z = 0.88$, 24% specificity at 100% sensitivity. <i>Patient-by-patient</i> : 39% specificity at 100% sensitivity.
Baker et al. (1995) [41]	CADx	BP-ANN	BI-RADS lesion descriptors and medical history variables	133 benign and 73 malignant cases. Leave-one-out cross-validation.	PPV: 61% (ANN) versus 35% (radiologists). ROC index: $A_z = 0.89 \pm 0.02$ (ANN) versus 0.85 ± 0.03 (radiologists), $P = 0.29$. Specificity: 62% (ANN) versus 30% (radiologists) at 100% sensitivity ($P < 0.01$).
Lo et al. (1999) [42]	CADx	BP-ANN	BI-RADS lesion descriptors, age, and history variables	326 benign and 174 malignant cases. Leave-one-out cross-validation.	Only BI-RADS features: $A_z = 0.84 \pm 0.02$, 6% specificity at 100% sensitivity. BI-RADS + age: $A_z = 0.86 \pm 0.02$, 30% specificity at 100% sensitivity. All features: $A_z = 0.87 \pm 0.02$, 22% specificity at 100% sensitivity. Age variable significantly improves the A_z ($P = 0.028$).
Ayer et al. (2010) [43]	CADx	BP-ANN	Demographic, mammographic features, and BI-RADS categories	510 malignant and 61,709 benign cases. 10-fold cross-validation.	$A_z = 0.965$ (ANN) versus 0.939 (radiologists), $P < 0.001$. Specificity at 85% sensitivity: 94.5% (ANN) versus 88.2% (radiologists), $P < 0.001$.
Jesneck et al. (2007) [49]	CADx	BP-ANN	Mammographic features, sonographic features, and history features	296 malignant and 507 benign cases. 500 for training and validation, 303 for testing.	Training and validation set: $A_z = 0.92 \pm 0.01$, Testing set: $A_z = 0.91 \pm 0.02$.
Tourassi et al. (2003) [51]	CADx	CSNN	BI-RADS features, age and history	Training set: 174 malignant and 326 benign cases. Testing set: 358 malignant and 672 benign cases.	On training set: $A_z = 0.84 \pm 0.02$ On testing set: $A_z = 0.81 \pm 0.02$ CSNN is also capable to impute missing data.
Ort (2001) [54]	CADx and risk estimation	BP-ANN	Age and radiographic features	185 malignant and 1,103 benign cases. 490 for training and the rest for testing.	$A_z = 0.89$ (surgeons) versus 0.86 (ANN), $P = 0.004$. ANN is possible for risk stratification.

CADx: computer-aided detection, CADx: computer-aided diagnosis, ANN: artificial neural network, BP-ANN: back-propagation artificial neural network, FP: false positive, TP: true positive, ROI: region of interest, SGLD: spatial grey level dependence, PPV: positive prediction value, BI-RADS: the breast imaging reporting and data system, CSNN: constraint satisfaction neural network, and SI-ANN: shift-invariant artificial neural network.

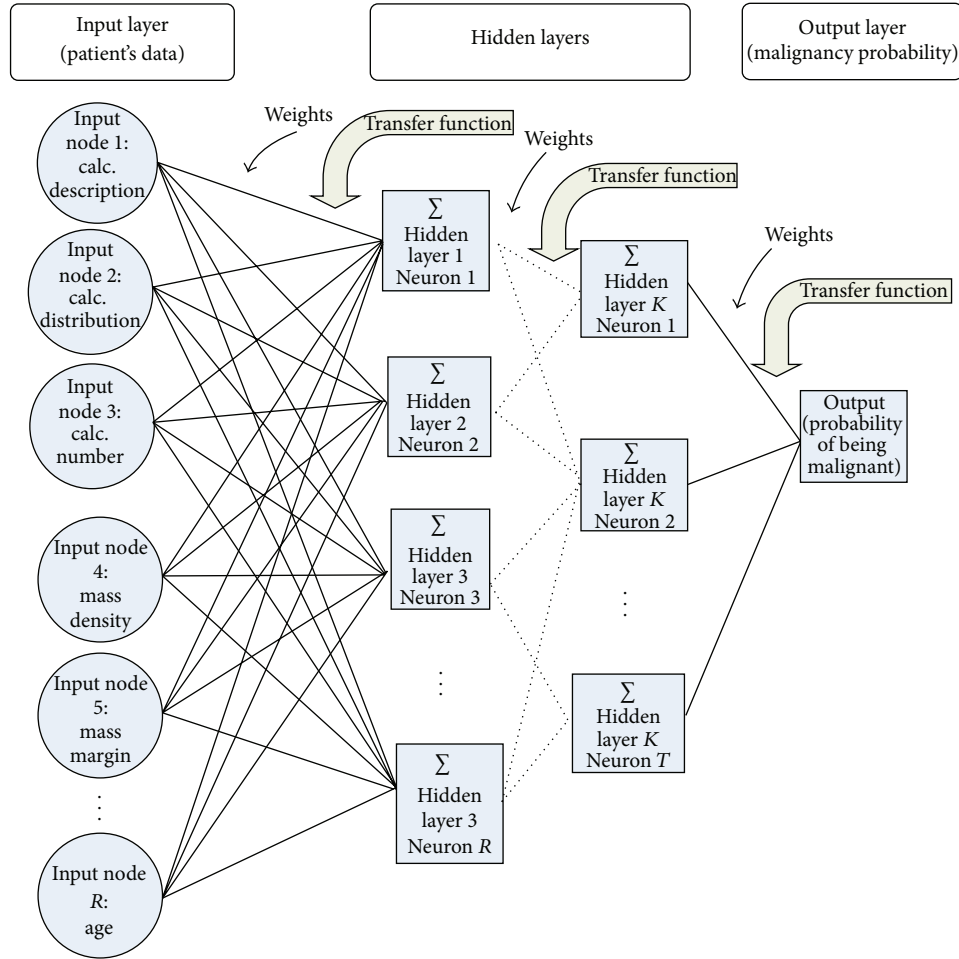


FIGURE 1: Inputs to the network are lesion descriptors and family history of the patient. Nodes at each layer are connected to the nodes at the succeeding layer by weighted arcs. Each hidden node in the first hidden layer performs a nonlinear weighted sum of all input values. The outputs of the last hidden layer are then similarly combined to the output layer. The single output value shows the probability of the lesion being malignant.

classical back-propagation ANN (BP-ANN) was used instead, then the locations of the microcalcification clusters implicitly had to be encoded as the inputs of this neural network. The performance of the SI-ANN was evaluated using a database of 168 ROIs of 55×55 pixels and various network configurations. Using this method, the highest area under the ROC curve (A_Z) of 0.91 ± 0.02 was achieved. The neural network was able to eliminate approximately 55% of false positive ROIs without missing any of true-positive ROIs. Furthermore, the SI-ANN showed a superior performance over the classic BP-ANN [34].

Chan et al. [35] investigated the effectiveness of a convolutional neural network (CNN) in detecting microcalcifications on mammograms. The CNN was different from the classic ANN in its structure where nodes in hidden layers were organized in groups. In the CNN, the same values were enforced for the weights connecting the nodes in groups of subsequent layers, which enabled the neural network to incorporate the neighborhood information around each pixel on mammograms during the training process. The output of the CNN

was a decision score. The performance of the CNN was evaluated on a data set of 52 mammograms. The average A_Z was 0.9, which was substantially robust to different network configurations. The CNN further reduced the number of false-positive clusters per image by more than 70% at all true-positive rates.

As a second approach, instead of learning directly from images, ANNs can also learn from the features extracted from preprocessed image signals. Several ANN applications for reducing false-positive (FP) cases in microcalcification detection followed this approach [36–39]. Among these studies, Nagel et al. [36], for example, built an ANN for identifying microcalcifications based on five extracted features: area, contrast, first moment of the power spectrum, mean pixel value, and edge gradient. This ANN was trained on 39 mammograms, and its output represented the likelihood of being a microcalcification. A feature-wise threshold was computed based on the training data to minimize the number of false positives while maintaining a high enough true-positive (TP) rate. For comparison purposes, a rule-based method of FP

reduction was also built. The average number of FPs per image were 1.9 for the rule-based method, 1.6 for the ANN, and 0.8 for the combined method at a sensitivity of 83%, when they were evaluated on an independent test set of 50 mammograms.

Following the detection of microcalcifications, radiologists should decide whether to biopsy or not. This decision relies on the ability of the radiologist to accurately differentiate benign and malignant features. To aid in biopsy decision making, several ANN-based CADx models based on radiologists' observations have been developed since 1990s [40–43].

As an alternative to feature extraction based on radiologists' observations, algorithms were developed to automatically extract features from digital mammography images. These automatically extracted features can be used as input to feed the CADx models. Chan et al. [44] provided a comprehensive summary of such methods. Jiang et al. [45] first integrated the computerized feature analysis and discrimination. Only the initial identification of microcalcification clusters was performed by radiologists. Based on eight morphological features extracted from the image, the ANN identified 100% of the malignant and 82% of the benign cases. The accuracy was significantly higher than that of five radiologists without computer aid ($P = 0.03$). In a follow-up study, Jiang et al. [46] compared the automated discrimination methods and routine clinical performance by ten radiologists using an ROC analysis. The ROC index A_Z increased from 0.61 without aid to 0.75 with computer aid ($P < 0.0001$). This improvement was also reflected in sensitivity (73.5% to 87.4%) and specificity (31.6% to 41.9%). In the method proposed by Huo et al. [47], mass regions were identified automatically and then features related to the margin and density of each mass were extracted. The results showed that the discrimination performance of the ANN ($A_Z = 0.94$) was slightly better than that of an experienced mammographer ($A_Z = 0.91$) and significantly better than the average radiologists ($A_Z = 0.81$, $P = 0.13$). Similarly, in Kallergi [22], features were automatically extracted from digital images by detection/segmentation methods. The ANN based on fourteen morphological (for individual calcifications) and distributional (for the clusters) descriptors was shown to achieve high sensitivity and specificity (100% and 85%), and be robust against false positive signals.

In addition to morphological features extracted from mammography images, texture features were also used to feed ANNs in classifying malignant and benign microcalcifications, such as in the study by Chan et al. [48]. In this study, thirteen texture features were derived from spatial grey level dependence (SGLD) matrices, which were constructed from the background-corrected ROIs. Several representative subsets of features were evaluated by a stepwise procedure. The feature set consisting of six features achieved the highest accuracy ($A_Z = 0.88$). The sensitivity was 100% at a specificity of 24% when decision threshold was set to 0.85. The results of this study showed that computerized methods were able to capture the changes of texture features in malignant, which were not visually apparent on mammograms.

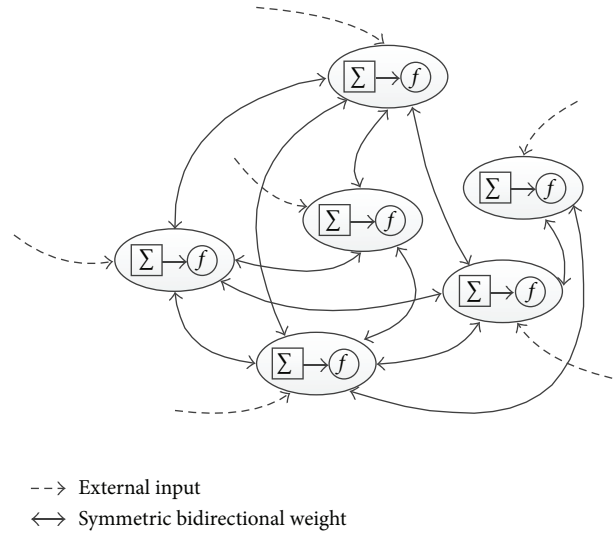


FIGURE 2: Neurons are organized in a non-hierarchical structure in constraint satisfaction neural network (CSNN). Each neuron is assigned a value (activation level). These values represent the network state. Inputs to each neuron include both the external input and the activation levels of other neurons connected by the bidirectional symmetric weights. The activation levels are updated by passing the weighted sum of input values through a transfer function. The training is terminated when the network achieves a globally stable state with all constraints satisfied.

Obviously, mammographic features are not the only considerations for physicians in breast cancer diagnosis. Other relevant findings, such as a patient's medical history and clinical factors, can also be informative for a successful diagnosis. Baker et al. [41] built an ANN model based on ten descriptors from breast imaging reporting and data system (BI-RADS) and eight features of patients' medical history such as age, personal and family history of breast cancer, and menopausal status. In this study, the specificity of the ANN was significantly greater than that of radiologists (62% and 30% at 95% sensitivity, $P < 0.01$). Later, Lo et al. [42] observed similar findings and showed that age was a strong diagnostic predictor in the retrospective evaluation of the follow-up study. Considering age together with seven BI-RADS findings in the ANN significantly enhanced the discrimination performance measured in A_Z ($P = 0.028$).

In addition to mammographic features, some studies built ANN models that also considered sonographic features. Among them, the first one, Jesneck et al. [49] examined 803 breast mass lesions (296 malignant and 507 benign) from 737 patients. To assess the discrimination performance, ROC analysis was used in a training, validation, and retest scheme. Results showed that the ANN model achieved a high performance ($A_Z = 0.92 \pm 0.01$), and consideration of sonography variables improved the performance.

Although ANNs have been successful in mammographic diagnosis, they have often been regarded as black box since they do not provide much clinical intuition. To overcome this limitations, Tourassi et al. [50] proposed an innovative ANN, the constraint satisfaction neural network (CSNN), as illustrated in Figure 2. An appealing property of this

nonhierarchical and flexible CSNN model was the capability to discover trends and hidden associations (e.g., to identify the risk factors) and extract decision rules. As inputs, 10 mammographic and six patient clinical features of 500 breast lesions (174 malignant and 326 benign) from BI-RADS database were used. Based on a 50%-50% cross-validation scheme, the ROC index A_Z was shown to be 0.84 ± 0.02 , which was comparable with the performance of a classic ANN [42]. Later, Tourassi et al. [51] validated this approach using a larger testing data set of additional 1,030 cases.

In addition to improving diagnostic accuracy, ANNs have also been useful in reducing variability in radiologists' interpretations. In the literature, significant variability in radiologists' interpretations has been reported. For example, a recent study by Beam et al. [52] showed that the sensitivity of mammography ranged from 59% to 100% and specificity ranged from 35% to 98%, depending on the reading radiologist. To reduce this interobserver variability, Jiang et al. [46], for the first time, presented evidence for the ability of an ANN model to reduce variability of mammography interpretation among radiologists. In another study, Jiang et al. [53] assessed the variability in interpretation among radiologists with and without an ANN model. The ANN estimated the likelihood of malignancy, and ten radiologists were instructed in how to utilize the output of the ANN. The findings of this study verified that ANNs were not only useful for improving diagnostic accuracy but also for decreasing variability in mammography interpretation. In particular, they showed that (1) the range in sensitivity was reduced from 35% to 26% and the standard deviation (SD) of A_Z reduced by 46% (from 0.056 to 0.030); (2) on average, complete agreements were achieved in 33 (32%) cases with computer aid compared with 13 (13%) cases without the aid ($P < 0.001$), and the occurrence of conflicting was reduced from 43 (41%) cases to 28 (27%) cases ($P = 0.02$); (3) substantial disagreements in recommendation (biopsy versus routine follow-up, measured by pairwise frequency and per-patient frequency (see [15]), were reduced significantly with computer aid for all cases and for cancer cases only ($P < 0.04$).

The results of mammography are often conveyed as positive or negative. In reality, however, the result of any test that is imperfect would ideally be expressed in terms of a post-test probability of disease which would help an individual better understand his or her personal risk given the sensitivity and specificity of the test. Recall that the output of an ANN is often a probability indicating the similarity of the test case to the malignant or benign findings. Then, a preset threshold value is used to determine whether the test case is malignant or benign. In this regard, ANNs can also be viewed as risk assessment models. However, most ANN studies in the literature have only focused on discrimination but did not consider calibration. Orr [54] explored the value of quantifying the risk of malignancy using an ANN. A standard back-propagation network with a single hidden layer was trained and tested on a dataset of size 1,288 (75% for training and 25% for testing). The ROC index A_Z of the ANN in the test set was 0.89, which was significantly better than that of the physicians alone ($A_Z = 0.86$, $P < 0.01$). In a retrospective examination of the training data, the author observed that among the patients

with an ANN output of 0, none had cancer, and for those with an output greater than 0.75, 71% of them had cancer. To assess the risk stratification capability of ANN (i.e., calibration), patient data were divided into four quartiles, four subgroups of almost equal size based on the magnitude of the ANN output, where those in the lowest quartile had minimal risk of malignancy. Results showed that the risks of cancer were well separated among the four subgroups ($2/391 = 0.5\%$, $7/272 = 2.6\%$, $37/341 = 10.9\%$, and $139/295 = 47.1\%$, resp.).

Risk estimations provided by ANNs could provide useful information for physicians for a successful diagnosis, risk stratification, and risk communication. As noted by Cook [55], a comprehensive evaluation of such models should include both discrimination and calibration. The discrimination ability represents the capability to separate the malignant findings from the benign ones, as measured by ROC index A_Z , sensitivity and specificity. Discrimination assessment is commonly used as we see in studies reviewed above. However, discrimination measures cannot assess how well the predictions agree with the actual observations, which needs to be evaluated via the model calibration. The purpose of calibration is to improve the accuracy of risk prediction by estimating the absolute risk of cancer. A well-calibrated model means that the predicted risks match the observed risks within each subgroup [56]. However, unlike discrimination, calibration did not receive much attention in performance assessment of the existing ANN models.

There is a tradeoff between discrimination and calibration, and perfect calibration and discrimination cannot be achieved simultaneously in clinical practice [57–59]. Several studies have shown that given a perfectly calibrated risk estimation model, the ROC index A_Z varied with the distribution of the observed risk in the population.

Ayer et al. [43] revisited the use of ANN models in breast cancer risk estimation and assessed both discrimination and calibration. On a large data set consisting of 62,219 consecutive mammography findings, the risk prediction was obtained using 10-fold cross-validation. The ANN model achieved an A_Z of 0.965, which was significantly higher than that of the radiologists, 0.939 ($P < 0.001$). The calibration of the ANN was assessed by the Hosmer-Lemeshow (H-L) goodness-of-fit statistic test. The H-L statistic was 12.46 ($P > 0.1$, $df = 8$), which indicated a good match between the risk estimates and the actual malignancy prevalence.

In clinical practice, missing data is a common problem [51]. Obviously, incomplete inputs may have an impact on the prediction accuracy of a trained ANN. Markey et al. [27] investigated the impact of missing data in classifying testing data on ANNs. The ANNs were trained with complete data and tested on a dataset with missing components. Four levels of missing data (10%, 20%, 30%, and 40%) were tested in a back-propagation ANN (BP-ANN) and a CSNN model. For the BP-ANN, missing values were (1) replaced with zeros, (2) replaced with mean value from the training set, and (3) imputed by using a multiple imputation procedure. The results showed that the replacing of the missing values with zeros was not very efficient and could lead to misleading results. The decrease of A_Z was significant ($P < 0.01$) even with only 10% missing data (0.84 ± 0.03) compared with

the complete data (0.94 ± 0.01). The other two methods were shown to be more accurate and efficient. Their findings showed that with data imputation, the models achieved reasonable performance for up to about 30% missing data.

Imbalanced data presents another challenge to ANN development, testing, and performance. A data set is considered imbalanced if the number of instances of one class is significantly smaller than that of the other class. In the context of breast cancer, the proportion of patients with breast cancer is significantly lower due to the actual prevalence of the disease. Mazurowski et al. [60] showed that this influence could significantly reduce the performance of an ANN. In general, two methods, undersampling and oversampling, are commonly used to compromise data imbalance. Undersampling randomly chooses samples from the majority class so that the size of the majority class is similar to that of the minority class. Oversampling, on the other hand, will randomly duplicate or interpolate the samples from the minority class to mitigate this imbalance. Mazurowski et al. [61] investigated the effects of imbalanced data on the discrimination performance for a classic ANN. A database consisting 1,005 biopsy-proven masses (370 malignant and 645 benign) collected at the Duke University Medical Center was used to compare the effects of oversampling and undersampling. This study verified the detrimental effects of the class imbalance in training dataset and showed that oversampling in general achieved a higher ROC performance compared with undersampling.

3. Discussion and Conclusions

Several studies have verified that ANNs have the potential to successfully aid in mammography interpretation and breast cancer diagnosis. However, for successful applications of ANNs, both advantages and disadvantages of these models should be well understood and be carefully considered by researchers and the end users. Advantages and disadvantages of ANNs have been previously discussed in several studies in the literature (see, e.g., [62, 63]). To summarize, the advantages of ANNs include the ease of model building, the capability in capturing the interactions between predictors, and ability to consider complicated nonlinearities between predictors and outcomes (Table 2).

Besides the advantages, ANNs have several disadvantages as well. In medical practice, the clinical insights obtained from the prediction models obviously play an important role. As Tu [63] noted, ANNs however suffer from the limited capability to explicitly explain the causal relationships between predictive factors and outcomes, which is probably the most major drawback. Another drawback is that a well-trained model would be difficult to share with other researchers. This is because the knowledge discovered from the data is all encoded into a huge weight matrix, which is difficult to interpret and share. Furthermore, the complexity of the model structure in ANNs makes it more prone to overfitting, the case where the network overlearns and mimics the training dataset but performs poorly when presented to an external dataset. Ayer et al. [25] also noted the need for confidence intervals, which are, unlike statistical methods, not straightforward to obtain from ANN models.

TABLE 2: Advantages and disadvantages of ANNs.

Advantage	Disadvantage
(i) Easy model building with less formal statistical knowledge required.	(i) Clinical interpretation of model parameters is difficult (black boxes).
(ii) Capable of capturing interactions between predictors.	(ii) Sharing an existing ANN model is difficult.
(iii) Capable of capturing nonlinearities between predictors and outcomes.	(iii) Prone to overfitting due to the complexity of model structure.
(iv) Users can apply multiple different training algorithms	(iv) Confidence intervals of the predicted risks are difficult to obtain.
	(v) The model development is empirical. Few guidelines exist to determine the best network structures and training algorithms.

4. Future Research in ANNs for Breast Cancer Detection and Diagnosis

There is a growing interest in developing successful ANN models for breast cancer detection and diagnosis, due to high computational power and practical use of ANNs. However, many studies in the literature share some common limitations, which make their applications limited. As noted by Schwarzer et al. [64], the most common major limitations include (1) lacking a comprehensive assessment of the discrimination accuracy, (2) overfitting, and (3) the complexity issues. First, most studies in the literature do not evaluate the performance of the trained ANNs using an independent test set. If testing the model on an independent dataset is not feasible due to data limitation or other concerns, at least cross-validation should be done to minimize the potential bias. However, many studies lacked such evaluations and as a result, in most cases, the error rates were dramatically underestimated. Second, most studies did not pay close attention to overfitting. The generalizability of the neural networks substantially depends on the number of hidden nodes in the hidden unit. When they are too few, the network is limited in its capability of representing the causal relationships. On the other hand, when they are excessive, the network is prone to overfitting. Many studies in the literature reported the use of very large the number of hidden nodes as compared with the size of the training data but did not assess whether overfitting occurred. Lastly, in many studies, the computational complexity of the ANN was not properly reported. Some measured the complexity only using the number of input units which would underestimate the computational complexity. Properly reporting the complexity of an ANN model is important because the computational power as well as many potential problems such as overfitting are closely related to the complexity of the model. The future studies in this domain should carefully consider and overcome these limitations for successful applications of ANNs in mammography interpretation.

Acknowledgment

The authors acknowledge the National Institute of Health Awards R01LM010921 and R01CA165229.

References

- [1] S. H. Parker, F. Burbank, R. J. Jackman et al., "Percutaneous large-core breast biopsy: a multi-institutional study," *Radiology*, vol. 193, no. 2, pp. 359–364, 1994.
- [2] L. M. Wun, R. M. Merrill, and E. J. Feuer, "Estimating lifetime and age-conditional probabilities of developing cancer," *Lifetime Data Analysis*, vol. 4, no. 2, pp. 169–186, 1998.
- [3] American Cancer Society, *Breast Cancer Facts & Figures 2011-2012*, American Cancer Society, Atlanta, Ga, USA, 2011.
- [4] H. C. Zuckerman, "The role of mammography in the diagnosis of breast cancer," *Breast Cancer—Diagnosis and Treatment*, pp. 152–172, 1987.
- [5] R. A. Smith, D. Saslow, K. A. Sawyer et al., "American cancer society guidelines for breast cancer screening: update 2003," *CA: A Cancer Journal for Clinicians*, vol. 53, no. 3, pp. 141–169, 2003.
- [6] National Center for Health Statistics Health (NCHS), *United States, 2005 with Chartbook on Trends in the Health of Americans Hyattsville*, National Center for Health Statistics Health, Hyattsville, Md, USA, 2005.
- [7] Census.gov, Basic Counts/Population, 2005, http://factfinder.census.gov/servlet/ACSSAFFPeople?_submenuId=people_0&_sse=on.
- [8] M. L. Brown, F. Houn, E. A. Sickles, and L. G. Kessler, "Screening mammography in community practice: positive predictive value of abnormal findings and yield of follow-up diagnostic procedures," *The American Journal of Roentgenology*, vol. 165, no. 6, pp. 1373–1377, 1995.
- [9] Breastcancer.org, Biopsy, 2006, http://www.breastcancer.org/testing_biopsy.html.
- [10] E. A. Sickles, D. E. Wolverton, and K. E. Dee, "Performance parameters for screening and diagnostic mammography: specialist and general radiologists," *Radiology*, vol. 224, no. 3, pp. 861–869, 2002.
- [11] R. Smith-Bindman, P. W. Chu, D. L. Miglioretti et al., "Comparison of screening mammography in the United States and the United Kingdom," *The Journal of the American Medical Association*, vol. 290, no. 16, pp. 2129–2137, 2003.
- [12] American College of Radiology, *Breast Imaging Reporting and Data System (BIRADS)*, American College of Radiology, Reston, Va, USA, 4th edition, 2003.
- [13] M. L. Giger, "Computer-aided diagnosis in radiology," *Academic Radiology*, vol. 9, no. 1, pp. 1–3, 2002.
- [14] D. Kahneman, P. Slovic, and A. Tversky, *Judgment under Uncertainty: Heuristics and Biases*, Cambridge University Press, Cambridge, UK, 2001.
- [15] J. G. Elmore, C. K. Wells, C. H. Lee, D. H. Howard, and A. R. Feinstein, "Variability in radiologists' interpretations of mammograms," *The New England Journal of Medicine*, vol. 331, no. 22, pp. 1493–1499, 1994.
- [16] E. C. Y. Chan, "Promoting an ethical approach to unproven screening imaging tests," *Journal of the American College of Radiology*, vol. 2, no. 4, pp. 311–320, 2005.
- [17] B. J. Hillman, "Informed and shared decision making: an alternative to the debate over unproven screening tests," *Journal of the American College of Radiology*, vol. 2, no. 4, pp. 297–298, 2005.
- [18] E. Picano, "Informed consent and communication of risk from radiological and nuclear medicine examinations: how to escape from a communication inferno," *The British Medical Journal*, vol. 329, no. 7470, pp. 849–851, 2004.
- [19] L. Hadjiiski, B. Sahiner, M. A. Helvie et al., "Breast masses: computer-aided diagnosis with serial mammograms," *Radiology*, vol. 240, no. 2, pp. 343–356, 2006.
- [20] H. P. Chan, B. Sahiner, M. A. Helvie et al., "Improvement of radiologists' characterization of mammographic masses by using computer-aided diagnosis: an ROC study," *Radiology*, vol. 212, no. 3, pp. 817–827, 1999.
- [21] Z. Huo, M. L. Giger, C. J. Vyborny, and C. E. Metz, "Breast cancer: effectiveness of computer-aided diagnosis—observer study with independent database of mammograms," *Radiology*, vol. 224, no. 2, pp. 560–568, 2002.
- [22] M. Kallergi, "Computer-aided diagnosis of mammographic microcalcification clusters," *Medical Physics*, vol. 31, no. 2, pp. 314–326, 2004.
- [23] Y. Jiang, C. E. Metz, R. M. Nishikawa, and R. A. Schmidt, "Comparison of independent double readings and computer-aided diagnosis (CAD) for the diagnosis of breast calcifications," *Academic Radiology*, vol. 13, no. 1, pp. 84–94, 2006.
- [24] M. Giger, Z. Huo, and M. Kupinski, "Computer-aided diagnosis in mammography," in *Handbook of Medical Imaging*, vol. 2, pp. 917–986, SPIE, Washington, DC, USA, 2000.
- [25] T. Ayer, J. Chhatwal, O. Alagoz, C. E. Kahn, R. W. Woods, and E. S. Burnside, "Comparison of logistic regression and artificial neural network models in breast cancer risk estimation," *RadioGraphics*, vol. 30, no. 1, pp. 13–22, 2010.
- [26] J. E. Dayhoff and J. M. DeLeo, "Artificial neural networks: opening the black box," *Cancer*, vol. 91, no. 8, supplement, pp. 1615–1635, 2001.
- [27] M. K. Markey, G. D. Tourassi, M. Margolis, and D. M. DeLong, "Impact of missing data in evaluating artificial neural networks trained on complete data," *Computers in Biology and Medicine*, vol. 36, no. 5, pp. 516–525, 2006.
- [28] J. Lawrence, *Introduction to Neural Networks*, California Scientific Software, Nevada City, Calif, USA, 1993.
- [29] A. J. Maren, C. T. Harston, and R. M. Pap, *Handbook of Neural Computing Applications*, edited by A. J. Maren, C. T. Harston, R. M. Pap, Academic Press, San Diego, Calif, USA, 1990.
- [30] W. Zhang, K. Doi, M. L. Giger, Y. Wu, R. M. Nishikawa, and R. A. Schmidt, "Computerized detection of clustered microcalcifications in digital mammograms using a shift-invariant artificial neural network," *Medical Physics*, vol. 21, no. 4, pp. 517–524, 1994.
- [31] M. P. Sampat, M. K. Markey, and A. C. Bovik, "Computer-aided detection and diagnosis in mammography," in *Handbook of Image and Video Processing*, vol. 2, pp. 1195–1217, 2005.
- [32] K. Kerlikowske, P. A. Carney, B. Geller et al., "Performance of screening mammography among women with and without a first-degree relative with breast cancer," *Annals of Internal Medicine*, vol. 133, no. 11, pp. 855–863, 2000.
- [33] R. G. Stafford, J. Beutel, D. J. Mickewich, and S. L. Albers, "Application of neural networks to computer-aided pathology detection in mammography," in *Medical Imaging 1993: Physics of Medical Imaging*, vol. 1896 of *Proceedings of SPIE*, pp. 341–352, February 1993.
- [34] Y. Wu, K. Doi, M. L. Giger, and R. M. Nishikawa, "Computerized detection of clustered microcalcifications in digital mammograms: applications of artificial neural networks," *Medical Physics*, vol. 19, no. 3, pp. 555–560, 1992.

- [35] H. P. Chan, S. C. B. Lo, B. Sahiner, K. L. Lam, and M. A. Helvie, "Computer-aided detection of mammographic microcalcifications: pattern recognition with an artificial neural network," *Medical Physics*, vol. 22, no. 10, pp. 1555–1567, 1995.
- [36] R. H. Nagel, R. M. Nishikawa, J. Papaioannou, and K. Doi, "Analysis of methods for reducing false positives in the automated detection of clustered microcalcifications in mammograms," *Medical Physics*, vol. 25, no. 8, pp. 1502–1506, 1998.
- [37] A. Papadopoulos, D. I. Fotiadis, and A. Likas, "An automatic microcalcification detection system based on a hybrid neural network classifier," *Artificial Intelligence in Medicine*, vol. 25, no. 2, pp. 149–167, 2002.
- [38] G. Rezaei-Rad and S. Jamarani, "Detecting microcalcification clusters in digital mammograms using combination of wavelet and neural network," in *Proceedings of the International Conference on Computer Graphics, Imaging and Vision: New Trends*, pp. 197–201, July 2005.
- [39] L. Zhang, W. Qian, R. Sankar, D. Song, and R. Clark, "A new false positive reduction method for MCCs detection in digital mammography," in *Proceedings of the IEEE International Conference on Acoustics, Speech, and Signal Processing*, vol. 2, pp. 1033–1036, Salt Lake City, Utah, USA, May 2001.
- [40] Y. Wu, M. L. Giger, K. Doi, C. J. Vyborny, R. A. Schmidt, and C. E. Metz, "Artificial neural networks in mammography: application to decision making in the diagnosis of breast cancer," *Radiology*, vol. 187, no. 1, pp. 81–87, 1993.
- [41] J. A. Baker, P. J. Kornguth, J. Y. Lo, M. E. Williford, and C. E. Floyd, "Breast cancer: prediction with artificial neural network based on BI-RADS standardized lexicon," *Radiology*, vol. 196, no. 3, pp. 817–822, 1995.
- [42] J. Y. Lo, J. A. Baker, P. J. Kornguth, and C. E. Floyd, "Effect of patient history data on the prediction of breast cancer from mammographic findings with artificial neural networks," *Academic Radiology*, vol. 6, no. 1, pp. 10–15, 1999.
- [43] T. Ayer, O. Alagoz, J. Chhatwal, J. W. Shavlik, C. E. Kahn, and E. S. Burnside, "Breast cancer risk estimation with artificial neural networks revisited: discrimination and calibration," *Cancer*, vol. 116, no. 14, pp. 3310–3321, 2010.
- [44] H. P. Chan, B. Sahiner, K. L. Lam et al., "Computerized analysis of mammographic microcalcifications in morphological and texture feature spaces," *Medical Physics*, vol. 25, no. 10, pp. 2007–2019, 1998.
- [45] Y. Jiang, R. M. Nishikawa, D. E. Wolverton et al., "Malignant and benign clustered microcalcifications: automated feature analysis and classification," *Radiology*, vol. 198, no. 3, pp. 671–678, 1996.
- [46] Y. Jiang, R. M. Nishikawa, R. A. Schmidt, C. E. Metz, M. L. Giger, and K. Doi, "Improving breast cancer diagnosis with computer-aided diagnosis," *Academic Radiology*, vol. 6, no. 1, pp. 22–33, 1999.
- [47] Z. Huo, M. L. Giger, C. J. Vyborny, D. E. Wolverton, R. A. Schmidt, and K. Doi, "Automated computerized classification of malignant and benign masses on digitized mammograms," *Academic Radiology*, vol. 5, no. 3, pp. 155–168, 1998.
- [48] H. P. Chan, B. Sahiner, N. Patrick et al., "Computerized classification of malignant and benign microcalcifications on mammograms: texture analysis using an artificial neural network," *Physics in Medicine and Biology*, vol. 42, no. 3, pp. 549–567, 1997.
- [49] J. L. Jesneck, J. Y. Lo, and J. A. Baker, "Breast mass lesions: computer-aided diagnosis models with mammographic and sonographic descriptors," *Radiology*, vol. 244, no. 2, pp. 390–398, 2007.
- [50] G. D. Tourassi, M. K. Markey, J. Y. Lo, and C. E. Floyd, "A neural network approach to breast cancer diagnosis as a constraint satisfaction problem," *Medical Physics*, vol. 28, no. 5, pp. 804–811, 2001.
- [51] G. D. Tourassi, J. Y. Lo, and M. K. Markey, "Validation of a constraint satisfaction neural network for breast cancer diagnosis: new results from 1,030 cases," in *Medical Imaging 2003: Image Processing*, vol. 5032 of *Proceedings of SPIE*, pp. 207–214, February 2003.
- [52] C. A. Beam, E. F. Conant, and E. A. Sickles, "Association of volume-independent factors with accuracy in screening mammogram interpretation," *Journal of the National Cancer Institute*, vol. 95, no. 4, pp. 282–290, 2003.
- [53] Y. Jiang, R. M. Nishikawa, R. A. Schmidt, A. Y. Toledano, and K. Doi, "Potential of computer-aided diagnosis to reduce variability in radiologists' interpretations of mammograms depicting microcalcifications," *Radiology*, vol. 220, no. 3, pp. 787–794, 2001.
- [54] R. K. Orr, "Use of an artificial neural network to quantitate risk of malignancy for abnormal mammograms," *Surgery*, vol. 129, no. 4, pp. 459–466, 2001.
- [55] N. R. Cook, "Use and misuse of the receiver operating characteristic curve in risk prediction," *Circulation*, vol. 115, no. 7, pp. 928–935, 2007.
- [56] N. R. Cook, "Statistical evaluation of prognostic versus diagnostic models: beyond the ROC curve," *Clinical Chemistry*, vol. 54, no. 1, pp. 17–23, 2008.
- [57] G. A. Diamond, "What price perfection? Calibration and discrimination of clinical prediction models," *Journal of Clinical Epidemiology*, vol. 45, no. 1, pp. 85–89, 1992.
- [58] M. H. Gail and R. M. Pfeiffer, "On criteria for evaluating models of absolute risk," *Biostatistics*, vol. 6, no. 2, pp. 227–239, 2005.
- [59] P. W. F. Wilson, R. B. D'Agostino, D. Levy, A. M. Belanger, H. Silbershatz, and W. B. Kannel, "Prediction of coronary heart disease using risk factor categories," *Circulation*, vol. 97, no. 18, pp. 1837–1847, 1998.
- [60] M. A. Mazurowski, P. A. Habas, J. M. Zurada, and G. D. Tourassi, "Impact of low class prevalence on the performance evaluation of neural network based classifiers: experimental study in the context of computer-assisted medical diagnosis," in *Proceedings of the International Joint Conference on Neural Networks (IJCNN '07)*, pp. 2005–2009, Orlando, Fla, USA, August 2007.
- [61] M. A. Mazurowski, P. A. Habas, J. M. Zurada, J. Y. Lo, J. A. Baker, and G. D. Tourassi, "Training neural network classifiers for medical decision making: the effects of imbalanced datasets on classification performance," *Neural Networks*, vol. 21, no. 2-3, pp. 427–436, 2008.
- [62] S. Dreiseitl and L. Ohno-Machado, "Logistic regression and artificial neural network classification models: a methodology review," *Journal of Biomedical Informatics*, vol. 35, no. 5-6, pp. 352–359, 2002.
- [63] J. V. Tu, "Advantages and disadvantages of using artificial neural networks versus logistic regression for predicting medical outcomes," *Journal of Clinical Epidemiology*, vol. 49, no. 11, pp. 1225–1231, 1996.
- [64] G. Schwarzer, W. Vach, and M. Schumacher, "On the misuses of artificial neural networks for prognostic and diagnostic classification in oncology," *Statistics in Medicine*, vol. 19, no. 4, pp. 541–561, 2000.

Research Article

GND-PCA-Based Statistical Modeling of Diaphragm Motion Extracted from 4D MRI

Windra Swastika,¹ Yoshitada Masuda,² Rui Xu,³ Shoji Kido,³
Yen-Wei Chen,⁴ and Hideaki Haneishi⁵

¹ Graduate School of Engineering, Chiba University, Chiba 263-8522, Japan

² Chiba University Hospital, Chiba 260-8677, Japan

³ Graduate School of Medicine, Yamaguchi University, Yamaguchi 755-8505, Japan

⁴ Graduate School of Science and Engineering, Ritsumeikan University, Shiga 525-8577, Japan

⁵ Research Center for Frontier Medical Engineering Chiba University, Chiba 263-8522, Japan

Correspondence should be addressed to Windra Swastika; windra.swastika@graduate.chiba-u.jp

Received 18 January 2013; Revised 16 April 2013; Accepted 17 April 2013

Academic Editor: Chung-Ming Chen

Copyright © 2013 Windra Swastika et al. This is an open access article distributed under the Creative Commons Attribution License, which permits unrestricted use, distribution, and reproduction in any medium, provided the original work is properly cited.

We analyzed a statistical model of diaphragm motion using regular principal component analysis (PCA) and generalized N-dimensional PCA (GND-PCA). First, we generate 4D MRI of respiratory motion from 2D MRI using an intersection profile method. We then extract semiautomatically the diaphragm boundary from the 4D-MRI to get subject-specific diaphragm motion. In order to build a general statistical model of diaphragm motion, we normalize the diaphragm motion in time and spatial domains and evaluate the diaphragm motion model of 10 healthy subjects by applying regular PCA and GND-PCA. We also validate the results using the leave-one-out method. The results show that the first three principal components of regular PCA contain more than 98% of the total variation of diaphragm motion. However, validation using leave-one-out method gives up to 5.0 mm mean of error for right diaphragm motion and 3.8 mm mean of error for left diaphragm motion. Model analysis using GND-PCA provides about 1 mm margin of error and is able to reconstruct the diaphragm model by fewer samples.

1. Introduction

4D-MRI is an advanced imaging technique that reconstructs a 3D MRI with time series from a set of time sequential images of 2D MRI. For respiratory motion, the use of 4D MRI has an important role in many clinical applications such as lung cancer radiotherapy planning, examining pulmonary diseases, and analyzing diaphragm motion. However, current MRI is unable to acquire 4D MRI directly. Therefore, in the recent years some methods have been proposed to reconstruct 4D MRI of respiratory organs based on the sequential 2D MRI [1–3].

von Siebenthal et al. [1] proposed a method to obtain 4D image using internal respiratory gating and reconstructed it by retrospective sorting of dynamic 2D MR images. It showed the detailed deformation of an organ during

free breathing. Tokuda also proposed an adaptive imaging method to acquire a series of 3D MR images of respiratory organs as the extension of respiratory gating [2]. Our previous study successfully achieved 4D MR imaging of organs with respiratory motion using a method called intersection profile method [3]. In this method, we reconstructed 4D MRI of respiratory organ from time sequential images of 2D MRI under natural respiration. We not only successfully visualized 4D MRI of respiratory organ, but also proposed to construct diaphragmatic function map that can be used to evaluate diaphragm motion quantitatively. Previous related works on 4D respiratory motion modeling include [4–8].

Recent statistical model of respiratory motion was proposed by Li et al. [9]. It was a statistical model of lung based on principal component analysis (PCA) and applied to clinical data. The lung motion model, however, was based on two

types of respiratory phantoms and cosine function which will only be idealistic for phantom motion. Extraction and statistical modeling of lung motion field were also demonstrated in [10]. The experiment extracted motion fields from a 4D-CT data set and built a motion model for both intra- and intersubject. Although it focused on the lung motion, the results showed that the use of diaphragm as a stimulator to drive the motion model could reduce the prediction error. Simultaneous registration of all dynamic MR images and modeling processing were performed in [11] for the purpose to improve the accuracy of motion estimation. However, this approach may only be feasible for simple rigid or affine motion model. Applying this model to organs that have complex or nonrigid motion will significantly increase the number of parameter and consequently execution time also becomes much larger.

The statistical modeling was focusing on how to model respiratory motion based on lung motion [9–11] or internal liver motion [12]. In this paper, instead of extracting lung to obtain respiratory motion, we focus on extracting diaphragm motion from 4D-MRI and analyzing it using PCA. As one of the major determinants in respiratory motion, diaphragm has greater superior-interior translation compared with other respiratory organs such as lung or liver. Thus, by modeling and analyzing diaphragm motion, the variability of respiratory motion can be clearly visualized. As mentioned in [13], GND-PCA method can construct MR T1-weighted brain volumes and CT lung volumes using fewer training samples compared with regular PCA. Hence, we also interested to analyze the efficacy of GND-PCA compared with regular PCA in modeling the diaphragm motion.

To the best of our knowledge, this is the first study of modeling and analyzing diaphragm motion extracted from 4D MRI.

2. Materials and Methods

The process of constructing and analyzing the diaphragm motion model consists of four parts. The first is diaphragm segmentation and motion tracking. We will briefly review the methodology we used to create 3D model of diaphragm shape. Second is data normalization. We will cover how to normalize the data obtained from the previous step. This step is primarily important to generalize the data from different subjects. Third is model analysis using PCA and GND-PCA. Basic theory of PCA and GND-PCA will be described. Last is data evaluation, in which we will explain how to validate the constructed model.

2.1. 3D Diaphragm Segmentation and Motion Tracking. Right-handed Cartesian coordinate system is used to cover the whole diaphragm area. A number of MRI data slices, size of 256×256 pixels in coronal view are set along the y -axis (Figure 1(a)). Each data slice position is denoted by y_i where $i = 1, \dots, S$. To assess the diaphragm motion, we also use T time-sequential images for each data slice of y_i . We denote one data slice as $f_{\text{data}}(x, y_i, z, t)$, where $t = 1, 2, \dots, T$. A first shape of diaphragm is obtained from $f_{\text{data}}(x, y_i, z, t)$ for

$i = 1, 2, \dots, S$ and $t = 1$. The diaphragm shape is determined as follows. Several points are selected in each data slice (y_i) that represents diaphragm boundary shown as white dots in Figure 1(a). The number of points varies from 10 to 15 depending on the curve of diaphragm boundary. Generally, more points are required if the diaphragm boundary has a rounded or curvature shape. The points are then connected by spline interpolation. By conducting this operation for all y_i , the area of diaphragm in xy plane is defined as shown in Figure 1(b). We denote this shape as Ω . Note that we ignore the area below the heart because it is strongly affected by heart beat and apart from respiratory motion. The entry of this matrix represents z value of diaphragm surface at (x, y) . The 3D representation of diaphragm surface is shown in Figure 1(c). In this step, $S \times 256$ matrix for one whole diaphragm area is generated, where S is the number of slice. Depending on the acquisition process, S will vary between 16 and 24.

Once the 3D shape on diaphragm area Ω is obtained for $t = 1$ (as shown in Figure 1(b)), the 3D shape of diaphragm over the area of Ω is tracked in the next frame. In order to do so, a profile of $f_{\text{data}}(x, y_i, z, t)$ along Z at position (x, y) over Ω is compared with a profile of $f_{\text{data}}(x, y_i, z, t - 1)$ at the same position (x, y_i) , and is found a value of displacement of diaphragm along z -axis by using normalized cross-correlation.

Figure 2 summarizes the flow diagram of diaphragm motion tracking method. Complete reference regarding this motion tracking method can be found in [3].

2.2. Data Normalization. The acquisition of diaphragm motion based on the previously explained method cannot be generalized for all diaphragms due to the wide range of variability of diaphragm shape and size among the subjects. Hence, the acquired data need to be normalized. The normalization process takes four steps.

First, we divide the diaphragm area into two parts: right and left diaphragm areas.

Second, to represent a detailed and unique diaphragm region, we calculate gradient edges of all diaphragm shapes and choose one that has the highest gradient edges as reference image. Affine registration is then performed for all diaphragm shapes to ensure the same location and size of all diaphragm shape before the analysis is performed.

Third, for each diaphragm area, we set the top left and bottom right coordinate to limit the diaphragm area into a rectangular shape. The distance of new top left position is 1/10 of the diaphragm area width and so is the new bottom right position. Figure 2 shows how to set new region of diaphragm area. Selecting the region of diaphragm area ensures that the analysis is only done in the main part of the diaphragm area and ignores the area that has small movement. This also maintains the correspondence on different subjects since the top and bottom areas will constantly represent same anterior and posterior positions of all subjects.

The last step of normalization process consists of two parts, temporal and spatial normalization. Temporal normalization makes all subjects have the same number of

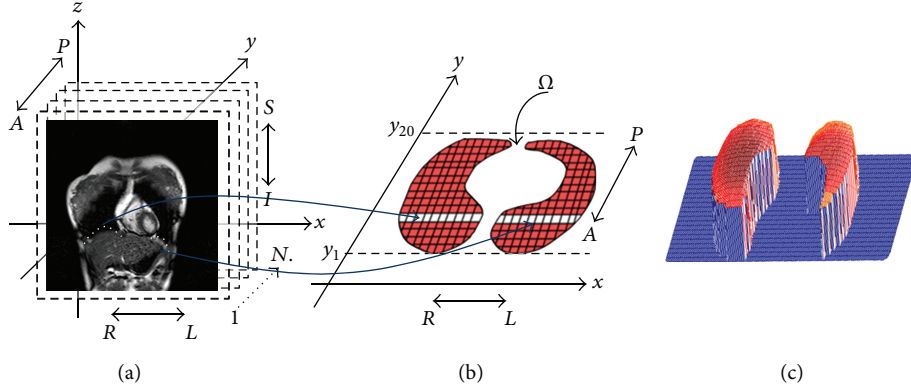


FIGURE 1: Coordinate definition of 4D MRI and diaphragm extraction. (a) Manually selected several points (white dots) of one data slice to extract diaphragm surface, (b) complete extraction of diaphragm surface from y_1 to y_{20} , and (c) representation of diaphragm area.

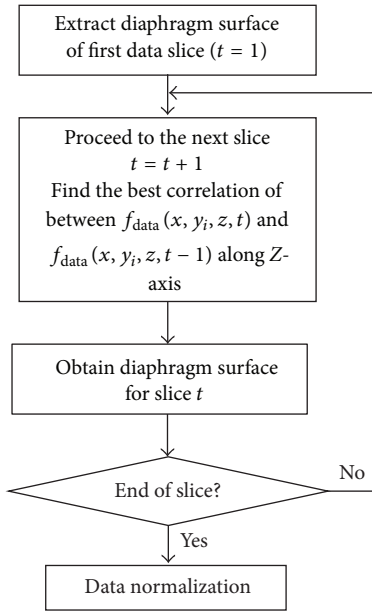


FIGURE 2: Flow diagram of diaphragm motion tracking method.

frames, while spatial normalization only normalizes the size of diaphragm area.

Let $Z(x, y, t)$ denotes the z value of diaphragm surface (or target image) at (x, y) position and t th frame $(1, 2, \dots, T)$. After temporal normalization, $Z(x, y, t)$ can be denoted as $Z(x, y, t^*)$, where t^* ranges from 1 to 20. The following operator is used to define t^* :

$$t^* = \left\lceil \frac{20-1}{T-1} (t-1) + 1 \right\rceil. \quad (1)$$

Here the operator $\lceil \cdot \rceil$ represents ceiling function which returns a decimal number to its smallest integer.

Due to the fact that the coordinate position and the size of rectangular area shown in Figure 3(b) vary among the subjects, the last part in the normalization process is to fix the rectangular area for both y and x axes. The purpose is that

all the data will have the same size and position. The size of the reference image is represented by $W_{\text{ref}} \cdot H_{\text{ref}}$. In our study, we used 60×100 pixels for $W_{\text{ref}} \cdot H_{\text{ref}}$. Actual normalization process is described as follows.

- (1) *Normalization of y-Axis.* To normalize the diaphragm area into Y axis, the origin image is scaled and fixed to the reference image. The following operator is used to scale diaphragm area in y -axis,

$$Z'(x, y, t) = Z\left(x, \left\lceil \frac{H_{\text{target}}}{H_{\text{ref}}} y \right\rceil, t^*\right), \quad (2)$$

where H_{target} is height of the image target and H_{ref} is the height of the reference image. Operator $\lceil \cdot \rceil$ represents ceiling function which rounds up the decimals into an integer. This scaling process is done for all x and y . The results of y -axis normalization is called intermediate image.

- (2) *Normalization of x-Axis.* The width of the reference image is also fixed by horizontal scaling. The operator used to scale diaphragm area in x -axis is written as

$$\begin{aligned} Z''(x, y, t) &= Z'\left(\left\lceil \frac{W_{\text{target}}(n) - W_{\text{target}}(1)}{W_{\text{ref}}} x + W_{\text{target}}(1) \right\rceil, y, t^*\right), \end{aligned} \quad (3)$$

where $W_{\text{target}}(n)$ and $W_{\text{target}}(1)$ are the last and first nonzero positions in the current y -axis and W_{ref} is the width of the reference image. This horizontal scaling is done for all x, y . The result of x -axis normalization is a final image with the same width and height of the reference image.

Since there are both right and left diaphragm areas, scaling the area using the reference image is done for both diaphragm areas. This process is repeated for each data frame obtained from the previous algorithm starting from the first time-sequential image to the last one ($t^* = 1 \cdots 20$).

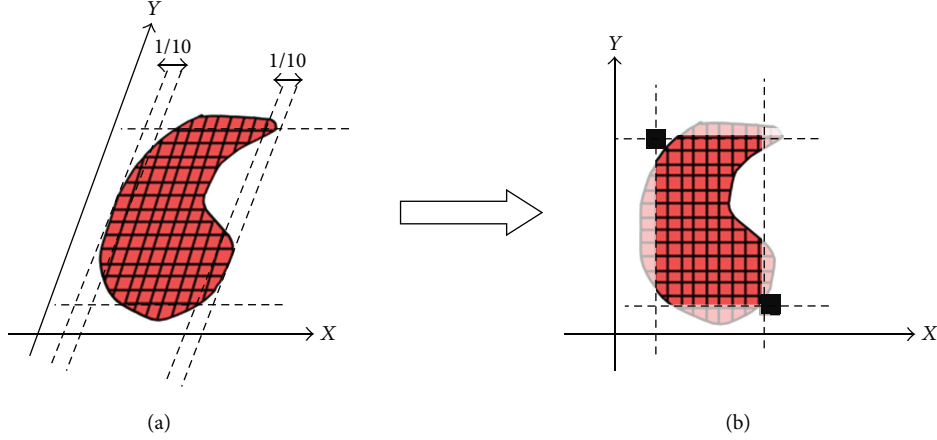


FIGURE 3: Set the top left and bottom right coordinate to limit the diaphragm area.

The matrix dimension of diaphragm motion after normalization is $W_{\text{ref}} \times H_{\text{ref}} \times 20$ or equals to $60 \times 100 \times 20$ (spatial size of reference image $\times 20$ frames) for each side of diaphragm. To ensure that the diaphragm motion is represented as a whole diaphragm and keeping the shape variance, we merge the right and left sides of diaphragm into a matrix. The final matrix dimension after the merging is $60 \times 200 \times 20$. Considering the data as high-dimensional data, linear statistical analysis is possible to be carried out by applying principal component analysis (PCA). It reduces the data set and reveals the hidden pattern as maintaining the majority of the variation in the original data.

The upper part of Figure 3 shows the spatial normalization process of certain frame. After modeling using PCA, we reverse the image into the original diaphragm shape. Firstly, we create a mask based on the original diaphragm shape. Using this mask, the modeled image is then resized and reshaped to the original diaphragm shape. The bottom part of Figure 3 shows the reversing process from a frame modeled by PCA to a diaphragm shape image.

2.3. PCA and GND-PCA Diaphragm Motion Model. Generally, PCA is a statistical method to transform a set of correlated variables into a smaller number of uncorrelated variables or principal components (PCs). The PCs are sorted in a descending order of importance. The purpose of PCA is that the first few PCs are able to explain large proportion of the variation in the original variables, and only those PCs are retained for further analysis.

The following paragraphs describe how PCA is used to analyze diaphragm motion. Let \mathbf{z} be a vector of z value of the spatiotemporally normalized for both right and left diaphragm. Vector \mathbf{z} can be expressed as 1D array:

$$\mathbf{z} = [z_1, z_2, z_3, \dots, z_N]^T, \quad (4)$$

where

$$z_i = Z(x, y, t) \quad (5)$$

and i is the index obtained by the following equation:

$$i = (t - 1) H_{\text{ref}} W_{\text{ref}} + (y - 1) H_{\text{ref}} + x. \quad (6)$$

For m subjects, we denote $\mathbf{z}^{(j)}$ ($j = 1, 2, 3, \dots, m$) as a diaphragm motion data set from j th subject.

Principal components are the eigenvectors with its corresponding eigenvalues of covariance matrix of \mathbf{z} . The sorted eigenvectors by decreasing order of its corresponding eigenvalues is the most optimal with respect to information loss.

Another method to build a statistical method is GND-PCA. It is a method to model a series of multidimensional array proposed by McQuaid et al. [14]. Instead of using one long vector to represent a motion model, GND-PCA uses a tensor to represent a shape or motion model. The tensor itself is a multidimensional array whose order is the number of dimensions, also known as ways or modes. We will give a brief explanation of GND-PCA. More details about GND-PCA can be read in [14].

An N th-order tensor, denoted by \mathcal{A} , where $\mathcal{A} \in R^{I_1 \times I_2 \times I_3 \times \dots \times I_n}$ and R^n denotes the set of all vectors with n real components. In tensor point of view, a vector and a matrix are a tensor of order one and order two, respectively. One diaphragm motion can be considered as third-order tensor \mathcal{M} , where $\mathcal{M} \in R^{I_1 \times I_2 \times I_3}$ ($I_1 \times I_2$ is the spatial dimension of the diaphragm in each frame and I_3 is the number of frame).

Here, let \mathcal{M}_i ($i = 1, 2, 3, \dots, m$) denote m samples of third-order tensor that represents diaphragm motion from m subjects. A series of lower rank tensors $\mathcal{M}_i^* \in R^{J_1 \times J_2 \times J_3}$ is defined as the most accurate approximation of original tensors \mathcal{M}_i , where $J_1 < I_1$, $J_2 < I_2$ and $J_3 < I_3$. To obtain \mathcal{M}_i^* , we decompose the tensors into smaller core tensors, and their corresponding orthogonal mode matrices are shown by:

$$\mathcal{M}_i^* = \mathcal{C}_i \times_1 \mathbf{Y} \times_2 \mathbf{X} \times_3 \mathbf{T}. \quad (7)$$

The product $\times_n \mathbf{X}$ denotes the n -mode product between the tensor and the mode matrices [14]. Figure 4 shows the illustration of 3rd-order tensor decomposition of diaphragm motion model.

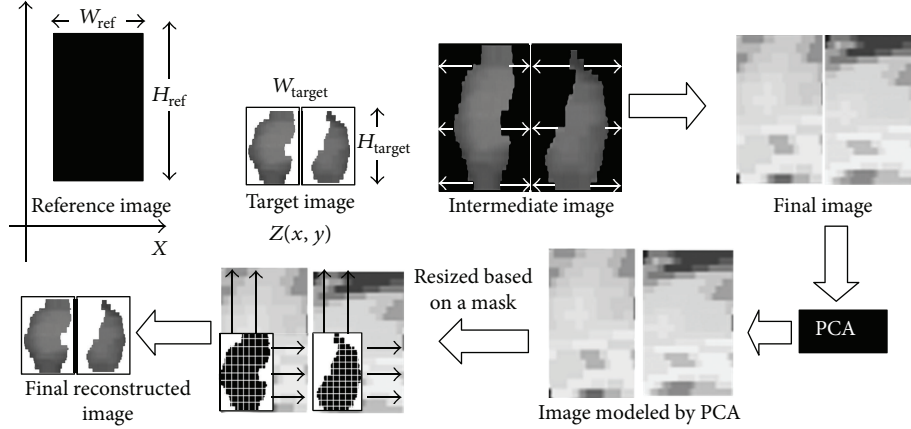


FIGURE 4: Diagram of spatial normalization and its reconstruction process to obtain diaphragm original shape.

The orthogonal mode matrices capture the variation along the spatial ($\mathbf{Y} \in R^{I_1 \times J_1}$ and $\mathbf{X} \in R^{I_2 \times J_2}$) and time ($\mathbf{T} \in R^{I_3 \times J_3}$) dimension. The core tensors ($\mathcal{C}_i \in R^{I_1 \times J_2 \times J_3}$) control the interaction between mode matrices and can be seen as the compressed version of the original tensor. The mode matrices can be obtained by solving the following equation:

$$\min \|\mathcal{M}_i - \mathcal{M}_i^*\| = \min \|\mathcal{M}_i - \mathcal{C}_i \times_1 \mathbf{Y} \times_2 \mathbf{X} \times_3 \mathbf{T}\|. \quad (8)$$

2.4. Evaluation Methods. In this study, we evaluate the performance of the diaphragm motion model by calculating the mean and maximum errors of the constructed model. Leave-one-out method is used for this evaluation [15].

The error of approximated model from each subject can be obtained by simply subtracting each of the elements of constructed model from the original shape and getting the absolute value. The error of right and left diaphragm shapes of j th subject can be mathematically written as

$$e^{(j)}(x, y, t) = |\hat{z}^j(x, y, t) - z^{(j)}(x, y, t)|. \quad (9)$$

Here, we redefined the shape of normalized diaphragm by $z^{(j)}(x, y, t)$. We also represent the estimate by the statistical model by $\hat{z}^{(j)}(x, y, t)$.

Based on this definition of error, some kinds of mean or maximum error can be expressed. For instance, mean error of each subject is given by

$$e_{\text{mean}}^{(j)} = \frac{1}{n^{(j)}T} \sum_{t=1}^T \sum_{x,y \in \Omega^{(j)}} e_k^{(j)}(x, y, t), \quad (10)$$

where $n^{(j)}$ is the number of nonzero values in the diaphragm area $\Omega^{(j)}$ of j th subject. Intersubject average of $e_{k,\text{mean}}^{(j)}$ is given by:

$$e_{\text{mean}} = \frac{1}{m} \sum_{j=1}^m e_{\text{mean}}^{(j)}. \quad (11)$$

The maximum error for j th subject is given by

$$e_{\text{max}}^{(j)} = \max(e^{(j)}(x, y, t)). \quad (12)$$

We can also calculate the intersubject average of maximum error by

$$e_{\text{max}} = \frac{1}{m} \sum_{j=1}^m e_{\text{max}}^{(j)}. \quad (13)$$

Another evaluation method we used is frame-by-frame error calculation. Frame-by-frame error is important to analyze which respiratory phase gives the largest or smallest error. Frame-by-frame mean error of each subject is given by

$$e^{(j)}(t) = \frac{1}{n^{(j)}} \sum_{x,y} e^{(j)}(x, y, t). \quad (14)$$

Intersubject average of frame-by-frame error is given by

$$e(t) = \frac{1}{m} \sum_{j=1}^m e^{(j)}(t). \quad (15)$$

3. Experimental Results

Ten healthy subjects within the age ranging from 23 to 46 participated in this study. For diaphragm motion studies, MR images are particularly preferred than CT images since MR images provide high soft tissue contrast to produce detailed respiratory organs. The high contrast of MR images will be useful during the manual diaphragm boundary segmentation process.

In this study, MR Images were acquired using 1.5 T INTERA ACHIVA nova-dual (Philips Medical Systems) whole-body scanner with a 16ch SENSE TORSO XL Coil. A 2D balanced FFE sequence was used. The imaging parameters are as follows: SENSE factor: 2.2, flip angle: 45° , TR: 2.2 ms, TE: 0.9 ms, FOV: 384 mm, in-plane resolution 256×256 pixels and $1.5 \times 1.5 \text{ mm}^2$, slice thickness: 7.5 mm, slice gap = 6.0 mm, and scan time: 150 ms/frame and 400 frame/slice. Normal breathing was instructed for all subjects during the acquisition process. This image acquisition experiment was conducted under an approval of Ethical Review Board of Chiba University.

The software used for PCA is MATLAB 7.10 and running on PC with Intel Core 2 Quad, 2.66 GHz, 16 GB RAM.

TABLE 1: Percent variations and cumulative contribution up to three principal components of 10 healthy subjects.

PC	%	Cum. %
1	97.4	97.4
2	1.1	98.5
3	0.7	99.2

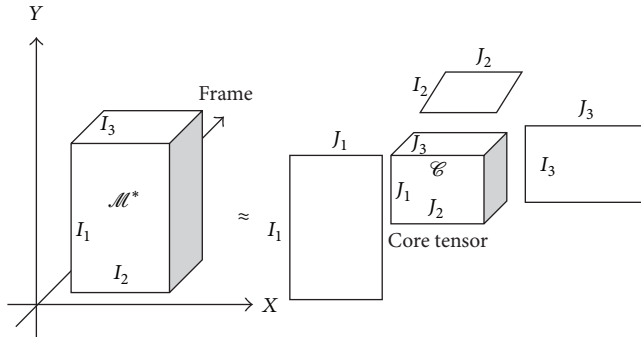


FIGURE 5: Decomposition of 3rd-order tensor into one core tensor and three mode matrices.

3.1. PCA and GND-PCA Model Output. The contribution ratio and cumulative up to three principal components of right and left diaphragm motion are listed in Table 1. The percentage of variance of first principal component is 97.4% and 99.2% for the first three principal components.

Mapping the error of z coordinates in the constructed model using different number of PCs will be useful for further analysis. Figures 5 and 6 illustrate color mapping of the error in the first frame of the first subject given by

$$e^{(1)}(x, y, 1) = \hat{z}^{(1)}(x, y, 1) - z^{(1)}(x, y, 1). \quad (16)$$

Note that the error is not an absolute value as expressed in (9).

The white area represents the exact approximation, red and blue areas indicate that estimated z coordinates are higher and lower than the actual position, respectively.

Figure 6 is the case when first one, first two, and first three PCs are used in regular PCA, respectively. As shown in Figure 6(c), the red and blue areas are decreasing. This indicates that the model well approximated the actual shape when the first three PCs were used.

The similar results are also shown by GND-PCA construction as illustrated in Figure 7. The error color mappings were obtained by reconstructing the model with $4 \times 2 \times 1$, $8 \times 4 \times 2$, $16 \times 8 \times 4$, $32 \times 16 \times 8$, and $64 \times 32 \times 16$ core tensors respectively and subtracting them from the original shape of diaphragm. The last three core tensors showed that the red and blue colors on the diaphragm area almost disappeared, which means the constructed models are very similar to the original shape.

In term of number of coefficients required to construct the model, regular PCA outperformed the GND-PCA. Table 2 shows the comparison of the number of coefficients

TABLE 2: Comparison of the number of coefficients required to construct diaphragm motion model.

PC	Regular PCA		GND-PCA	
	Coef.	Core tensor	Coef.	Core tensor
First PC	1	$4 \times 2 \times 1$	8	$4 \times 2 \times 1$
First two PCs	2	$8 \times 4 \times 2$	64	$8 \times 4 \times 2$
First three PCs	3	$16 \times 8 \times 4$	512	$16 \times 8 \times 4$

required to construct diaphragm motion model between regular PCA and GND-PCA.

3.2. Leave-One-Out Method Validation. We omitted one subject as a testing subject and constructed the diaphragm motion model using training data from the remaining nine subjects. This model was then applied to the testing subject. The mean error of the testing subject was calculated using (10). The whole procedure is repeated till each of ten subjects has become testing subject once.

Figure 8(a) shows the mean error of each subject in case of model using regular PCA and GND-PCA, respectively. For regular PCA model, the mean error ranges are 3.8–13.4 mm for first PC, 3.6–10.2 mm for first two PCs, and 3.5–10.6 mm for first three PCs. Although more than 98% variability of the diaphragm motion can be covered by the first three PCs as shown in Table 1, the validation using leave-one-out method showed that intersubjecting the average of mean error of the model given by (11) is more than 4 mm.

Contrary to the regular PCA, the error mean of model by GND-PCA as shown in Figure 8(b) is much smaller. The mean error ranges are 1.4–9.0 mm for $4 \times 2 \times 1$ core tensor, 1.4–4.0 mm for $8 \times 4 \times 2$ core tensor, and 0.8–2.1 mm for $16 \times 8 \times 4$ core tensor.

Figure 9 showed frame-by-frame mean error $e(t)$ of the model by regular PCA. As shown in this figure, 18–20th frames indicate low mean error (about 3.9 mm on average) and 9–11th frames indicate high mean error (about 9.0 mm on average). It is probably caused by the smaller variability in the 18–20th frames and higher variability in 9–12th frames.

Different results were obtained using GND-PCA as shown in Figure 10. Since GND-PCA can capture both spatial and time variability; there were no large differences of mean error among the frames. For instance, the standard deviation of mean error from $16 \times 8 \times 4$ core tensors is 0.37 mm, while for three principal components of regular PCA the mean error is 2.2 mm.

Tables 2 and 3 summarize the average of mean error e_{mean} and average of maximum error e_{max} . The results of GND-PCA showed consistent reconstruction with smaller error compared with the model constructed using regular PCA.

4. Discussion

In this paper, we described how to build a statistical model of diaphragm motion using PCA and GND-PCA. The model was obtained from 4D MRI that reconstructed from time sequential images of thoracic 2D MRI of ten healthy subjects.

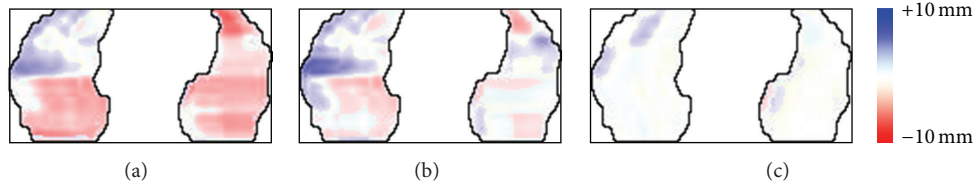


FIGURE 6: Regular PCA Error position mapping of one frame using (a) first PC, (b) first two PCs, and (c) first three PCs.

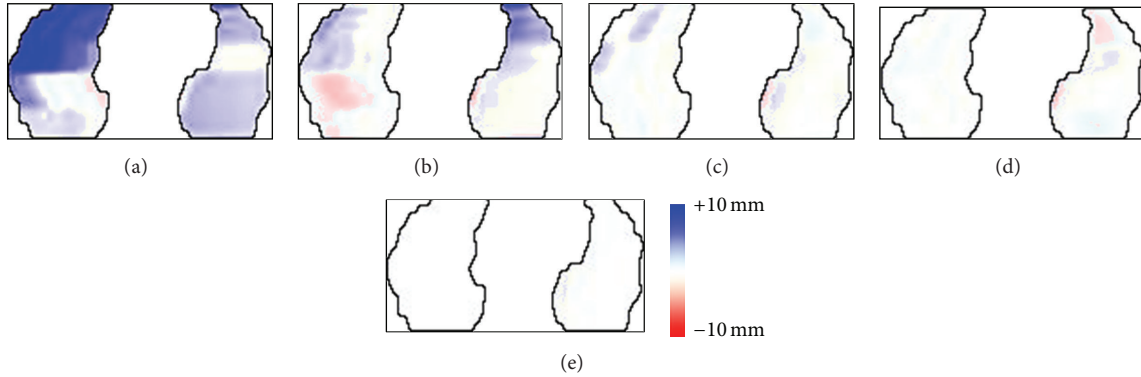


FIGURE 7: GND-PCA error position mapping of one frame using (a) $4 \times 2 \times 1$, (b) $8 \times 4 \times 2$, (c) $16 \times 8 \times 4$, (d) $32 \times 16 \times 8$, and (e) $64 \times 32 \times 16$, core tensors.

TABLE 3: Leave-one-out method validation using regular PCA: mean and average of maximum error position (in mm).

Used PC	Regular PCA		GND-PCA	
	Mean	Max	Mean	Max
1st PC	9.2	15.7	5.5	13.5
1st + 2nd PCs	6.5	17.3	2.4	8.1
1st-3rd PCs	6.3	17.2	1.3	5.5

The modeling process involves manual segmentation of diaphragm boundary, automatic motion tracking based on the intersection profile method [3], constructing region of interest for right and left areas of diaphragm, and normalization of diaphragm shape.

The developed model using regular PCA can accurately describe more than 98% of the total variation by including the first three PCs. This indicates that most of the diaphragm motion variability is adequately described using a few number of parameters. Consequently, the description and motion of the diaphragm are greatly simplified by this model.

Leave-one-out validation was employed to evaluate the performance of the model. As shown in Table 2, the results of regular PCA illustrated that mean error position of both sides of diaphragm was more than 6.0 mm, which considered as significant error.

To build a better statistical modeling, we applied GND-PCA [14]. Differing from regular PCA, GND-PCA is not necessarily unfolding the diaphragm motion model into one long vector. Instead, it decomposes the model into a core tensor and several mode matrices for dimensionality reduction. The mode matrices can represent the principal axes of variation. Several numbers of core tensors are chosen

to construct the motion model. The smallest size of core tensor is $4 \times 2 \times 1$ which is able to construct the motion model under leave-one-out validation with mean error of 5.5 mm. Among the three sizes of core tensor ($4 \times 2 \times 1$, $8 \times 4 \times 2$, and $16 \times 8 \times 4$); the best model construction is achieved by $16 \times 8 \times 4$ core tensor which gives mean error of 1.3 mm. The maximum error is also significantly reduced to 5.6 mm. Compared with regular PCA using first three PCs, the results of GND-PCA showed significant improvement to the motion model. Mean error obtained from frame-by-frame analysis shown in Figure 10 also confirmed that GND-PCA is able to capture the motion variability of the diaphragm. One of the major drawbacks of GND-PCA is that it requires more coefficients to construct the model compared with regular PCA.

There are some considerations regarding the diaphragm motion model in this study. The first is the resolution of MR images used in this study limits the motion model for being used in the clinical application such as radiotherapy planning. At this stage, our main focus is to demonstrate that GND-PCA can model the diaphragm motion with smaller number of sample data compared with regular PCA. The model cannot be applied for the clinical application due to the low MR image resolution. Higher resolution of MR image is required if one needs to apply the model for a clinical application.

Second is about shape modeling approach. In this study, we used simple spatial and temporal normalization. Although this simple normalization is sufficient to show the efficacy of GND-PCA compared with regular PCA, the use of other spatial normalization techniques such as active point distribution model [16] or nonrigid registration [17] such as thin-plate splines or cubic B-splines will provide a better

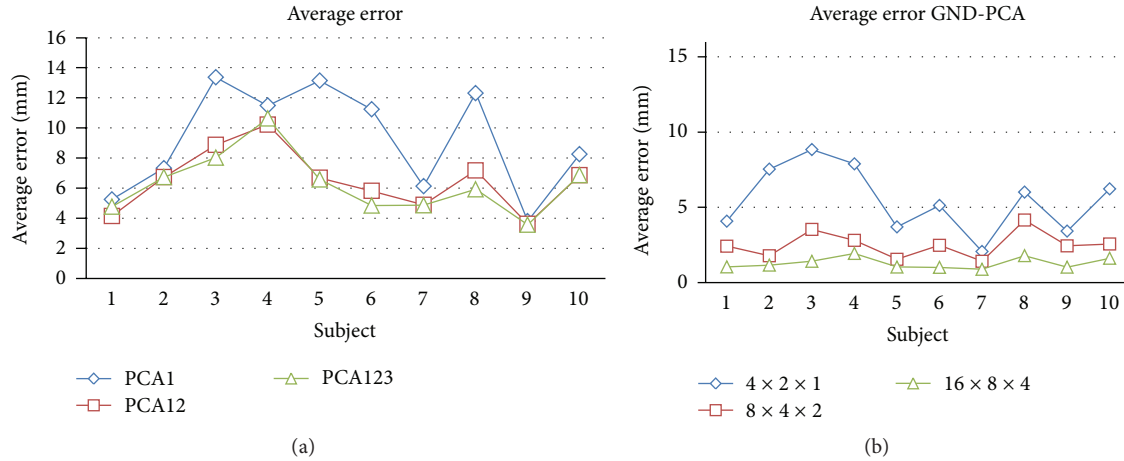


FIGURE 8: The mean error of the model by (a) regular PCA from and (b) GND-PCA. The measurement unit is in mm.

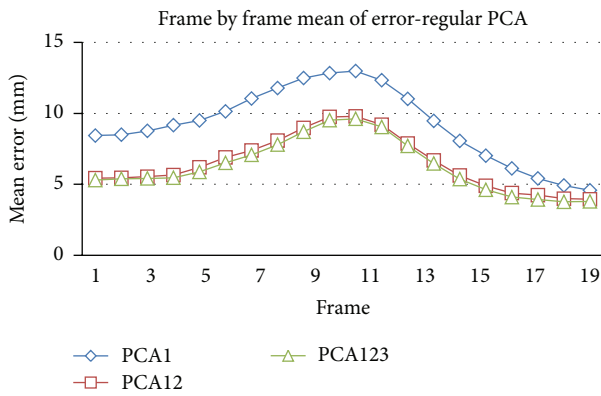


FIGURE 9: Regular PCA mean of error frame-by-frame.

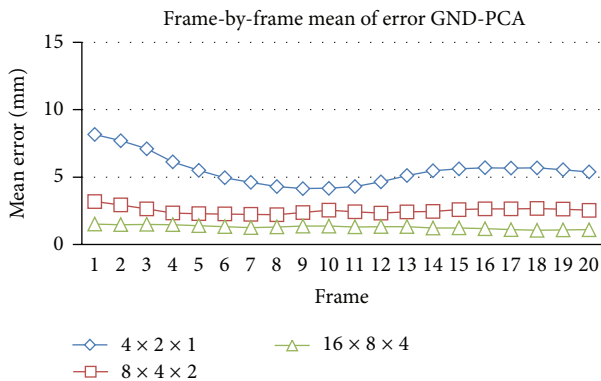


FIGURE 10: GND-PCA mean of error frame-by-frame.

diaphragm motion modeling. We will consider this issue in our future works.

Other consideration is that the manual segmentation of diaphragm area can affect the final results. Manual segmentation of diaphragm boundary is very subjective to the experience of the user. Hence, the variability of the diaphragm motion may change when the diaphragm area is resegmented. An automatic statistical shape model of diaphragm area from

thoracic 2D MRI is needed to be developed for further work. Although the proposed method in [15] can be used to develop a statistical shape model of diaphragm, it is suited only for respiratory-gated CT data sets. Several adjustments need to be done to apply the method to thoracic 2D MRI.

5. Conclusion

We have developed a statistical method to model diaphragm motion using PCA. Time-sequential 2D MRI was constructed from a 4D MRI and extracted to obtain a 3D diaphragm motion model. Regular PCA and GND-PCA were then applied to construct model. In the experiment, we investigated that three eigenvectors or PCs with the largest eigenvalues are sufficient to accurately describe diaphragm motion model from ten healthy subjects. Model validation using leave-one-out showed that GND-PCA gives more stable reconstruction compared with regular PCA. This concludes that GND-PCA can model the motion better with a small number of sample data. Further works to be done include automatic segmentation of diaphragm area and investigation of compactness, generality, and specificity of the model.

Acknowledgments

This work was supported in part by Grant-in-Aid for Scientific Research on Innovative Areas (No. 22103504 and No. 24103703), Computational Anatomy, from the MEXT, Japan.

References

- [1] M. von Siebenthal, G. Székely, U. Gamper, P. Boesiger, A. Lomax, and P. Cattin, "4D MR imaging of respiratory organ motion and its variability," *Physics in Medicine and Biology*, vol. 52, pp. 1547–1564, 2007.
- [2] J. Tokuda, S. Morikawa, H. A. Haque et al., "Adaptive 4D MR imaging using navigator-based respiratory signal for MRI-guided therapy," *Magnetic Resonance in Medicine*, vol. 59, no. 5, pp. 1051–1061, 2008.

- [3] Y. Masuda and H. Haneishi, "4D MR imaging of respiratory organ motion using intersection profile method," in *Medical Imaging: Visualization, Image-Guided Procedures, and Modeling*, vol. 7625 of *Proceedings of SPIE*, 2010.
- [4] R. Werner, J. Ehrhardt, T. Frenzel et al., "Motion artifact reducing reconstruction of 4D CT image data for the analysis of respiratory dynamics," *Methods of Information in Medicine*, vol. 46, pp. 254–260, 2007.
- [5] R. Werner, J. Ehrhardt, R. Schmidt, and H. Handels, "Modeling respiratory lung motion—a biophysical approach using finite element methods," in *Medical Imaging: Physiology, Function, and Structure from Medical Images*, vol. 9616 of *Proceedings of SPIE*, February 2008.
- [6] J. R. McClelland, J. M. Blackall, S. Tarte et al., "A continuous 4D motion model from multiple respiratory cycles for use in lung radiotherapy," *Medical Physics*, vol. 33, no. 9, pp. 3348–3358, 2006.
- [7] M. Georg, R. Souvenir, A. Hope, and R. Pless, "Manifold learning for 4D CT reconstruction of the lung," in *Proceedings of the IEEE Computer Society Conference on Computer Vision and Pattern Recognition Workshops (CVPR '08)*, pp. 1–8, June 2008.
- [8] M. Lyksborg, R. Paulsen, C. Brink, and R. Larsen, "4D lung reconstruction with phase optimization," in *Proceedings of the World Congress on Medical Physics and Biomedical Engineering*, pp. 2227–2230, September 2009.
- [9] R. Li, J. H. Lewis, X. Jia et al., "PCA-based lung motion model," in *Proceedings of the 16th International Conference on the Use of Computers in Radiation Therapy*, Amsterdam, The Netherlands, 2010.
- [10] T. Klinder, C. Lorenz, and J. Ostermann, "Free-breathing intra- and intersubject respiratory motion capturing, modeling, and prediction," in *Proceedings of the Medical Imaging: Image Processing*, vol. 7259 of *Proceedings of SPIE*, p. 72590T, February 2009.
- [11] A. P. King, C. Buerger, and T. Schaeffter, "Cardiac respiratory motion modelling by simultaneous registration and modelling from dynamic MRI images," in *Biomedical Image Registration: 4th International Workshop*, pp. 222–233, 2010.
- [12] W. Wein, J. Cheng, and A. Khamene, "Ultrasound based respiratory motion compensation in the abdomen," in *Proceedings of the Workshop on Image Guidance and Computer Assistance for Soft-Tissue Interventions (MICCAI '08)*, vol. 32, 2008.
- [13] R. Xu and Y. W. Chen, "Generalized N-dimensional principal component analysis (GND-PCA) and its application on construction of statistical appearance models for medical volumes with fewer samples," *Neurocomputing*, vol. 72, no. 10–12, pp. 2276–2287, 2009.
- [14] S. J. McQuaid, T. Lambrou, V. J. Cunningham, V. Bettinardi, M. C. Gilardi, and B. F. Hutton, "The application of a statistical shape model to diaphragm tracking in respiratory-gated cardiac PET images," *Proceedings of the IEEE*, vol. 97, no. 12, pp. 2039–2052, 2009.
- [15] S. J. Martin, J. Dey, M. A. King, and B. F. Hutton, "Segmenting and tracking diaphragm and heart regions in gated-CT datasets as an aid to developing a predictive model for respiratory motion-correction," in *Proceedings of the IEEE Nuclear Science Symposium and Medical Imaging Conference*, pp. 2680–2685, November 2007.
- [16] T. F. Cootes, C. J. Taylor, D. H. Cooper, and J. Graham, "Active shape models—their training and application," *Computer Vision and Image Understanding*, vol. 61, no. 1, pp. 38–59, 1995.
- [17] Z. Qiu, H. Tang, and D. Tian, "Non-rigid medical image registration based on the thin-plate spline algorithm," in *Proceedings of the WRI World Congress on Computer Science and Information Engineering (CSIE '09)*, vol. 2, pp. 522–527, April 2009.

Research Article

Construction of Classifier Based on MPCA and QSA and Its Application on Classification of Pancreatic Diseases

Huiyan Jiang,^{1,2} Di Zhao,¹ Tianjiao Feng,¹ Shiyang Liao,¹ and Yenwei Chen³

¹ Software College, Northeastern University, Shenyang 110819, China

² Key Laboratory of Medical Image Computing of Ministry of Education, Shenyang 110819, China

³ Department of Information Science and Engineering, Ritsumeikan University, Shiga 525-8577, Japan

Correspondence should be addressed to Huiyan Jiang; hyjiang@mail.neu.edu.cn

Received 18 January 2013; Revised 29 April 2013; Accepted 1 May 2013

Academic Editor: Younghae Do

Copyright © 2013 Huiyan Jiang et al. This is an open access article distributed under the Creative Commons Attribution License, which permits unrestricted use, distribution, and reproduction in any medium, provided the original work is properly cited.

A novel method is proposed to establish the classifier which can classify the pancreatic images into normal or abnormal. Firstly, the brightness feature is used to construct high-order tensors, then using multilinear principal component analysis (MPCA) extracts the eigentensors, and finally, the classifier is constructed based on support vector machine (SVM) and the classifier parameters are optimized with quantum simulated annealing algorithm (QSA). In order to verify the effectiveness of the proposed algorithm, the normal SVM method has been chosen as comparing algorithm. The experimental results show that the proposed method can effectively extract the eigenfeatures and improve the classification accuracy of pancreatic images.

1. Introduction

Pancreatic carcinoma is a frequent digestive tract tumor. The malignant degree of this kind of cancer is always very high, and it is difficult to be early diagnosed and treated. Due to the fact that pancreatic carcinoma is often diagnosed when it is advanced, very few pancreatic tumors can be removed by operation. As we know, many famous people died of this disease. So, it is necessary to diagnose pancreatic carcinoma as early as possible. Computer-aided diagnosis (CAD) [1] technology was established with the development of image-processing technology and pattern recognition technology. Researching of CAD technology shows that CAD can provide advisory opinions for the doctor and help to improve the diagnostic rate. With the development of medical imaging, it is important to represent the pancreas by a model and it is also important to try to distinguish different appearance of pancreas.

Tensors are geometrical quantity that is used to describe linear relations among vectors, scalars, and other tensors. In this paper, the pancreas CT images can be treated as several third-order tensors, and then we extract the feature to gain the eigentensors for classification.

Principal component analysis (PCA) [2] is a famous method used in the recognition of subspace, which is one of the classical methods based on statistical feature. The core idea of PCA is to reduce the dimensionality of a dataset that consisted of a larger number of interrelated variables and, in the meantime, try to retain the variation in the original dataset as much as possible [3]. But this method has two problems.

- (1) Basic using of PCA to transfer tensor objects to high-dimension vector (vectorization) obviously results in high cost of processing and memory in next step [4]. For example, if there is a gray image (640×640), the vector which the image transfers to will be 409600×1 .
- (2) In using PCA, reshaping breaks the natural structure and correlation in the original data [4], which may affect the subsequent operation and lead to bad results.

In order to solve these problems, this paper uses multilinear principal component analysis (MPCA) referred to in [4]. MPCA follows the classical PCA paradigm and multilinear algorithm, to ensure the fact that it is able to reduce all the tensor dimensionality and that it is also able to get more

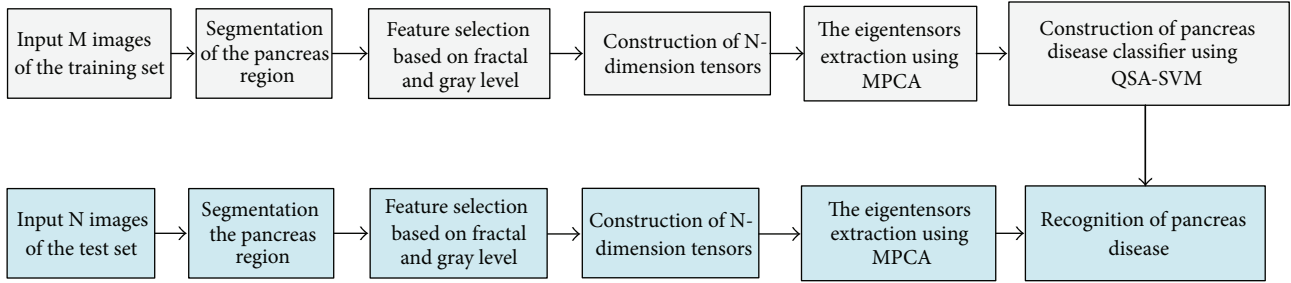


FIGURE 1: The main flow of the proposed method.

variational forms among the original tensors with tensorial mapping to keep original structure and correlation [4].

Support vector machine (SVM) [5] is commonly used to train a classifier. The main factor to affect the classification performance is the parameters used in SVM. Recently, there are many algorithms for SVM parameters optimization, such as ant colony (ACO) algorithm [6], simulated annealing (SA) algorithm, genetic algorithm (GA) [7], and quantum genetic algorithm (QGA) [8, 9]. SA is a generic probabilistic algorithm, which is good at locating the optimal solution of the variable in a large search space. The advantages of SA are described as follows.

- (1) The objective function can be nonlinear, discontinuous, and random.
- (2) The objective function can have any boundary conditions and constraints.
- (3) The programming workload of SA is low, so that it is easy to be implemented.
- (4) In statistics, we can find the optimal solutions.

But there are also some problems of SA. For example, rapid cooling can lead to simulation hardening which cannot be ensured to find the optimal solution. Quantum evolution algorithm (QEA) [10] is also a probability optimization algorithm. QEA has good searching ability for low dimensional functions. However, it is not good for high dimensional functions. Therefore, in this paper, we use quantum simulated annealing algorithm (QSA) [11], which is the combination of SA and QEA, to optimize SVM parameters for training classifier of pancreatic diseases. This paper is organized as follows. Section 2 introduces the proposed method; firstly, we will explain the construction of high-order tensor, then we briefly introduce the method of MPCA for feature extraction, and finally we introduce the support vector machine of quantum simulated annealing algorithm optimization (QSA-SVM) for classification. Section 3 presents the construction of pancreas images after MPCA and the results of classification, and we discuss the future of clinical implications of the results. In Section 4, we conclude the works in this paper.

2. Materials and Method

In this section, firstly we will introduce the whole procedure of the proposed method, which is shown in Figure 1, and then we give a detailed explanation of each process.

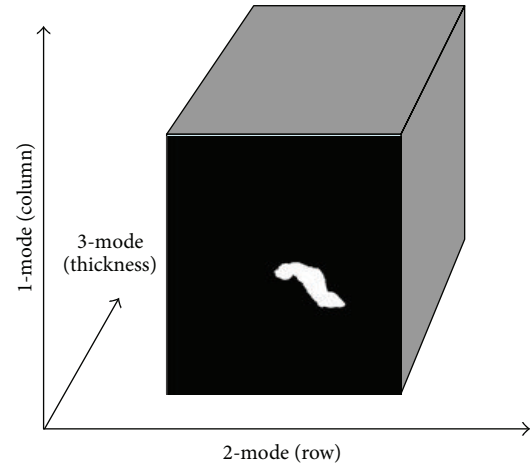


FIGURE 2: Illustration of the pancreatic CT image as a third-order tensor.

The process of the proposed method is as follows.

- (1) Image preprocessing: first, we segment the CT images of abdomen to gain the pancreas region of image, and then we normalized the images after segmentation.
- (2) High-order tensors construction: at first, we collect a group of pancreatic images and then combine them into a new dataset.
- (3) The feature extraction: in this paper, we use the method of MPCA to extract the eigentensors for classification.
- (4) Pancreas diseases classification based on QSA-SVM: after we obtain the eigentensors by MPCA, we can treat the eigentensors as samples, and then we use the approach of SVM optimized by QSA to classify pancreas diseases.

2.1. Construction of Tensors. We treat the segmented pancreatic CT images as several third-order tensors with the column, row, and thickness modes. In this paper, we treat each CT image as one data sample. Hence, the input is several third-order tensors and the spatial column space, row space, and the thickness space were regarded as its three modes, as shown in Figure 2.

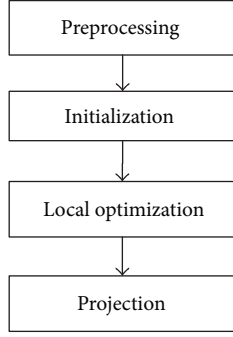
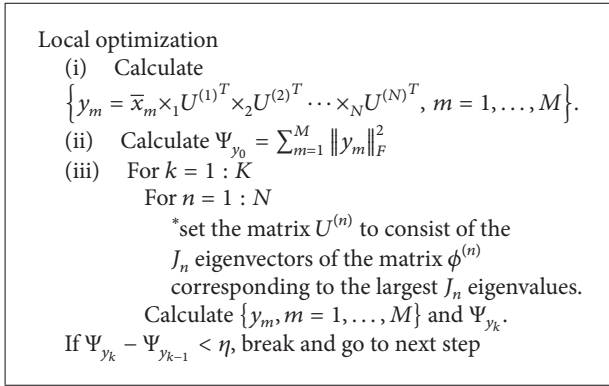


FIGURE 3: The flow of MPCA algorithm.



PSEUDOCODE 1: Pseudocode of the local optimization.

The size of each image is standard 128×128 ; the thickness of the CT image is 2.77 mm. Before providing the samples to MPCA, the tensorial inputs need to be normalized to the same dimension in each mode, so the three modes of the tensor are normalized by default, and we can consider one sample as $A \in R^{I_1 \times I_2 \times D_3}$.

2.2. Feature Extraction Based on MPCA. In this paper, an MPCA [4] solution to the problem of dimensionality reduction for tensor objects is introduced; its research and analysis are also included. First we provided a series of zero-mean value N -order tensor $x_m \in R^{I_1 \times I_2 \times \dots \times I_N}$, we need to gain a group of new N -order tensor, $y_m \in R^{J_1 \times J_2 \times \dots \times J_N}$ ($J_n < I_n$), that needs to be closed to the original tensor as much as possible. The procedure of MPCA algorithm is shown in Figure 3.

In the preprocessing phase, we center the input original tensors x_m as $\bar{x}_m = x_m - \bar{x}$, $m = 1, \dots, M$, where M is the number of the samples, and the tensor mean can be described as follows:

$$\bar{x} = \frac{1}{M} \sum_{m=1}^M x_m. \quad (1)$$

In the initialization phase, we calculate the eigendecomposition of $\phi^{(n)*} = \sum_{m=1}^M \bar{x}_{m(n)} \cdot \bar{x}_{m(n)}^T$ and set the n th mapping matrix $U^{(n)}$ which consists of the eigenvectors corresponding to the most significant J_n eigenvalues, for $n = 1, \dots, N$ ($N = 3$).

In the local optimization phase, we will focus on doing the local optimization to obtain the new N -order tensors y_m ; the detailed method of the optimization is given in [4] and the pseudocode of the method is shown as Pseudocode 1. In the pseudocode, Ψ_y is the total tensor scatter of $y_m, m = 1, \dots, M$, M is the number of the samples, and $\phi^{(n)}$ can be defined as (2). In (2), $\bar{U}_{\phi^{(n)}}$ is the mean mapping matrix of $\phi^{(n-1)}$:

$$\phi^{(n)} = \sum_{m=1}^M Z_{(n)} \cdot \bar{U}_{\phi^{(n)}} \cdot \bar{U}_{\phi^{(n)}}^T \cdot Z_{(n)}^T, \quad (2)$$

$$Z_{(n)} = X_{m(n)} - \bar{X}_{(n)},$$

$$\bar{U}_{\phi^{(n)}} = \left(\bar{U}^{(n+1)} \otimes \dots \otimes \bar{U}^{(n+N)} \otimes \bar{U}^{(1)} \otimes \dots \otimes \bar{U}^{(n-1)} \right).$$

In the projection phase, we project the centralized eigentensors \bar{x}_m using the n th mapping matrix $U^{(n)}$ obtained by the local optimization phase to get the new eigentensors y_m . It is shown as follows:

$$y_m = \bar{x}_m \times_1 U^{(1)T} \times_2 U^{(2)T} \dots \times_N U^{(N)T}, \quad m = 1, \dots, M. \quad (3)$$

We used the eigenvector y_m^* projected by the eigentensors y_m for classification [4].

2.3. Construction of the Classifier

2.3.1. Concept of Quantum Bit and Quantum Gate. The term quantum comes from quantum mechanics. Quantum, which is the general name of all microscopic particles in the microscopic world, is different from the macroscopic object. Its movements obey the statistical law, not the deterministic law. Compared with the classical computing using 0 and 1 to represent information, the quantum computing uses $|0\rangle, |1\rangle$ and their superposition state to represent information. The superposition state is as follows:

$$|\varphi\rangle = \alpha |0\rangle + \beta |1\rangle, \quad \text{s.t. } \alpha^2 + \beta^2 = 1. \quad (4)$$

The measurement of quantum state can cause the collapse of quantum state, so that the final state can be confirmed. The relationship of quantum state, superposition state, and the collapse caused by measurement is shown in Figure 4.

In the quantum computing, the quantum state changes when we have a series of unitary transformations on it. The equipment (a unitary matrix) is called quantum gate which is as follows:

$$\begin{bmatrix} \cos \theta & -\sin \theta \\ \sin \theta & \cos \theta \end{bmatrix}. \quad (5)$$

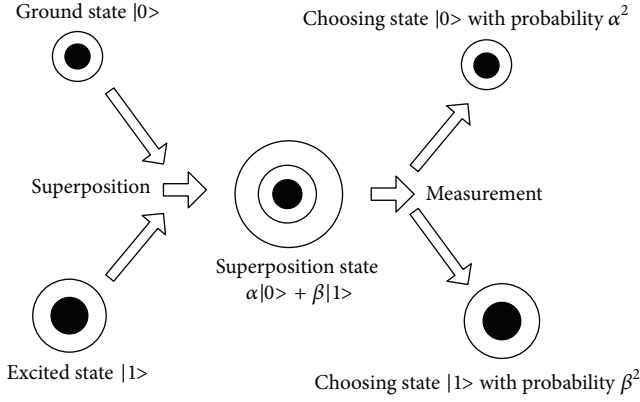


FIGURE 4: The relationship of the three states.

We exchange two probability amplitudes of a quantum bit by the quantum gate as follows

$$\begin{bmatrix} 0 & 1 \\ 1 & 0 \end{bmatrix} \begin{bmatrix} \alpha \\ \beta \end{bmatrix} = \begin{bmatrix} \beta \\ \alpha \end{bmatrix}. \quad (6)$$

2.3.2. Construction of the Classifier Based on QSA. We use SVM to train the classifier. SVM can be used to solve some problems, such as the small number of samples, nonlinear, high dimension pattern recognition, and local minimum point, but if the selection of the kernel function parameters, penalty factor C , or other parameters is not reasonable, the SVM prediction accuracy will be greatly reduced in classification process.

In this paper, QSA is used for optimizing the SVM parameters, penalty factor C , and the parameter of RBF γ .

We assume that there are m chromosomes in the population and n quantum bits in a chromosome. In QSA, the two probability amplitudes of the quantum bit are treated as the chromosome gene. In the fixed population scale, it can make the search space double, so that the convergence speed will be fast. In fact, the optimal solution is embodied in the optimal probability amplitude of the quantum bit of the optimal chromosome. We assume that the optimal probability amplitude is $(\cos \varphi_1, \cos \varphi_2, \dots, \cos \varphi_n)$, when another chromosome has the quantum bits $(\pi/2 - \varphi_1, \pi/2 - \varphi_2, \dots, \pi/2 - \varphi_n)$, the sine item of this chromosome also has the optimal solution.

In the following description, we set that Φ_i is the i th chromosome in the population, θ_{ij} is the phase, $1 \leq i \leq m$, $1 \leq j \leq n$. For C , its value ranges from 2^{-10} (min c) to 2^9 (max c) and for γ , its value ranges from 2^{-10} (min g) to 2^{10} (max g).

The main flow of QSA-SVM is shown in Figure 5.

Step 1. Initialization of parameters.

Step 2. Coding the chromosome using phase, $\phi_i = [\theta_{i1}, \theta_{i2}, \dots, \theta_{i3}]$.

Step 3. Solution space transformation for chromosomes and computing fitness. For the quantum bit, $[\cos \theta_{ij}, \sin \theta_{ij}]^T$, we

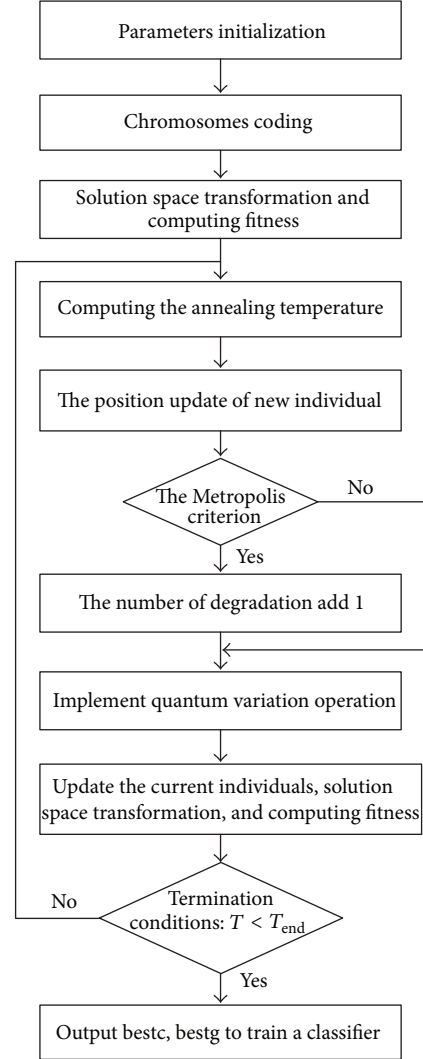


FIGURE 5: The flow of QSA-SVM.

use the linear transformation [12] as (7) to transform to the solution space. In (7), X^j is one gene on chromosome, min and max, respectively, are minimum and maximum of X^j in practice, X_{ic}^j is the corresponding cos solution of phase θ_{ij} , and X_{is}^j is the sin solution. In our method, X^j can represent the penalty factor C or the parameter of RBF γ :

$$\begin{bmatrix} X_{ic}^j \\ X_{is}^j \end{bmatrix} = \frac{1}{2} \begin{bmatrix} 1 + \cos \theta_{ij} & 1 - \cos \theta_{ij} \\ 1 + \sin \theta_{ij} & 1 - \sin \theta_{ij} \end{bmatrix} \begin{bmatrix} \max \\ \min \end{bmatrix}, \quad X^j \in [\min, \max]. \quad (7)$$

We use the SVM prediction accuracy as the fitness of chromosomes and leave one out (LOO) to evaluate. Then, we keep all information of the optimal individual.

Step 4. Computing the annealing temperature T . In (8), gen is the iterations, T_0 is the initial temperature, and α is

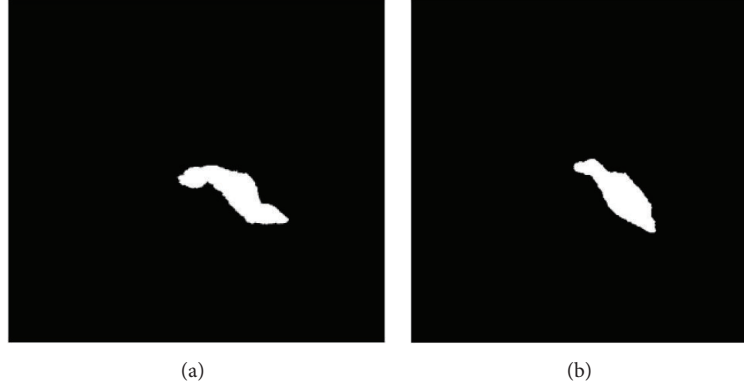


FIGURE 6: Illustration of samples. (a) Normal pancreas. (b) Abnormal pancreas.

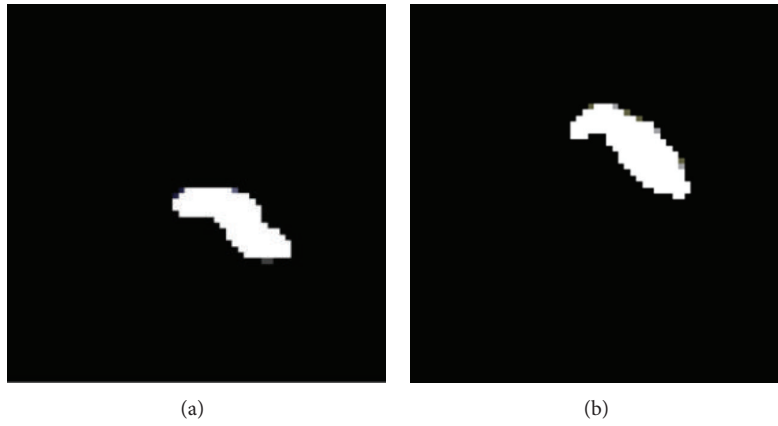


FIGURE 7: Illustration of the mean figure of the samples. (a) The mean of the normal samples. (b) The mean of the abnormal samples.

the cooling ratio of simulated annealing to control the rate of cooling:

$$T = \alpha^{\text{gen}} \times T_0. \quad (8)$$

Step 5. The position update of new individual. We divide the neighborhood space for phase and then generate a random update vector S , which specifies the location of the phase for updating. One phase is selected randomly to get a new chromosome in the neighborhood space. If the fitness of new chromosome is better than the old one, we will replace the old with the new one. We update the designated quantum bits by S through quantum gate according to the above.

Step 6. According to the Metropolis criterion, we update the chromosomes. The probability of new chromosomes acceptance obeys the Boltzmann probability distribution. In (9), $\text{fit}(\phi_i)$ is the fitness of parent chromosome ϕ_i and $\text{fit}(\phi'_i)$ is the fitness of child chromosome. If $\text{fit}(\phi'_i)$ is greater than $\text{fit}(\phi_i)$, the new chromosome will be accepted with probability 1. Otherwise, the new chromosome will be accepted with probability p_i :

$$P(\phi_i = \phi'_i) = \begin{cases} 1 & \text{fit}(\phi'_i) > \text{fit}(\phi_i) \\ p_i & \text{fit}(\phi'_i) \leq \text{fit}(\phi_i) \end{cases},$$

$$p_i = \frac{1}{1 + \exp[(\text{fit}(\phi'_i) - \text{fit}(\phi_i))/T]}. \quad (9)$$

Step 7. Implement quantum variation operation using the following:

$$\theta'_{ij} = \frac{\pi}{2} - \theta_{ij}. \quad (10)$$

Step 8. Update the current individuals and execute Step 3 to get the global optimal individual.

Step 9. Determine if it has met the end conditions true is the end to return the optimal parameters and false goes to Step 4.

Step 10. Use the optimal parameters to train an SVM classifier.

After we obtain the classifier using optimal parameters, we will use it to classify the testing samples. Then, we compare the classification labels with the known labels, so that we can get the classification accuracy for evaluating the performance of classifier. It is shown as (11). TN is the total number of

TABLE 1: Accuracy of centered data and not centered data using SVM.

γ	C	Centered data	Not centered data
0.375	145	71.43%	46.33%
0.165	120	71.42%	43.66%
0.100	200	68.29%	38.54%
0.325	350	65.63%	37.53%

TABLE 2: Experiments result of QSA-SVM.

γ	C	Accuracy	Time
412.3415	20.0268	92.8571%	134.33 s
459.1865	127.9188	94.6429%	134.83 s
357.8127	95.1239	91.0714%	114.28 s
465.7957	30.7913	96.4286%	111.06 s
1020.5	267.1588	98.2143%	152.23 s

testing samples, and CN is the number of testing samples which are classified correctly:

$$\text{Accuracy} = \frac{CN}{TN}. \quad (11)$$

3. Results and Discussion

We select 114 groups of pancreas images; among them 81 groups are normal and 33 groups are abnormal. The resolution of each image is 128×128 and the thickness is 2.77 mm. Among these 114 groups, we select 40 groups of normal images and 16 groups of abnormal images as the testing samples and others as the training samples.

Figure 6 shows two images; one of them is normal data and the other one is abnormal data. The pancreatic morphology of abnormal data is thick and big.

We can see the mean of the samples of each 81 normal pancreas and 33 abnormal pancreas in Figure 7.

In this paper, we use the SVM method to classify the pancreas data. We can see several results in Table 1. In Table 1, γ is the parameter gamma of the kernel function RBF and C is the penalty factor. From Table 1, we can see that the results on centered data are significantly better than the results on the data without centering, so the variation capture with respect to the data center is more powerful in classification than variation capture with respect to the original data.

The experimental result of 5 groups of QSA-SVM is shown in Table 2. We can see that the mean operation duration is approximate 129.35 s, the mean accuracy of classification is 94.64%, the parameter gamma of the kernel function RBF γ , and the mean values of penalty factor C are 543.12728 and 108.20392.

Compared with other classifiers, the accuracy of QSA-SVM is better which is shown in Figure 8. And in Figure 9, the comparison of running time is shown.

Classifier BPNN is BP neural network, the accuracy is 25% and the running time is 6.76 s; classifier Fisher is fisher linear classifier, the accuracy and running time are 35% and 0.98 s; classifier SVM is the common SVM, the accuracy is

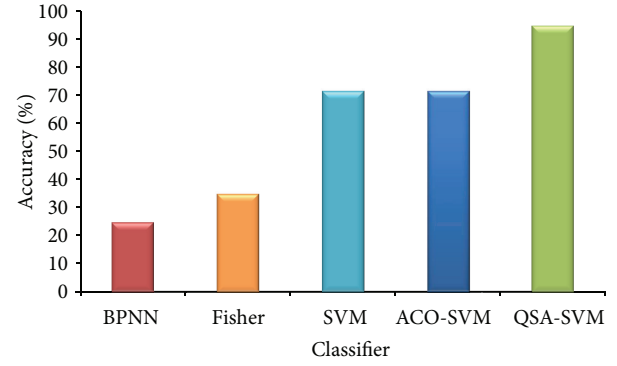


FIGURE 8: Classification accuracy of pancreas images using 5 classifiers.

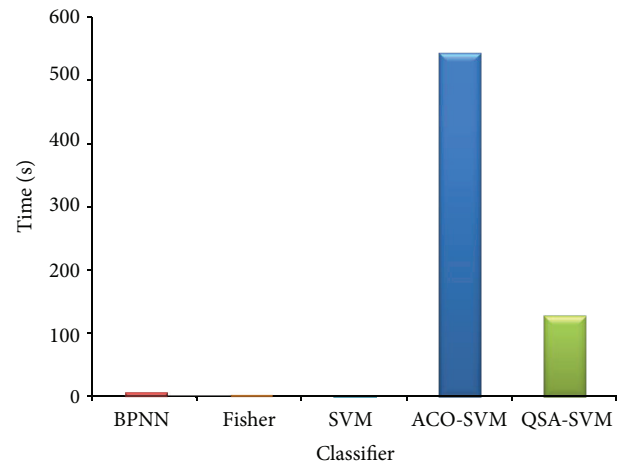


FIGURE 9: Classification time of pancreas images using 5 classifiers.

71.4286% and the running time is only 0.13 s; classifier ACO-SVM [13, 14] is the optimized classifier SVM using ant colony algorithm which has the same accuracy with common SVM, but the running time is 544.51 s, it is much slower than the proposed method. As Figure 8 shows, QSA-SVM has better efficiency in classification than others, and in Figure 9, it is slower than several methods, but it is faster than ACO-SVM which is also able to optimize the parameters of SVM.

At present, radiologists usually diagnose pancreatic diseases with their own experience and the morphology information of image. But missed diagnosis sometimes inevitably happened due to individual differences of patients or limitation of doctor's knowledge of image information. Hence, the proposed method can be used in CAD technology and give early diagnosis of pancreatic diseases in the acceptable time of doctor, so that the classifier can help doctors to diagnose the disease of patient and improve diagnosis rate of disease.

4. Conclusions

In this paper, tensors have been used to represent the image and MPCA extended linear PCA to multilinear subspace learning for the tensor object analysis, and QSA-SVM method has been proposed to classify images. As an application for

classifying pancreatic images, the method combining MPCA and QSA-SVM achieved the better classification accuracy, because MPCA method can preserve the relationship of features in the original tensor and the structure of the original image as much as possible; in the acceptable time, QSA which was used for optimizing SVM classified model is able to find the optimal model parameters. Therefore, the proposed method can improve the classification accuracy of pancreatic images and then assist doctors to diagnose diseases.

Acknowledgments

The research is supported by the National Natural Science Foundation of China (no. 61272176, no. 60973071) and the Fundamental Research Funds for the Central Universities (no. 110718001).

References

- [1] H. Fujita, Y. Uchiyama, T. Nakagawa et al., "Computer-aided diagnosis: the emerging of three CAD systems induced by Japanese health care needs," *Computer Methods and Programs in Biomedicine*, vol. 92, no. 3, pp. 238–248, 2008.
- [2] V. P. Kshirsagar, M. R. Baviskar, and M. E. Gaikwad, "Face recognition using Eigenfaces," in *Proceedings of the 3rd International Conference on Computer Research and Development (ICCRD '11)*, vol. 2, pp. 302–306, March 2011.
- [3] I. T. Jolliffe, *Principal Component Analysis*, Springer, New York, NY, USA, 2nd edition, 2002.
- [4] H. Lu, K. N. Plataniotis, and A. N. Venetsanopoulos, "MPCA: multilinear principal component analysis of tensor objects," *IEEE Transactions on Neural Networks*, vol. 19, no. 1, pp. 18–39, 2008.
- [5] B. Liu, Z. F. Hao, and X. W. Yang, "Nesting support vector machine for multi-classification," in *Proceedings of the International Conference on Machine Learning and Cybernetics (ICMLC '05)*, pp. 4220–4225, August 2005.
- [6] M. Dorigo, V. Maniezzo, and A. Colorni, "Ant system: optimization by a colony of cooperating agents," *IEEE Transactions on Systems, Man, and Cybernetics B*, vol. 26, no. 1, pp. 29–41, 1996.
- [7] A. Narayanan and M. Moore, "Quantum-inspired genetic algorithms," in *Proceedings of the IEEE International Conference on Evolutionary Computation*, pp. 61–66, 1996.
- [8] X. L. Xu, J. J. Jiang, and J. Jieetal, "An improved real coded quantum genetic algorithm and its applications," in *Proceedings of the International Conference on Computational Aspects of Social Networks*, pp. 307–310, 2010.
- [9] P. K. Tiwari and D. P. Vidyarthi, "A variant of quantum genetic algorithm and its possible applications," *Advances in Intelligent and Soft Computing*, vol. 130, no. 1, pp. 797–811, 2012.
- [10] K. H. Han and J. H. Kim, "Quantum-inspired evolutionary algorithm for a class of combinatorial optimization," *IEEE Trans Evolutionary Computation*, vol. 6, no. 6, pp. 580–593, 2002.
- [11] W. L. Du, B. Li, and Y. Tian, "Quantum annealing algorithms: state of the art," *Journal of Computer Research and Development*, vol. 45, no. 9, pp. 1501–1508, 2008.
- [12] J. Yang, Q. Xu, J. Zhang, and C. Cao, "A novel quantum ant colony optimizing algorithm," *Acta Scientiarum Naturalium Universitatis Sunyatseni*, vol. 48, no. 3, pp. 22–27, 2009.
- [13] X. Y. Fang and B. Tao, "Share price prediction using wavelet transform and ant colony algorithm for parameters optimization in SVM," in *Proceedings of the WRI Global Congress on Intelligent Systems (GCIS '09)*, vol. 3, pp. 288–292, May 2009.
- [14] X. Y. Liu, H. Y. Jiang, and F. Z. Tang, "Parameters optimization in SVM based on ant colony optimization algorithm," in *Proceedings of the International Conference on Nanotechnology and Computer Engineering*, pp. 470–475, 2010.

Research Article

Volume-Rendering-Based Interactive 3D Measurement for Quantitative Analysis of 3D Medical Images

Yakang Dai, Jian Zheng, Yuetao Yang, Duojie Kuai, and Xiaodong Yang

Suzhou Institute of Biomedical Engineering and Technology, Chinese Academy of Sciences, No. 88 Keling Road, New District, Suzhou 215163, China

Correspondence should be addressed to Yakang Dai; daiyk@sibet.ac.cn

Received 3 January 2013; Revised 8 April 2013; Accepted 17 April 2013

Academic Editor: Younghae Do

Copyright © 2013 Yakang Dai et al. This is an open access article distributed under the Creative Commons Attribution License, which permits unrestricted use, distribution, and reproduction in any medium, provided the original work is properly cited.

3D medical images are widely used to assist diagnosis and surgical planning in clinical applications, where quantitative measurement of interesting objects in the image is of great importance. Volume rendering is widely used for qualitative visualization of 3D medical images. In this paper, we introduce a volume-rendering-based interactive 3D measurement framework for quantitative analysis of 3D medical images. In the framework, 3D widgets and volume clipping are integrated with volume rendering. Specifically, 3D plane widgets are manipulated to clip the volume to expose interesting objects. 3D plane widgets, 3D line widgets, and 3D angle widgets are then manipulated to measure the areas, distances, and angles of interesting objects. The methodology of the proposed framework is described. Experimental results indicate the performance of the interactive 3D measurement framework.

1. Introduction

Modern medical imaging (such as CT, MRI, and optical CT) can produce 3D images, which have been widely used to assist qualitative and quantitative diagnosis in clinical applications. One of the commonest needs in these image-guided diagnoses is quantitative measurement of the interesting object in the image. Although various automated and semiautomated image processing methods (such as segmentation and registration) have been proposed to improve measurement efficiency, they have not achieved the accuracy by interactive measurement with human experience. Therefore, currently interactive measurement methods are still commonly used in practical applications. However, most existing methods perform interactive measurement on each of the three orthogonal slices. This way is not intuitive enough and requires the operator to reconstruct stereoscopic structure of the interesting object in his mind. The idea to directly perform interactive measurement in 3D space is thus inspired, where volume visualization technology should be used.

Surface rendering and volume rendering are two main branches of volume visualization. After segmentation and reconstruction, surface rendering can display the extracted surface very fast with powerful graphics hardware. Compared

with surface rendering, volume rendering is computationally expensive. However, it can visualize the volume directly without the segmentation and reconstruction operations. With the growing of the computational performance of the modern computer, the volume rendering is becoming very popular for volume visualization. Generally, volume rendering is just used for qualitative display of the volume. To achieve vivid and accurate 3D measurement based on volume rendering, two key problems should be addressed: (1) how to interactively explore the volume in 3D space and measure the interesting object; (2) how to display the volume, interesting object, and human-machine interaction tool in the 3D scene properly. We have proposed a volume-rendering-based interactive 3D measurement framework, which integrates 3D widgets and volume clipping with volume rendering, to address the above problems.

Volume clipping is the commonest way to cut away unwanted parts of the volume and expose the interesting object. In [1], clipping geometries based on stencil buffer test were introduced to cut the volume. Taking advantages of 3D texture operations on graphics hardware, Sommer et al. [2] implemented arbitrary clip planes for volume exploration. Several clipping methods, such as depth-based clipping and volumetric clipping, were proposed in [3] to implement complex

geometries for volume exploration. Besides, Khanduja and Karki [4] combined clipping with multiresolution rendering to visualize large-scale 3D datasets. Although these methods achieved good clipping results, they did not attempt to manipulate the clipping immersively in 3D space. Thus, we use 3D widgets, instead of traditional panel widgets such as push-buttons and sliders, to assist immersive volume clipping and implement 3D measurement.

3D widget was introduced by Conner et al. [5]. It can be considered as an encapsulation of geometry and behavior that is used to adjust the controlled objects. Many publications have reported the use of 3D widgets in immersive volume clipping [6–11]. For instance, McGuffin et al. [12] applied 3D widgets to browse volumetric data. Huff et al. [10] developed three interactive 3D widgets (i.e., eraser, digger, and clipper) for volume sculpting and visualization. However, almost all reported volume-rendering-based immersive clipping and measurement methods (with 3D widgets) depended on texture-based volume rendering [13]. Immersive volume clipping and measurement strategies based on other volume rendering algorithms (such as ray casting, splatting, and shear warp) are seldom described. For texture-based volume rendering, the volume is resampled to multiple textured polygons (with depth information), which are then rendered in 3D space. Therefore, using texture-based volume rendering, the clipped volume, intersection images between the volume and clipping geometries, and 3D widgets can be displayed correctly in 3D space. Nevertheless, for the other volume rendering algorithms, a 2D projection image is calculated directly as the final rendering result; therefore, intermediate textured polygons with depth information cannot be obtained, making the realization of vivid clipping and measurement in 3D space challenging.

Compared with existing measurement methods, the features of our interactive 3D measurement framework are described as follows: (1) 3D plane widgets are designed to immersively manipulate volume clipping to expose interesting objects and also measure areas of interesting objects; (2) various volume rendering algorithms (such as ray casting, splatting, and shear warp) are supported, regardless of CPU-based or GPU-based implementations; (3) the clipped volume, intersection images between the volume and clip planes, and 3D widgets can be displayed correctly; (4) 3D line widgets and 3D angle widgets are designed to measure distances and angles of interesting objects, respectively. The methodology of our interactive 3D measurement framework is introduced in Section 2. Representative experimental results using the measurement framework are demonstrated in Section 3. The conclusion and future work are presented in Section 4.

2. Methods

To achieve immersive volume clipping and measurement with 3D widgets, two requirements must be fulfilled: (1) all models (such as the clipped volume, intersection images between the volume and clipping geometries, and 3D widgets) in the 3D scene should be rendered correctly; (2) the widgets should be manipulated “look right” and the parameters adjusted by the widgets should be precise. We thus place

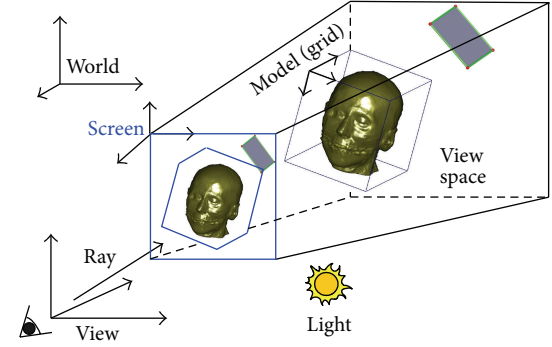


FIGURE 1: Integrated rendering environment. There are five coordinate systems. All models (such as the clipped volume, intersection images between clipping geometries and the volume, and 3D widgets) placed in the view space are rendered onto the screen.

all models in an integrated rendering environment (which is illustrated in Figure 1) for accurate rendering and immersive volume clipping and measurement. It is worth noting that the center of the volume is always located in the intermediate plane (see Figure 5) of the view space.

2.1. Integrated Rendering Environment. There are five coordinate systems in the rendering environment, including the coordinate system of the volume grid space G , the coordinate system of the volume model space M , the world coordinate system W , the coordinate system of the view space V , and the screen coordinate system S . W is the absolute coordinate system where the volume and widgets are placed. The view space defines the visible region in W . The coordinate transformation from the grid space to the screen space can be written as

$${}^S X = {}^S T_V \cdot {}^V T_W \cdot {}^W T_M \cdot {}^M T_G \cdot {}^G X, \quad (1)$$

where ${}^G X$ is the position of each voxel in G and ${}^S X$ is the transformed coordinate value in S . Both of them can be denoted as $[x, y, z, 1]^T$. ${}^M T_G$, ${}^W T_M$, ${}^V T_W$, and ${}^S T_V$ can be written in a unified format ${}^J T_I$, which is a 4×4 matrix representing the transformation from the coordinate system I to the coordinate system J . In the environment, each widget is rendered using OpenGL directly, while the clipped volume is rendered using volume rendering (such as ray casting, splatting, and shear warp).

2.2. 3D Widgets. A 3D widget can be regarded as an integration of geometry and manipulation, which is used to adjust other controlled objects [12]. The 3D plane widget, 3D line widget, and 3D angle widget used in our interactive 3D measurement framework are illustrated in Figure 2. The 3D plane widget (see Figure 2(a)) is composed of a clip plane, four vertices (implemented with spheres), and four edges (implemented with cylinders). The 3D plane widget can be manipulated by 2D mouse to achieve the following operations (see Figure 2(d), from left to right, top to bottom): rotation around a central axis, horizontal translation, arbitrary

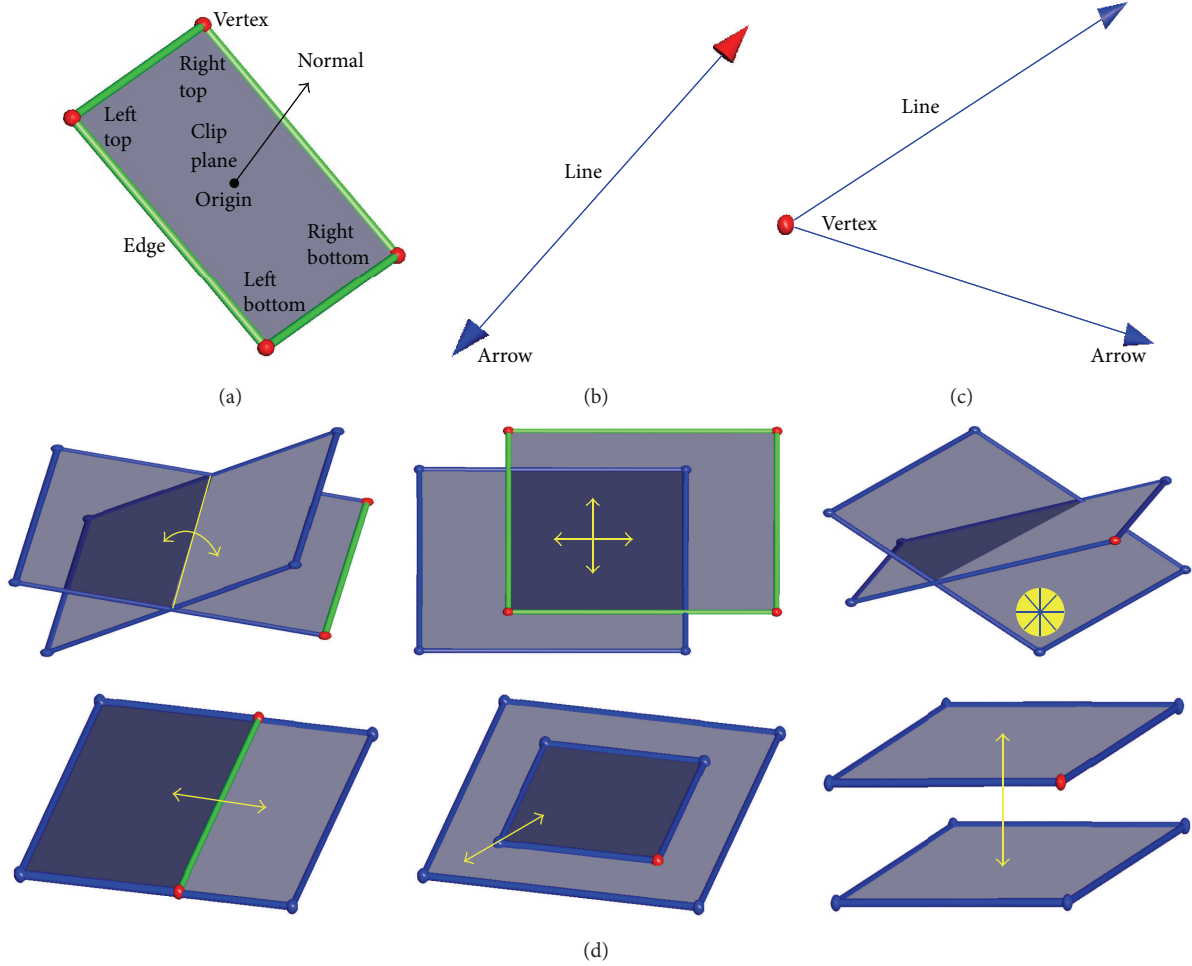


FIGURE 2: 3D widgets used in our interactive 3D measurement framework. (a) 3D plane widget. (b) 3D line widget. (c) 3D angle widget. (d) Operations related to the 3D plane widget. 3D plane widgets are used to clip the volume and measure the areas of interesting objects. 3D line widgets and 3D angle widgets are used to measure distances and angles of interesting objects, respectively.

rotation, extension or shrinkage, zoom, and vertical translation. Using 3D plane widgets, the volume can be clipped immersively to expose interesting objects (details on volume clipping with 3D plane widgets are described in Section 2.3). Similarly, 3D line widgets (see Figure 2(b)) and 3D angle widgets (see Figure 2(c)) can be manipulated immersively in 3D space to measure distances and angles of interesting objects, respectively.

With the selection mechanism of OpenGL, the widget in W can be manipulated by 2D mouse. We take the manipulation of the 3D line widget for an example to depict the implementation detail. Given that an arrow of the 3D line widget is selected and moved, the position of the arrow in the world coordinate system W is ${}^W X_a$. The previous and current positions of the mouse cursor on the screen are, respectively, $[x_{\text{old}}, y_{\text{old}}, 0, 1]^T$ and $[x_{\text{new}}, y_{\text{new}}, 0, 1]^T$. Then we can get the corresponding coordinates, denoted as ${}^W X_{\text{old}}$ and ${}^W X_{\text{new}}$, in W by

$${}^W X = {}^W T_V \cdot {}^V T_S \cdot S X, \quad (2)$$

whereafter, the vector of the mouse movement in W can be calculated by

$${}^W V = {}^W X_{\text{new}} - {}^W X_{\text{old}}. \quad (3)$$

Then the new position of the arrow in W can be obtained as follows:

$${}^W X_a \leftarrow {}^W X_a + {}^W V. \quad (4)$$

The manipulations of the 3D angle widget and 3D plane widget are similar.

Provided that the positions of the two arrows of the 3D line widget in the world coordinate system W are ${}^W X_a$ and ${}^W X_b$, respectively, then the distance of the 3D line can be calculated easily as $\|{}^W X_a - {}^W X_b\|$. Given the three vertices for the 3D angle widget and four vertices for the 3D plane widget (see Figure 2), the respective angle and area can also be calculated very easily.

2.3. Volume Clipping with 3D Plane Widgets. The clipped volume and 3D plane widgets are rendered by two steps. First,

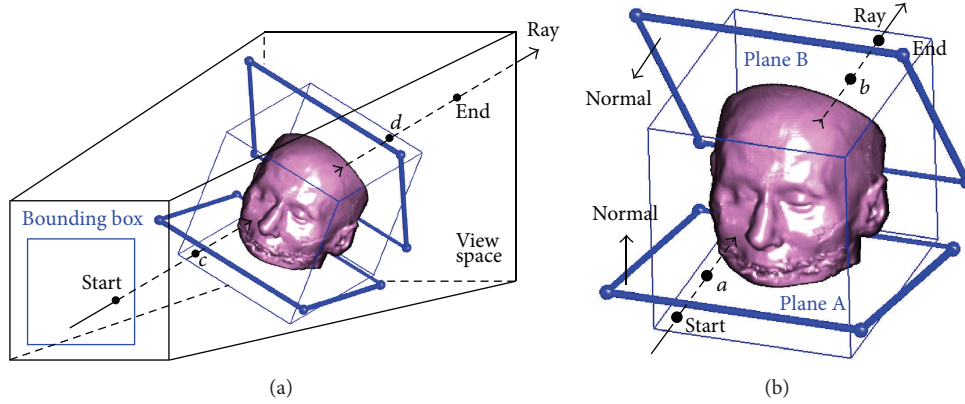


FIGURE 3: The calculation of the projection image using ray casting. (a) Intersections between the ray and volume. (b) Intersections between the ray and clip planes.

the projection image of the clipped volume is calculated by volume rendering. Then, the projection image and 3D plane widgets are rendered to obtain the final rendering image.

2.3.1. Projection of the Clipped Volume Using Volume Rendering. We have implemented three volume renderers to obtain the projection image of the clipped volume, including *ray casting*, *splatting*, and *shear warp*, which are based on the ray-casting, splatting, and shear-warp algorithms, respectively. All of these algorithms finally can come down to the recursive front-to-back composition [7]:

$$\begin{aligned} c &\leftarrow C_S \cdot \alpha_S \cdot (1 - \alpha) + c, \\ \alpha &\leftarrow \alpha_S \cdot (1 - \alpha) + \alpha, \end{aligned} \quad (5)$$

where c and α are, respectively, the accumulated color and accumulated opacity and C_S and α_S are, respectively, the current sampling color and sampling opacity. However, the ray-casting, splatting, and shear warp are implemented differently (i.e., image order, object order, and hybrid, resp.). The implementation details of the renderers are described as below.

The Ray-Casting Renderer. Figure 3 illustrates the approach used by *ray casting* to obtain the projection image. The bounding box formed by projecting the volume to the screen is figured out in advance. The accumulated color and accumulated opacity of each pixel in the bounding box are initialized to zeros. The finally accumulated value of each pixel in the bounding box is calculated as follows.

- (1) Cast a ray from the origin of V to the pixel and initialize S and E to the start and end positions of the ray in the view space, respectively.
- (2) Assume the ray intersects against the volume sequentially at c and d and let $S = c$ and $E = d$.
- (3) For each clip plane, the half space of the normal is preserved, and the rest is removed.
- (4) Assume the two intersections between the ray and the planes are a and b , respectively. Discard the line

segments out of the clip planes, and let $S = a$ and $E = b$.

- (5) Traverse from S to E , calculate opacity and color at each sampling place, and compute the final accumulated color and accumulated opacity recursively according to (5).

After all pixels within the bounding box are processed, the projection image is obtained.

The Splatting and Shear Warp Renderers. The two renderers calculate the projection image based on the sheet which is an axis-aligned volume slice that is most parallel to the screen.

- (A) **Splatting:** voxels are splatted scanline by scanline in a sheet. For each scanline in the sheet, all segments out of the clip planes are removed (the clipping of scanline is described in “(C) Scanline Clipping” and illustrated in Figure 4). In the preserved segment, the color and opacity of each voxel are calculated. Then all voxels are projected onto the screen and the splats are added into a sheet buffer. After all scanlines within the sheet are processed, the sheet buffer is composited with an accumulated buffer by (5). The final projection image is obtained by traversing the volume from the nearest sheet to the farthest sheet.
- (B) **Shear warp:** the volume is also traversed from the nearest sheet to the farthest sheet, and each sheet is traversed in scanline order as well. After each scanline in a sheet is clipped, its preserved segment is transformed to the shear space. Then each voxel in the segment is projected onto the plane of the intermediate image. The color and opacity of each voxel are distributed to a sheet buffer. After traversing all scanlines within the sheet, we composite the sheet buffer with the intermediate image according to (5). Once the intermediate image is formed after processing all sheets, the final projection image is obtained by projecting the intermediate image onto the screen.
- (C) **Scanline clipping:** in *splatting* and *shear warp*, each scanline is clipped in the coordinate system G .

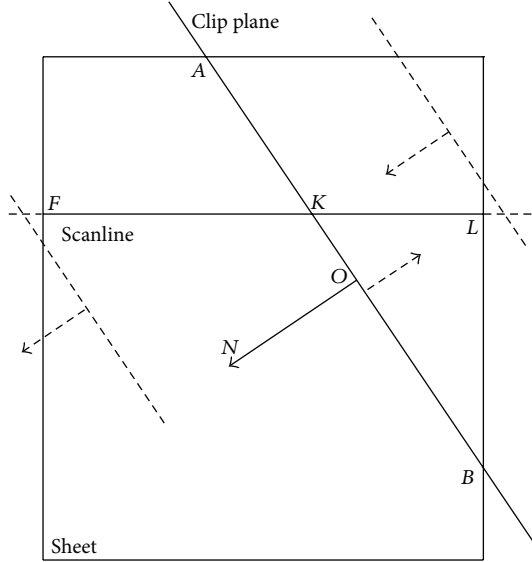


FIGURE 4: The clipping of a scanline. The segment (\overrightarrow{FK} in this figure) in the half space of the normal (N in this figure) of the clip plane is finally preserved and used for splatting and shear warp.

Figure 4 illustrates the clipping of a scanline. Assume that (1) the origin and normal of the clip plane in the grid space are O and N , respectively; F and L are, respectively, the first and last voxels in the scanline; the scanline intersects against the clip plane at K ; V_S and V_E are, respectively, the first and last voxels of the finally preserved segment. Then the scanline is clipped as follows.

- (1) Let $V_S = F$ and $V_E = L$.
- (2) Calculate the dot product of \overrightarrow{OF} and N by $D_F = \overrightarrow{OF} \cdot N$ and the dot product of \overrightarrow{OL} and N by $D_L = \overrightarrow{OL} \cdot N$.
- (3) If $D_F > 0$ and $D_L < 0$, let $V_E = K$. If $D_F < 0$ and $D_L > 0$, let $V_S = K$.
If $D_F > 0$ and $D_L > 0$, the entire scanline is preserved and keep $V_S = F$ and $V_E = L$.
Else the entire scanline is removed and let $V_S = 0$ and $V_E = 0$.

2.3.2. Rendering the Projection Image and 3D Plane Widgets. Assume that (1) A , B , C , and D (see Figure 5) are the four vertices of the projection image obtained in Section 2.3.1; (2) O is the origin of V ; (3) OA , OB , OC , and OD intersect against the intermediate plane of the view space at E , F , G , and H , respectively. The projection image is then textured and mapped onto the rectangle $EFGH$. Finally, all widgets are rendered at exact positions. As shown in Figure 5, there may be an intersection error between the mapped texture of the projection image and each clip plane. By setting the clip planes to be completely transparent, we can eliminate the intersection errors. However, sometimes we also want to

display the intersection images between the volume and clip planes, which can be achieved by the following steps.

- (1) After creating the texture T_P from the projection image, compute the intersection images between the volume and clip planes, and creating textures from the intersection images.
- (2) Map T_P onto the rectangle $EFGH$ and render the 3D plane widgets with completely transparent clip planes.
- (3) For each 3D plane widget, map the texture of the intersection image onto the clip plane if the intersection image faces the view direction.

3. Experimental Results

A group of experiments are performed on a Windows PC (with an Intel Core2 1.86 GHz processor and 1 GB physical memory) to demonstrate the validity of our interactive 3D measurement framework. Firstly, a simulated volume with four highlighted voxels is tested for the validation of the accuracy of the interactive 3D measurement. Secondly, realistic CT and MR images are tested in the experiments. The simulated volume is shown in Figure 6(a). The simulation is described as below: (1) the volume size and voxel size are $81 \times 81 \times 81$ and $1 \times 1 \times 1 \text{ mm}^3$, respectively; (2) the values of the background, edges, and 4 highlighted voxels of the volume are 10, 50, and 255, respectively; (3) the 4 highlighted voxels make a square whose edge length is 40 mm. The realistic CT image is from the School of Psychology at the University of Nottingham, and the MR image is from Beijing Shougang Hospital. The size and spacing of the CT image are $208 \times 256 \times 225$ and $1 \times 1 \times 1 \text{ (mm}^3\text{)}$, respectively. The size and spacing of the realistic MR image are $256 \times 256 \times 124$ and $0.86 \times 0.86 \times 1.7 \text{ (mm}^3\text{)}$, respectively.

To validate the accuracy of the interactive 3D measurement, we interactively explore the simulated volume and measure the length of the edge, the half angle between the neighboring edges, and the area of the square by using the 3D line widget, 3D angle widget, and 3D plane widget, respectively. The measured length (40.05 mm), angle (45.03 deg), and area (1600.4 mm^2) are very close to the simulated ones (40 mm, 45 deg, and 1600 mm^2 , resp.). The measurement errors are within 1 mm, 1 deg, and 1 mm^2 . It is worth noting that more accurate measurement results could be reached by interactively manipulating the 3D widgets more carefully. The experiments indicate that the interactive 3D measurement technology can achieve sufficient accuracy.

The CT image is interactively explored using 3D plane widgets. Figure 7 shows representative volume clipping results based on *ray casting*, *splatting*, and *shear warp* renderers. In addition, the rendering efficiency is measured using the following parameters.

- (1) The screen size is 948×618 . The volume model is rotated to a certain orientation to form a 290×386 projection image.
- (2) The volume is rendered without shading. Each intensity is mapped to $(r, g, b, \text{ and } a)$. We map 0 to $(0.0, 0.0,$

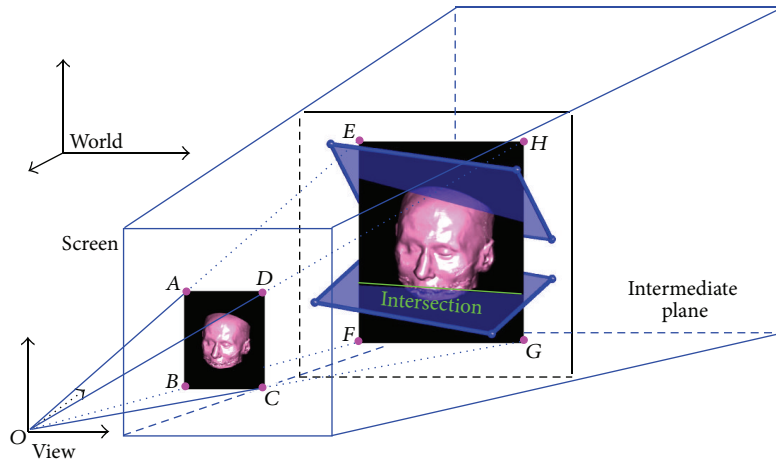


FIGURE 5: The rendering of the projection image and 3D plane widgets. The projection image is generated by projecting the clipped volume onto the screen using volume rendering. It is worth noting that the center of the volume is always located in the intermediate plane. The projection image is textured and mapped onto the intermediate plane, reconstructing the depth information of the projection image. This depth information is the basis to correctly display the combination of the projection image and 3D plane widgets.

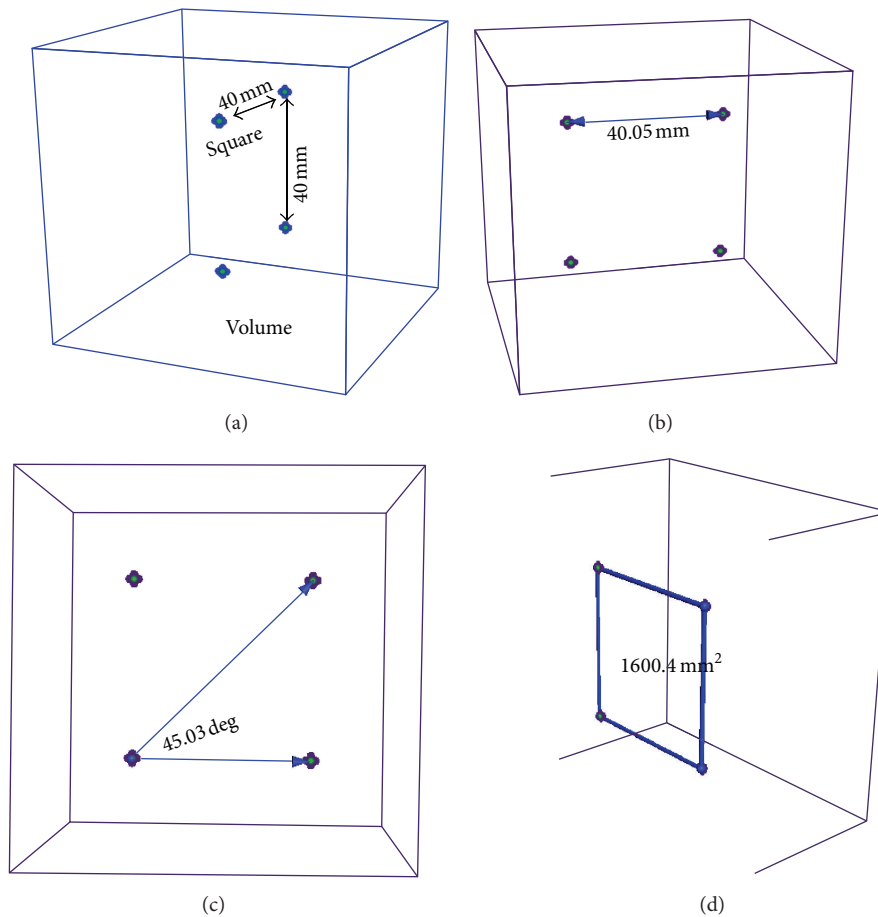


FIGURE 6: Validation of the accuracy of interactive 3D measurement. (a) The simulated volume with 4 highlighted voxels. (b) Distance measurement. (c) Angle measurement. (d) Area measurement.

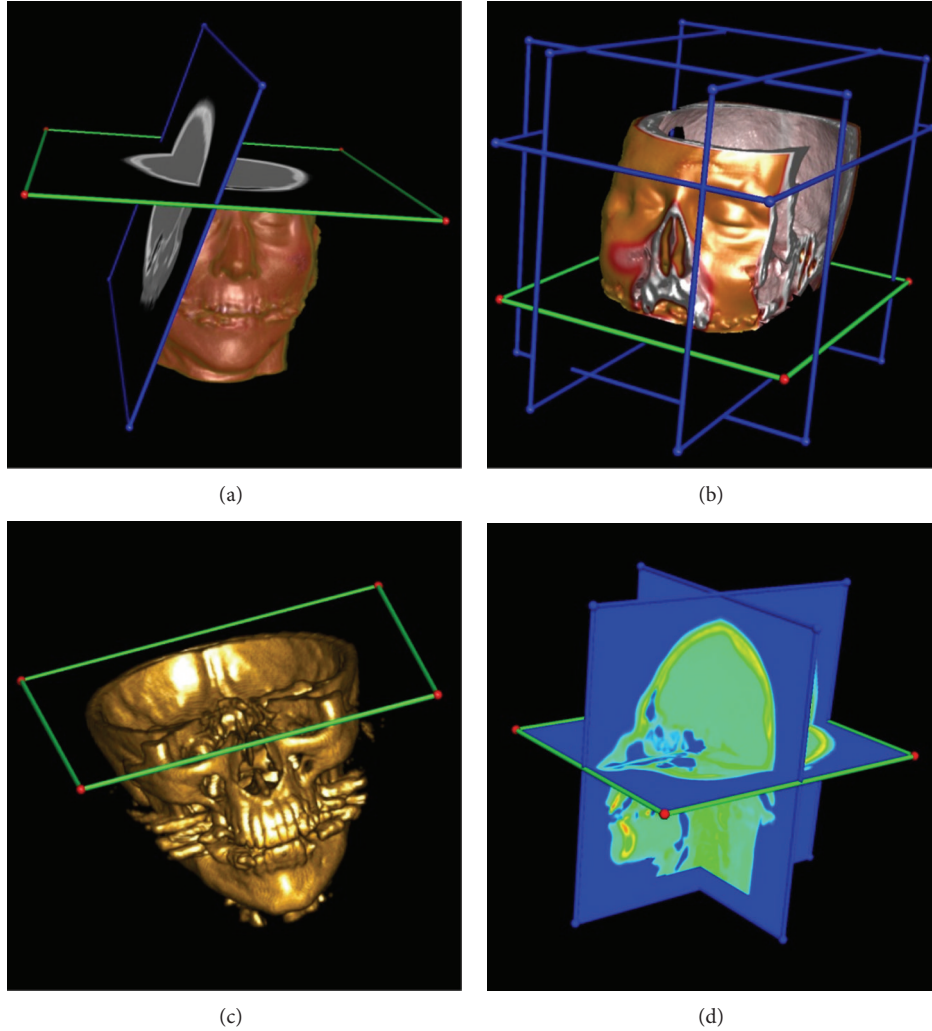


FIGURE 7: Interactive volume clipping. (a) Ray casting with reslicing. (b) Ray casting with cubic clipping. (c) Splatting without reslicing. (d) Shear warp with pseudocolor.

0.0, 0.0) and 255 to (0.8, 0.8, 0.2, 0.5). Other intensities are mapped by linear interpolation.

- (3) The half brain is clipped by a 3D plane widget and reslicing is enabled. Rough rendering is performed while the volume or widget is being manipulated, and refined rendering is performed while the manipulation is stopped.

The average frame rates of scene rendering (i.e., rendering of all models) under different circumstances are shown in Table 1.

The CT and MR images are interactively clipped and measured. Figure 8 shows the interactive measurement results for the CT image. Figure 9 shows the instances of measuring the position and size of the tumor in the brain MR image.

4. Conclusion and Future Work

In this paper, an interactive 3D measurement framework based on volume rendering is implemented for quantitative

TABLE 1: Rendering efficiency of the volume clipping. It can be seen that interactive rendering rate can be achieved. It's worth noting that all the volume renderers in this paper are software-based. The rendering speed can be further accelerated if the volume renderers are implemented using the GPU.

Frames/second	Rough rendering during manipulation	Refined rendering
Ray casting	28.3	1.2
Splatting	9.1	0.5
Shear warp	37.4	2.6

analysis of 3D medical images. 3D plane widgets are manipulated to interactively clip the volume and expose interesting objects. The 3D plane widgets are also manipulated to measure the areas of interesting objects. Further, 3D line widgets and 3D angle widgets are manipulated to measure the distances and angles of interesting objects, respectively. The volume and 3D widgets can be manipulated interactively and

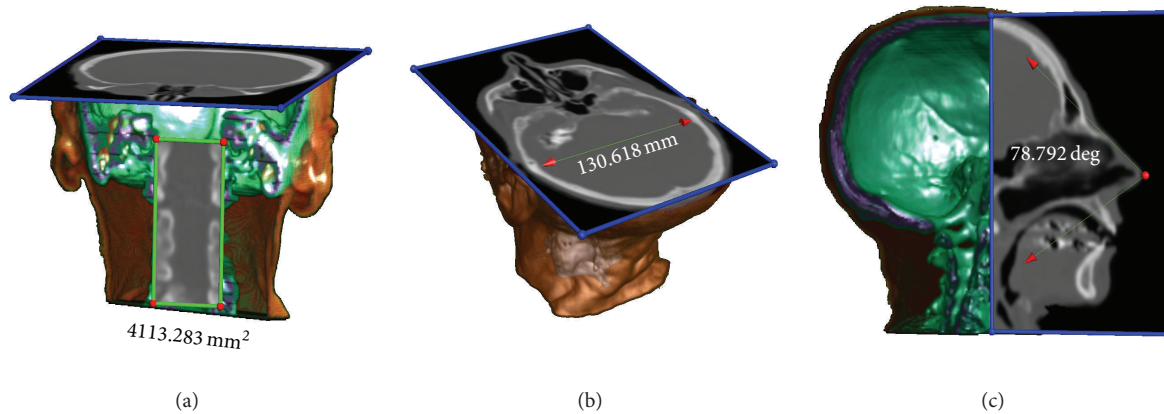


FIGURE 8: Interactive 3D measurement of the CT image. (a) Area measurement based on splatting. (b) Distance measurement based on ray casting. (c) Angle measurement based on shear warp.

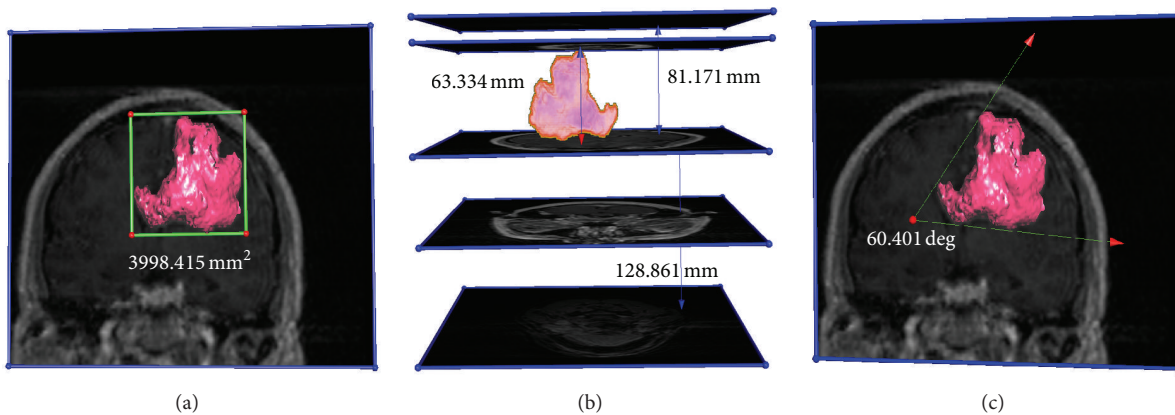


FIGURE 9: Interactive 3D measurement of the tumor in the brain MR image. First, the tumor is segmented from the MR image using a region growing method automatically. Then, the tumor model and the original MR image are put in the same rendering environment for interactive 3D measurement. (a) Area measurement (surface model of the tumor is used and rendered by surface rendering). (b) Distance measurement (volume model of the tumor is used and rendered by ray casting). (c) Angle measurement (surface model of the tumor is used and rendered by surface rendering).

intuitively as if they were manipulated by the operator in a real 3D space. With level-of-detail rendering, we can achieve satisfactory frame rates during manipulation and obtain rendering images of high quality after manipulation.

Various volume rendering algorithms (including ray-casting, splatting, and shear warp) are supported in our framework. Compared with these algorithms, the texture-based volume rendering algorithm is faster. However, for the texture-based algorithm, the rendering quality and the size of the rendered volume are restricted by the texture of the graphics hardware. Therefore, our framework is a necessary complement to the interactive 3D measurement using texture-based volume rendering [10, 12]. In addition, it is worth noting that the performance of our framework can be improved largely if the ray-casting, splatting, and shear-warp algorithms are implemented using the GPU.

Currently only 3D plane widgets are used for volume clipping. Although they can be combined to construct some clipping widgets (e.g., cube widgets), more useful clipping

widgets are required to expose complex objects of interest. In the future, we will design more types of clipping widgets (such as sphere and cylinder widgets). Furthermore, we will design more practical 3D measurement widgets in addition to the 3D line and angle widgets. Our interactive 3D measurement framework has been integrated in the Medical Imaging ToolKit (MITK) [14], which can be downloaded freely from <http://www.mitk.net>.

Acknowledgments

This work was supported in part by the SIBET projects Y053011305 and Y243011304, NSFC Grants 61201117 and 11105096, and NSFJ Grant BK2011331.

References

- [1] R. Westermann and T. Ertl, "Efficiently using graphics hardware in volume rendering applications," in *Proceedings of the Annual*

- Conference on Computer Graphics (SIGGRAPH '98)*, pp. 169–176, July 1998.
- [2] O. Sommer, A. Dietz, R. Westermann, and T. Ertl, “Interactive visualization and navigation tool for medical volume data,” *Computers and Graphics*, vol. 23, no. 2, pp. 233–244, 1999.
 - [3] D. Weiskopf, K. Engel, and T. Ertl, “Interactive clipping techniques for texture-based volume visualization and volume shading,” *IEEE Transactions on Visualization and Computer Graphics*, vol. 9, no. 3, pp. 298–312, 2003.
 - [4] G. Khanduja and B. Karki, “Visualization of 3D scientific datasets based on interactive clipping,” in *Proceedings of the of International Conference in Central Europe on Computer Graphics, Visualization and Computer Vision (WSCG '05)*, pp. 33–36, 2005.
 - [5] B. D. Conner, S. S. Snibbe, K. P. Herndon, D. C. Robbins, R. C. Zeleznik, and A. van Dam, “Threedimensional widgets,” in *Proceedings of the Interactive 3D Graphics Symposium*, pp. 183–188, 1992.
 - [6] J. Kniss, G. Kindlmann, and C. Hansen, “Multidimensional transfer functions for interactive volume rendering,” *IEEE Transactions on Visualization and Computer Graphics*, vol. 8, no. 3, pp. 270–285, 2002.
 - [7] D. Charles and C. R. J. Hansen, *The Visualization Handbook*, Elsevier Academic Press, 2004.
 - [8] C. A. Dietrich, L. P. Nedel, S. D. Olabarriaga et al., “Real-time interactive visualization and manipulation of the volumetric data using GPU-based methods,” in *Medical Imaging 2004: Visualization, Image-Guided Procedures, and Display*, vol. 5367 of *Proceedings of SPIE*, pp. 181–192, February 2004.
 - [9] O. Konrad-Verse, B. Preim, and A. Littmann, “Virtual resection with a deformable cutting plane,” in *Proceedings of the Simulation und Visualisierung*, pp. 203–214, 2004.
 - [10] R. Huff, C. A. Dietrich, L. P. Nedel, C. M. D. S. Freitas, J. L. D. Comba, and S. D. Olabarriaga, “Erasing, digging and clipping in volumetric datasets with one or two hands,” in *Proceedings of the ACM International Conference on Virtual Reality Continuum and Its Applications (VRCIA '06)*, pp. 271–278, June 2006.
 - [11] L. K. Wee, H. Y. Chai, and E. Supriyanto, “Interactive computing and measurement in three dimensional ultrasound fetal volumetric reconstruction using visualization toolkit,” *International Journal of the Physical Sciences*, vol. 6, no. 23, pp. 5520–5527, 2011.
 - [12] M. J. McGuffin, L. Tancau, and R. Balakrishnan, “Using deformations for browsing volumetric data,” in *Proceedings of the IEEE Visualization Conference (VIS '03)*, pp. 401–408, October 2003.
 - [13] J. Kniss, P. McCormick, A. McPherson et al., “Interactive texture-based volume rendering for large data sets,” *IEEE Computer Graphics and Applications*, vol. 21, no. 4, pp. 52–61, 2001.
 - [14] J. Tian, J. Xue, Y. Dai, J. Chen, and J. Zheng, “A novel software platform for medical image processing and analyzing,” *IEEE Transactions on Information Technology in Biomedicine*, vol. 12, no. 6, pp. 800–812, 2008.

Research Article

Segmentation and Morphometric Analysis of Cells from Fluorescence Microscopy Images of Cytoskeletons

Yoshihiro Ujihara,¹ Masanori Nakamura,² Hiroshi Miyazaki,³ and Shigeo Wada³

¹ Department of Physiology, Kawasaki Medical School, 577 Matsushima, Kurashiki, Okayama 701-0192, Japan

² Graduate School of Science and Engineering, Saitama University, Saitama, Saitama 338-8570, Japan

³ Graduate School of Engineering Science, Osaka University, Toyonaka, Osaka 560-8531, Japan

Correspondence should be addressed to Yoshihiro Ujihara; ujihara@med.kawasaki-m.ac.jp

Received 12 January 2013; Revised 18 March 2013; Accepted 18 April 2013

Academic Editor: Younghae Do

Copyright © 2013 Yoshihiro Ujihara et al. This is an open access article distributed under the Creative Commons Attribution License, which permits unrestricted use, distribution, and reproduction in any medium, provided the original work is properly cited.

We developed a method to reconstruct cell geometry from confocal fluorescence microscopy images of the cytoskeleton. In the method, region growing was implemented twice. First, it was applied to the extracellular regions to differentiate them from intracellular noncytoskeletal regions, which both appear black in fluorescence microscopy imagery, and then to cell regions for cell identification. Analysis of morphological parameters revealed significant changes in cell shape associated with cytoskeleton disruption, which offered insight into the mechanical role of the cytoskeleton in maintaining cell shape. The proposed segmentation method is promising for investigations on cell morphological changes with respect to internal cytoskeletal structures.

1. Introduction

Advances in imaging modalities and technologies have enabled the investigation of organ structure-function relationships. Organ segmentation in medical image volumes allows three-dimensional (3D) anatomical visualization, leading to quantitative estimates of organ structures and the development of anatomically realistic computational models used in biology, physiology, and medicine. The same approach can be applied to analyze cell structure-function relationships.

Cell functions, including growth, differentiation, motility, and apoptosis, are associated with cell shape and structure [1–4]. Cells change shape by altering their internal structures, mainly the cytoskeleton, in response to changes in the mechanical environment. Mechanical stimuli acting on the extracellular matrix are transmitted to the cell via transmembrane adhesion receptors, including integrins, which induce cytoskeleton rearrangement, allowing the cell to recover mechanical balance internally and with respect to the extracellular matrix [5]. This dynamic rearrangement induces changes not only in the 3D shape but also in the function of cells [6]. Therefore, relating cell morphology and

internal cytoskeletal structure is important to gain a better understanding of cell mechanics.

Cell morphology is characterized by cell length, diameter, height, projection area, and volume [7–12]. Although these are useful for classifying cell shape, the three-dimensionality of cells often leads to misinterpretations. For example, a circular cone cannot be distinguished from different 3D bodies with the same projection area and height, such as cylindrical columns or ellipsoidal bodies. Therefore, the 3D shape of a cell must be known before characterizing its morphology.

Microscopy imaging techniques for cell observation include phase contrast, differential interference contrast, scanning electron, atomic force, and confocal laser scanning microscopy. Confocal laser scanning microscopy is superior in illuminating intracellular structures, including the cytoskeleton, and providing a series of focused images of an object at selected depths. These serial images are analogous to those acquired by computational tomography and magnetic resonance imaging. Therefore, a similar methodology can be applied to segmenting cells using a series of images of a cell at selected depths.

Numerous segmentation techniques exist [13–19] for producing image series, which can be classified as either boundary or region based. Active contour models, such as snakes [14, 17], are the most popular frameworks for boundary-based methods. Active contour models have been developed for tracking deformable moving objects [14, 17]. This framework attempts to minimize an energy function associated with a contour and find its local minimum at the object boundary. The main drawbacks of active contour models are their high sensitivity to noise and strong dependency on the initial settings, making them insufficiently adaptive to topology, and the relatively high operator interactions. The level set methods [7] are an extension of active contour modeling. They are more robust, versatile, and efficient. They can define sharp corners, topological changes, and 3D effects. Although the computational cost is the same as that of other methods based on fast, narrowband adaptive techniques, the level set methods are slow to converge and can get stuck in local minima. In addition, they require considerable preparation to determine appropriate velocities for advancing the level set function. Region-growing methods [13, 20] are representative of the region-based approach. In the region-growing methods, the region of interest expands from a seed area by assimilating adjoining voxels with properties homogenous to those of the seed voxel according to specified parameters. In contrast to the active contour models, they have heavy computational costs and depend strongly on predefined homogeneity criteria. However, they are relatively insensitive to noise and can correctly separate regions based on defined criteria.

Segmenting cells using fluorescence microscopy images of the cytoskeleton is difficult using conventional methods. Active contour models are only efficient if they are close to the final solution. When studying a complex cell structure, these models often fail if the initial guesses are far from the solution. In addition, the cytoskeleton varies greatly between cells and creating a general model is difficult. Considering the color distinction between the cytoskeleton and other structures in fluorescent images, the region-growing method is the best option. However, in fluorescent images of cytoskeletons, intracellular noncytoskeletal regions, including the nuclear region, are the same color as extracellular regions. Consequently, differentiating them solely based on color and intensity is impossible. Therefore, it was necessary to develop a new method that allows us to quantify 3D shape of a cell and observe the structure and distribution of cytoskeletons in the same cell.

In this paper, we introduce a new method, based on the region-growing method, to segment cells using confocal fluorescence microscopy images of the cytoskeleton. Our motivation for the study is to quantitatively assess 3D shape of a cell while observing the structure and distribution of cytoskeletons in the same cell in order to understand how cytoskeletons contribute to maintaining cell morphology. To demonstrate the utility of the new method, we investigate the shape of intact cells and cells with disrupted actin filaments and microtubules that are the main components of cytoskeletons.

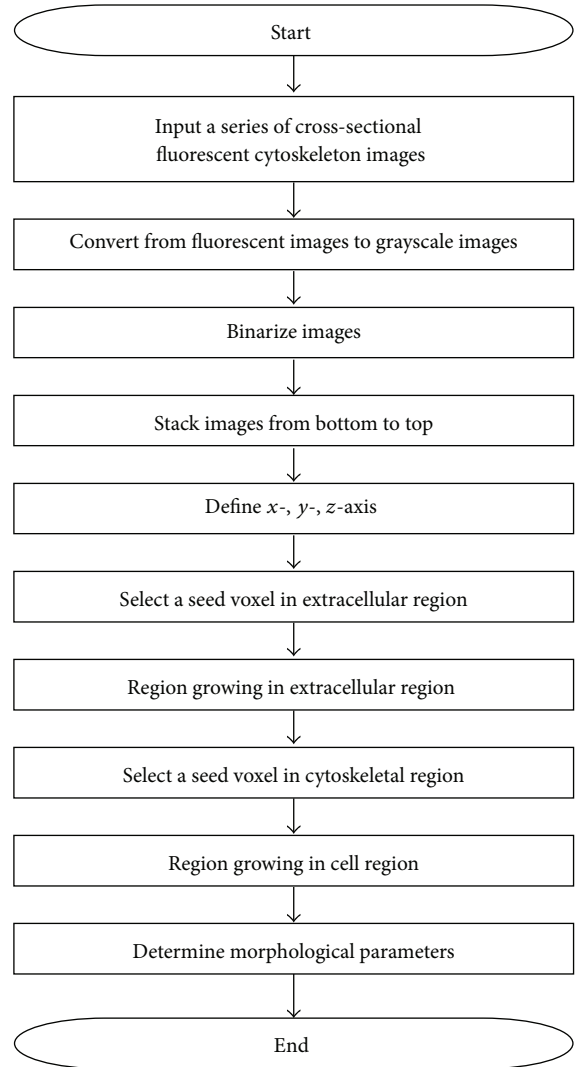


FIGURE 1: Flowchart of segmentation and morphometric analysis of cells from fluorescence microscopy images of cytoskeletons.

2. Materials and Methods

2.1. Cell Preparation. Fibroblasts obtained from rabbit patellar tendons and cultured in Dulbecco's modified Eagle's medium with 10% fetal bovine serum were used as described previously [12]. The cells ($P = 8-12$) seeded to coverslips were treated either with cytochalasin D ($10 \mu\text{g}/\text{mL}$) for 3 h to disrupt actin filaments or colchicine ($0.6 \mu\text{g}/\text{mL}$) for 2 h at 37°C to disrupt microtubules. Then, the cells were washed with phosphate-buffered saline (PBS) and fixed with 3.7% formaldehyde in PBS for 20 min at 4°C . The cells were washed with PBS again and permeabilized with PBS containing 0.1% Triton X-100 for 1 min. Next, the cells were washed in PBS and incubated with monoclonal anti-beta-tubulin antibody (Chemicon International, Temecula, CA, USA) in PBS containing 1% bovine serum albumin (BSA; Sigma-Aldrich, St. Louis, MO, USA) for 1 h at room temperature. After washing with PBS, the cells were incubated with Alexa Fluor 488-conjugated anti-mouse-IgG antibody (Molecular

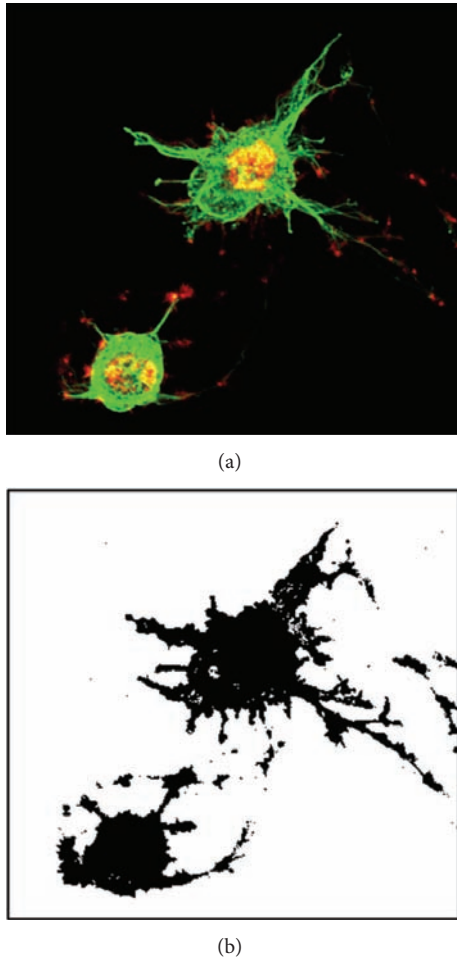


FIGURE 2: A height-wise superimposed fluorescence microscopy image of actin filaments (red) and microtubules (green) (left) and its binarized version, in which the cytoskeletons are black (right).

Probes, Eugene, OR, USA) in PBS containing 1% BSA for 45 min at room temperature for microtubule staining. To stain actin filaments, the cells were incubated with rhodamine- phalloidin (Molecular Probes) in PBS containing 1% BSA for 20 min at room temperature and then washed with PBS. The cells were washed again with PBS, and excess solution was removed from the coverslips. Next, one drop of the antifade reagent SlowFade Gold (Invitrogen, Carlsbad, CA, USA) was applied to each coverslip, which was mounted upside down on glass slides and fixed using melted paraffin wax.

The experiment followed the Guidelines for Animal Experiments, Graduate School of Engineering Science, Osaka University, Osaka, Japan.

2.2. Confocal Laser Scanning Microscopy. Samples were observed under a confocal laser scanning microscope (FV500; Olympus, Tokyo, Japan) with a 60× oil immersion objective (N.A. = 1.40; Olympus). An Ar laser set to 488 nm was used to excite samples labeled with Alexa Fluor 488 mouse IgG antibody, and a He-Ne laser set to 543 nm was used for

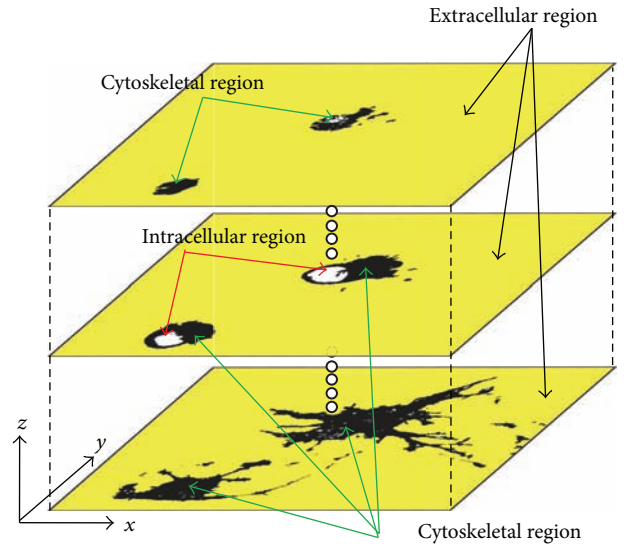


FIGURE 3: The extracellular region was determined by implementing region growing in all directions (x, y, z) from a seed voxel established outside the cell. The extracellular region is yellow, the cytoskeletal region is black, and the intracellular noncytoskeletal region is white.

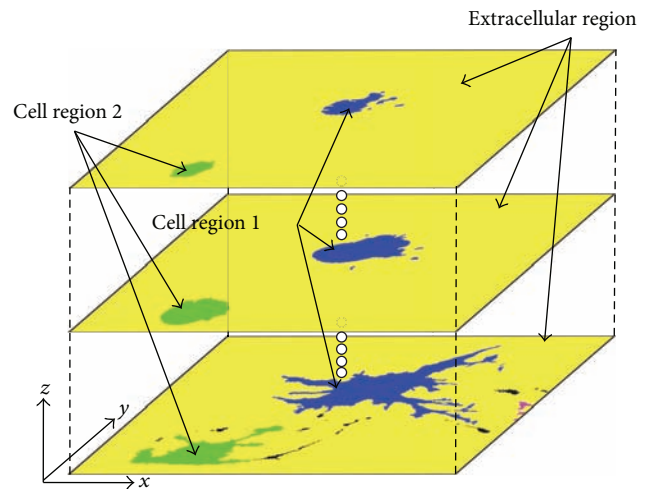


FIGURE 4: Results of cell segmentation using the region-growing method. For identification, the different cells are colored blue and green.

the rhodamine-phalloidin-labeled samples. The laser power was controlled at 5.0% for the 488 nm and 50% for the 543 nm wavelengths. For the double-stained samples, images were acquired sequentially, allowing us to obtain images optimized for the labeling materials. The photomultiplier was adjusted to maximum sensitivity with no saturation. To reduce background noise and signals, image intensities less than the offset value were determined to be zero. Images were scanned at medium speed by default. If an image was too noisy, the scan speed was changed to slow. Images were formatted in a 24-bit colored bitmap with a resolution

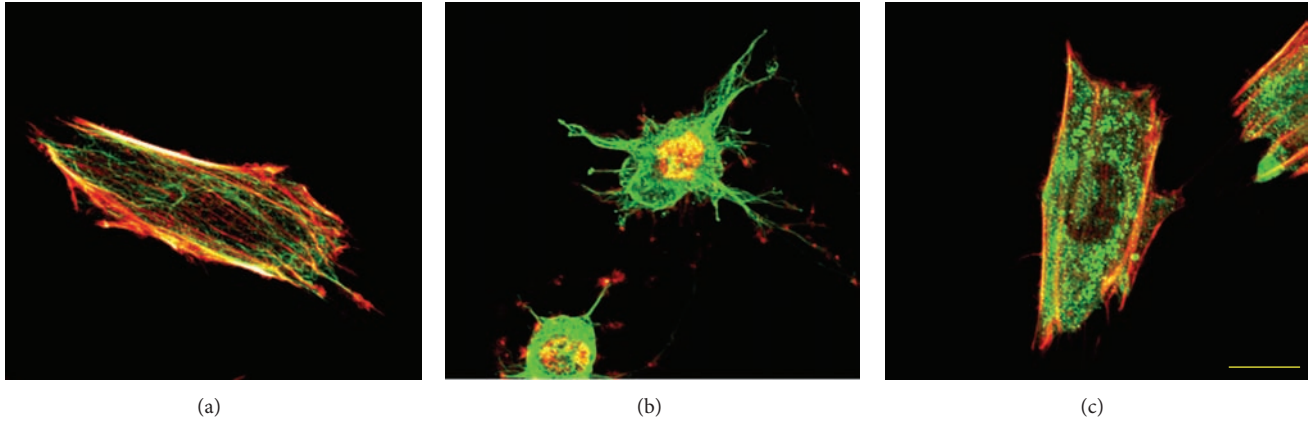


FIGURE 5: (a) Height-wise superimposed fluorescence microscopy images of actin filaments (red) and microtubules (green) of an intact cell (CON), (b) cells treated with cytochalasin D (CD), and (c) cells treated with colchicine (COL). Yellow bar = 20 μm .

of 1024×768 pixels ($0.24 \times 0.24 \mu\text{m}/\text{pixel}$). The z -axis scan interval was 0.25 μm .

Images acquired with the FV 500 photomultiplier are 12-bit grayscale. However, since the image format for 12-bit grayscale is unique to the FV 500, we chose a more general image format, bitmap, to facilitate later analyses. Of the bitmap formats, 24-bit color was chosen to maintain image quality. Image compression from 12-bit (0–4095) to 24-bit RGB color (3×8 bit) was done with software installed to the FV500. For fluorescent images of microtubules, the grayscale intensity of 0–4095 was converted linearly to green, 0–255, with red and blue zeroed. Similarly, the grayscale intensity in fluorescent images of actin filaments was converted to red, 0–255, with green and blue zeroed.

2.3. Cell Segmentation from Confocal Fluorescence Microscopy Images. Cell geometry was determined from a series of cross-sectional fluorescent cytoskeleton images using the region-growing method. The region of interest expands from a seed area based on predefined criteria [21] by assimilating adjoining voxels only with properties similar to those of the seed voxel, such as grayvalue or color. We modified the region-growing method to determine the 3D cell shape from fluorescence microscopy images of cytoskeletons using an in-house C-language program.

Figure 1 shows a flowchart of segmentation and morphometric analysis of cells from fluorescence microscopy images of cytoskeletons. Fluorescence microscopy images of cytoskeletons were doubly stained with the dyes fluorescein isothiocyanate and rhodamine, illuminated green, yellow, or red. Black pixels represented either the extracellular region or intracellular non-cytoskeletal regions, including the cytosol, nucleus, and organelles. No color-based criteria can differentiate the extracellular matrix and non-cytoskeletal regions. For subsequent image analyses, the originally 24-bit color formatted image was converted to a grayscale image using (1),

$$\text{GI} = 0.3R_{bv} + 0.59G_{bv} + 0.11B_{bv}, \quad (1)$$

where GI is the grayscale intensity and R_{bv} , G_{bv} , and B_{bv} are the RGB intensities ranging from 0 to 255. The images

were binarized using a grayscale of 1 as the global threshold, so cytoskeletal regions appeared black and non-cytoskeletal regions white (Figure 2). To create a 3D cell image, the reformatted images were stacked from bottom to top to convert the pixels into voxels. Although confocal laser scanning microscopy has high-depth resolution, unfocused objects were imaged onto focused cross sections. Consequently, uncalibrated volume rendering of images resulted in height-wise stretching. We corrected this stretching using fluorescent spherical beads as a reference [12]. The z -axis was defined as the cell height with the bottom image set at $z = 0$. The x - and y -axes were set to form a right-hand Cartesian coordinate system. Voxels in cytoskeletal and non-cytoskeletal regions were then numbered 0 and 1, respectively.

Before cell segmentation, we identified the extracellular region by introducing a seed voxel in the non-cytoskeletal region. Note that non-cytoskeletal regions were present not only outside but also inside cells where nucleus and cytoplasmic components were present. Therefore, care was taken to not introduce the seed voxel inside cells. Regional growth was then applied from the seed voxel in all directions (x , y , z) to assimilate adjoining voxels flagged 1, non-cytoskeletal regions, from the seed voxel. Figure 3 shows the result of this process whereby extracellular voxels of the non-cytoskeletal region are colored yellow with a flag of 2, while the rest is colored white with a flag of 3.

Finally, cells were identified using the region-growing method for voxels with a flag of 0, the cytoskeletal region, in all directions (x , y , z). The region was grown for voxels flagged either 0 or 3. Through this process, both cytoskeleton voxels and intracellular non-cytoskeleton voxels are assimilated to the seed voxel. To identify individual cells when multiple cells were in one image, the seed voxel of each cell was flagged with a unique number, and the voxels assimilated to the seed voxel were reflagged with the unique flag identifier. Cell identification was repeated until no voxels flagged with 0 or 3 remained in the images. Using this procedure, we segmented cells from a series of fluorescence microscopy images (Figure 4).

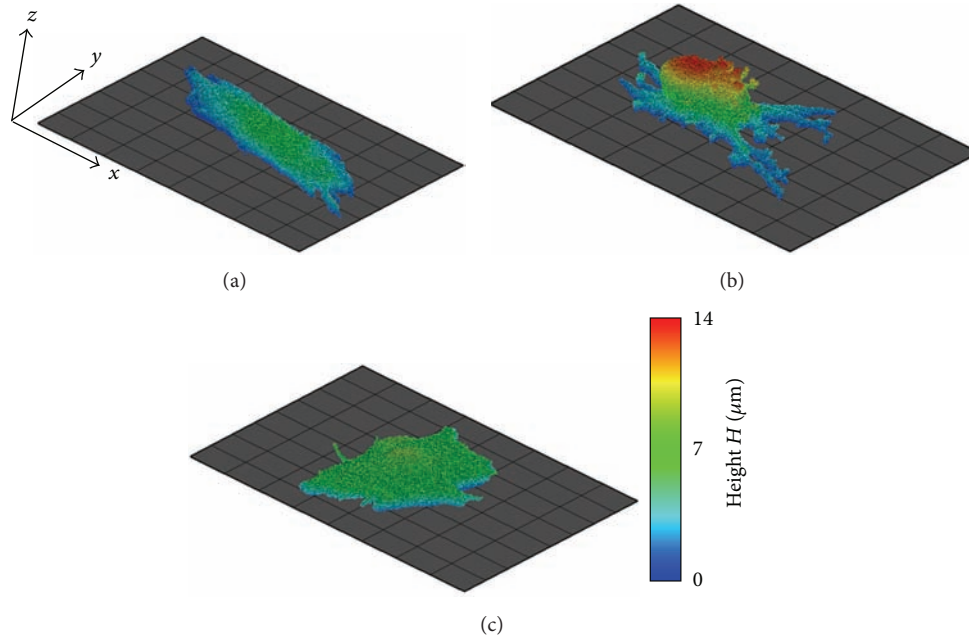


FIGURE 6: (a) Voxel images of cells segmented from fluorescence microscopy images of actin filaments and microtubules of an intact cell (CON), (b) a cell treated with cytochalasin D (CD), and (c) a cell treated with colchicine (COL). The grid base is $10 \times 10 \mu\text{m}$. Color represents the z -coordinate of each voxel.

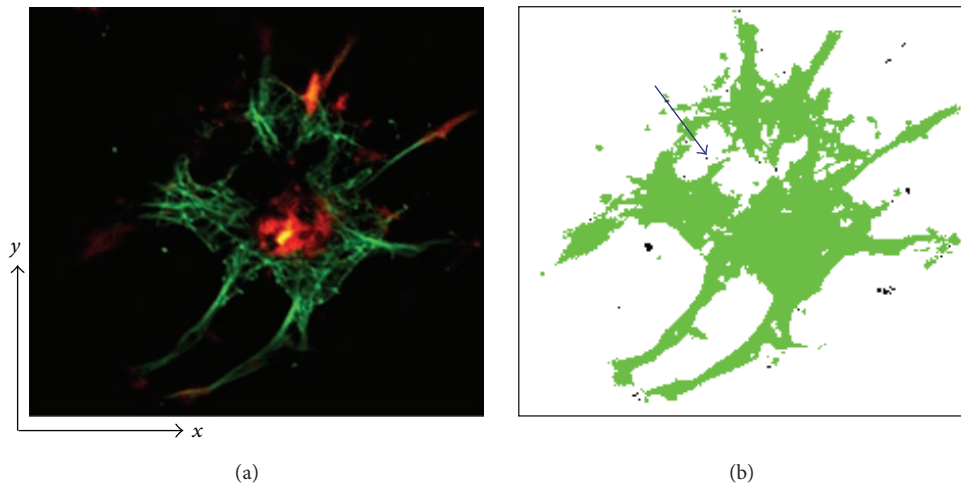


FIGURE 7: (a) A fluorescent image of cytoskeletons (red and green) on noncytoskeletal regions (black). (b) A cell image extracted using a conventional region-growing method in which a region is defined based on a difference in color or intensity.

3. Results

Figure 5 shows confocal laser scanning micrographs of actin filaments (red) and microtubules (green) in intact cells (CON) and cells treated with cytochalasin D (CD) or colchicine (COL). The x - y plane was superimposed on the z -axis in Figures 5(a)–5(c). Actin filaments and microtubules were observed throughout the cells, except in the nuclear region. Actin filaments appeared as thick actin bundles running parallel to the major axis of the CON cell, which was elongated elliptically in one direction (Figure 5(a)).

Thick actin bundles were rarely seen in the CD cells, which had fragmented actin filaments gathered in the central region of the cell (Figure 5(b)). Microtubules were well preserved with thin processes protruding radially from the round cell body (Figure 5(b)). CD cells underwent drastic shape changes compared to CON cells (Figure 5(b)). While the microtubules of COL cells were almost completely fragmented, actin filaments remained whole (Figure 5(c)). Comparing CON and COL images revealed that microtubule disruption caused slight cell shrinkage.

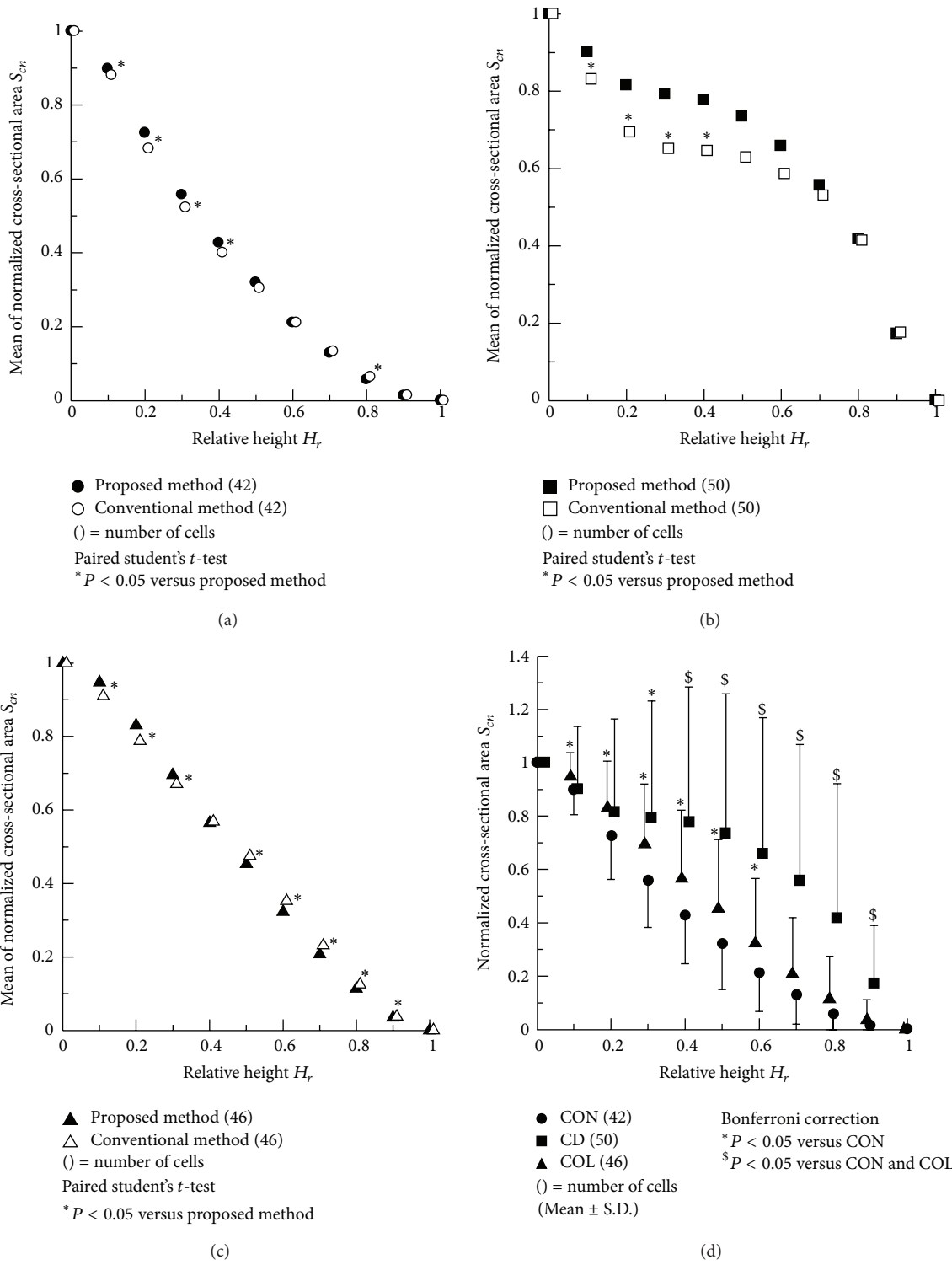


FIGURE 8: The cross-sectional area of cells normalized with adhesion areas (cross-sectional area at $z = 0$) in relation to their relative height H_r . The mean of normalized cross-sectional area of (a) CON, (b) CD, and (c) COL extracted by a proposed method and by the conventional region-growing method. (d) A comparison of the normalized cross-sectional area of three groups extracted by a proposed method.

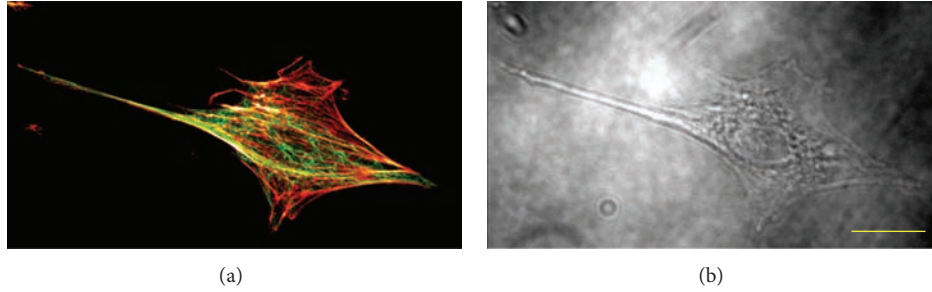


FIGURE 9: (a) A confocal laser scanning micrograph of actin filaments and microtubules and (b) an optical micrograph of the same cell. Yellow bar = 20 μm .

TABLE 1: The summary of the volume, adhesion area, and fibroblast height of the three cell groups.

	CON ($n = 42$)	CD ($n = 50$)	COL ($n = 46$)
Volume V (μm^3)			
Proposed method	2742 \pm 1529	2165 \pm 1151	2201 \pm 949
Conventional method	2440 \pm 1340*	1777 \pm 917* [#]	1811 \pm 743* [#]
Adhesion area S_a (μm^2)			
Proposed method	989 \pm 480	357 \pm 178 [§]	722 \pm 389 [#]
Conventional method	902 \pm 454*	320 \pm 157* [§]	609 \pm 327* [#]
Height H (μm)			
Proposed method	7.4 \pm 2.0	10.7 \pm 1.6 [§]	7.5 \pm 2.4
Conventional method	7.5 \pm 2.0*	10.7 \pm 1.7* [§]	7.5 \pm 2.4*

* $P < 0.05$ versus proposed method (paired Student's t -test).

[#] $P < 0.05$ versus CON, [§] $P < 0.05$ versus CON and COL (Bonferroni correction).

Figure 6 illustrates 3D reconstructions of the cells shown in Figure 5. We successfully segmented the complicated cell shapes in all groups. Comparing three-dimensionally reconstructed cells showed a drastic change in the morphological features of the CD cell (Figure 6(b)), which shrank lengthwise, while the height increased, resulting in a hemispherical body with some processes. The shape and height of the COL cell were similar to those of the CON cell (Figures 6(a) and 6(c)).

Table 1 summarizes three morphological parameters of the cells extracted by a proposed method and a conventional region-growing method: volume, V , adhesion area, S_a , and height, H . Statistical differences in each parameter of all groups were present between the proposed method and the conventional method. Especially, volume and adhesion area of cells extracted with the conventional method were significantly smaller than those extracted with the proposed method. This was because the conventional method failed to extract the voxels of intracellular non-cytoskeletal components as a part of the cell as shown in Figure 7. We used the Bonferroni correction to statistically compare these parameters among the three groups. A significant difference was not found between the groups when the proposed method was used, while CD and COL volume were significantly smaller

than CON when the conventional method was applied. Cell adhesion area was ordered CON, COL, and CD, size-wise. Statistical differences in the adhesion area were present between both CON and COL ($P < 0.05$) and COL and CD ($P < 0.05$) obtained by both methods. CD height was significantly larger than CON and COL, whereas COL height did not differ statistically from CON obtained by both methods.

The mean cross-sectional area, S_c , of each 10% increment of cell height was normalized using the adhesion area. The normalized cross-sectional area, S_{cn} , was plotted against relative height (Figure 8). In all groups, the mean of the normalized cross-sectional area decreased from the bottom to the top. The mean of normalized cross-sectional area of CD groups obtained by the conventional method was significantly smaller than that obtained by the proposed method in the range of $H_r = 0.1$ – 0.6 although the mean of normalized cross-sectional area of CON and COL groups of the conventional method was nearly the same as those of the proposed method, respectively. As shown in Figure 8(d), the normalized cross-sectional areas of CD and COL extracted by the present method were significantly larger than those of CON in the range of $H_r = 0.3$ – 0.9 and 0.1 – 0.6 , respectively (both $P < 0.05$, Bonferroni correction). The standard deviation of the CD normalized cross-sectional area was much greater than those of CON and COL.

4. Discussion

Analyzing the effects of actin filament and microtubule disruption on cell morphology using simple parameters, including projection area and height, is difficult because of the 3D cell shape. For example, distinguishing among a circular cone, a cylindrical column, and an ellipsoidal body is impossible if they have the same projection area and height. We rebuilt 3D cell shapes using fluorescence images of actin filaments and microtubules. Although segmenting cells with fluorescence microscopy images of the cytoplasm and nucleus would presumably be easier and more accurate, we were interested in the relationship between cytoskeletal structures and cell shape, which necessitated cell shape segmentation from cytoskeleton images. Cytoskeleton outlines do not strictly coincide with the surface configuration of cells. As a result, we may have omitted cytoplasmic and other intracellular

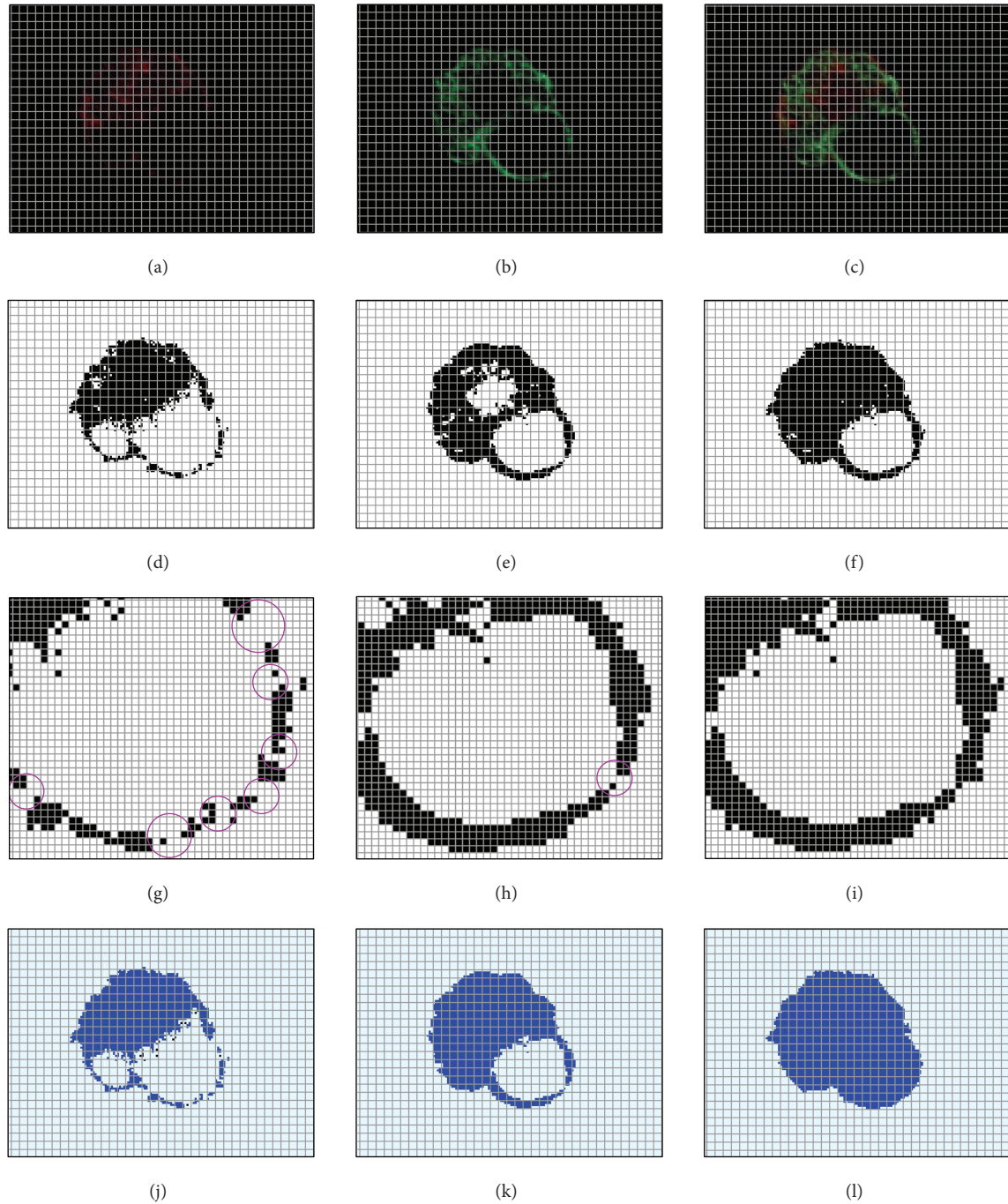


FIGURE 10: A fluorescent image of (a) actin filaments, (b) microtubules, and (c) both. Binarized images of the previous images (d)–(f) without and (g)–(i) with magnification. (j)–(l) Images of the extracted cell regions from (d)–(f) using the described method. The purple circles mark intracellular or nucleus regions not completely encompassed within the cytoskeleton.

components, especially superficial ones, and underestimated cell volumes. Nevertheless, our pilot study confirmed that the cell outline delineated by cytoskeletons was almost the same as that observed using optical microscopy (Figure 9). Therefore, a cell segmented from fluorescence microscopy images of cytoskeletons represents cell geometry accurately enough to examine the mechanical role of cytoskeletons in maintaining cell shape.

Double-staining the cytoskeleton worked complementarily to help delineate cell shape. In the algorithm, regional growth is first implemented to define the extracellular region. However, the program fails when an intracellular region, especially the nuclear region where cytoskeletons are not present, is not perfectly isolated from extracellular regions by the cytoskeleton. The example in Figure 10 includes fluorescent images of actin filaments and microtubules separately

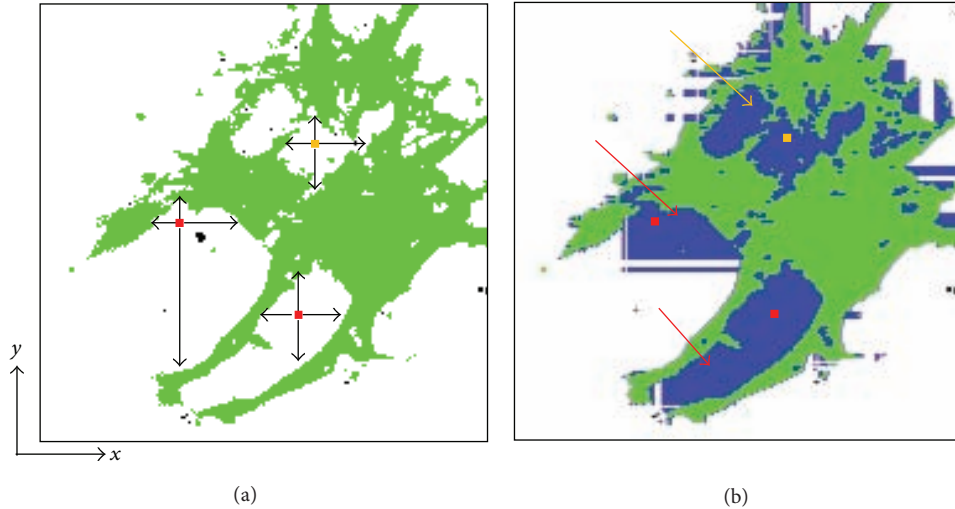


FIGURE 11: Differentiation of intracellular noncytoskeletal regions from the extracellular region. (a) Green regions represent the cytoskeletal pixels, while white ones represent the non-cytoskeletal pixels. The presence of cytoskeletal pixels surrounding $(\pm x, \pm y)$ a non-cytoskeletal pixel of interest was used to distinguish the intracellular non-cytoskeletal region from the extracellular region. If cytoskeletal pixels surrounded the pixel of interest on the x - and y -axes, it was recognized as an intracellular pixel. The yellow and red pixels are recognized as intracellular pixels, although red pixels should be identified as extracellular. (b) The resulting image of this process. Blue regions represent pixels recognized as intracellular as a result of this process. The red arrows show where this process incorrectly labeled some of the extracellular region.

and overlapped (a)–(c), binarized images of (a)–(c) without (d)–(f) and with magnification (g)–(i), and extracted cell regions of (d)–(f) using our method (j)–(l). When extracting cell regions from fluorescent images of either actin filaments or microtubules alone, the program falsely labeled the intracellular region as extracellular because it was not perfectly encompassed by the cytoskeleton (Figures 10(g) and 10(h)). To minimize the missing links, we overlapped the actin filament and microtubule fluorescent images (Figure 10(i)), with success (Figure 10(l)). Although this technique is not perfect, it drastically reduced the failure rate.

The method was developed to reconstruct cell geometry using fluorescent cytoskeleton images. Conventionally, the region-growing method segments an object using image volumes. Voxels are grouped into larger regions by examining the properties of adjacent voxels radiating from a seed using predefined criteria [21], usually color intensity, including RGB and CT values [22]. Even using conventional methods, distinguishing objects of the same intensity or color is possible in terms of their domain, including the cytoplasm and nucleus [13, 20]. Nevertheless, since the voxels of intracellular non-cytoskeleton components and the extracellular matrix are black in fluorescence microscopy images (Figure 7(a)), differentiating them based solely on color intensity is impossible since only cytoskeletons are recognized as a part of the cell (Figure 7(b)). As a result, volume and adhesion area of cells extracted with the conventional method were significantly smaller than those extracted with the proposed method as shown in Table 1. The mean of normalized cross-sectional area of CD groups obtained by the conventional method was significantly smaller than that obtained by the proposed method as shown in Figure 8(b). These results were attributable to the deficiency of the

conventional method; the conventional method failed to extract the voxels of intracellular non-cytoskeletal components as a part of the cell as shown in Figure 7. Therefore, a new algorithm was added, so that non-cytoskeleton pixels surrounded $(\pm x, \pm y)$ by cytoskeleton pixels were recognized as a part of the cell (Figure 11(a)). This algorithm was expected to distinguish the intracellular noncytoskeletal and extracellular regions. Although this process helped fill out the intracellular region, the resulting image included areas thought to be extracellular (Figure 11(b)). The method was revised to exclude pixels in the extracellular region from the previous process, which was accomplished by applying the region-growing method to the extracellular region. All nonextracellular, noncytoskeletal pixels must be intracellular and belong to one of the cells in the image. Applying the region-growing method to the extracellular region before the intracellular region is unique to this algorithm, as the region-growing method is normally used to segment only the region of interest.

Regional growth was implemented three-dimensionally (Figure 12). The tips of three-dimensionally extending cytoskeletons appear isolated from the main body of the cell and would be absent if two-dimensional regional growth was performed on the top image. However, by expanding the region in the z , in addition to x and y directions, the three-dimensionally protruding processes were successfully extracted. This method facilitates the separate identification of each cell, even when multiple cells appear in one image (Figure 13). If cells are touching, they must be separated manually before running the program.

As observed in previous studies, disrupting actin filaments and microtubules induced 3D changes in cell shape [2, 7, 11]. In adherent cells, actin filaments generate contraction

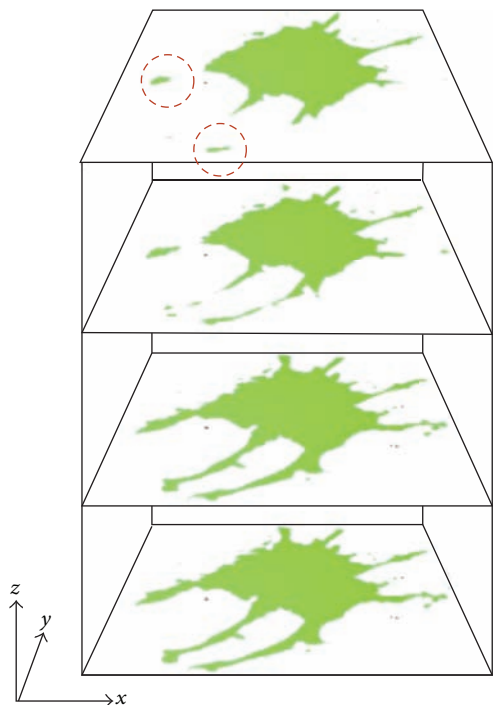


FIGURE 12: Cross-sectional images of a cell extracted using our method whereby the region was grown three-dimensionally. The red circles highlight the tips of parts of the cytoskeleton that appear to be separate from the main cell body in the top image. If the region were grown only in the x - y plane, these areas would be absent.

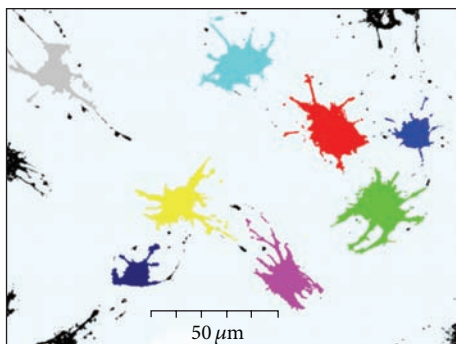


FIGURE 13: Cell segmentation obtained using our method. Eight cells in one image was identified individually using the program.

forces [23], and with focal adhesions, fasten the cell to the extracellular matrix. Therefore, the disruption of actin filaments leads to intracellular mechanical instability, causing partial detachment of the cell from the extracellular matrix at some focal adhesions [11, 24, 25]. In addition, a decrease in the actin filament contraction force induces a relative increase in cortical tensions. Therefore, the partial detachment and reduction in the contraction force of cells due to actin filament disruption results in an increase in cell height and decrease in cell adhesion area. In contrast to actin filaments, microtubules, together with the extracellular matrix, are

thought to bear compressive forces that negate the contraction force at focal adhesions [11]. Therefore, microtubule disruption leads to a relative increase in contraction force, which overwhelms the compressive force exerted by the extracellular matrix.

The segmentation method we described has some limitations. It cannot be used on overlapping cytoskeletons of different cells because our algorithm examines only intensity-based flags of each voxel and cannot differentiate the cytoskeletons of two cells if they overlap. Hence, we excluded overlapping cells from the analysis. Another limitation lies in differentiating voxels of the extracellular matrix from those of intracellular components, which is problematic when cytoskeletons do not form a loop enclosing intracellular components. In such cases, intracellular voxels were merged with extracellular matrix voxels in the process of defining the extracellular region, which hollowed the cell body. Although these limitations must be addressed in future analyses, the morphometric data obtained suggest the potential of this method.

5. Summary and Conclusions

We developed a new method to reconstruct cell geometry from confocal fluorescence microscopy images of cytoskeletons. Extracting extracellular regions first to differentiate intracellular noncytoskeletal and extracellular regions, which both appear black in fluorescent images of cytoskeletons, is unique to this method. Cell geometry was successfully segmented from confocal fluorescence microscopy images of cytoskeletons, which outlined the cell. The analysis of the morphometric data revealed that actin filament and microtubule disruption lead to mechanical disequilibrium within the cell and at focal adhesions, causing the cell to reshape. The results indicate that this is a promising segmentation method for examining changes in cell morphological in relation to internal cytoskeletal structures. Using cell segmentation to reveal the cytoskeleton can be used to develop a more detailed cell structure model and to study the relationships among cell mechanics, functions, and structures.

Conflict of Interests

The authors do not have any conflict of interests to disclose.

Acknowledgments

This work was partly supported by “Grant-in-Aid for JSPS Fellows (21-1007),” Japan Society for the Promotion of Science (JSPS), and “The Next-Generation Integrated Simulation of Living Matter,” part of the Development and Use of the Next-Generation Supercomputer Project of the Ministry of Education, Culture, Sports, Science and Technology (MEXT). The authors thank Dr. Kenichiro Koshiyama and Mr. Yasuhiro Shimada for their useful comments on this work.

References

- [1] C. S. Chen, M. Mrksich, S. Huang, G. M. Whitesides, and D. E. Ingber, "Geometric control of cell life and death," *Science*, vol. 276, no. 5317, pp. 1425–1428, 1997.
- [2] D. E. Ingber, "Fibronectin controls capillary endothelial cell growth by modulating cell shape," *Proceedings of the National Academy of Sciences of the United States of America*, vol. 87, no. 9, pp. 3579–3583, 1990.
- [3] R. Singhvi, A. Kumar, G. P. Lopez et al., "Engineering cell shape and function," *Science*, vol. 264, no. 5159, pp. 696–698, 1994.
- [4] V. M. Weaver, S. Lelièvre, J. N. Lakins et al., " β 4 integrin-dependent formation of polarized three-dimensional architecture confers resistance to apoptosis in normal and malignant mammary epithelium," *Cancer Cell*, vol. 2, no. 3, pp. 205–216, 2002.
- [5] S. R. Heidemann, S. Kaech, R. E. Buxbaum, and A. Matus, "Direct observations of the mechanical behaviors of the cytoskeleton in living fibroblasts," *Journal of Cell Biology*, vol. 145, no. 1, pp. 109–122, 1999.
- [6] T. Lecuit and P. F. Lenne, "Cell surface mechanics and the control of cell shape, tissue patterns and morphogenesis," *Nature Reviews Molecular Cell Biology*, vol. 8, no. 8, pp. 633–644, 2007.
- [7] G. T. Charras and M. A. Horton, "Single cell mechanotransduction and its modulation analyzed by atomic force microscope indentation," *Biophysical Journal*, vol. 82, no. 6, pp. 2970–2981, 2002.
- [8] D. E. Ingber, D. Prusty, Z. Sun, H. Betensky, and N. Wang, "Cell shape, cytoskeletal mechanics, and cell cycle control in angiogenesis," *Journal of Biomechanics*, vol. 28, no. 12, pp. 1471–1484, 1995.
- [9] I. Karl and J. Bereiter-Hahn, "Cell contraction caused by microtubule disruption is accompanied by shape changes and an increased elasticity measured by scanning acoustic microscopy," *Cell Biochemistry and Biophysics*, vol. 29, no. 3, pp. 225–241, 1998.
- [10] A. Kim and W. Matthew Petroll, "Microtubule regulation of corneal fibroblast morphology and mechanical activity in 3-D culture," *Experimental Eye Research*, vol. 85, no. 4, pp. 546–556, 2007.
- [11] K. Nagayama and T. Matsumoto, "Contribution of actin filaments and microtubules to quasi-in situ tensile properties and internal force balance of cultured smooth muscle cells on a substrate," *American Journal of Physiology*, vol. 295, no. 6, pp. C1569–C1578, 2008.
- [12] Y. Ujihara, H. Miyazaki, and S. Wada, "Morphological study of fibroblasts treated with cytochalasin D and colchicine using a confocal laser scanning microscopy," *The Journal of Physiological Sciences*, vol. 58, no. 7, pp. 499–506, 2008.
- [13] R. Adams and L. Bischof, "Seeded region growing," *IEEE Transactions on Pattern Analysis and Machine Intelligence*, vol. 16, no. 6, pp. 641–647, 1994.
- [14] P. Bamford and B. Lovell, "Unsupervised cell nucleus segmentation with active contours," *Signal Processing*, vol. 71, no. 2, pp. 203–213, 1998.
- [15] D. Cremers, M. Rousson, and R. Deriche, "A review of statistical approaches to level set segmentation: integrating color, texture, motion and shape," *International Journal of Computer Vision*, vol. 72, no. 2, pp. 195–215, 2007.
- [16] S. L. Horowitz and T. Pavlidis, "Picture segmentation by tree traversal algorithm," *Journal of the Association for Computing Machinery*, vol. 23, no. 2, pp. 368–388, 1976.
- [17] M. Kass, A. Witkin, and D. Terzopoulos, "Snakes: active contour models," *International Journal of Computer Vision*, vol. 1, no. 4, pp. 321–331, 1988.
- [18] E. Sifakis, C. Garcia, and G. Tziritas, "Bayesian level sets for image segmentation," *Journal of Visual Communication and Image Representation*, vol. 13, no. 1-2, pp. 44–64, 2002.
- [19] A. Yezzi, A. Tsai, and A. Willsky, "A fully global approach to image segmentation via coupled curve evolution equations," *Journal of Visual Communication and Image Representation*, vol. 13, no. 1-2, pp. 195–216, 2002.
- [20] C. Wählby, J. Lindblad, M. Vondrus, E. Bengtsson, and L. Björkesten, "Algorithms for cytoplasm segmentation of fluorescence labelled cells," *Analytical Cellular Pathology*, vol. 24, no. 2-3, pp. 101–111, 2002.
- [21] R. C. Gonzalez and R. E. Woods, *Digital Image Processing*, Prentice Hall, New Jersey, NJ, USA, 2nd edition, 2002.
- [22] M. Nakamura, S. Wada, T. Miki, Y. Shimada, Y. Suda, and G. Tamura, "Automated segmentation and morphometric analysis of the human airway tree from multidetector CT images," *The Journal of Physiological Sciences*, vol. 58, no. 7, pp. 493–498, 2008.
- [23] D. E. Ingber, "Cellular tensegrity: defining new rules of biological design that govern the cytoskeleton," *Journal of Cell Science*, vol. 104, no. 3, pp. 613–627, 1993.
- [24] D. Choquet, D. P. Felsenfeld, and M. P. Sheetz, "Extracellular matrix rigidity causes strengthening of integrin-cytoskeleton linkages," *Cell*, vol. 88, no. 1, pp. 39–48, 1997.
- [25] D. E. Ingber, "Tensegrity II. How structural networks influence cellular information processing networks," *Journal of Cell Science*, vol. 116, no. 8, pp. 1397–1408, 2003.

Research Article

Discrimination between Alzheimer's Disease and Mild Cognitive Impairment Using SOM and PSO-SVM

Shih-Ting Yang,¹ Jiann-Der Lee,¹ Tzyh-Chyang Chang,^{1,2} Chung-Hsien Huang,¹
Jiun-Jie Wang,³ Wen-Chuin Hsu,^{4,5} Hsiao-Lung Chan,¹ Yau-Yau Wai,^{3,6} and Kuan-Yi Li⁷

¹ Department of Electrical Engineering, Chang Gung University, Tao-Yuan 333, Taiwan

² Department of Occupational Therapy, Bali Psychiatric Center, New Taipei City 249, Taiwan

³ Department of Medical Imaging and Radiological Sciences, Chang Gung University, Tao-Yuan 333, Taiwan

⁴ Department of Neuroscience, Chang Gung Memorial Hospital, Tao-Yuan 333, Taiwan

⁵ Chang Gung Dementia Center, Chang Gung Memorial Hospital, Tao-Yuan 333, Taiwan

⁶ Department of Medical Imaging and Intervention, Chang Gung Memorial Hospital, Tao-Yuan 333, Taiwan

⁷ Department of Occupational Therapy, Chang Gung University, Tao-Yuan 333, Taiwan

Correspondence should be addressed to Jiann-Der Lee; jdlee@mail.cgu.edu.tw

Received 15 February 2013; Accepted 13 April 2013

Academic Editor: Chung-Ming Chen

Copyright © 2013 Shih-Ting Yang et al. This is an open access article distributed under the Creative Commons Attribution License, which permits unrestricted use, distribution, and reproduction in any medium, provided the original work is properly cited.

In this study, an MRI-based classification framework was proposed to distinguish the patients with AD and MCI from normal participants by using multiple features and different classifiers. First, we extracted features (volume and shape) from MRI data by using a series of image processing steps. Subsequently, we applied principal component analysis (PCA) to convert a set of features of possibly correlated variables into a smaller set of values of linearly uncorrelated variables, decreasing the dimensions of feature space. Finally, we developed a novel data mining framework in combination with support vector machine (SVM) and particle swarm optimization (PSO) for the AD/MCI classification. In order to compare the hybrid method with traditional classifier, two kinds of classifiers, that is, SVM and a self-organizing map (SOM), were trained for patient classification. With the proposed framework, the classification accuracy is improved up to 82.35% and 77.78% in patients with AD and MCI. The result achieved up to 94.12% and 88.89% in AD and MCI by combining the volumetric features and shape features and using PCA. The present results suggest that novel multivariate methods of pattern matching reach a clinically relevant accuracy for the a priori prediction of the progression from MCI to AD.

1. Introduction

Alzheimer's disease (AD) [1] is the most common type of dementia. Clinical signs are characterized by progressive cognitive deterioration, together with declining activities of daily living and by neuropsychiatric symptoms or behavioral changes. The early detection of AD is potentially challenging because of several reasons. First of all, there existed no known biomarkers. The disease usually has an insidious onset which can be a combination of genetic and environmental factors. It is difficult to differentiate other types of dementia.

Mild cognitive impairment (MCI) is a transitional stage between normal aging and demented status. The syndrome

is defined by the greater cognitive decline than age and education matched individuals, but no interference of daily function [2]. According to the major symptoms, MCI is characterized with memory loss and cognitive impairment. Research has reported that MCI has a risk between 10% to 64% developing AD [3, 4]. AD is a progressively neurodegenerative disorder and is distinguished from MCI by the progressive deterioration of daily function. The prevalence of AD increases dramatically at age 65 and it affects approximately 26 million people worldwide, which may increase fourfolds by the year of 2050. Recent reports in the treatment or prevention of AD lead to a growing concerns in the early diagnosis. Therefore, the detection of changes in

brain tissues that reflect the pathological processes of MCI would prevent or postpone the disease progresses either from normal control to MCI or from MCI to AD. If MCI can be diagnosed at an early stage and effectively intervened, then it is possible to reduce the advanced damages.

Since the poor performance in memory and execution function indicates the high risk of dementia, the probable AD patients are usually evaluated by standardized neuropsychological tests [5–8]. Additionally, many studies have been proposed to examine the predictive abilities of nuclear imaging with respect to AD and other dementia illnesses [9–13]. However, under the consideration of imaging cost and noninvasive requirement, magnetic resonance imaging (MRI) has been widely used for early detection and diagnosis of MCI and AD [14–17].

Atrophy typically starts in the medial temporal and limbic areas, subsequently extending to parietal association areas, and finally to frontal and primary cortices. Early changes in hippocampus and entorhinal cortex have been demonstrated with the help of MRI, and these changes are consistent with the underlying pathology of MCI and AD. Many studies have used manual or automatic methods to measure hippocampus and entorhinal cortex [18–20]. Hippocampal volumes and entorhinal cortex measures have been found to be equally accurate in distinguishing between AD and normal cognitive elderly subjects [21]. However, the segmentation and identification of hippocampus or entorhinal cortex are usually sensitive to the subjective opinion of the operator and also time consuming. In addition, the enlargement of ventricles is also a significant characteristic of AD due to neuronal loss. Ventricles are filled with cerebrospinal fluid (CSF) and surrounded by gray matter (GM) and white matter (WM). As a result, by measuring the ventricular enlargement, hemispheric atrophy rate shows higher correlation with the disease progression.

In this study, we have designed an MRI-based classification framework to distinguish the patients of MCI and AD from normal individuals using multiple features and different classifiers. Since the features adopted here are volume-related and shape-related, we also aimed to investigate whether the combination of both statistical analysis and principal component analysis (PCA) would improve the accuracies of classification than using volume-related alone, shape-related alone, or all features. Our hypothesis was that the combination of all MRI-based features is helpful for distinguishing the patients with early Alzheimer’s disease from the subjects with mild cognitive impairment and healthy controls, respectively.

The remainder of this paper is organized as follows. Section 2 illustrated the proposed scheme, including features extraction and used classifiers, that is, self-organizing map (SOM), support vector machine (SVM), particle swarm optimization (PSO), and the proposed hybrid PSO-SVM. Statistical analysis, experimental results, and discussion are revealed in Section 3. Finally, conclusions are included in Section 4.

2. The Proposed Schemes

Figure 1 is the flowchart that demonstrated the system we proposed. In the step of *Feature Extraction*, spatial normalization

is performed by coregistering the brain MRI data from each individual to a T1-weighted MRI template such that these images of the investigated subjects will be in the same scale space. Next, with the aids of segmentation and morphological procedures, all MRI brain images are segmented into GM, WM, CSF, and ventricle’s tissues and shape descriptors. Here, volume-related and shape-related features are utilized for further classification. The step of *Feature Reduction* is divided into two parts: (1) Mann-Whitney U test is adopted to filter out the features with low discriminative power; (2) principal component analysis (PCA) is applied to reduce the dimensions of feature space. Route I only uses U test; Route II is combined with U test and PCA. At last, a classifier, for example, SOM, SVM, and PSO-SVM, is employed to classify tested volunteers into three categories: normal individuals, MCI, and AD patients. The details of the proposed method are described below.

2.1. Spatial Normalization of MRI Data. Spatial normalization of the brain images is useful for determining what happens generically over individuals. It is a procedure to register an MRI data set to a standard coordinate system, also known as Talairach and Tournoux coordinate system [22]. With the aid of normalization, all images were spatially normalized to stereotactic space ICBM-152 [23] via a 12-degrees-of-freedom affine transformation which normalizes the brain in terms of dimensions, position, and spatial orientation.

2.2. Volume Features Extraction. The volumes of brain tissues such as GM, WM, and CSF indicate important information, especially in brain degeneration diseases [24]. A clustering-based segmentation algorithm provided by SPM8 [25] is using a modified Gaussian mixture model to extract GM, WM and CSF probability maps from whole-brain MRI data. The intensities of voxels belonging to each of these clusters conform to a normal distribution which can be described by a mean, a variance, and the number of voxels belonging to the distribution. Here, the volumes of GM, WM, CSF, and whole-brain are calculated by

$$\begin{aligned} \text{volume}_{\text{tissue}} &\approx \sum_{\forall i \in I} (P(C_{\text{tissue}} | f(i)) > 0.5), \\ \text{volume}_{\text{whole}} &\approx \sum_{\forall i \in I} (P(C_{\text{GMVWM}} | f(i)) > 0.5), \end{aligned} \quad (1)$$

where i is any pixel of the MRI data and $f(i)$ stands for the gray level of i . C means the cluster. tissue stands for the parts of GM, WM, or CSF. Figure 2 illustrates the segmentation results of the normal individual and AD patient used in this study.

Next, we employ region growing and double threshold algorithm [26] to extract binary ventricle volume data, that is, $M(x, y, z)$. The morphological operators, for example, erosion and dilation, are used to obtain the binary ventricle regions. And the edges of binary images are detected by applying Sobel operation on a slice-by-slice basis. Then, this segmented region will construct a binary mask image. In

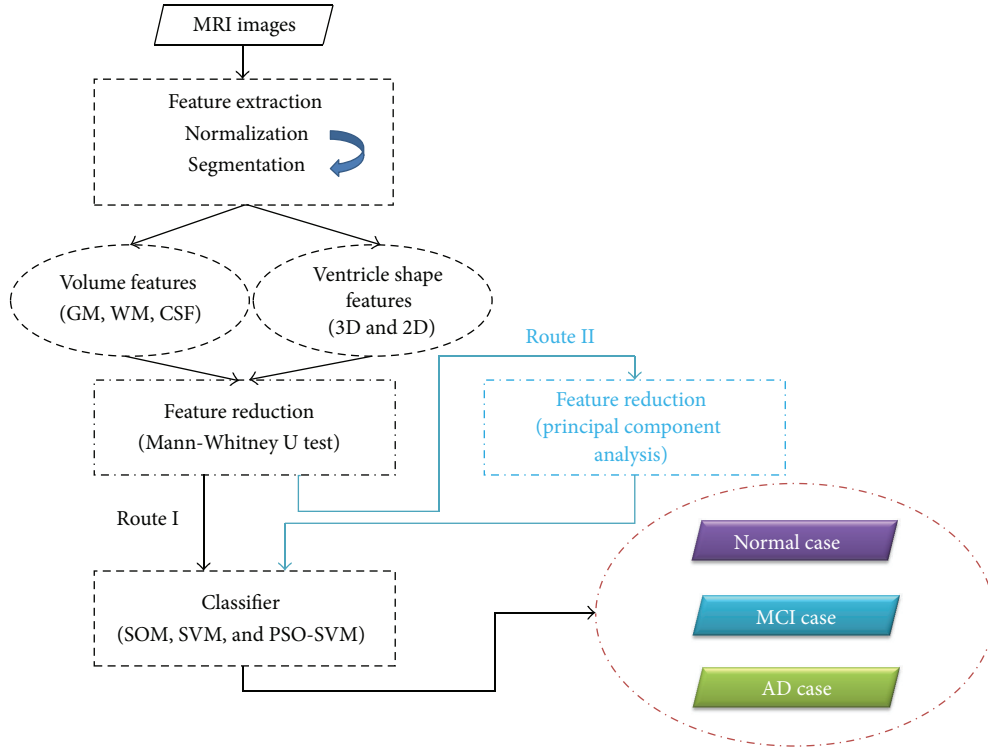


FIGURE 1: Flowchart of the proposed image-aided diagnosis system.

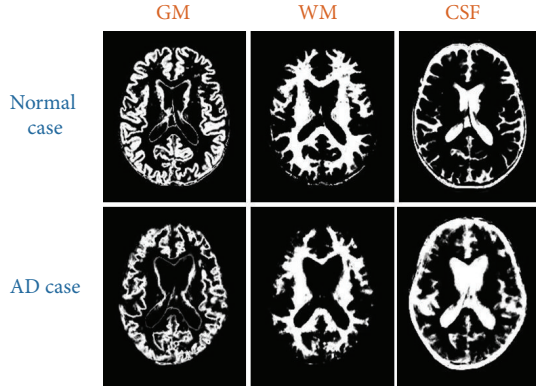


FIGURE 2: Segmentation results of a normal individual and an AD patient used in this study.

this mask image, 1 (white) denotes the ventricle pixel, and 0 (black) denotes the nonventricle pixel. Finally, we can calculate the volume of cerebral ventricle by

$$\text{volume}_{\text{ventricle}} \approx \sum_{i \in M} (P(C_{\text{ventricle}} | f(i)) = 1), \quad (2)$$

where i is any pixel of the mask data, M is the mask image, and $f(i)$ denotes the gray level of i .

2.3. Shape Features Extraction. The volume features, which are extracted from the whole three dimensional volume, cannot capture the variation of the anatomical shape. Wang

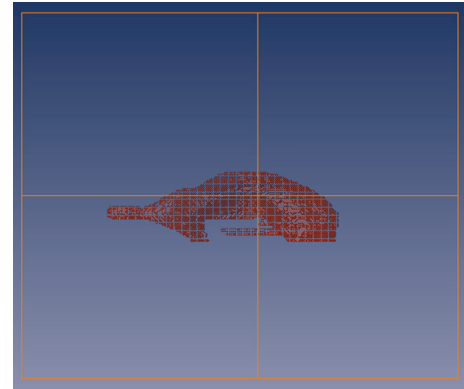


FIGURE 3: Sagittal view of segmented ventricle.

et al. [27, 28] proposed a ventricle shape-based method for improved classification of Alzheimer's patients. Therefore, to enhance the accuracy of the classification, in addition to the volume features, we also added ventricle shape features. Figure 3 shows the sagittal view of ventricle that we segmented. The shape features we analyzed are composed of two types: three-dimensional shape features and two-dimensional shape features. The algorithms to obtain these features are illustrated in the following subsections.

2.3.1. 3D Shape Features. To obtain the feature of 3D shape, a leave-one-out method is used to construct training set and

testing set following Wang's method. Three sets of probability map were then built using

$$P_t(x, y, z) = \frac{1}{N} \sum_{i=1}^N I_t^i(x, y, z), \quad (3)$$

where t indicates the type of the subjects, inclusive of normal control, AD, and MCI. N is the number of training samples, and I denotes the gray level of the ventricular mask image. In order to compare the differences of patients (AD and MCI) and normal controls, we subtracted the normal probability map from the patient probability map to obtain the discriminate map. At last, a matching coefficient (MC) between a testing input and the discriminate map is calculated by

$$\begin{aligned} \text{MC}_{\text{Normal or patient}}^i &= \sum_{\forall x, y, z} D(x, y, z) \\ &\times T_{\text{Normal or patient}}^i(x, y, z), \end{aligned} \quad (4)$$

where $D(x, y, z)$ is the discriminate map and T denotes the testing ventricular mask image.

2.3.2. 2D Shape Features. The 2D shape features are extracted from the segmented ventricles on a slice-by-slice basis. In 2D viewpoint, there are many 2D ventricle slices for each case. In order to effectively compare the differences in each case, we selected the slices with maximum areas from 3D ventricle data sets as the datum plane. These 2D shape features used herein are referred to the work of Yang et al. [29] and listed as follows: (1) *Area*, (2) *Perimeter*, (3) *Compactness*, (4) *Elongation*, (5) *Rectangularity*, (6) *Distances*, (7) *Minimum thickness*, and (8) *Mean signature value*.

2.4. Learning Methods for Classification. Machine learning algorithms can be organized into a taxonomy based on the desired outcome of the algorithm or the type of input available during training the machine. They are often divided into supervised, unsupervised, and reinforcement learning (RL). Supervised learning requires the explicit provision of input-output (I/O) pairs and the task is one of constructing a mapping from one to the other. Non-supervised learning has no concept of target data and performs processing only on the input data. In contrast, RL uses a scalar reward signal to evaluate I/O pairs and hence discover, through trial and error, the optimal outputs for each input. In this sense, RL can be thought of as intermediary to supervised and non-supervised learning since some form of supervision is present, albeit in the weaker guise of the reward signal. As such, the trained algorithm may be treated as a "black box" encapsulating knowledge gleaned from the training data whose inputs are useful for producing the expected outcome. For this reason, machine learning and computer-aided diagnostics (CADs) have been of growing interest in the field of medical applications. To evaluate whether the performance of supervised and non-supervised methods is good or not, we used three classifiers to produce the outcome.

In many researches of pattern recognition, dataset is often divided into two subsets of training and testing. The former

is used to create the model, and the latter is used to assess the accuracy of the model to predict the unknown sample. This method can be called Train-and-Test method. Cross-validation is the experimental method to effectively estimate the generalization error. In this study, leave-one-out cross-validation (LOOCV) is adopted in three classifiers to estimate dependable generalization error. LOOCV involves using a single observation from the original sample as the validation data, and the remaining observations as the training data. In this section, the classifiers we adopted are illustrated in the following subsections particularly.

2.4.1. Self-Organizing Map Architecture. A self-organizing map (SOM) is a type of artificial neural network for the visualization of high-dimensional data. In general, SOMs are divided into two parts: training and mapping. Training builds the map using input examples, called a Kohonen map [30]. An SOM consists of components called nodes or neurons. Each node has a set of neighbors. When this node wins a competition, not only its weight is adjusted, but those of the neighbors are also changed. They are not changed as much though. The further the neighbor is from the winner, the smaller its weight change. Furthermore, as training goes on, the neighborhood gradually shrinks. At the end of training, the neighborhoods have shrunk to zero size.

When a training example is fed to the network, its Euclidean distance to all weight vectors is computed by using (5). Here n denotes the dimension of data, and t is the index of the data item in a given sequence,

$$x(t) = \{\zeta_1(t), \zeta_2(t), \dots, \zeta_n(t)\}. \quad (5)$$

The neuron with weight vector most similar to the input is called the best matching unit (BMU). The weights of the BMU and neurons close to it in the SOM lattice are adjusted towards the input vector. The magnitude of the change decreases with time and with distance from the BMU. The update formula for a neuron with weight vector is

$$m_i(t+1) = m_i(t) + \alpha(t) h_{ci}(t) [x(t) - m_i(t)], \quad (6)$$

where $\alpha(t)$ is a monotonically decreasing learning coefficient and $x(t)$ is the input vector. The neighborhood function $h_{ci}(t)$ depends on the lattice distance between the BMU and neuron. The neighborhood function $h_{ci}(t)$ is

$$h_{ci}(t) = \frac{e^{-\|r_i - r_c\|^2}}{2\sigma^2(t)}. \quad (7)$$

Figure 4 illustrates the procedure of SOM classifier. In this study, we use a two-stage method for learning [31]. First, we adopt less iterative time, higher learning rate, and large neighborhood distance for learning and make it convergence speedily. After repeating many times, we can acquire network parameters which have the best convergence. Next, combining higher iterative time, less learning rate, and small neighborhood distance with network parameters obtained in first stage to conduct second learning and adjust network parameters slowly. At last, we obtain these parameters:

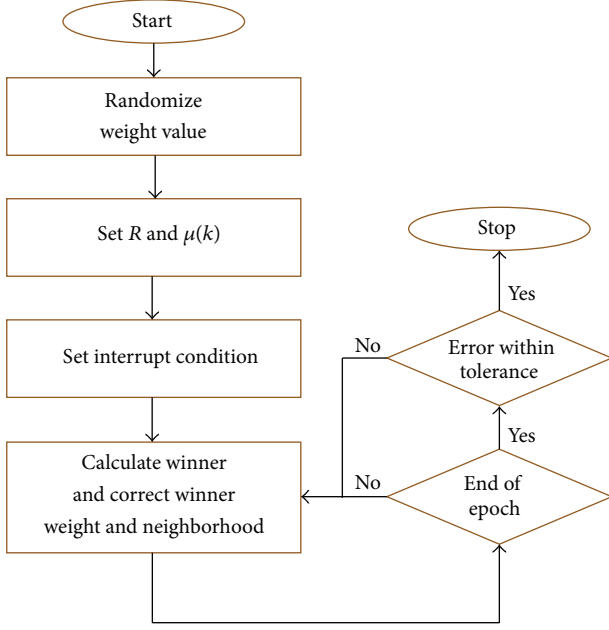


FIGURE 4: Basic procedure of SOM classifier.

iterative time is set as 1000 epochs, ordering phase learning rate = 0.9, tuning phase learning rate = 0.5, and tuning phase neighborhood distance = 0.5. In order to verify the stability of SOM to generalize the correct tendency, the classifier was trained 10 times to get reliable results. Thirty cases are chosen (AD = 7, Normal = 7, MCI = 8) to be the training set randomly. Scaling of variables is of special importance in our model since the SOM algorithm uses Euclidean metric to measure distances between vectors. In order to solve this problem, we achieved this by linearly scaling all variables so that their variances were equal to one.

2.4.2. Support Vector Machine. SVM is a type of artificial neural networks that is, trained by using supervised learning, have shown their advantage on reducing training-and-testing errors, resulting in obtaining higher recognition accuracy [32]. However, some feature data are linearly nonseparable. In some situations, features are not perfectly separable, especially at the border between categories. To allow some flexibility in separating the categories, SVMs utilize a cost parameter, denoted as C , to control the trade-off between allowing training errors and forcing rigid margins. The cost function with C is defined as (8), where ζ_i is a slack variable,

$$\text{Cost} = C \sum_{i=1}^N (\zeta_i). \quad (8)$$

Mapping the patterns in a high dimension feature space is generated through combining features to form a kernel matrix. The kernel matrix is usually constructed by using a kernel function which takes two patterns as arguments and outputs a value. In this study, a radial basis function (RBF) kernel, as shown in (9), is employed. We use one-against-rest assemblies classifiers that distinguish one from all

TABLE I: Demographic data and cognitive scores.

Group	Normal control	MCI	AD
Individuals (male/female)	17 (10/7)	18 (9/9)	17 (9/8)
Mean age (yrs)	71.43 ± 4.43	72.50 ± 4.00	72.70 ± 3.93
Education time (yrs)	10.17 ± 5.21	8.22 ± 5.25	5.24 ± 5.36
MMSE scores	28.18 ± 1.70	25.06 ± 4.11	13.29 ± 6.69

the other classes. This strategy consists of constructing one SVM per class, which is trained to distinguish the samples of one class from the samples of all remaining classes. Usually, classification of an unknown pattern is done according to the maximum output among all SVMs,

$$k(x_i, y_j) = e^{-\gamma \|x_i - y_j\|^{\text{Fit}_p}}, \quad i = j = 1, 2, \dots, n, \quad (9)$$

where x_i denotes the input vector, y_j denotes the j th prototype vector, and $\text{Fit}_p = \text{correctly-classified}/\text{total number of testing data}$. Finally, the optimal solution can be solved by using Lagrange method,

$$L_p \equiv \frac{1}{2} \|w\|^2 + C \sum_{i=1}^m \zeta_i - \sum_{i=1}^m \alpha_i \{y_i (w \cdot x_i + b) - 1 + \zeta_i\},$$

$$L_D \equiv \sum_{i=1}^m \alpha_i - \frac{1}{2} \sum_{i=1}^m \alpha_i \alpha_j y_i y_j^k (x_i, y_j), \quad (10)$$

where $\|w\|$ is the Euclidean norm of w , α_i that stands for the Lagrange multipliers, L_p is the Lagrange function, and L_D is the dual solution of L_p . C and γ are used to control the trade-off between training errors and generalization ability in SVM with RBF kernel. Therefore, a PSO was utilized to find the optimal combination of C and γ .

2.4.3. Hybrid PSO-SVM. Particle swarm optimization (PSO) algorithm [33, 34] uses particles moving in an m -dimensional space to search solutions of an optimization problem with m variables. In our approach, PSO is initialized and searches for the optimal particle iteratively. Each particle represents a candidate solution. SVM classifier is built for each candidate solution to evaluate its performance. Velocity and position of particles can be updated by

$$v_{ij}^{t+1} = w \cdot v_{ij}^t + c_1 \text{rand}_1(\text{pbest}_{ij}^t - x_{ij}^t) + c_2 \text{rand}_2(\text{gbest}_{ij}^t - x_{ij}^t)$$

$$x_{ij}^{t+1} = x_{ij}^t + v_{ij}^{t+1}, \quad (11)$$

where t is evolutionary generation, v_{ij} is the velocity of particle i on dimension j , and x_{ij} stands for the position of particle i on dimension j . Inertia weight w is used to balance the global exploration and local exploitation, rand_1 and rand_2 are random functions, and c_1 and c_2 are personal and social learning factors. As we know, if the number of particles,

TABLE 2: Statistical analysis of features.

Features	Mean volume \pm SD				
	Normal	MCI	AD	P value (NC versus MCI)	P value (NC versus AD)
Volume					
V_{GM}	862.4 \pm 42.7	824.6 \pm 57.8	789.7 \pm 84.3	0.016	0.007
V_{WM}	637.6 \pm 45.8	601.8 \pm 21.2	558.1 \pm 63.4	0.021	0.019
V_{CSF}	863.1 \pm 112.9	909.7 \pm 128.5	971.8 \pm 132.5	0.038	0.017
Shape					
Area	1792.4 \pm 278.5	1903.5 \pm 426.6	2361.1 \pm 802.3	0.029	0.024
Area (PR)	673.5 \pm 121.5	874.9 \pm 132.5	911.4 \pm 183.2	0.024	0.018
Area (PL)	647.1 \pm 137.2	872.5 \pm 142.5	910.9 \pm 183.5	0.031	0.011
Area (FR)	151.9 \pm 117.6	231.5 \pm 162.4	262.4 \pm 167.8	0.020	0.009
Area (FL)	162.7 \pm 91.0	258.2 \pm 144.3	278.5 \pm 189.2	0.022	0.010
Perimeter	226.7 \pm 23.1	276.9 \pm 20.2	289.8 \pm 27.6	0.029	0.019
Circularity	45.6 \pm 4.9	39.8 \pm 3.6	38.2 \pm 2.7	0.039	0.021
Elongation	1.1 \pm 0.4	1.4 \pm 0.6	1.3 \pm 0.2	0.016	0.009
Rectangularity	0.5 \pm 0.2	0.6 \pm 0.4	0.6 \pm 0.1	0.028	0.016
$d(A, G)$	37.3 \pm 2.1	38.4 \pm 3.7	40.6 \pm 4.2	0.031	0.037
$d(B, G)$	36.1 \pm 1.8	39.2 \pm 3.1	43.1 \pm 6.1	0.034	0.028
$d(C, G)$	38.6 \pm 4.3	41.4 \pm 2.9	42.9 \pm 4.6	0.042	0.030
$d(D, G)$	34.7 \pm 2.9	39.7 \pm 1.4	42.8 \pm 4.1	0.022	0.028
$d(A, C)$	72.8 \pm 4.3	81.7 \pm 8.4	83.8 \pm 8.4	0.009	0.011
$d(B, D)$	72.5 \pm 4.9	78.2 \pm 3.1	81.6 \pm 8.2	0.011	0.007
Min thickness	27.4 \pm 3.8	29.0 \pm 2.6	30.1 \pm 3.4	0.020	0.009
Mean Sig.	25.6 \pm 3.1	27.9 \pm 2.7	29.8 \pm 3.1	0.032	0.013

TABLE 3: PCs and their proportion of total variation.

Features	No. of principal component								
	Proportion (%)	C1	C2	C3	C4	C5	C6	C7	C8
Volume features (3)		64.16*	31.57*	4.27					
Shape features (17)		48.79*	23.39*	9.43*	6.45*	3.28*	2.13*	1.01*	0.73*
Volume + shape (20)		49.31*	19.98*	13.62*	6.93*	4.47*	2.35*	0.99	0.72

denoted as P , is too large, it might cause the optimization process to be time consuming. On the contrary, if P is too small, then it is hard to find the optimal solution due to the limited search area. In the literature [35], it is proven that the optimal solution can be obtained when P is between 20 and 40. In this work, the number of the iterations and P is set to 200 and 30, respectively. Similarly, the parameters c_1 , c_2 , and w will affect the convergence of optimization process. If they are set too large, it causes the particle velocity to be speedy and thus cannot obtain the optimal solution. On the other hand, it is time consuming to find the optimal solution [36]. Therefore, we set c_1 , c_2 , and w to 2, 2, and 0.8, respectively.

More specifically, based on the approach [37], the proposed hybrid PSO-SVM aims at optimizing the accuracy of SVM classifier by randomly generating the parameters (C and γ) and estimating the best values for regularization of kernel parameters for SVM model. Basic operation of hybrid PSO-SVM proposed in this paper is given in Figure 5.

This process continues until the performance of SVM converges. The termination criteria are that the iteration

number reaches the maximum number of iterations (100%) or the value of global optimal fitness does not improve after 200 consecutive iterations. In this study, 22 cases were chosen (AD = 7, Normal = 7, MCI = 8) to be the training set.

3. Experimental Results and Discussion

3.1. Materials. According to the research [4], most patients with Alzheimer's disease are aged 65 years or older. Therefore, most of the subjects in the whole data we choose are over 65 years old. The image data used in this study were provided by Chang Gung Memorial Hospital, Lin-Kou, Taiwan. The degree of clinical severity for each participant was evaluated by experienced clinicians whom conducted independent semistructured interviews which included a set of questions regarding the functional status of the participant, along with a standardized neurologic, psychiatric, and health examinations. This interview generates an overall Clinical Dementia Rating (CDR) and Mini Mental State Examination

TABLE 4: Classification results (SOM).

Proportion	Volume features	Volume features + PCA	Shape features	Shape features + PCA	Volume + shape features	Volume + shape features + PCA
AD (versus NC)						
Accuracy	76.47%	82.35%	64.71%	70.59%	76.47%	88.24%
Sensitivity	81.25%	87.50%	68.75%	70.59%	76.47%	88.24%
Specificity	77.78%	83.33%	66.67%	70.59%	76.47%	88.24%
MCI (versus NC)						
Accuracy	61.11%	66.67%	50.00%	50.00%	66.67%	72.22%
Sensitivity	78.57%	85.71%	64.29%	64.29%	75.00%	86.67%
Specificity	66.67%	71.43%	57.14%	57.14%	68.42%	75.00%

TABLE 5: Confused matrix with SOM (volume + shape/volume + shape + PCA).

	NC	MCI	AD
NC	13/15	2/2	1/0
MCI	3/2	12/13	3/5
AD	1/0	4/3	13/15

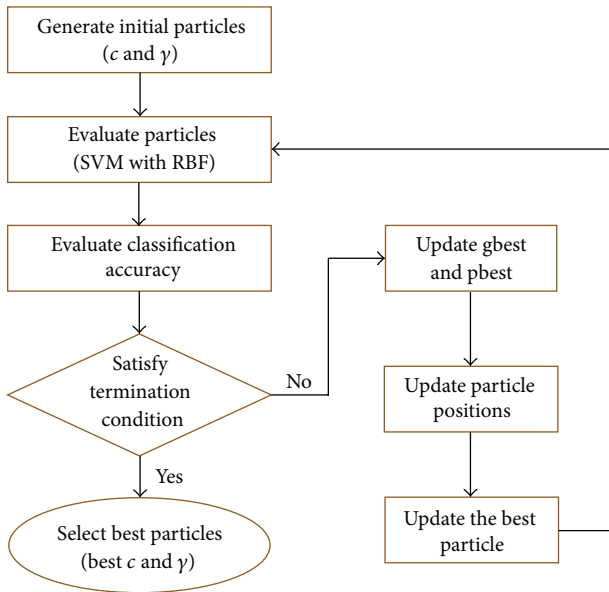


FIGURE 5: Basic operation of proposed PSO-SVM approach.

(MMSE) score. The whole dataset consists of three groups comprising normal control, MCI, and AD. Demographic information is provided in Table 1.

The whole-brain MRI scans were obtained by a 3T MR scanner (Trio A TIM system, Siemens, Erlangen, Germany). T1-weighted images were acquired by magnetization-prepared 180 degrees radio-frequency pulses and rapid gradient-echo (T1-MPRAGE) series. The following imaging parameters were used: repetition time (TR) = 2000 ms, echo time (TE) = 4.16 ms, and flip angle = 9 degrees. The results

were represented as a 224×256 matrix, and slice thickness = 1 mm in 160 slices.

3.2. Statistical Analysis and Classification. Through image processing techniques, we obtained individual volume and shape features. In order to confirm whether there is a significant effect of the classification for these features, we use statistical MW test to compare differences between three groups on various features (continuous variables).

The MW test, also called a Mann-Whitney U or Mann-Whitney Wilcoxon test, is a nonparametric rank-based test for identifying the difference between populations with respect to their medians or means. The test does not require sample data to be normal (sample > 30), and it is relatively insensitive to the nonhomogeneity of the variance of sample data. The null hypothesis is that the two populations from which samples have been drawn have equal medians or means. The alternatives are that the populations do not have equal medians. The two samples are combined, and all sample observations are ranked from smallest to largest. It was performed on each feature to evaluate its discriminative power, as shown in (12). U_{obt} is the smaller value taken from the sum of U_1 and U_2 , where n_1 and n_2 are the sizes of the first and second samples, respectively,

$$Z_U = \frac{U_{\text{obt}} - (n_1 n_2 / 2)}{\sqrt{n_1 n_2 (n_1 + n_2 + 1) / 12}}. \quad (12)$$

The P values obtained from the tests can provide the probability that a variation would assume a value greater than or equal to the observed value strictly by chance. It is known that the P value which is less than the predetermined significance level (0.05) would result in the rejection of the null hypothesis at the 5% (significance) level. All statistical results of volume and shape features we adopted (< 0.05) are shown in Table 2, inclusive of three volume features and seventeen shape features.

3.3. Results. Although the features we adopted have statistical significance (< 0.05) between three groups, some of the features may be redundant or have high correlation. Therefore, principal component analysis (PCA) [38] is used to reduce the dimensionality of a data set consisting of a

TABLE 6: Classification results (SVM).

Proportion	Volume features	Volume features + PCA	Shape features	Shape features + PCA	Volume + shape features	Volume + shape features + PCA
AD (versus NC)						
Accuracy	70.59%	70.59%	58.82%	64.71%	76.47%	82.35%
Sensitivity	70.59%	66.67%	66.67%	78.57%	76.47%	87.50%
Specificity	70.59%	68.75%	63.16%	70.00%	76.47%	83.33%
MCI (versus NC)						
Accuracy	55.56%	61.11%	44.44%	50.00%	77.78%	83.33%
Sensitivity	66.67%	64.71%	61.54%	75.00%	77.78%	88.24%
Specificity	60.00%	61.11%	54.55%	60.87%	76.47%	83.33%

TABLE 7: Confused matrix with SVM (volume + shape/volume + shape + PCA).

	NC	MCI	AD
NC	13/15	0/1	1/0
MCI	3/2	14/15	3/3
AD	1/0	4/2	13/14

large number of interrelated variables, while retaining as much as possible of the variation present in the data set. On the other hand, it can also improve the computation time required for classification. This is achieved by transforming to a new set of variables, the principal components (PCs), which are uncorrelated and are ordered so that the first few retain most of the variation present in all of the original variables. In order to effectively represent all the data, we used the PCs that captured 95% total variation in data set. To train a volume-feature-based classification, the first two principal components were adopted. To train a shape-feature-based classification, only the first eight principal components were adopted. When we integrated volume and shape features into classification, the first six principal components were used to stand for all of the features. Table 3 gives the variances and the coefficients of the PCs, when the analysis is done on the correlation matrix. The symbol * indicates that this PCA coefficient is used as a feature for classification. SOM, SVM, and PSO-SVM were used to train a classifier, and the results were presented in Tables 4, 5, 6, 7, 8, and 9.

It showed the results of accuracy (proportion of all subjects correctly classified), sensitivity (proportion of individuals with a true positive result), and specificity (proportion of individuals with a true negative result) when using different features. The derivations of accuracy, sensitivity, and specificity were expressed in (13), where TP = true positive, TN = true negative, and FP = false positive. Obviously, incorporating shape features, volume features, and PCA provided excellent classification ability than using only one of them,

$$\text{Accuracy (ACC)} = \frac{(\text{TP} + \text{TN})}{(\text{P} + \text{N})}$$

Sensitivity or true positive rate (TPR)

$$= \frac{\text{TP}}{\text{P}} = \frac{\text{TP}}{(\text{TP} + \text{FN})}$$

Specificity or True Negative Rate (TNR)

$$= \frac{\text{TN}}{\text{N}} = \frac{\text{TN}}{(\text{FP} + \text{TN})}$$

(13)

3.4. Discussion. In this study, we investigated the feasibility of using anatomical MR images to extract different types of features as a predictive marker for AD and MCI. We employed multiple features and different classifiers to identify the patients with AD and MCI from normal participants. From the results, volumetric analysis, inclusive of gray/white matter, cerebrospinal fluid, and local shape analysis on ventricle, provides significant atrophy information. Especially, the properties of gray matter volume, ventricular area, elongation, mean signature value, and distances show the statistical significance (<0.01). This implies that using the volume and shape features have the potential ability to identify normal control, AD, and MCI.

By combining both the volumetric features and shape features, the classification accuracy of SOM reached up to 76.47% and 66.67% in patients with AD and MCI, respectively. Moreover, with the help of PCA algorithm, the classification result was improved up to 88.24% and 72.22% in patients with AD and MCI, respectively. The classification accuracy of SVM reached up to 76.47% and 77.78% in patients with AD and MCI, respectively. Moreover, with the help of PCA algorithm, the classification result was improved up to 82.35% and 83.33% in patients with AD and MCI, respectively. With the hybrid classification framework based on PSO, the result achieved up to 82.35% and 77.78% in AD and MCI. Moreover, with the help of PCA algorithm, the classification result was improved up to 94.12% and 88.89% in patients with AD and MCI, respectively. According to the results, combining PSO-SVM with statistical analysis and principal component analysis (PCA) would improve the accuracy of classification.

It was also noted that the classification ability was significant for AD and normal control than the patients with

TABLE 8: Classification results (PSO-SVM).

Proportion	Volume features	Volume features + PCA	Shape features	Shape features + PCA	Volume + shape features	Volume + shape features + PCA
AD (versus NC)						
Accuracy	76.47%	76.47%	70.59%	76.47%	82.35%	94.12%
Sensitivity	76.47%	76.47%	70.59%	76.47%	87.50%	94.12%
Specificity	76.47%	76.47%	70.59%	76.47%	83.33%	94.12%
MCI (versus NC)						
Accuracy	66.67%	66.67%	55.56%	50.00%	77.78%	88.89%
Sensitivity	75.00%	75.00%	66.67%	69.23%	87.50%	94.12%
Specificity	68.42%	68.42%	60.00%	59.09%	78.95%	88.88%

TABLE 9: Confused matrix with PSO-SVM (volume + shape/volume + shape + PCA).

	NC	MCI	AD
NC	15/16	1/1	0/0
MCI	2/1	14/16	3/1
AD	0/0	3/1	14/16

MCI. MCI is a transitional stage between normal cognitive aging and dementia. Therefore, the characteristics of patients with MCI were similar to AD subjects. On the other hand, the characteristic of patients with MCI was also possibly similar to normal participants. Combination with other features was essential to improve the accuracy of classification ability for patients with MCI in an early stage.

4. Conclusion

In this paper, we compared different methods for the classification of patients with AD and MCI based on anatomical T1-weighted MRI. To evaluate and compare the performances of each method, two classification experiments were performed: CN versus AD and CN versus MCI. It is observed that the volume features and shape features can be integrated to increase classification accuracy with the low computational complexity. Classification results also verify our hypothesis that the combination of multimodal features, including volume and shape features, outperforms a single modality of features, possibly because different features are mutually complementary. Furthermore, it is proven that statistical analysis and PCA can achieve accuracies significantly better than all the features that are adopted. In the performance of classifiers used here, it is shown that PSO-SVM can achieve the best accuracy, sensitivity, and specificity, no matter for CN versus AD and CN versus MCI.

For the moment, the classified results are greater for patients with AD and normal participants than for patients with MCI. It can provide clinically useful information at the large-scale population-based screening studies. The results would be welcomed for prognosticating disease progression and providing an objective evaluation of cognitive rehabilitation treatments for dementing illness.

Acknowledgments

The work was supported by National Science Council, Taiwan, under Grant no. NSC98-2221-E-182-040-MY3 and Chang Gung Memorial Hospital with Grant no. CMRP D270053.

References

- [1] S. Gauthier, B. Reisberg, M. Zaudig et al., "Mild cognitive impairment," *The Lancet*, vol. 367, no. 9518, pp. 1262–1270, 2006.
- [2] D. M. Geslani, M. C. Tierney, N. Herrmann, and J. P. Szalai, "Mild cognitive impairment: an operational definition and its conversion rate to Alzheimer's disease," *Dementia and Geriatric Cognitive Disorders*, vol. 19, no. 5-6, pp. 383–389, 2005.
- [3] R. C. Petersen, "Mild cognitive impairment as a diagnostic entity," *Journal of Internal Medicine*, vol. 256, no. 3, pp. 183–194, 2004.
- [4] *Alzheimer's disease facts and figures*, 2012, http://www.alz.org/alzheimers_disease_facts_figures.asp?type=homepage.
- [5] M. F. Folstein, S. E. Folstein, and P. R. McHugh, "Mini mental state: A practical method for grading the cognitive state of patients for the clinician," *Journal of Psychiatric Research*, vol. 12, no. 3, pp. 189–198, 1975.
- [6] C. P. Hughes, L. Berg, and W. L. Danziger, "A new clinical scale for the staging of dementia," *British Journal of Psychiatry*, vol. 140, no. 6, pp. 566–572, 1982.
- [7] E. L. Teng, K. Hasegawa, A. Homma et al., "The cognitive abilities screening instrument (CASI): a practical test for cross-cultural epidemiological studies of dementia," *International Psychogeriatrics*, vol. 6, no. 1, pp. 45–58, 1994.
- [8] T. N. Tombaugh, "Trail Making Test A and B: normative data stratified by age and education," *Archives of Clinical Neuropsychology*, vol. 19, no. 2, pp. 203–214, 2004.
- [9] P. Padilla, J. M. Górriz, J. Ramírez et al., "Analysis of SPECT brain images for the diagnosis of Alzheimer's disease based on NMF for feature extraction," *Neuroscience Letters*, vol. 479, no. 3, pp. 192–196, 2010.
- [10] R. Chaves, J. Ramirez, J. M. Górriz, and C. G. Puntonet, "Alzheimer's Disease Neuroimaging Initiative, Association rule-based feature selection method for Alzheimer's disease diagnosis," *Expert Systems With Applications*, vol. 39, no. 14, pp. 11766–11774, 2012.
- [11] J. Ramírez, J. M. Górriz, F. Segovia et al., "Computer aided diagnosis system for the Alzheimer's disease based on partial

- least squares and random forest SPECT image classification,” *Neuroscience Letters*, vol. 472, no. 2, pp. 99–103, 2010.
- [12] A. Gallix, J. M. Gorriz, J. Ramirez, I. A. Illan, and E. W. Lang, “On the empirical mode decomposition applied to the analysis of brain SPECT images,” *Expert Systems With Applications*, vol. 39, no. 18, pp. 13451–13461, 2012.
- [13] D. Salas-Gonzalez, J. M. Gorriz, J. Ramirez et al., “Two approaches to selecting set of voxels for the diagnosis of Alzheimer’s disease using brain SPECT images,” *Digital Signal Processing*, vol. 21, pp. 746–755, 2012.
- [14] J. E. Iglesias, J. Jiang, C. Y. Liu, and Z. Tu, “Alzheimer’s Disease Neuroimaging Initiative, Classification of Alzheimer’s disease using a self-smoothing operator,” in *Proceedings of the 14th International Conference on Medical Image Computing and Computer Assisted Intervention*, 2012.
- [15] P. Vemuri, J. L. Gunter, M. L. Senjem et al., “Alzheimer’s disease diagnosis in individual subjects using structural MR images: validation studies,” *NeuroImage*, vol. 39, no. 3, pp. 1186–1197, 2008.
- [16] D. Zhang, Y. Wang, L. Zhou, H. Yuan, and D. Shen, “Multimodal classification of Alzheimer’s disease and mild cognitive impairment,” *NeuroImage*, vol. 55, no. 3, pp. 856–867, 2011.
- [17] P. Vemuri, H. J. Wiste, S. D. Weigand et al., “MRI and CSF biomarkers in normal, MCI, and AD subjects: predicting future clinical change,” *Neurology*, vol. 73, no. 4, pp. 294–301, 2009.
- [18] K. Juottonen, M. P. Laakso, K. Partanen, and H. Soininen, “Comparative MR analysis of the entorhinal cortex and hippocampus in diagnosing Alzheimer disease,” *American Journal of Neuroradiology*, vol. 20, no. 1, pp. 139–144, 1999.
- [19] O. Colliot, G. Chételat, M. Chupin et al., “Discrimination between Alzheimer disease, mild cognitive impairment, and normal aging by using automated segmentation of the hippocampus,” *Radiology*, vol. 248, no. 1, pp. 194–201, 2008.
- [20] J. H. Morra, Z. Tu, L. G. Apostolova et al., “Automated mapping of hippocampal atrophy in 1-year repeat MRI data from 490 subjects with Alzheimer’s disease, mild cognitive impairment, and elderly controls,” *NeuroImage*, vol. 45, no. 1, pp. S3–S15, 2009.
- [21] K. Kantarci, “Magnetic resonance markers for early diagnosis and progression of Alzheimer’s disease,” *Expert Review of Neurotherapeutics*, vol. 5, no. 5, pp. 663–670, 2005.
- [22] J. Talairach and P. Tournoux, *Co-Planar Stereotaxic Atlas of the Human Brain*, Thieme, New York, NY, USA, 1988.
- [23] J. Mazziotta, A. Toga, A. Evans et al., “A probabilistic atlas and reference system for the human brain: International Consortium for Brain Mapping (ICBM),” *Philosophical Transactions of the Royal Society B*, vol. 356, no. 1412, pp. 1293–1322, 2001.
- [24] K. H. Fritzsche, A. von Wangenheim, D. D. Abdala, and H. P. Meinzer, “A computational method for the estimation of atrophic changes in Alzheimer’s disease and mild cognitive impairment,” *Computerized Medical Imaging and Graphics*, vol. 32, no. 4, pp. 294–303, 2008.
- [25] UCL Institute of Neurology, <http://www.fil.ion.ucl.ac.uk/spm/>.
- [26] C. F. Jiang, C. H. Huang, and S. T. Yang, “Using maximal cross-section detection for the registration of 3D image data of the head,” *Journal of Medical and Biological Engineering*, vol. 31, no. 3, pp. 217–226, 2011.
- [27] J. Wang, A. Ekin, and G. De Haan, “Shape analysis of brain ventricles for improved classification of alzheimer’s patients,” in *Proceedings of the 15th IEEE International Conference on Image Processing (ICIP ’08)*, pp. 2252–2255, October 2008.
- [28] J. Wang, G. De Haan, D. Unay, O. Soldea, and A. Ekin, “Voxel-based discriminant map classification on brain ventricles for Alzheimer’s disease,” in *Medical Imaging: Image Processing*, vol. 7259 of *Proceedings of SPIE*, February 2009.
- [29] S. T. Yang, J. D. Lee, C. H. Huang, J. J. Wang, W. C. Hsu, and Y. Y. Wai, “An image-aided diagnosis system for dementia classification based on multiple features and self-organizing map,” *Lecture Notes in Computer Science*, vol. 6444, no. 2, pp. 462–469, 2010.
- [30] T. Kohonen, “The self-organizing map,” *Proceedings of the IEEE*, vol. 78, no. 9, pp. 1464–1480, 1990.
- [31] S. Wu and T. W. S. Chow, “Self-organizing and self-evolving neurons: a new neural network for optimization,” *IEEE Transactions on Neural Networks*, vol. 18, no. 2, pp. 385–396, 2007.
- [32] C. Cortes and V. Vapnik, “Support-vector networks,” *Machine Learning*, vol. 20, no. 3, pp. 273–297, 1995.
- [33] J. Kennedy and R. Eberhart, “Particle swarm optimization,” in *Proceedings of the IEEE International Conference on Neural Networks*, vol. 4, pp. 1942–1948, December 1995.
- [34] Z. Cui, L. Wang, and Y. Tan, “Particle swarm optimization with active congregation,” *ICIC Express Letters*, vol. 4, no. 4, pp. 1167–1172, 2010.
- [35] M. Kudo and J. Sklansky, “Comparison of algorithms that select features for pattern classifiers,” *Pattern Recognition*, vol. 33, no. 1, pp. 25–41, 2000.
- [36] Y. Shi and R. Eberhart, “Modified particle swarm optimizer,” in *Proceedings of the IEEE International Conference on Evolutionary Computation (ICEC ’98)*, pp. 69–73, May 1998.
- [37] C. J. Tu, L. Y. Chuang, J. Y. Chang, and C. H. Yang, “Feature selection using PSO-SVM,” *IAENG International Journal of Computer Science*, vol. 33, no. 1, pp. 138–143, 2007.
- [38] I. T. Jolliffe, *Principal Component Analysis*, Springer Series in Statistics, Springer, New York, NY, USA, 2nd edition, 2002.

Research Article

Transfer Function Analysis of Respiratory and Cardiac Pulsations in Human Brain Observed on Dynamic Magnetic Resonance Images

Yi-Hsuan Kao,¹ Wan-Yuo Guo,^{2,3} Adrain Jy-Kang Liou,³ Ting-Yi Chen,^{1,3}
Chau-Chiun Huang,¹ Chih-Che Chou,^{1,4} and Jiing-Feng Lirng^{2,3}

¹ Department of Biomedical Imaging and Radiological Sciences, National Yang-Ming University, Taipei 112, Taiwan

² School of Medicine, National Yang-Ming University, Taipei 112, Taiwan

³ Department of Radiology, Taipei Veterans General Hospital, Taipei 112, Taiwan

⁴ Laboratory of Integrated Brain Research, Department of Medical Research and Education, Taipei Veterans General Hospital, Taipei 112, Taiwan

Correspondence should be addressed to Yi-Hsuan Kao; yhkao@ym.edu.tw

Received 17 January 2013; Accepted 27 March 2013

Academic Editor: Younghae Do

Copyright © 2013 Yi-Hsuan Kao et al. This is an open access article distributed under the Creative Commons Attribution License, which permits unrestricted use, distribution, and reproduction in any medium, provided the original work is properly cited.

Magnetic resonance (MR) imaging provides a noninvasive, *in vivo* imaging technique for studying respiratory and cardiac pulsations in human brains, because these pulsations can be recorded as flow-related enhancement on dynamic MR images. By applying independent component analysis to dynamic MR images, respiratory and cardiac pulsations were observed. Using the signal-time curves of these pulsations as reference functions, the magnitude and phase of the transfer function were calculated on a pixel-by-pixel basis. The calculated magnitude and phase represented the amplitude change and temporal delay at each pixel as compared with the reference functions. In the transfer function analysis, near constant phases were found at the respiratory and cardiac frequency bands, indicating the existence of phase delay relative to the reference functions. In analyzing the dynamic MR images using the transfer function analysis, we found the following: (1) a good delineation of temporal delay of these pulsations can be achieved; (2) respiratory pulsation exists in the ventricular and cortical cerebrospinal fluid; (3) cardiac pulsation exists in the ventricular cerebrospinal fluid and intracranial vessels; and (4) a 180-degree phase delay or inverted amplitude is observed on phase images.

1. Introduction

Human brain mostly is comprised of brain tissues, blood, and cerebrospinal fluid (CSF). These components maintain a fixed volume, while they are protected by and confined in the skull. According to the Monro-Kellie doctrine, in a fixed volume an increase in the volume of one cranial component must be compensated by the decrease in volume of other cranial components [1]. The modulations of intracranial pressure by respiratory and cardiac pulsations are observed by using lumbar, cisternal, and ventricular puncture [2]. Magnetic resonance (MR) imaging, however, provides a noninvasive, *in vivo* imaging technique for studying respiratory and cardiac pulsations in human brains [3–9], because these pulsations

can be recorded as flow-related enhancement on dynamic MR images.

Independent component (IC) analysis is a blind source separation technique [10]. It is described as a partial volume calculation technique when applied to analyze dynamic MR images [11]. The outputs of IC analysis are IC images and corresponding signal-time curves. The output IC images provide a coarse segmentation for voxels with different signal-time curves, and the IC images are assumed to be spatially independent. It has been used to analyze functional MR images [12–14] and to detect cluster microcalcification breast cancer [15]. By applying IC analysis to dynamic MR images, respiratory and cardiac pulsations are observed at intracranial arteries and CSF [16]. However, the propagation

of respiratory and cardiac pulsations in the brain is not yet clear and needs further investigation.

The transfer function analysis is used to study the relationship between input and output signals of a linear time-invariant system [17]. The magnitude and phase of a transfer function reflects the amplitude change and temporal delay from input signals to output signals at different frequency bands. The transfer function between arterial blood pressure and cerebral blood flow velocity in the middle cerebral arteries is used to study cerebral autoregulation in normal subjects [18], in patients with occlusive cerebrovascular diseases and arteriovenous malformations [19], and in patients with carotid stenosis [20]. In functional MR imaging research, transfer function provides information on the temporal delays between regions for investigating how these regions within a network interact with each other [21]. In this study, we applied transfer function analysis to dynamic MR images to investigate the respiratory and cardiac pulsations in the brain of normal subjects.

2. Materials and Methods

2.1. Data Acquisition. Dynamic MR images were acquired from normal subjects on a 1.5-Tesla MR scanner (Signa CV/i, GE Medical Systems, Milwaukee, WI, USA). Written informed consent was obtained. A single-shot, gradient-echo, echo-planar imaging pulse sequence was used for acquiring the images. The scan parameters were $T_E/T_R = 60/200$ ms, flip angle = 90° , field of view = 24×24 cm, image matrix = 128×128 , slice thickness = 5 mm, and one signal averaging. The wavelength of the crusher gradient was increased from 1 ms to 10 ms for suppressing residual transverse magnetic dipole moment [22]. Five hundred and twelve dynamic images were acquired from transaxial planes through and above the third ventricle. The subjects were instructed to breathe normally during the scanning. Image postprocessing procedure was done offline on a personal computer by using software programs written in MATLAB (MathWorks, Inc., Natick, MA, USA).

2.2. Periodogram. The frequencies of respiratory and cardiac pulsations measured from a subject were not stationary during the scan. We calculated a periodogram [23] from the acquired images for choosing an appropriate segment of the data for postprocessing procedure. The 512 dynamic images were arranged into 213 segments with each segment containing 300 sequential dynamic images. Within each segment, the amplitude spectra for the 300 dynamic images were calculated on a pixel-by-pixel basis by using discrete Fourier transform. The sum of the amplitude spectra of all pixels was used to represent this segment. A two-dimensional periodogram was generated, in which the horizontal axis was the starting image number, in which the vertical axis was the frequency, and the gray level was used to represent the amplitude spectra. A segment with most stationary respiratory and cardiac pulsations in the periodogram was selected for the following postprocessing procedure.

2.3. Independent Component Analysis. Temporal mean and standard deviation images were calculated from the selected 300 dynamic images. The temporal mean was subtracted from the dynamic images to produce zero-temporal-mean dynamic images. The FastICA technique [10] was applied to the zero-temporal-mean dynamic images for finding respiratory and cardiac pulsations. We used four output ICs in this experiment.

2.4. Transfer Function Analysis. For a linear time-invariant system, the output signal, $y(t)$, can be expressed as a convolution of the input signal, $x(t)$, and the system response function, $h(t)$, described by

$$y(t) = x(t) \otimes h(t), \quad (1)$$

where \otimes indicates a convolution calculation [17]. The previous equation also can be expressed in the frequency domain as

$$Y(f) = X(f) H(f), \quad (2)$$

where $X(f)$, $Y(f)$, and $H(f)$ are the Fourier transform of $x(t)$, $y(t)$, and $h(t)$, respectively. The transfer function, $H(f)$, is calculated as

$$H(f) = |H(f)| \exp\{i\phi(f)\} = \frac{Y(f)}{X(f)}, \quad (3)$$

where $|H(f)|$ and $\phi(f)$ are the magnitude and phase of the transfer function at frequency f , respectively. The magnitude and phase of $H(f)$ reflect the amplitude change and temporal delay from $x(t)$ to $y(t)$ at different frequencies, respectively. A phase delay can be calculated as the following equation:

$$\tau_p(f) = -\frac{\phi(f)}{2\pi f}. \quad (4)$$

The $\tau_p(f)$ value provides information on the temporal delay of the output signal, $y(t)$, in a periodical waveform at this specific frequency, as compared with the input signal, $x(t)$.

For a global analysis, the transfer function analysis was applied to the four complex-valued output spectra of the FastICA calculation results, by using one spectrum as $X(f)$ and the other three spectra as $Y(f)$ functions. For a pixel-by-pixel analysis of the zero-temporal-mean dynamic images, the signal-time curve at each pixel was Fourier transformed into a complex-valued spectrum, and they were $Y(f)$. The spectra of the FastICA segmentation results showing either good respiratory or cardiac pulsations were selected as the reference spectra, $X(f)$. By using (3), the complex $H(f)$ value were calculated. The averaged values of $|H(f)|$ and $\phi(f)$ within a selected frequency band was calculated to represent the strength and temporal delay information of the pulsation at this frequency band, respectively.

3. Results

The postprocessing procedure for a dataset acquired from a slice through the ventricle is demonstrated in Figures 1–3. The FastICA calculation results for 300 zero-temporal-mean dynamic images are shown in Figure 2, including four

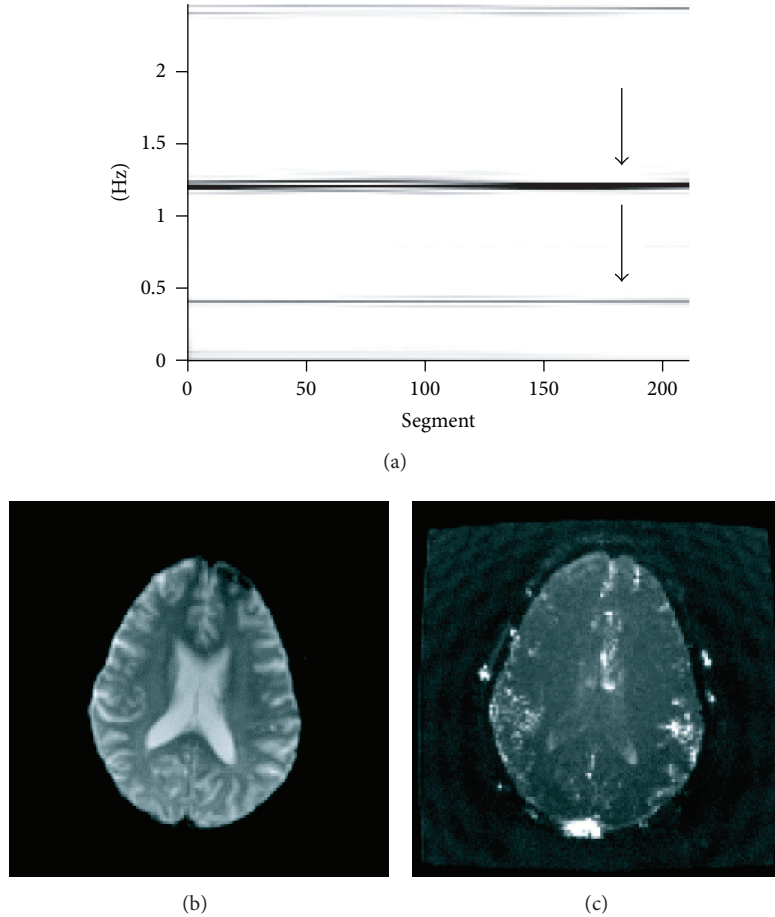


FIGURE 1: Analysis of a dataset acquired from a slice through the third ventricle. The 180th to the 479th dynamic images had stable respiratory and cardiac pulsations (pointed by arrows) as shown in the periodogram (a). The first image of the 512 dynamic images is used to display anatomy (b). Temporal-standard-deviation image illustrates the flow-related enhancement caused by oscillatory flows (c).

output images (a–d) and corresponding signal-time curves (e). Spatiotemporal patterns for the respiratory and cardiac pulsations are well demonstrated in these results. Figure 2(f) displays the corresponding amplitude spectra. Peaks were found at the respiratory (0.42 Hz) and the first harmonic (1.22 Hz) of cardiac frequency bands, which are marked by yellow shaded areas. Figure 2(g) plots the phase, $\phi(f)$, of the transfer function, $H(f)$, obtained from complex divisions using the first (black), third (red), and fourth (blue) spectra of the FastICA segmentation results, divided by the second (green) spectrum of the FastICA segmentation results. Near constant phases were found at the marked respiratory and cardiac frequency bands, indicating the existence of phase delay at these frequency bands.

The $|H(f)|$ and $\phi(f)$ images at frequency bands that correspond to respiratory and cardiac pulsations are displayed in Figure 3. In the transfer function calculation, the green signal-time curve displayed in Figure 2(e) was used as $x(t)$. A 180-degree phase delay or inverted amplitude is observed at pixels with red versus green colors or pixels with yellow versus white colors.

The FastICA segmentation results for a slice above the ventricle are shown in Figure 4. Pixels at the inner and

outer sides of the brain surface are displayed in white and black colors in Figure 4(d). This phenomenon indicates that the signal-time curves at these two regions had either a 180-degree phase delay or inverted amplitudes. The $|H(f)|$ and $\phi(f)$ images at frequency bands that correspond to respiratory and cardiac pulsations are displayed in Figure 5. Again, the 180-degree phase delay or inverted amplitude is observed at pixels with yellow versus white colors in Figure 5(b).

4. Discussion

We analyzed the respiratory and cardiac pulsations in human brain using the transfer function analysis. By using the reference spectra produced from the FastICA segmentation results, the magnitude and phase images at the respiratory and cardiac frequency bands were calculated. The magnitude represented the strength of these pulsations observed at different brain locations. The phase was related to the temporal delay in the periodical waveforms compared with the reference signals. The respiratory and cardiac pulsations were analyzed separately. The assumption of spatial independency used in the IC analysis was not needed in the transfer function

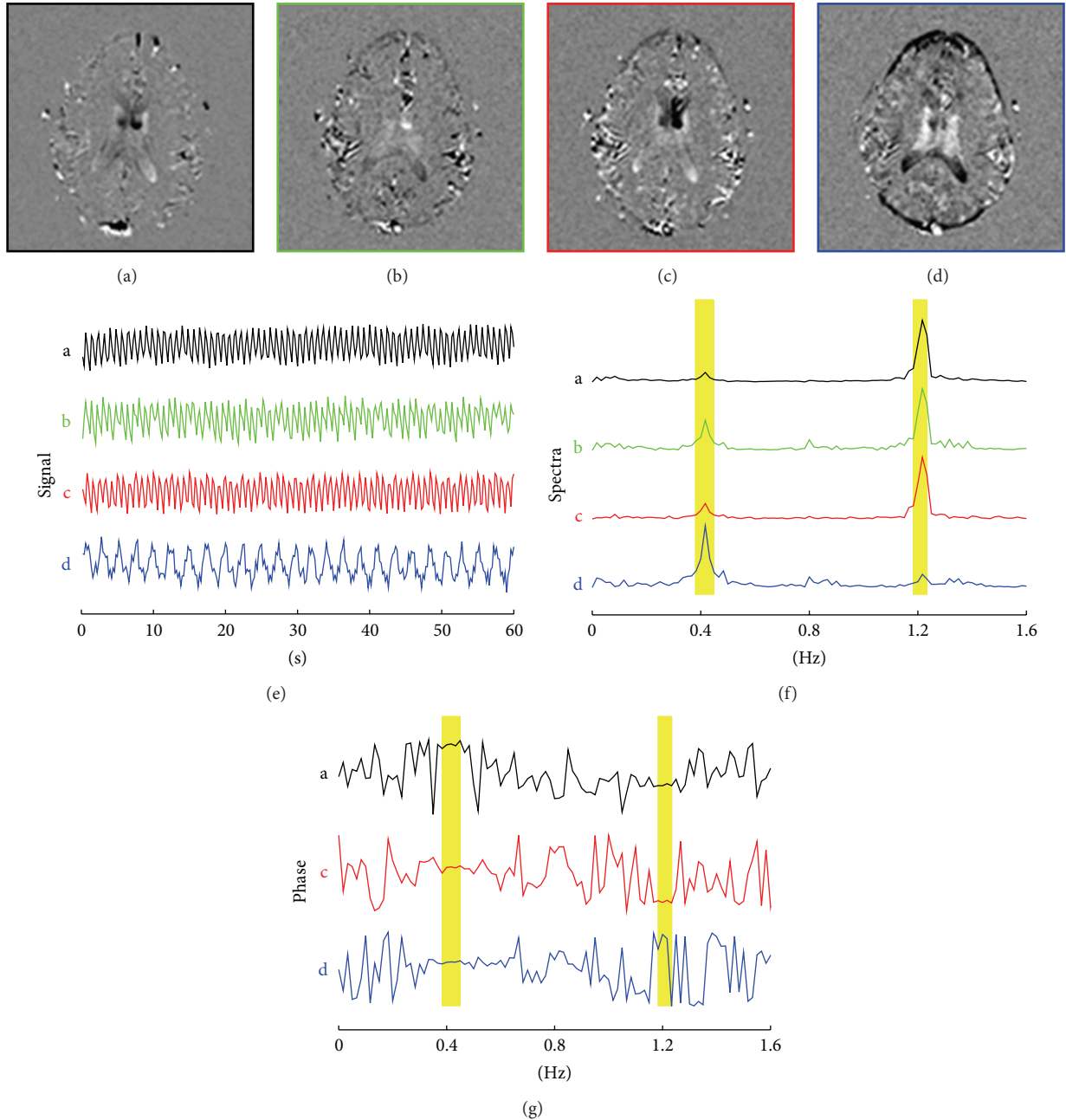


FIGURE 2: FastICA segmentation results for the dynamic images are displayed in Figure 1, which include the following: four output images with their frames displayed in different colors (a–d), corresponding signal-time curves (e), and corresponding amplitude spectrum (f). The phase, $\phi(f)$, calculated by using transfer function analysis and the complex-valued spectrum of the green signal-time curve as a reference function are illustrated in (g). The respiratory and cardiac frequency bands are marked by yellow shaded areas. Note that constant phases are observable at the respiratory (black, red, and blue curves) and cardiac pulsations (black and red curves).

analysis. Furthermore, the phases, as well as the temporal delays, were calculated as continuous numbers as shown in Figures 3 and 5. On the contrary, only black and white colors were used on the output of FastICA segmentation results as shown in Figures 2 and 4. The temporal delay information is limited to either 0 degree or 180 degrees in the IC analysis.

It is not surprising to know that the cardiac pulsation is observed at intracranial vessels as illustrated in Figures

3(c), 3(d), 5(c), and 5(d). In the ventricle, both respiratory and cardiac pulsations were observed as shown in Figure 3. We postulate that the respiratory pulsation is propagated through venous blood and is originated by far-away intrathoracic pressure changes, secondary to respiration. Meanwhile, the cardiac pulsation might be caused by a nearby cardiac pulsation at either choroid plexus or brain matter.

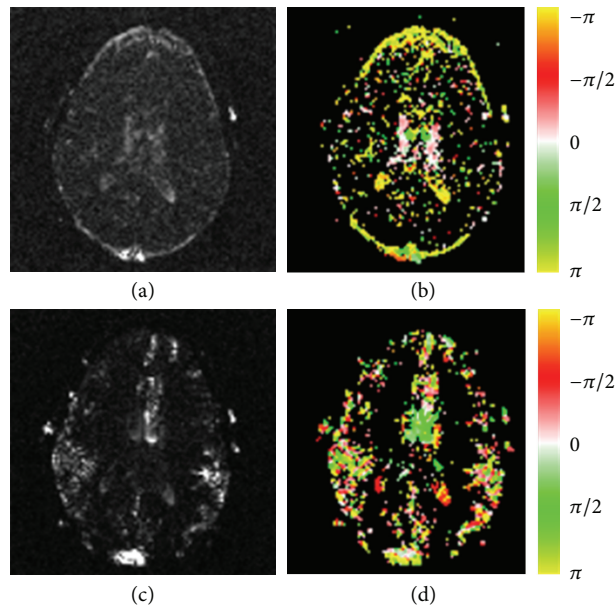


FIGURE 3: The amplitude (first column) and phase (second column) images are calculated by using the transfer function analysis for the respiratory (first row) and cardiac (second row) frequency bands. A pixel with a negative value (displayed in red color) has a signal-time curve leading the reference function. A pixel with a positive value (displayed in green color) indicates its signal-time curve is lagging the reference signal. The white color implies no or very small delays, and yellow color implies either a leading or a delay of $T/2$.

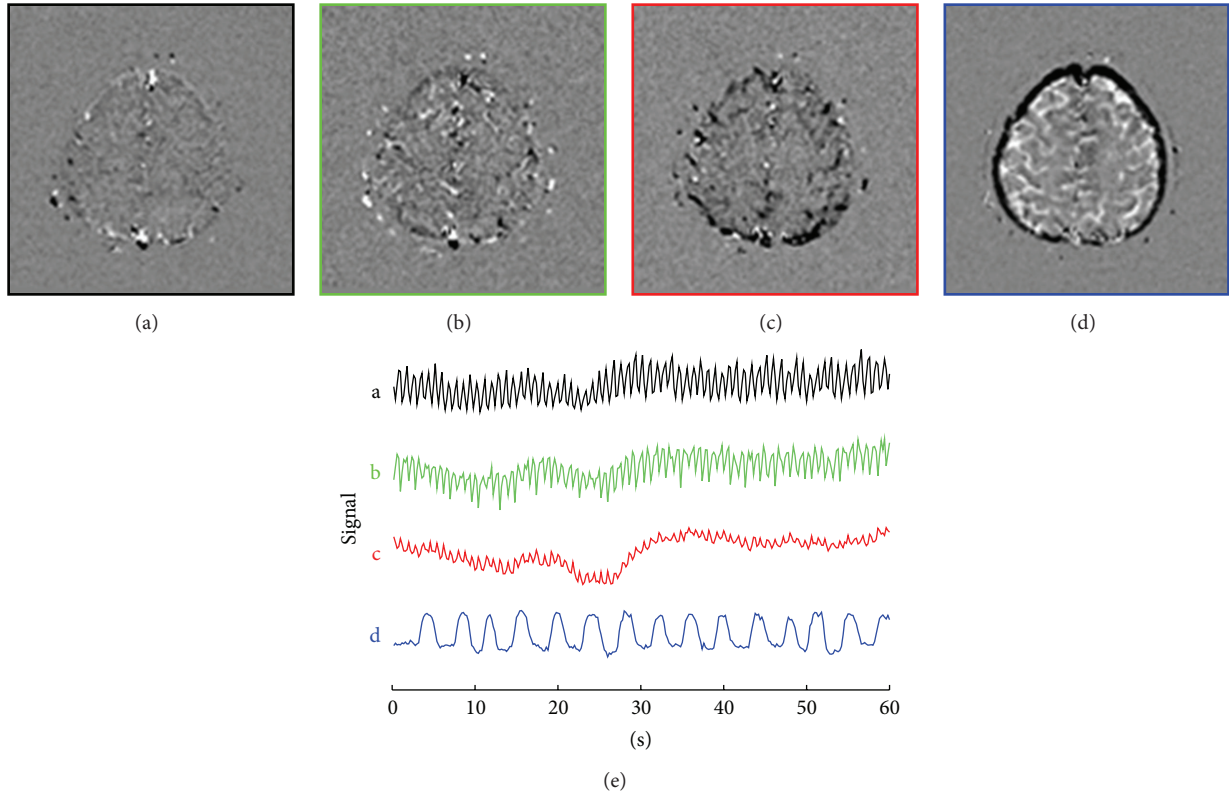


FIGURE 4: FastICA segmentation results for a slice location above the third ventricle, including four output images (a–d), and corresponding signal-time curves (e).

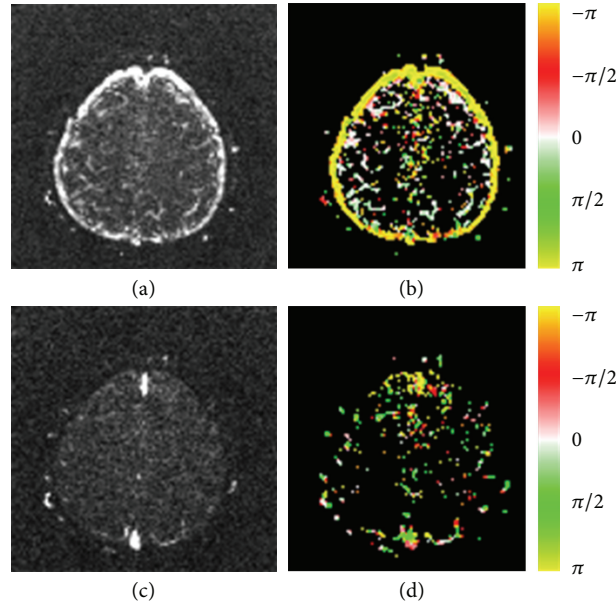


FIGURE 5: Transfer function analysis of the dynamic images shown in Figure 4. The amplitude (first column) and phase (second column) images were calculated by using the transfer function analysis for the respiratory (first row) and cardiac (second row) frequency bands. The color coding is the same as that in Figure 3.

Because the CSF space is part of a closed system, oscillatory CSF flow that went into one direction must be compensated by the same amount of oscillatory CSF flow that went to the opposite direction. It is likely that the flow pattern of the cortical CSF at the brain surface is accompanied by the opposite CSF flow pattern in the brain as shown in Figures 4(d) and 5(b).

The CSF is produced in the choroid plexus and circulates through the ventricular system, subsequently draining into the CSF space on brain surface, where it is resorbed from the superior sagittal and other sinuses before returning to the systemic circulation [2, 24, 25]. The intracranial pressure or CSF space will increase when there is overproduction of CSF, obstruction of CSF circulation, or brain atrophy. These three conditions all result in ventricular dilatation although their intracranial pressures are different. Clinically, the former two conditions are correctable while brain atrophy is irreversible. In addition to the CSF bulk flow mentioned previously, animal models have shown that either an increase or a decrease of cardiac pulsation in ventricular CSF causes ventricular dilatation [26]. It is reasonable to propose that CSF bulk flow and CSF pulsation are related to each other, and an imbalance of these flow dynamics may cause CSF flow obstruction with resulting ventricular dilatation. For clinical applications, the spatiotemporal patterns of respiratory and cardiac pulsations in patients with ventricular dilatation or hydrocephalus might provide information on the circulation of CSF.

There are two drawbacks in the transfer function analysis. The first drawback is that the phase is limited between $\pm\pi$. As a consequence, the temporal phase delay, $\tau_p(f)$, is limited between $\pm T/2$, where $T = 1/f$. This condition may cause ambiguity in clinical applications [18], because an inverted signal cannot be distinguished from a signal

with a phase delay of $T/2$ for a periodical waveform. The inverted amplitude or 180-degree phase delay phenomenon was observed on Figures 3(b), 3(d), and 5(b).

The second drawback is that the second harmonic of cardiac pulsation is limited by the Nyquist sampling rate of the dynamic images. In this study, the Nyquist sampling rate is calculated as $1/T_R/2 = 2.5$ Hz [27]. For the second harmonic of the cardiac pulsation to be observable on the dynamic images, the fastest heart rate is limited to 1.25 Hz, which corresponds to 75 heart beats per minute. If a subject's heart rate exceeds this limit, the second harmonic of the cardiac pulsation cannot be found in the dynamic images, and aliasing effect may interfere with respiratory pulsation.

5. Conclusion

This paper presented a protocol for analyzing the spatiotemporal patterns of respiratory and cardiac pulsations in human. The respiratory and cardiac pulsations can be recorded as flow-related enhancement on dynamic MR images. The segmentation results of IC analysis can be used to provide a reference function for the transfer function analysis. In the transfer function analysis, we found the following: (1) a good delineation of temporal delay of these pulsations can be achieved; (2) respiratory pulsation exists in the ventricular and cortical CSF; (3) cardiac pulsation exists in the ventricular CSF and intracranial vessels; and (4) a 180-degree phase delay or inverted amplitude is observed on phase images.

Acknowledgment

The authors thank Hing-Chiu Chang of GE medical systems for modifying the MR imaging pulse sequence for this study.

This research was partially supported by the National Science Council, Taiwan, ROC (Grant no. 100-2221-E-010-002).

References

- [1] B. Mokri, "The Monro-Kellie hypothesis: applications in CSF volume depletion," *Neurology*, vol. 56, no. 12, pp. 1746–1748, 2001.
- [2] J. E. A. O'Connell, "The vascular factor in intracranial pressure and the maintenance of the cerebrospinal fluid circulation," *Brain*, vol. 66, no. 3, pp. 204–228, 1943.
- [3] D. A. Feinberg and A. S. Mark, "Human brain motion and cerebrospinal fluid circulation demonstrated with MR velocity imaging," *Radiology*, vol. 163, no. 3, pp. 793–799, 1987.
- [4] D. Greitz, R. Wirestam, A. Franck, B. Nordell, C. Thomsen, and N. Stahlberg, "Pulsatile brain movement and associated hydrodynamics studied by magnetic resonance phase imaging. The Monro-Kellie doctrine revisited," *Neuroradiology*, vol. 34, no. 5, pp. 370–380, 1992.
- [5] G. Schroth and U. Klose, "Cerebrospinal fluid flow. I. Physiology of cardiac-related pulsation," *Neuroradiology*, vol. 35, no. 1, pp. 1–9, 1992.
- [6] G. Schroth and U. Klose, "Cerebrospinal fluid flow. II. Physiology of respiration-related pulsations," *Neuroradiology*, vol. 35, no. 1, pp. 10–15, 1992.
- [7] G. Schroth and U. Klose, "Cerebrospinal fluid flow. III. Pathological cerebrospinal fluid pulsations," *Neuroradiology*, vol. 35, no. 1, pp. 16–24, 1992.
- [8] U. Klose, C. Strik, C. Kiefer et al., "Detection of a relation between respiration and CSF pulsation with an echo planar technique," *Journal of Magnetic Resonance Imaging*, vol. 11, pp. 438–444, 2000.
- [9] C. Strik, U. Klose, M. Erb, H. Strik, and W. Grodd, "Intracranial oscillations of cerebrospinal fluid and blood flows: analysis with magnetic resonance imaging," *Journal of Magnetic Resonance Imaging*, vol. 15, no. 3, pp. 251–258, 2002.
- [10] A. Hyvarinen, J. Karhunen, and E. Oja, *Independent Component Analysis*, John Wiley & Sons, New York, NY, USA, 2001.
- [11] Y. H. Kao, W. Y. Guo, Y. T. Wu et al., "Hemodynamic segmentation of MR brain perfusion images using independent component analysis, thresholding, and Bayesian estimation," *Magnetic Resonance in Medicine*, vol. 49, no. 5, pp. 885–894, 2003.
- [12] M. J. McKeown, S. Makeig, G. G. Brown et al., "Analysis of fMRI data by blind separation into independent spatial components," *Human Brain Mapping*, vol. 6, pp. 160–188, 1998.
- [13] Y. O. Li, T. Adali, and V. D. Calhoun, "A feature-selective independent component analysis method for functional MRI," *International Journal of Biomedical Imaging*, vol. 2007, Article ID 15635, 12 pages, 2007.
- [14] R. E. Kelly, Z. Wang, G. S. Alexopoulos et al., "Hybrid ICA-seed-based methods for fMRI functional connectivity assessment: a feasibility study," *International Journal of Biomedical Imaging*, vol. 2010, Article ID 868976, 24 pages, 2010.
- [15] R. Gallardo-Caballero, C. J. Garcia-Orellana, A. Garcia-Manso et al., "Independent component analysis to detect clustered microcalcification breast cancers," *The Scientific World Journal*, vol. 2012, Article ID 540457, 6 pages, 2012.
- [16] Y. H. Kao, W. Y. Guo, A. J. K. Liou, Y. H. Hsiao, and C. C. Chou, "The respiratory modulation of intracranial cerebrospinal fluid pulsation observed on dynamic echo planar images," *Magnetic Resonance Imaging*, vol. 26, no. 2, pp. 198–205, 2008.
- [17] A. V. Oppenheim, A. S. Willsky, S. Hamid et al., *Signals and Systems*, Prentice Hall, Upper Saddle River, NJ, USA, 2nd edition, 1996.
- [18] T. B. J. Kuo, C. M. Chern, C. C. H. Yang et al., "Mechanisms underlying phase lag between systemic arterial blood pressure and cerebral blood flow velocity," *Cerebrovascular Diseases*, vol. 16, no. 4, pp. 402–409, 2003.
- [19] R. R. Diehl, D. Linden, D. Lucke, and P. Berlit, "Phase relationship between cerebral blood flow velocity and blood pressure: a clinical test of autoregulation," *Stroke*, vol. 26, no. 10, pp. 1801–1804, 1995.
- [20] H. H. Hu, T. B. J. Kuo, W. J. Wong et al., "Transfer function analysis of cerebral hemodynamics in patients with carotid stenosis," *Journal of Cerebral Blood Flow and Metabolism*, vol. 19, pp. 460–465, 1999.
- [21] F. T. Sun, L. M. Miller, and M. D'Esposito, "Measuring temporal dynamics of functional networks using phase spectrum of fMRI data," *Neuroimage*, vol. 28, pp. 227–237, 2005.
- [22] X. Zhao, J. Bodurka, A. Jesmanowicz et al., " B_0 -fluctuation-induced temporal variation in EPI image series due to the disturbance of steady-state free precession," *Magnetic Resonance in Medicine*, vol. 44, pp. 758–765, 2000.
- [23] A. Schuster, "On the investigation of hidden periodicities with application to a supposed 26 day period of meteorological phenomena," *Terrestrial Magnetism*, vol. 3, pp. 13–41, 1898.
- [24] F. H. Hetter, *Atlas of Human Anatomy, Circulation of Cerebrospinal Fluid*, Plate 103, Ciba-Geigy Corporation, Summit, NJ, USA, 1989.
- [25] A. Vander, J. Sherman, and D. Luciano, *Human Physiology: The Mechanisms of Body Function*, McGraw-Hill, Boston, Mass, USA, 8th edition, 2001.
- [26] J. R. Madsen, M. Egnor, and R. Zou, "Cerebrospinal fluid pulsatility and hydrocephalus: the fourth circulation," *Clinical Neurosurgery*, vol. 53, pp. 48–52, 2006.
- [27] H. Nyquist, "Certain topics in telegraph transmission theory," *Transactions of the American Institute of Electrical Engineer*, vol. 47, pp. 617–644, 1928.

Research Article

Detection of Pulmonary Nodules in CT Images Based on Fuzzy Integrated Active Contour Model and Hybrid Parametric Mixture Model

Bin Li,¹ Kan Chen,¹ Lianfang Tian,¹ Yao Yeboah,¹ and Shanxing Ou²

¹ School of Automation Science and Engineering, South China University of Technology, Guangdong, Guangzhou 510640, China

² Department of Radiology, Guangzhou General Hospital of Guangzhou Command, Guangdong, Guangzhou 510010, China

Correspondence should be addressed to Bin Li; binlee@scut.edu.cn

Received 17 January 2013; Revised 12 March 2013; Accepted 23 March 2013

Academic Editor: Chung-Ming Chen

Copyright © 2013 Bin Li et al. This is an open access article distributed under the Creative Commons Attribution License, which permits unrestricted use, distribution, and reproduction in any medium, provided the original work is properly cited.

The segmentation and detection of various types of nodules in a Computer-aided detection (CAD) system present various challenges, especially when (1) the nodule is connected to a vessel and they have very similar intensities; (2) the nodule with ground-glass opacity (GGO) characteristic possesses typical weak edges and intensity inhomogeneity, and hence it is difficult to define the boundaries. Traditional segmentation methods may cause problems of boundary leakage and “weak” local minima. This paper deals with the above mentioned problems. An improved detection method which combines a fuzzy integrated active contour model (FIACM)-based segmentation method, a segmentation refinement method based on Parametric Mixture Model (PMM) of juxta-vascular nodules, and a knowledge-based C-SVM (Cost-sensitive Support Vector Machines) classifier, is proposed for detecting various types of pulmonary nodules in computerized tomography (CT) images. Our approach has several novel aspects: (1) In the proposed FIACM model, edge and local region information is incorporated. The fuzzy energy is used as the motivation power for the evolution of the active contour. (2) A hybrid PMM Model of juxta-vascular nodules combining appearance and geometric information is constructed for segmentation refinement of juxta-vascular nodules. Experimental results of detection for pulmonary nodules show desirable performances of the proposed method.

1. Introduction

Pulmonary nodules in high-resolution CT images are potential manifestations of lung cancer. However, the interpretation of a great deal of CT images brings a huge workload upon the radiologist, which in turn increases the false negative rate due to observational oversights. CAD system for pulmonary nodules plays an important role in the diagnosis of lung cancer [1], which assists doctors in the interpretation of medical CT images and increases the detection of lung cancer by reducing the false negative rate as a result of observational oversights. Detection of different types of nodules in a CAD system is a difficult task. As pointed by the literatures [2, 3], despite much effort being devoted to the computer-aided nodule detection problem, CAD for various types of pulmonary nodules remains an ongoing research topic. One of the major difficulties is the task of

detecting nonsolid and part-solid GGO nodules with faint contrast and fuzzy margins. In particular, nonsolid nodules are extremely subtle with fuzzy boundaries, and part-solid nodules exhibit highly irregular intensity variations (intensity inhomogeneity) and boundary shapes. Studies have shown that nodules of nonsolid and part-solid nature are frequent and have higher risks of being malignant than solid ones [2]. Additionally, there are difficulties associated with the detection of nodules, that are adjacent to vessels when they have very similar intensities, and the detection of nodules, that are nonspherical in shape. Moreover, juxtavascular nodules account for the largest typology of lung nodules [3]. Thus, handling them under a united framework poses a great challenge to the task of segmentation of pulmonary nodules. Although various algorithms have been reported in the literatures [2–5] for tackling these problems, many technical issues still remain, including accurate segmentation

and detection. Furthermore, those that are applicable to various densities of GGO and juxtavascular nodules have not been available until recently. In such cases, traditional segmentation methods may lead to boundary leakage and also result in “weak” local minima. Additionally, purely intensity thresholding or model-based detection methods may fail to identify GGO and juxtavascular nodules, and their detection error rate may be unacceptably high. All these factors lead to the belief that the field is relatively new and requires further investigation. This paper deals with the above-mentioned problems. In this paper, an improved detection method for pulmonary nodules in CT images, which combines the FIACM-based segmentation, PMM-based segmentation refinement of juxtavascular nodules, and knowledge-based classifier, is proposed for detecting various types of pulmonary nodules, especially for GGO nodules (part-solid and nonsolid) and juxtavascular nodules.

1.1. Previous Work on Detection of Pulmonary Nodules. In CAD of pulmonary nodules, segmentation of potential nodule objects is the first necessary and crucial step. In the segmentation step, the potential nodule objects for training and testing data sets of classification are generated. However, the segmentation of GGO nodules and juxtavascular nodules is a very difficult task. It is difficult to acquire an ideal segmentation effect only by relying on general image-data-driven segmentation methods. Active contour models have been one of the most successful methods for image segmentation [6, 7], hence their implementation in the segmentation of pulmonary nodules [8]. However, for nonsolid/part-solid GGO nodules or juxtavascular nodules in real-world image, typical weak edges as well as intensity inhomogeneities may exist and hence boundaries are difficult to define. In such cases, the purely edge-based active contour models [9, 10], which rely on edge functionality to terminate the curve evolution for detecting objects with edges defined by gradient, are likely to yield undesirable local minima, so their performance is often inadequate. In addition, purely region-based active contour models [6, 7, 11] may be more sensitive to noise and cannot handle objects with ill-defined boundaries, hence may also cause problems of boundary leakage and “weak” local minima. To overcome the limitations of traditional region-based active contour model, Krinidis and Chatzis [12] used the fuzzy energy to provide a balanced technique with a strong ability to reject “weak” local minima. van Assen et al. [13] proposed a 3D active shape model driven by fuzzy inference (application to cardiac CT and MR). Li et al. [7] proposed a region-based active contour model incorporating a data fitting energy to overcome the difficulties caused by intensity inhomogeneities. Furthermore, there has been much research into the design of complex integrated active contour model combining edge and region energy [14] in order to overcome the limitations of traditional active contour models.

Besides handling nonsolid or part-solid GGO nodules, it is also important for a segmentation algorithm to be able to treat juxtavascular nodules. Juxtavascular nodules account for the largest typology of lung nodules [3]. Thus, handling them under a united framework presents a great challenge to the segmentation task of GGO and juxtavascular

nodules. Different approaches have been proposed to outline lung nodules close to vessels. Morphological operators were largely investigated for the separation of the nodule from blood vessels [3, 15, 16]. However, the sizes and shapes of vessels as well as those of nodules are irregular; hence it is very difficult to obtain an acceptable segmentation result if only morphological correction is relied upon. For example, Kostis et al. performed removal of vessels by means of a morphological operator having a constant size [15], which may lead to the problem of a small volume overestimation at the vessel attachment. Kuhnigk et al. [16] carried out a more complex morphological correction, supposing that the size of vessels decreases while the vessels evolve along the periphery of the lungs. However, this is not always the case, especially like those in vessel branches; hence the performance is inadequate. The methods for detachment of vessels from segmented nodules usually employ strategies which involve the entire nodule boundary with the possible drawback of making the segmentation worse where no attachment occurs. Hence, a better segmentation refinement method should be taken into consideration further. In addition, some literatures have aimed at building some statistical models for pulmonary nodules and blood vessels [17–19]. However, approaches utilizing simple criteria like shape rule or gray value evidence are typically not suitable to differentiate between different tubular tree structures and nodules. Models, in a broad sense, are embedded prior information about the target structures [20, 21]. To our knowledge, no hybrid models combining appearance and geometric information by incorporating assumptions on the spatial appearance of a vessel and its attached pulmonary nodules have been presented and discussed. Also present statistical models have not included both of the local intensity and structure features.

After the potential nodule objects are segmented exactly, every potential nodule object is evaluated and classified individually for the probability of true positive. There are a number of classification techniques used in the stage of the nodule detection CAD systems: rule-based or linear classifier [22–24], neural network [25], multilayer perception, SVM (support vector machine) [4], and so on. For example, Hardie et al. [26] also recently proposed a CAD system for identifying lung nodules in 2D chest radiographs that consists in using a weighted mean convergence index detector and an adaptive distance-based threshold algorithm to segment the detected nodule candidates. In the literature [26], a set of 114 features is computed for each candidate. This is followed by a classifier to reduce FPs. A Gaussian Bayes linear classifier, a Fisher linear discriminant (FLD) classifier, and a quadratic classifier are compared. Many other groups have also recently presented systems and performance studies for detecting nodules [27]. However, as for nonsolid/part-solid GGO nodules and juxtavascular nodules, the error rate of purely intensity or model-based detection methods may be much higher. For this reason, we believe that the field is relatively new and requires further investigation.

1.2. Our Approach. This paper deals with the above-mentioned problems. In this paper, an improved detection method of pulmonary nodules in chest CT images,

combining the FIACM-based segmentation, PMM-based segmentation refinement for juxtavascular nodules, and a knowledge-based C-SVM classifier, is proposed for detecting various types of pulmonary nodules, especially for GGO nodules (part-solid and nonsolid) and juxtavascular nodules. The flowchart of the proposed detection algorithm for pulmonary nodules under a united framework is shown in Figure 1.

Compared with existing traditional methods, our approach has several novel aspects:

- (1) in order to overcome the problems of boundary leakage and “weak” local minima in segmentation of part-solid/nonsolid GGO and juxtavascular nodules using traditional segmentation methods, the paper proposes a fuzzy integrated active contour model (FIACM), in which edge and local region information is incorporated. A new edge-stopping function is specified based on posterior probability. The statistical information of local region in a dynamic mask, combining the fuzzy energy, is introduced into the active contour energy function model, and the fuzzy energy is used as the model motivation power for the evolution of the active contour.
- (2) To overcome the problem of a small volume over-estimation at the vessel attachment and get a good segmentation result of juxtavascular nodules under a united segmentation framework, a hybrid PMM of juxtavascular nodules combining appearance and geometric information is constructed for segmentation refinement of juxtavascular nodules.
- (3) A knowledge-based C-SVM classifier is constructed, using some 2D and 3D features.

The remainder of this paper is organized as follows. In Sections 2 and 3, the proposed segmentation methods of potential nodule objects are first introduced. Then, the proposed classification algorithm based on knowledge-based C-SVM classifier is presented in Section 4. Finally, the experimental results of our method are given in Section 5, followed by some discussions in Section 6. This paper is summarized in Section 7.

2. Fuzzy Integrated Active Contour Model-Based Segmentation

2.1. The Proposed Fuzzy Integrated Active Contour Model (FIACM). Let $\Omega \subset R^3$ be the image domain, and let $D : \Omega \rightarrow R$ be the given medical CT image sequence or 3D data set. The segmentation result of the images or data set (for 3D data set) D is achieved by finding a surface ϕ , which separates Ω into disjoint regions. Ω_1 and Ω_2 represent the inside regions and outside regions of ϕ , respectively. Besides intensity, more features are used in our active contour model. Taking both

the edge and local region information into consideration, our proposed energy function model is given as follows:

$$\begin{aligned}
 E(f_1, f_2, \phi) &= \mu \int_{\phi} \delta\phi(p) g_{\text{color}} |\nabla\phi| dp \\
 &+ \int_{\Omega_1} \lambda_1 [u(p)]^m (I(p) - f_1(x))^2 H\phi(p) dp \\
 &+ \int_{\Omega_2} \lambda_2 [1 - u(p)]^m (I(p) - f_2(x))^2 (1 - H\phi(p)) dp,
 \end{aligned} \tag{1}$$

where $E(f_1, f_2, \phi)$ is the proposed energy function model; $f_1(x)$ and $f_2(x)$ are two values that approximate image intensities in the local regions Ω_1 and Ω_2 , respectively. $x(x, y, z) \in \Omega$ is a given pixel/voxel, also a location variable.

On the right-hand side of (1), $p(x, y, z) \in \Omega$ is a location variable like x ; $I(p)$ represents the intensity value in p ; the first term $\mu \int_{\phi} \delta\phi(p) g_{\text{color}} |\nabla\phi| dp$ is the edge-driven energy term, which is used for curved surface to improve the evolved ability in concave regions; μ is the weight of edge-driven energy term; $\delta\phi(p)$ is the smoothed version of the Dirac delta; g is the stop function. The second and third terms are the region-driven energy terms, which are used to control the image force based on statistical region-intensity information; λ_1 and λ_2 are the weights for region-driven energy term. The membership function $u(p) \in [0, 1]$ is the degree of membership of D , and m is a weighting exponent on each fuzzy membership. The degree of membership is decided by not only the intensity feature, but also the shape feature: local shape index. $H\phi$ is the smoothed Heaviside function.

The proposed FIACM model differs from the model used in the literatures [7, 12–14], which has several novel aspects. (1) the right-hand side of (1) consists of the edge-driven energy term and region-driven energy terms. The edge and local region information is incorporated into the proposed FIACM model. (2) In the second and third terms of right-hand side of (1), the statistical information of local region in a dynamic mask, combining the fuzzy energy, is introduced into the active contour energy function model. This will be explained in detail below in Section 2.2. (3) The fuzzy energy is used as the model motivation power evolving the active contour, which is represented and communicated by the membership function $u(p)$ in the second and third terms of right-hand side of (1). The degree of membership is decided by not only the intensity feature, but also the shape feature: local shape index. So more features, including intensity and local shape index, are used in the proposed active contour model. This will be explained in detail below in Section 2.3. (4) In the first term of right-hand side of (1), a new edge-stopping function g is specified based on posterior probability. This will be explained in detail below in Section 2.4.

In the simple case, it is obvious that the boundary of the object ϕ_0 is the minimizer of the energy functional. The energy function model as (1) is solved by using variational level set approach, and by taking the first variation of this

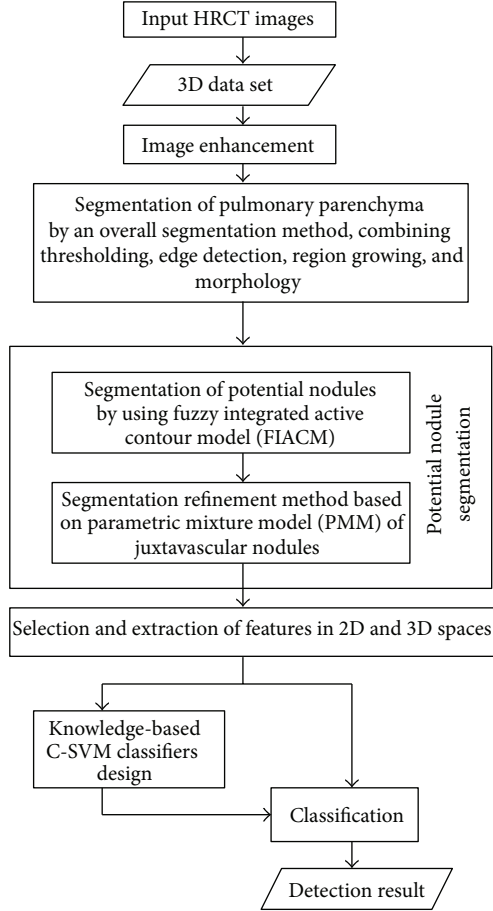


FIGURE 1: Overview of the proposed detection method for pulmonary nodules.

energy with respect to ϕ the following evolution equation is obtained follows:

$$\frac{\partial \phi}{\partial t} = \delta_\epsilon \left\{ \mu \operatorname{div} \left(g_{\text{color}} \frac{\nabla \phi}{|\nabla \phi|} \right) - \sum_{i=1}^k \lambda_1^{(i)} [u(p)]^m (I(p) - f_1^{(i)}(x))^2 + \sum_{i=1}^k \lambda_2^{(i)} [1 - u(p)]^m (I(p) - f_2^{(i)}(x))^2 \right\}. \quad (2)$$

2.2. Local Region-Scalable Flexible Fitting Energy in FIACM Model. In order to improve the capability of handling intensity inhomogeneity and objects with ill-defined boundaries, while reducing the computation cost, the statistical information of a local region is considered in the active contour energy function model. We utilize a local intensity fitting energy as the region-scalable fitting energy. In our energy function model as in (1), $f_1(x)$ and $f_2(x)$ are flexible fitting values, which are two values that approximate image intensities in the local region decided by a flexible mask of $B(k)$. That is, the intensities $I(p)$ that are effectively involved

in the above fitting energy are in a local region centered at the point x , whose size can be controlled by the mask $B(k)$.

A 3D mask, $B(k)$ as described by (3), possesses statistical information of the local region. It is a characteristic function and is introduced into the energy function:

$$B(k) = \begin{cases} \frac{1}{(2\pi)^{n/2} \sigma^n} e^{-|k|^2/2\sigma^2}, & k \in \{\Omega_1 \cup \Omega_2\} \\ 0, & \text{otherwise.} \end{cases} \quad (3)$$

The kernel function, $B(k)$, with a scale parameter σ , is controlled by the mean of the degrees of membership in the region. In our proposed model as illustrated in (1), a window will be defined; so $k = x - p$.

Therefore, the local intensity fitting energy in (3) is called as the region-scalable fitting (RSF) energy of a contour C at a point x . Using the statistical information of local region, the means $f_1(x)$ and $f_2(x)$ in the interior region Ω_1 and exterior region Ω_2 can be computed from (4). Therefore, the evolution of the point in the image domain is only related to the intensities in surrounding region, while it is independent of the region beyond the mask field. Hence, the difficulties caused by intensity inhomogeneities are overcome:

$$f_1(x) = \frac{B(x-p) * [H\phi(x)I(x)]}{B(x-p) * H\phi(x)}, \quad (4)$$

$$f_2(x) = \frac{B(x-p) * [(1-H\phi(x))I(x)]}{B(x-p) * (1-H\phi(x))}.$$

2.3. The Degree of Membership in FIACM Model. In our FIACM model, the fuzzy energy is used as the model motivation power evolving the active contour. As shown in (1), $u(p) : X \rightarrow [0, 1]$ defines the membership degree of a pixel p in data set D to the nodule class cluster center. The corresponding degree of membership of each pixel in the data set should be calculated. Thus, the degree of membership for each sample $X_i = (x_i, y_i, SI_i, I_i)$ in our FIACM model is calculated by using the fuzzy clustering algorithm based on intensity and local shape index. Meanwhile, the fuzzy morphological opening operation [28] is used to eliminate noise. Here, in the clustering space, a sample is $X_i = (x_i, y_i, SI_i, I_i)$; x_i and y_i is the position feature; I_i is the intensity feature and SI_i is the local volumetric shape index. The volumetric shape index (SI) [4] is a measure of local shape characteristics. The local shape index $SI(p)$ at pixel p can be defined by

$$SI(p) = \frac{1}{2} - \frac{1}{\pi} \arctan \frac{k_1(p) + k_2(p)}{k_1(p) - k_2(p)}, \quad (5)$$

where $k_1(p)$ and $k_2(p)$ are principal curvatures at pixel p . This index can be used to distinguish spherical from cylindrical shapes: values close to 1 indicate spherical shapes, while values close to 0.75 indicate cylindrical shapes. However, pulmonary nodules are hard to distinguish if merely the intensity or the shape index features are utilized. Therefore, the degree of membership is an important feature for segmentation or even the detection of GGO or juxtavascular pulmonary

nodules. Generally speaking, the degree of membership of pulmonary nodules is greater than 0.5, and the degree of membership of blood vessel is less than 0.5. An example is illustrated in Figure 2.

The intensity values, shape index values, and the degree of membership values of a GGO juxtavascular pulmonary nodule and its attached blood vessel are shown in Figure 2. As shown in Figures 2(b), 2(c), 2(f), and 2(g), pulmonary nodules are hard to distinguish if only intensity or the shape index features are relied upon. As shown in Figures 2(d) and 2(h), some noise, indicated in red, occurs when the data are transformed into the fuzzy domain. The fuzzy morphological filtering is, therefore, adopted to eliminate the noise. As shown in Figures 2(e) and 2(i), the degree of membership of pulmonary nodules is greater than 0.5, and the degree of membership of blood vessel is less than 0.5. This implies that the degree of membership is an important feature for segmentation or even detection of GGO or juxtavascular nodule.

2.4. Selection of Edge-Stopping Function Based on Posterior Probability. In the proposed FIACM model, a new edge-stopping function is specified based on posterior probability. The edge-stopping function is important and has a strong impact on the final outcome of curved surface evolution. As for nonsolid or part-solid GGO pulmonary nodules with faint contrast and fuzzy margins, rough and weak edges or even concave edges are often exhibited, and their regions often possess intensity inhomogeneities. Since real images do not contain ideal edges, an edge-stopping function, g , must be specified. The main goal of stopping function, g , is actually to stop the evolving curved surface when it arrives at the objects boundaries.

The edge-stopping function, g , is a nonlinear strictly increasing function, which is like the weather vane of convergence of curved surface evolution. In the active contour model based on curvature diffusion, the edge-stopping function is often selected as $g(\nabla I_\sigma) = 1/(1 + (|\nabla I_\sigma|/K)^2)$ or $g(\nabla I_\sigma) = e^{-(|\nabla I_\sigma|/K)^2}$ (where $\nabla I_\sigma = \nabla I * G_\sigma$ is Gaussian gradient), whose function curves are shown in Figure 3. These two functions are similar to the Butterworth or Gaussian high-pass filter response function. As in the frequency domain analysis, the image edge corresponds to the high-frequency signals; hence these two functions can produce a strong response to the edge region. However, these two functions are also relatively very sensitive to noise; therefore, false edges are bound to be formed. Furthermore, they have a difficulty in handling concavities within the boundary. In this case, it is necessary to select an appropriate stopping function in our model. The specified new edge stopping function, illustrated in (6), is shown in Figure 3. The edge-stopping function we selected can be controlled by two gradient module thresholds a and b . The thresholds a and b are determined using posterior probability, and the conditional probability density function is defined as a Gaussian function of intensity and gradient, whose parameters are calculated using the expectation maximization algorithm. When $t \leq a$, $g = 1$, this represents the homogeneous region; when

$t \geq b$, $g = 0$, the edge region is represented. Essentially, the stopping function describes the changing process in transition region (between the homogeneous region and edge region) using a second-order nonlinear smooth function. The edge stop function quantitatively describes the weak boundaries of the image, which can enhance the robustness of noise region and improve the evolution performance in intensity inhomogeneities situations and concave edges:

$$g(t) = \begin{cases} 1 & t \leq a \\ 1 - 2\left(\frac{t-a}{b-a}\right)^2 & a < t \leq \frac{a+b}{2} \\ 2\left(b - \frac{t}{b-a}\right)^2 & \frac{a+b}{2} < t \leq b \\ 0 & t > b. \end{cases} \quad (6)$$

2.5. Implementation of Potential Pulmonary Nodule Segmentation Based on FIACM Model. The implementation algorithm for the FIACM model is as follows.

- (1) Compute the degree of membership $u(p)$ according to Section 2.3.
- (2) Initialize the contour of the FIACM model based on adaptive local threshold segmentation. In the level set method for the proposed FIACM model, selection of the initial contour ϕ_0 has a different effect on the efficiency of the algorithm implementation. As the lung is essentially a bag of air in the body, it shows up as a dark region in CT scans. Pulmonary nodules are often calcified tissues. This contrast between pulmonary nodules and surrounding tissues forms the basis for the majority of the segmentation schemes. So in this paper, the segmentation result of adaptive local threshold segmentation method is used as the initial contour of the following hybrid level set model, which greatly reduces the number of iterations of curved surface evolution and ensures that the desired segmentation effect is achieved.
- (3) Compute the scale parameter σ of the kernel function, $B(k)$, which is controlled by the mean of the degrees of membership in a region, for example, a circle. Then proceed to compute the region-scalable fitting energies $f_1(p)$ and $f_2(p)$.
- (4) Determine the thresholds a and b of the stop function term using posterior probability and then specify the stop function term.
- (5) Implement the numerical algorithm of the proposed FIACM model. In this paper, the proposed FIACM model given as (2) is implemented by an efficient numerical algorithm based on an additive operator splitting (AOS) and Thomas algorithm [29].

3. Segmentation Refinement of Juxtavascular Nodules Based on Hybrid PMM

Compared with existing ones, the proposed hybrid PMM-based segmentation of juxtavascular nodules has several distinct features that include the following.

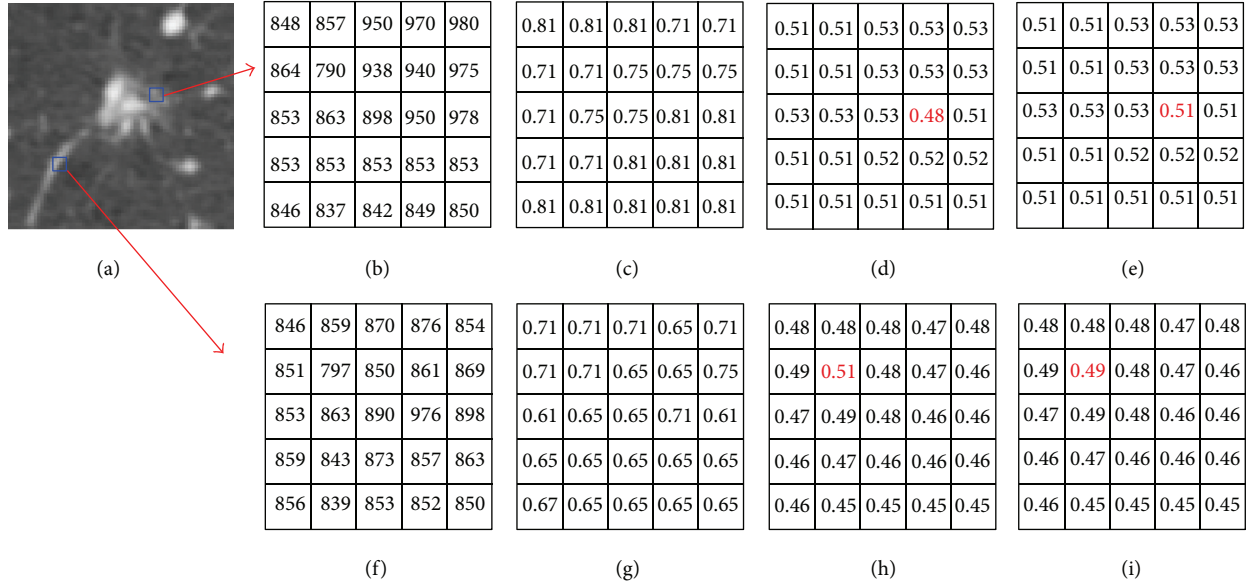


FIGURE 2: Intensity values, shape index values, and the degree of membership of a GGO juxtavascular pulmonary nodule and its attached vessel. (a) Original CT image; (b) intensity of juxtavascular nodule; (c) shape index values of juxtavascular nodule; (d) the degree of membership of vessel before the fuzzy morphological filtering; (e) the degree of membership of juxtavascular nodule; (f) intensity of vessel; (g) shape index values of vessel; (h) the degree of membership of vessel before the fuzzy morphological filtering; and (i) the degree of membership of vessel after the fuzzy morphological filtering.

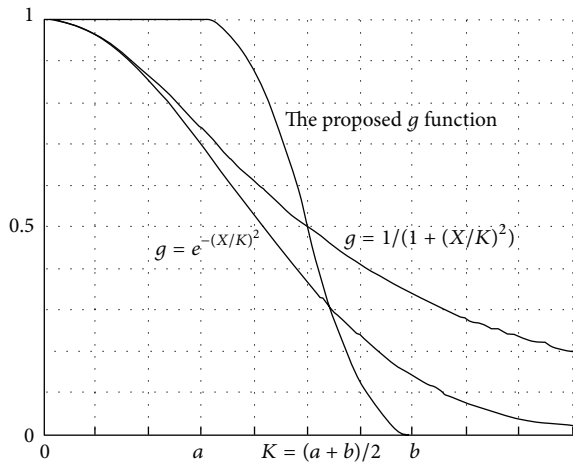


FIGURE 3: The specified edge-stopping function.

(1) Various types of pulmonary nodules, especially for GGO nodules (part-solid and nonsolid) and juxtavascular nodules, are segmented under a united segmentation framework. In order to overcome the problem of a small volume overestimation at the vessel attachment and obtain a good segmentation result of juxtavascular nodules under a single-segmentation framework, a hybrid PMM of juxtavascular nodules is constructed for segmentation refinement of juxtavascular nodules. The refinement procession is just used for the pixels in some regions containing the blood vessels and juxtavascular nodules; hence the

correction and refinement methods have the advantage of local refinement of the nodule segmentation along recognized vessel attachments only, without modifying the nodule boundary elsewhere. Moreover, it has the potential to reduce the computation cost involved.

(2) The hybrid model takes both the appearance and geometric information into consideration. The hybrid model combines appearance and geometric information by incorporating assumptions on the spatial appearance of a vessel.

3.1. The Proposed Hybrid PMM of Juxtavascular Nodules

3.1.1. Observation Vector Generation in the Proposed Hybrid PMM of Juxtavascular Nodules. In the models of juxtavascular nodules, in a broad sense, prior information about the target structures is embedded. Because CT values of pulmonary nodules and that of blood vessels are almost uniform, it is difficult to estimate exactly the parameters and segment the blood vessels and the attached nodules if merely the intensity feature is utilized and a statistical model is built based merely on the intensity feature. Our proposed hybrid PMM model takes both the appearance and geometric information into consideration. That is, a set of observation vectors are defined and extracted to include the appearance and geometric information. Appearance information expresses prior knowledge on the luminance properties of the vascular structures and the attached nodules. Depending on the application in segmentation and detection of juxtavascular

nodules, additional knowledge about the specific geometric shape might be incorporated.

Thus, we define an extended observation vector as

$$v = (I_i, u_i, o_i), \quad (7)$$

where v is the observation vector in position (x, y) ; I_i is the intensity feature; u_i is the degree of membership, which is from the volumetric shape index SI_i , reflecting the geometric shape; the membership function $u(p) \in [0, 1]$ and o_i is the regularized flow direction vector.

3.1.2. The Regularized Flow Direction Feature of Nodules Adjacent to Blood Vessels. As vessels are characterized by a tubular model, the 3D gradient vectors in a vessel can be used to extract a vector in the direction of the vessel by identifying a vector that is approximately orthogonal to the gradients in a local neighborhood [17–19]. Hence, the flow direction can be used as a feature vector to build a statistical PMM for segmentation of blood vessels and attached nodules.

In this paper, the structure tensors are computed by directly using the gradient information of each voxel, which is different from the method given in the literature [19]. In the literature [19], a 3×3 correlation matrix GG^T is essentially a structure tensor defined by the statistical information of arithmetic average in local region, which will weaken local features in each voxel to a certain degree. We assume that T is the structure tensor, whose eigenvalues are λ_1, λ_2 , and λ_3 ($\lambda_1 \leq \lambda_2 \leq \lambda_3$). Let e_1 be the unit length eigenvector belonging to the eigenvalue λ_1 . A vector pointing in flow direction is set as

$$l_1 = \sqrt{\lambda_3} \cdot e_1. \quad (8)$$

Since vectors in opposite directions indicate the same direction of a blood vessel, it is possible to invert some of the vectors so that the majority of the vectors of the same blood vessel have consistent orientation. This can be achieved in a simple way by inverting all vectors with an angle difference in the range of $[0, \pi]$. Let e be the unit vector in the flow angle $\pi/2$. The regularized flow direction vector o_i is

$$o_i = \begin{cases} -l_i & \langle l_i, e \rangle \in [-1, 0) \\ l_i & \text{otherwise.} \end{cases} \quad (9)$$

3.1.3. The Proposed Hybrid PMM of Juxtavascular Nodules. As mentioned in Section 3.1.1, our proposed hybrid PMM takes both the appearance and geometric information into consideration. The observations, $v = (I_i, u_i, o_i)$, as described in Section 3.1.1, include both the appearance and geometric information. According to medical knowledge of anatomy, blood vessels are similar to tubes, whose flow directions show a Gaussian distribution [17]; and the pulmonary nodules are similar to spheres. Furthermore, the intensity values of pulmonary nodules and those of blood vessels are almost uniform. So assuming that the mixture components are multivariate Gaussian distributions [18, 19, 30], and that there

is a uniform noise component in the mixture, a statistical PMM for the blood vessel and juxta-nodule is obtained:

$$f(v | \theta) = \sum_{i=1}^{M-1} \alpha_i \phi(v | \mu_i, \Sigma_i) + \alpha_M p_M(v), \quad (10)$$

where $f(v | \theta)$ is the density of a parametric finite mixture model; v is the observation vector, $v = (I_i, u_i, o_i)$; $\theta = (\alpha_1, \dots, \alpha_M, \theta_1, \dots, \theta_M)$ is the vector of parameters; θ_i is composed of the elements of μ_i ; $\sum_i \phi(v | \mu_i, \Sigma_i)$ is the density of a multivariate Gaussian random vector with mean μ_i and covariance matrix Σ_i ; $p_M(v)$ is a multivariate uniform density function, $p_M(v) = 1/\pi$; α_i is the structure weight coefficient (the inner mixing proportion), $\sum_{i=1}^M \alpha_i = 1$. μ and σ are the mean and variance of the multivariate Gaussian distribution, respectively. Parametric models for nodules and vessels can be obtained from (9) when using $M = 3$.

3.2. Implementation of PMM-Based Segmentation Refinement of Juxtavascular Nodules. The algorithm for PMM-based segmentation refinement of juxtavascular nodules is carried out in the following steps.

- (1) Based on local structure analysis, the shape features, for example, compactness or sphericity factors, are used to distinguish segmented objects in Section 2 and judge whether or not they contain the blood vessels and juxtavascular nodules. Just some filtering objects/regions need to be refined by using the following PMM-based segmentation refinement method. The correction method locally refines the nodule segmentation along recognized vessel attachments only, without modifying the nodule boundary elsewhere. This allows for computation cost to be reduced.
- (2) All features including 3D gradient flow direction features are extracted and computed. PMM for juxtavascular nodules is constructed. Parameters are estimated by using the generalized mixture decomposition algorithm scheme (GMDAS) of EM (expectation maximization) algorithm.
- (3) Classification and performance assessment.

The basic reasoning behind this algorithmic family springs from our familiar Bayesian philosophy. We assume that there are m clusters, C_j , $j = 1, \dots, m$, underlying the data set. Each vector v_i , $i = 1, \dots, N$, belongs to a cluster C_j with probability $P(C_j | v_i)$. A vector v_i is appointed to the cluster C_j if

$$P(C_j | v_i) > P(C_k | v_i) \quad k = 1, \dots, m, \quad k \neq j. \quad (11)$$

4. Classification of Pulmonary Nodules Using Knowledge-Based and C-SVM Classifier

As mentioned above, pulmonary nodules are classified by using the knowledge-based C-SVM classifiers. First, the knowledge-based piecewise linear classification is used to remove easily dismissible nonodule objects. Then, C-SVM

classification is used to further classify nodule candidates and reduce the number of false positive (FP) objects. Here, the nodule candidates filtered by the knowledge-based piecewise linear classification are used as the training and testing samples set of C-SVM, and their intensity, shape and texture features in 2D space and 3D space, selected and extracted based on knowledge, are used as the input parameters of C-SVM.

4.1. Feature Selection and Extraction Based on Knowledge.

Feature selection and extraction play an important role in the intelligent recognition of pulmonary nodules. How to select and extract features is the key for intelligent detection of pulmonary nodules. In this paper, 2D and 3D features are calculated and used for detection of pulmonary nodules.

Clinical manifestation and pathological features of pulmonary nodules in CT include position, shape, lobulation, burr sign, notch, calcification, satellite lesion, and pleural retraction sign [31, 32]. According to the pathomorphology of pulmonary nodule lesions, a small lesion appears as a circle because it has not encountered many obstacles in its growing process; when the lesion grows to a certain degree, it shows spherical shape, and lobulation and notch signs appear due to the barrier of neighborhood bronchus trees and blood vessels; as the lesion grows further, it oppresses the bronchia, blood vessel, or pleura and exhibits rough edges, meanwhile continuous burr sign and lobulation appear. Moreover, burr sign, lobulation, and cavitation with GGO edges appear blur and uneven, which are the most important pathomorphological features in mid-later growing season; thus, they can be represented by the compact ratio. Therefore, shape features are still the most important features for the detection of true pulmonary nodules. Furthermore, nodule candidate extraction is often disturbed by bronchus and blood vessels in pulmonary hilar. So, we can, therefore, select some features for detecting pulmonary nodules according to expert knowledge. For example, the area feature reflects the size of the nodule. The compactness, reflecting degree close to circle and smoothness of region, can be used to detect rough edges; the rougher the edge is, the smaller the compactness is. The concavity ratio feature reflects the degree of concavity of the region boundary. The compactness and concavity ratio features correspond to the burr sign of pulmonary nodules. The inverse difference moment feature reflects smoothness, or the degree of alternately concave and convex change in the region boundary. In summary, some features in 2D space and 3D space described in Table 1 are calculated including gray, position, shape and texture features. Suppose the size of the CT image is $M \times N$, the gray value is $I(x, y)$ at the point (x, y) . In centroid calculation, m_{pq} is the $p + q$ -order origin moment; in diameter and ellipticity calculation, μ_{pq} is the $p + q$ -order central moment; in perimeter calculation; n_e is the even code number of chain code, and n_o is the odd code number; in circularity calculation, r_i is the radius of inscribed circle, and r_c is the radius of circumcircle; in slenderness and rectangle degree calculation, W is the width of the potential nodule object, and H is the height. Moreover, some features of the segmented object in 3D space are more useful to distinguish nodules and vessels, such as the volume

of the segmented object and the volumetric quotient which is the ratio of the volume of the segmented object to the volume of its circumsphere whose radius is half of the long axis. Given the fact that a nodule is generally either spherical or has local spherical elements, while a blood vessel is usually cylindrical, then the volumetric quotient of the pulmonary nodule is close to 1, yet that of the vessel is far less than 1.

4.2. Classifiers of Pulmonary Nodules Based on Knowledge-Based C-SVM

4.2.1. *Knowledge-Based Piecewise Linear Classifier in 3D Space.* A knowledge-based piecewise linear classifier in 3D space is designed to remove easily dismissible nonnodule objects from pulmonary nodule candidates. The feature space of knowledge-based piecewise linear classification is formed by four features, including volume, volumetric quotient, and mean and standard deviation of intensity in 3D space.

4.2.2. *Nodules Classification Based on Knowledge-SVM Classifier.* The C-SVM is used to solve the problem of unbalanced dataset. The nodule candidates set is a typical unbalanced dataset, in which the nodule samples are far less than the non-nodule samples; so the C-SVM is fit for the classification in an unbalanced dataset. In this paper, nodule candidates are regarded as the samples set $X = [s_1, s_2, \dots, s_N]^T$, where N denotes the number of total samples, and s_i ($i = 1, 2, \dots, N$) is a row vector, representing the feature set of any sample. The nodule candidates filtered by the knowledge-based classification are used as the training samples set of C-SVM, and their intensity, shape and texture features in 2D space and 3D space are taken as the input parameters of C-SVM. The input data of C-SVM are normalized to $[0, 1]$, and the class label of C-SVM $y_i \in \{+1, -1\}$, $i = 1, 2, \dots, N$ (where +1 corresponds to a nodule and -1 to a nonnodule) of the corresponding sample x_i is also given. Then the samples' label set is $Y = [y_1, y_2, \dots, y_N]^T$ and the dataset can be represented as (X, Y) . The decision function of the C-SVM is given as [33]:

$$f(s) = \text{sgn} \left[\sum_{i=1}^l a_i y_i K(s_i, s_j) + b \right], \quad (12)$$

where $K(s_i, s_j)$ is a nonlinear kernel function, $b \in R$, and a is constrained as follows: $0 \leq a_i \leq C_+$, for $y_i = +1$, and $0 \leq a_i \leq C_-$, for $y_i = -1$ where C_+ and C_- are penalties for class +1 and -1, respectively.

In order to increase the efficiency of the SVM, a training method is used to train the SVM, which uses the grid search method to search the optimal parameters of C-SVM and selects the sequential minimal optimization (SMO) working set, using second-order information to achieve fast convergence. Also the RBF (radical basis function) kernel function is used in this paper, defined as

$$K(s_1, s_2) = \exp(-\gamma \|s_1 - s_2\|^2), \quad (13)$$

where γ is the parameter.

TABLE 1: Features calculation of every potential nodule object.

	Features	Definition
Intensity	Mean value G_m	$G_m = \sum_{x=1}^M \sum_{y=1}^N I(x, y) / (M \times N)$, in 2D space
	Standard deviation G_u	$G_u = \sum_{x=1}^M \sum_{y=1}^N (I(x, y) - G_m)^2$, in 2D space
	Mean G_{m3D} of intensity	In 3D space
	Standard deviation G_{u3D} of intensity	In 3D space
Position	Centroid (i_0, j_0)	$i_0 = m_{10}/m_{00}$, $j_0 = m_{01}/m_{00}$
Shape	Area A	$A = \sum (f(x, y) = 1)$, in 2D space
	Perimeter L	$L = n_o + \sqrt{2}n_e$, in 2D space
	Diameter a	Long axis in 2D space, $a = 2 \times \left[2(\mu_{20} + \mu_{02} - \sqrt{(\mu_{20} - \mu_{02})^2 + 4\mu_{11}^2}) / \mu_{00} \right]^{1/2}$
	Ellipticity e	$e = a/b$, a, b are the long axis and short axis, respectively, in 2D space
	Circularity C	$C = r_i/r_c$, in 2D space
	Slenderness S	$S = \min(W, H) / \max(W, H)$, in 2D space
	Rectangle degree R	$R = A / (W \times H)$, in 2D space
	Compactness F	$F = 4\pi A / P^2$, P is the perimeter of region contour. A is the area in 2D space Compactness ratio reflects degree closing to circle and smoothness of region. And F can be used to detect the rough feature of edge
	Concavity ratio E	$E = S_e/S$, S is area of concave region, S_e is difference of convex hull and original region, and E reflects cupped degree of boundary
	Volume	In 3D space
	Volumetric quotient	In 3D space
	The long axis of the circumsphere	In 3D space
Texture	Energy, contrast, entropy, and adverse moment	In 2D space

TABLE 2: The number of GGO, juxtavascular, and other nodules.

Nodule type	GGO pulmonary nodule	Juxtavascular pulmonary nodule	Others	Total
Number	49	80	35	164

5. Experimental Results

Two databases were used to evaluate the effectiveness of the proposed method: one consisting of 60 thoracic CT scans obtained from LIDC database [34], another database consisted of 60 thoracic CT scans from several hospitals. The used medical CT slices were data sets with an intensity value of 16 bits and a resolution of $512 * 512$. Slice thickness varied from 0.5 to 2.5 mm and the total slice number for each scan varied from 52 to 384 with an average of 135/scan. The X-ray tube current ranged from 30 to 250 mA, and the pixel size ranged from 0.5 mm/pixel to 0.7 mm/pixel. Pulmonary nodules in CT images are solid or GGO (part-solid or nonsolid), whose sizes are from 3 mm to 30 mm. Moreover, locations of nodules are uncertain; some are isolated, others are adhered to lung wall or blood vessels. Each scan was read individually by members of a qualified panel and then a consensual gold standard was defined by the panel. This process defined ground truth of 164 nodules, and the number of different kinds of nodules is shown in Table 2.

The whole dataset was randomly split into training and testing datasets with the same number of scans (60 scans each). The latter was used as the independent testing for evaluating the performance of the trained classifiers, which has 86 nodules. Some experimental results in each step of the detection of pulmonary nodules as well as some discussions are presented below.

The whole dataset was randomly split into training and testing datasets with the same number of scans (60 scans each). The potential nodule objects for training and testing data sets of classification are generated by using the proposed segmentation method described in Sections 2 and 3. The latter was used as the independent testing for evaluating the performance of the trained classifiers, which has 86 nodules. Some experimental results in each step of the detection of pulmonary nodules as well as some discussions are presented below.

5.1. Segmentation of Potential Nodule Objects. The training dataset was processed, and 1377 potential nodule objects were segmented by using the proposed segmentation method described in Sections 2 and 3.

5.1.1. Qualitative Validation. In order to validate the effect of the proposed FIACM-based segmentation method and PMM-based refinement method, the clinical data with GGO

TABLE 3: Segmentation measure results (error rate).

CT image	The edge-based active model	The region-based active mode	The classical integrated active contour model	The proposed active contour model	
GGO pulmonary nodule	0.21	0.26	0.16	0.11	FIACM-based segmentation
Juxtavascular pulmonary nodule	0.21	0.29	0.19	0.13	FIACM-based segmentation + PMM-based refinement

TABLE 4: Experimental training data set (60 scans with 78 nodules).

Data set	Positive samples	Negative samples	Feature number
Pulmonary nodules	78	1299	21

nodules and juxtavascular nodules should be segmented and explored.

A comparison for segmentation of GGO nodule between the proposed FIACM-based segmentation method and the traditional approach, for example, region-based active contour model [7] and integrated active contour model [14], is shown in Figure 4. From Figure 4, the described segmentation method outperforms the traditional methods. As shown in Figures 4(c) and 4(d), the problem of boundary leakage at boundaries of a GGO pulmonary nodule occurs, while the problem is solved in Figure 4(e).

In this paper, juxtavascular nodules are segmented under a single segmentation framework. First, it is segmented by using FIACM-based segmentation method; then refinement is achieved by using PMM-based segmentation refinement method, shown in Figure 5. The refinement procession is only applied to pixels in some regions containing the blood vessels and juxtavascular nodules. For this reason, the correction and refinement method has the advantage of locally refining the nodule segmentation along recognized vessel attachments only, without modifying the nodule boundary elsewhere. Figures 5 and 6 illustrate the segmentation results. From Figures 5 and 6, the described segmentation method outperforms the traditional methods. Figure 6 shows the segmentation results of a juxtavascular pulmonary nodule using the proposed method, region-based active contour model [7], and the integrated active contour model [14], respectively. As shown in Figures 6(c) and 6(d), the problem of boundary leakage occurs in the adhesion place between the juxtavascular nodule and its attached vessel, while the problem of boundary leakage does not occur in Figure 6(e), which is solved by the proposed FIACM-based segmentation and PMM-based refinement method.

5.1.2. Quantitative Validation. Beyond the visual inspection, a quantitative analysis is necessary to ascertain the accuracy of the proposed segmentation method.

In this paper, the well-known Tanimoto/Jaccard error $A(C_m, C_o)$ [12] is used as the validation metrics, which refers to distances between segmentation results or to volume overlaps between the gold standard and the proposed segmentation

method. The gold standard typically is a high-quality reference segmentation carried out by experts. $A(C_m, C_o)$ is defined as

$$A(C_m, C_o) = 1 - \frac{\int_{C_m \cap C_o} dx dy dz}{\int_{C_m \cup C_o} dx dy dz}, \quad (14)$$

where C_m and C_o are the extracted and the desired contours, respectively.

In Table 3, the desired contour extracted manually and compared with the segmentation contours by the proposed method, the region-based active contour model using local region information, and the integrated active contour model combining curvature and statistical information. Table 3 shows that the errors of the proposed method are less than the other two traditional methods.

5.2. Training of SVM. After the preprocessing step, 1377 potential nodule objects in the training dataset were detected, including 78 pulmonary nodules and 1299 negative samples (nonnodules), shown in Table 4.

For the training dataset, the knowledge-based piecewise linear classifier was firstly used to remove easily dismissible FP regions. Some easily dismissible nonnodule objects are removed from pulmonary nodule candidates, and by using a knowledge-based piecewise linear classifier, in total, 395 nodule candidates were generated at the initial stage (317 nonnodule regions and 78 nodule regions). As discussed in Section 4.2.1, the four features, such as volume, volumetric quotient, and mean and standard deviation of intensity are calculated and used for knowledge-based piecewise linear classification. After the piecewise linear filtering, for the remaining nodule candidates, the weighted C-SVM was then employed to further remove FP regions. The weighted SVM was trained using the following scheme. The nodule candidates are classified by k-cross-validation training and testing the SVM. After that, the grid search method is used to search the optimal parameters C_+ and γ of C-SVM in this paper. In the grid search method, there should be a criterion to determine the optimal parameters. However, how to find a best criterion is still a difficult problem in the case of unbalanced dataset. Sensitivity and specificity are often used to measure the performance of the classification system; but they are often a tradeoff. The criterion of AUC (area under the ROC curve) is chosen to train C-SVM. When AUC reaches the maximum, the minimums of C_+ and γ meeting the AUC condition will be chosen. In Table 5, when sensitivity reaches

TABLE 5: K -fold CV results using the grid search for optimal parameters of C-SVM classifier.

Parameters	TP	FN	TN	FP	Sensitivity	Specificity	Accuracy	AUC
$K = 3, C_- = 0.5, \text{ and } \gamma = 1$	18	9	85	21	0.667	0.802	0.774	0.7529
$K = 4, C_- = 4, \text{ and } \gamma = 0.25$	13	7	72	8	0.650	0.9	0.85	0.7769
$K = 5, C_- = 4, \text{ and } \gamma = 2$	11	4	52	11	0.733	0.825	0.808	0.7359
$K = 6, C_- = 2, \text{ and } \gamma = 1$	10	3	46	7	0.769	0.868	0.848	0.7688
$K = 7, C_- = 2, \text{ and } \gamma = 4$	7	4	42	3	0.636	0.933	0.875	0.7769
$K = 8, C_- = 2, \text{ and } \gamma = 8$	7	2	36	3	0.778	0.923	0.896	0.8610
$K = 9, C_- = 0.5, \text{ and } \gamma = 0.125$	7	1	32	3	0.875	0.914	0.907	0.9116
$K = 10, C_- = 8, \text{ and } \gamma = 0.5$	7	1	30	1	0.875	0.968	0.949	0.9159

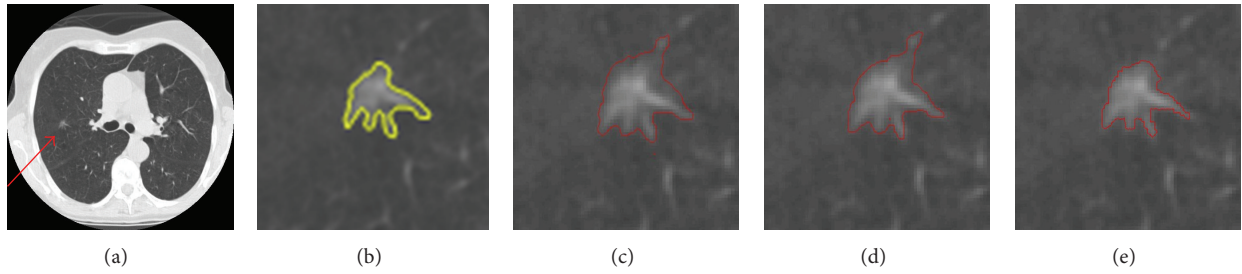


FIGURE 4: Segmentation result of a nonsolid GGO pulmonary nodule. (a) Original CT image; (b) the segmentation result carried out by experts; (c) the segmentation result by region-based active contour model; (d) the segmentation result by integrated active contour model; and (e) the segmentation result by the proposed FIACM model.

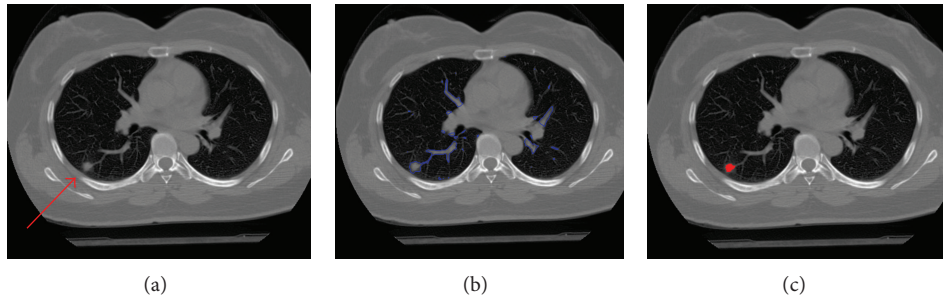


FIGURE 5: Segmentation results of the juxtavascular pulmonary nodule. (a) Original CT image, nodule adjacent to blood vessels; (b) whole segmentation result by FIACM-based method; and (c) segmented juxtavascular nodule after the fine segmentation by using PMM-based refinement method.

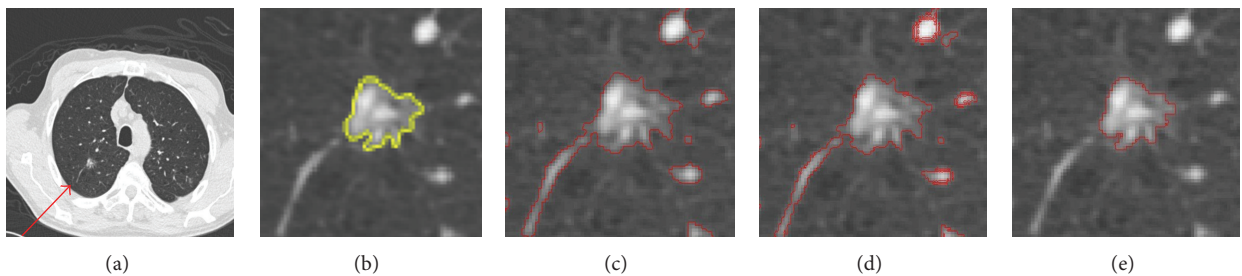


FIGURE 6: Segmentation results of the juxtavascular pulmonary nodule. (a) Original CT image; (b) the segmentation result carried out by experts; (c) the segmentation result by region-based active contour model; (d) the segmentation result by integrated active contour model; and (e) the segmentation result by the proposed FIACM-based segmentation and PMM-based refinement method.

TABLE 6: Detection performance of the proposed method on the testing dataset (60 scans with 86 nodules).

Total nodule	Nodule detected	Accuracy rate	FP per scan	Sensitivity
86	83	95.4%	1.1/scan	88.2%

TABLE 7: The variation of nodule detection performance over all cases on independence testing data based on the proposed method.

	Highest	Lowest	STD (standard deviation)
Sensitivity	100%	64%	0.089
Specificity	100%	81%	0.093
False positive	6	1	1.7

TABLE 8: The different nodule sizes on independent testing data.

Nodule type	≤ 5 mm	5–10 mm	10–20 mm	Total
GGO pulmonary nodule	3	10	16	29
Juxtavascular pulmonary nodule	2	27	12	41
Others	4	6	8	18

TABLE 9: Detection performance for GGO and juxtavascular pulmonary nodules (60 scans).

Nodule type	Total nodule	Nodule detected	Detection rate	FP per scan
GGO pulmonary nodule	29	28	96.5%	2.7/scan
Juxtavascular pulmonary nodule	41	39	95.1%	3.1/scan

87.5%, specificity is 96.8%, and the performance of the SVM is considered the optimum.

5.3. Validation of the Proposed Detection Method. The proposed detection method and trained model was tested on the independent data. Experimental results of recognition for pulmonary nodules show desirable performances of the proposed method. The experimental results using the proposed method indicate the performances with a detection rate of 95.4% with 1.1 FPs/scan (sensitivity of 88.2%), shown in Table 6.

By using the proposed method, Table 7 shows the variation in sensitivity and FP rate over all cases on the independent testing data. As it is known that different imaging parameters (e.g., different slice thickness and different tube currents) may affect the nodule detection performance, the proposed method tries to limit the influence by tuning the model (choosing the optimal parameters) on a wide range of nodules with different sizes, slice thickness, and radiation. The experimental results on the independent dataset demonstrate the generalizability of the proposed method.

Some detected results of the proposed method are shown in Figures 7, 8, and 9, which are the detection results of GGO nodules and juxtavascular nodules, respectively.

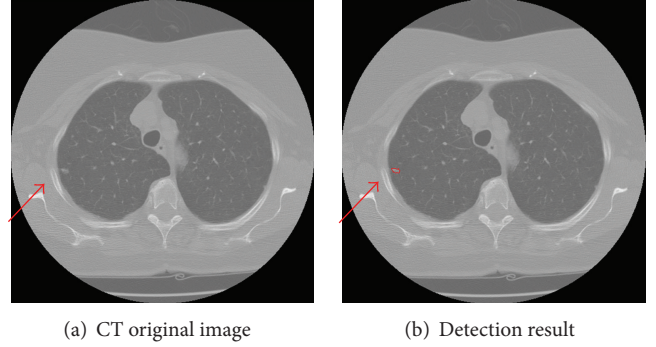


FIGURE 7: Detection result of the case containing a small GGO nodule.

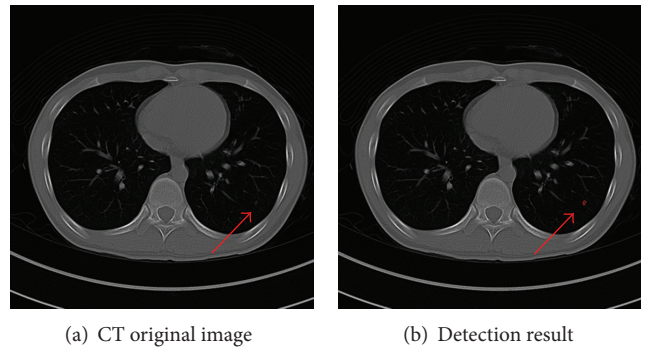


FIGURE 8: Detection result of the case containing a small pure GGO nodule.

Table 8 illustrates the final detection sensitivity based on the different nodule size groups for the GGO nodules, juxtavascular nodules, and others, by using the proposed method on the independent testing data. Others include some solid solitary nodules and juxtapleural nodules. And Table 9 shows the detection performance for GGO and juxtavascular pulmonary nodules. Some juxtavascular nodules are nonsolid, hence they are also GGO nodules. In our experiment, there are two types of nodules, juxtavascular nodules and GGO nodules. These types are registered, respectively.

The proposed CAD algorithm was implemented and tested on the computer with 2.13 * 2 GHz CPU, 4 GB Memory and Graphic Card FX 5800. On average, it takes about 1.06 min/scan.

6. Discussion

The experimental result shows a detection accuracy rate of 95.4% with 1.1 FPs/scan (sensitivity = 88.2%) for the proposed method using the independent dataset. The detection performance for GGO and juxtavascular pulmonary nodules was the detection of 96.5% with 2.7 FPs/scan, and the detection of 95.1% with 3.1 FPs/scan, respectively.

We attempt a comparison with the results reported by other research groups. Most of algorithms have been developed for solid nodules. Lee et al. [35] proposed a genetic algorithm (GA) template matching (GATM) technique for detecting nodules within the lung area. Shape and gradient

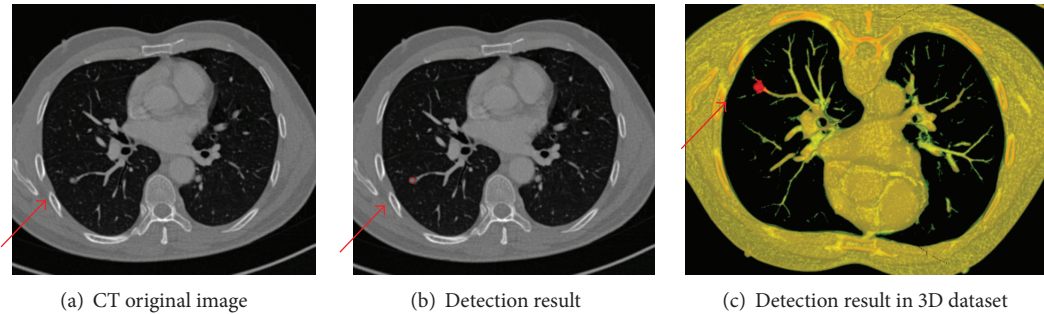


FIGURE 9: Detection results of the case containing a juxtavascular nodule.

features rules were used to reduce false positives (FPs). A sensitivity of 72% was achieved with 31 FP/scan. Paik et al. [5] proposed surface normal overlap (SNO) method to capture the concentration of normals by calculating derivatives of intensity images. Results on eight chest datasets were reported with 90% sensitivity and 5.6 FP/scan for solid nodules. Recently, for detection of GGO nodules, Kim et al. [36] used texture features and a three-layered neural network to detect GGO nodules. They tested 14 scans with tube dose from 200 to 400 mA and achieved a sensitivity of 94.3%. Ye et al. [4] proposed a shape-based SVM method for detecting nodules. The 3D local geometric and statistical intensity features were used to detect potential solid and GGO nodule. A detection rate of about 90.2% (including solid and GGO nodules) and FP at 8.2/scan was achieved. Unfortunately, most authors did not report quantitative results for different typologies of nodules according to proximity to surrounding structures (such as well-circumscribed, juxtavascular nodules). Bae et al. [37] used the morphologic matching algorithm to detect pulmonary nodules. An overall sensitivity of 95.1% for all nodules was achieved. The sensitivity for detecting nodules according to category was 97.4% for isolated nodules, 92.3% for juxtapleural nodules, and 94.1% for juxtavascular nodules. Diciotti et al. [3] refined the segmentation for juxtavascular nodules based on a local shape analysis of the initial segmentation making use of 3D geodesic distance map representations. They observed a percentage of successful segmentations of 84.8% in fully automated mode and of 91.0% by using an additional interactive mode (for improving the segmentation quality of juxtavascular nodules). However, nonsolid juxtavascular nodules (ground glass opacities) were not considered in their work.

Comparing with different CAD models covered in the literature [1, 4] and other reported literatures above, it seems that the proposed method's relatively high detection rate, fast computation, and applicability to different imaging conditions and nodule types show much promise for clinical applications. As a rule, nodule detection systems consist of several steps: (a) preprocessing; (b) object segmentation/candidate detection; (c) false positive reduction; and (d) classification. Most techniques often try to cheaply segment and detect the potential nodules in an attempt to drastically reduce the number of these FPs. These steps are, however, crucial in improving the detection rate and reducing the number of false positives. The reason why the proposed method has

a better performance for detecting all types of GGO and juxtavascular nodules are as follows.

- (1) Candidate detection: the purpose of candidate detection is to avoid missing potential nodules. Moreover in this step, the precise segmentation of potential nodule is often a necessary step to computer analysis, extraction, and computation of features, which is important for false positive reduction. As mentioned before, our solution for efficiently segmenting the potential nodule objects involves two steps: (i) a FIACM-based segmentation method for a whole segmentation and (ii) a segmentation refinement method based on PMM, for accurate segmentation of potential juxtavascular nodules. The former is especially used for low-contrast nodules such as part-solid and nonsolid GGO nodules, to overcome the problems of boundary leakage, "weak" local minima and high computational cost, while the latter, referred to as a fine segmentation, is used to segment potential juxtavascular nodules. So the correction method has the advantage that it locally refines the nodule segmentation along recognized vessel attachments only, without modifying the nodule boundary elsewhere.
- (2) False positive reduction: in this paper, pulmonary nodules are classified by using the knowledge-based C-SVM classifiers. First, the knowledge-based piecewise linear classification is used to remove easily dismissible nonnodule objects. Then, C-SVM classification is used to further classify nodule candidates and reduce the number of false positive (FP) objects. Moreover, 2D and 3D features are used for classification of potential nodule objects.

However, some nodules (false negatives) are missed by the proposed method. Typically, these nodules are too small (almost 2 mm) and juxtapleural nodules and of very low contrast, which makes it difficult to segment and extract the effective features.

To further improve the detection performance, some improvements need to be further investigated as follows: (a) in order to recognize small and juxtapleural pulmonary nodules in noisy image more effectively, an adaptive smoothing method needs to be further investigated, and the juxtapleural and pleural-tail nodules should be further researched; (b) in this paper, intelligent recognition of pulmonary nodules is

studied. However, intelligent differentiation of benign and malignant nodules is not considered. This requires further investigation.

7. Conclusions

In this paper, an improved detection method of pulmonary nodules in chest CT images, combining FIACM-based segmentation method, segmentation refinement method based on PMM of juxtavascular nodules, and knowledge-based C-SVM classifier, is proposed for detecting various types of pulmonary nodules, especially for GGO nodules (part-solid and nonsolid) and juxtavascular nodules. This study demonstrates the superiority of the proposed method. The described segmentation method outperforms the traditional methods, and evaluating the algorithm on the provided test data leads to an average Tanimoto/Jaccard error of 0.11 and 0.13 for GGO and juxtavascular nodules, respectively. The experimental results using the proposed method indicate the performances with a accuracy rate of 95.4% with 1.1 FPs/scan (sensitivity of 88.2%). Different types of challenging nodules such as low-contrast part-solid/nonsolid GGO nodules and juxtavascular nodules are identified. The detection performance for GGO and juxtavascular pulmonary nodules is the detection of 96.5% with 2.7 FPs/scan and the detection of 95.1% with 3.1 FPs/scan, respectively. Experimental results of recognition for pulmonary nodules show desirable performances of the proposed method.

Acknowledgments

The authors would like to thank Dr. Y. X. Guo, Dr. P. Chen, Dr. L. F. Wang, Dr. R. Bai, and Dr. F. Long for their helpful comments and advice which contributed much to this paper. This work is supported by the National Natural Science Foundation of China (61273249, 31100671), the Natural Science Foundation of Guangdong Province, China (S2012010009886, S2011010005811), the Specialized Research Fund for the Doctoral Program of Higher Education of China (200805610018), Guangdong-Hong Kong Technology Cooperation Funding under Grant (no. 2010Z11), Key Laboratory of Autonomous Systems and Network Control of Ministry of Education (SCUT of China), the National Engineering Research Center for Tissue Restoration and Reconstruction, and the Guangdong Key Laboratory for Biomedical Engineering (SCUT of China).

References

- [1] I. Sluimer, A. Schilham, M. Prokop, and B. van Ginneken, "Computer analysis of computed tomography scans of the lung: a survey," *IEEE Transactions on Medical Imaging*, vol. 25, no. 4, pp. 385–405, 2006.
- [2] T. Kubota, A. K. Jerebko, M. Dewan, M. Salganicoff, and A. Krishnan, "Segmentation of pulmonary nodules of various densities with morphological approaches and convexity models," *Medical Image Analysis*, vol. 15, no. 1, pp. 133–154, 2011.
- [3] S. Diciotti, S. Lombardo, M. Falchini, G. Picozzi, and M. Mascali, "Automated segmentation refinement of small lung nodules in CT scans by local shape analysis," *IEEE Transactions on Biomedical Engineering*, vol. 58, no. 12, pp. 3418–3428, 2011.
- [4] X. Ye, X. Lin, J. Dehmeshki, G. Slabaugh, and G. Beddoe, "Shape-based computer-aided detection of lung nodules in thoracic CT images," *IEEE Transactions on Biomedical Engineering*, vol. 56, no. 7, pp. 1810–1820, 2009.
- [5] D. S. Paik, C. F. Beaulieu, G. D. Rubin et al., "Surface normal overlap: a computer-aided detection algorithm with application to colonic polyps and lung nodules in helical CT," *IEEE Transactions on Medical Imaging*, vol. 23, no. 6, pp. 661–675, 2004.
- [6] T. F. Chan and L. A. Vese, "Active contours without edges," *IEEE Transactions on Image Processing*, vol. 10, no. 2, pp. 266–277, 2001.
- [7] C. Li, C. Y. Kao, J. C. Gore, and Z. Ding, "Minimization of region-scalable fitting energy for image segmentation," *IEEE Transactions on Image Processing*, vol. 17, no. 10, pp. 1940–1949, 2008.
- [8] T. W. Way, L. M. Hadjiiski, B. Sahiner et al., "Computer-aided diagnosis of pulmonary nodules on CT scans: segmentation and classification using 3D active contours," *Medical Physics*, vol. 33, no. 7, pp. 2323–2337, 2006.
- [9] W. B. Tao, "Iterative narrowband-based graph cuts optimization for geodesic active contours with region forces (GACWRF)," *IEEE Transactions on Image Processing*, vol. 21, no. 1, pp. 284–296, 2012.
- [10] V. Caselles, R. Kimmel, and G. Sapiro, "Geodesic active contours," *International Journal of Computer Vision*, vol. 22, no. 1, pp. 61–79, 1997.
- [11] S. Lankton and A. Tannenbaum, "Localizing region-based active contours," *IEEE Transactions on Image Processing*, vol. 17, no. 11, pp. 2029–2039, 2008.
- [12] S. Krinidis and V. Chatzis, "Fuzzy energy-based active contours," *IEEE Transactions on Image Processing*, vol. 18, no. 12, pp. 2747–2755, 2009.
- [13] H. C. van Assen, M. G. Danilouchkine, M. S. Dirksen, J. H. C. Reiber, and B. P. F. Lelieveldt, "A 3-D active shape model driven by fuzzy inference: Application to cardiac CT and MR," *IEEE Transactions on Information Technology in Biomedicine*, vol. 12, no. 5, pp. 595–605, 2008.
- [14] C. Sagiv, N. A. Sochen, and Y. Y. Zeevi, "Integrated active contours for texture segmentation," *IEEE Transactions on Image Processing*, vol. 15, no. 6, pp. 1633–1646, 2006.
- [15] W. J. Kostis, A. P. Reeves, D. F. Yankelevitz, and C. I. Henschke, "Three-dimensional segmentation and growth-rate estimation of small pulmonary nodules in helical CT images," *IEEE Transactions on Medical Imaging*, vol. 22, no. 10, pp. 1259–1274, 2003.
- [16] J. M. Kuhnigk, V. Dicken, L. Bornemann et al., "Morphological segmentation and partial volume analysis for volumetry of solid pulmonary lesions in thoracic CT scans," *IEEE Transactions on Medical Imaging*, vol. 25, no. 4, pp. 417–434, 2006.
- [17] F. Zana and J. C. Klein, "Segmentation of vessel-like patterns using mathematical morphology and curvature evaluation," *IEEE Transactions on Image Processing*, vol. 10, no. 7, pp. 1010–1019, 2001.
- [18] G. Agam, S. G. Armato, and C. Wu, "Vessel tree reconstruction in thoracic CT scans with application to nodule detection," *IEEE Transactions on Medical Imaging*, vol. 24, no. 4, pp. 486–499, 2005.

- [19] C. Wu and G. Agam, "Probabilistic nodule filtering in thoracic CT scans," in *Medical Imaging 2006: Image Processing*, J. M. Reinhardt and J. P. W. Pluim, Eds., vol. 6144 of *Proceedings of SPIE*, pp. 1–9, 2006.
- [20] D. Lesage, E. D. Angelini, I. Bloch, and G. Funka-Lea, "A review of 3D vessel lumen segmentation techniques: models, features and extraction schemes," *Medical Image Analysis*, vol. 13, no. 6, pp. 819–845, 2009.
- [21] C. Bauer, T. Pock, E. Sorantin, H. Bischof, and R. Beichel, "Segmentation of interwoven 3d tubular tree structures utilizing shape priors and graph cuts," *Medical Image Analysis*, vol. 14, no. 2, pp. 172–184, 2010.
- [22] K. Murphy, B. van Ginneken, A. M. R. Schilham, B. J. de Hoop, H. A. Gietema, and M. Prokop, "A large-scale evaluation of automatic pulmonary nodule detection in chest CT using local image features and k-nearest-neighbour classification," *Medical Image Analysis*, vol. 13, no. 5, pp. 757–770, 2009.
- [23] G. D. Rubin, J. K. Lyo, D. S. Paik et al., "Pulmonary nodules on multi-detector row CT scans: performance comparison of radiologists and computer-aided detection," *Radiology*, vol. 234, no. 1, pp. 274–283, 2005.
- [24] Q. Li and F. Li K, "Computerized detection of lung nodules in thin-section CT images by use of selective enhancement filters and an automated rule-based classifier," *Academic Radiology*, vol. 15, no. 2, pp. 165–175, 2008.
- [25] D. T. Lin, C. R. Yan, and W. T. Chen, "Autonomous detection of pulmonary nodules on CT images with a neural network-based fuzzy system," *Computerized Medical Imaging and Graphics*, vol. 29, no. 6, pp. 447–458, 2005.
- [26] R. C. Hardie, S. K. Rogers, T. Wilson, and A. Rogers, "Performance analysis of a new computer aided detection system for identifying lung nodules on chest radiographs," *Medical Image Analysis*, vol. 12, no. 3, pp. 240–258, 2008.
- [27] T. Messay, R. C. Hardie, and S. K. Rogers, "A new computationally efficient CAD system for pulmonary nodule detection in CT imagery," *Medical Image Analysis*, vol. 14, no. 3, pp. 390–406, 2010.
- [28] C. C. Hung, S. Kulkarni, and B. C. Kuo, "A new weighted fuzzy C-means clustering algorithm for remotely sensed image classification," *IEEE Journal on Selected Topics in Signal Processing*, vol. 5, no. 3, pp. 543–553, 2011.
- [29] J. Weickert and G. Kühne, "Fast methods for implicit active contour models," in *Geometric Level Set Methods in Imaging, Vision, and Graphics*, part 2, pp. 43–57, Springer, New York, NY, USA, 2003.
- [30] R. P. Browne, P. D. McNicholas, and M. D. Sparling, "Model-based learning using a mixture of Gaussian and uniform distributions," *IEEE Transactions on Pattern Analysis and Machine Intelligence*, vol. 34, no. 4, pp. 814–817, 2012.
- [31] E. Criado, M. Sanchez, J. Ramirez et al., "Pulmonary sarcoidosis: typical and atypical manifestations at high-resolution CT with pathologic correlation," *RadioGraphics*, vol. 30, no. 6, pp. 1567–1586, 2010.
- [32] F. Girvin and J. P. Ko, "Pulmonary nodules: detection, assessment, and CAD," *The American Journal of Roentgenology*, vol. 191, no. 4, pp. 1057–1069, 2008.
- [33] J. Levman, T. Leung, P. Causer, D. Plewes, and A. L. Martel, "Classification of dynamic contrast-enhanced magnetic resonance breast lesions by support vector machines," *IEEE Transactions on Medical Imaging*, vol. 27, no. 5, pp. 688–696, 2008.
- [34] A. P. Reeves, A. M. Biancardi, T. V. Apanasovich et al., "The lung image database consortium (LIDC). A comparison of different size metrics for pulmonary nodule measurements," *Academic Radiology*, vol. 14, no. 12, pp. 1475–1485, 2007.
- [35] Y. Lee, T. Hara, H. Fujita, S. Itoh, and T. Ishigaki, "Automated detection of pulmonary nodules in helical CT images based on an improved template-matching technique," *IEEE Transactions on Medical Imaging*, vol. 20, no. 7, pp. 595–604, 2001.
- [36] K. G. Kim, J. M. Goo, J. H. Kim et al., "Computer-aided diagnosis of localized ground-glass opacity in the lung at CT: initial experience," *Radiology*, vol. 237, no. 2, pp. 657–661, 2005.
- [37] K. T. Bae, J. S. Kim, Y. H. Na, K. G. Kim, and J. H. Kim, "Pulmonary nodules automated detection on CT images with morphologic matching algorithm—preliminary results," *Radiology*, vol. 236, no. 1, pp. 286–294, 2005.

Research Article

Automatic Vertebral Column Extraction by Whole-Body Bone SPECT Scan

Sheng-Fang Huang,¹ Hao-Yu Chao,² Pan-Fu Kao,^{3,4} Wei-Chih Shen,⁵
Yu-Hsiang Chou,⁶ and Shu-Hsin Liu^{7,8}

¹ Department of Medical Informatics, Tzu Chi University, Hualien 97004, Taiwan

² Institute of Medical Sciences, Tzu Chi University, Hualien 97004, Taiwan

³ School of Medicine, Chung Shan Medical University, Taichung 40201, Taiwan

⁴ Department of Nuclear Medicine, Chung Shan Medical University Hospital, Taichung 40201, Taiwan

⁵ Department of Computer Science and Information Engineering, Asia University, Taichung 41354, Taiwan

⁶ Department of Nuclear Medicine, Buddhist Tzu Chi General Hospital, Taipei Branch, New Taipei City 23142, Taiwan

⁷ Department of Nuclear Medical, Buddhist Tzu Chi Hospital, Hualien 97004, Taiwan

⁸ Department of Radiological Technology, Tzu Chi College of Technology, Hualien 97005, Taiwan

Correspondence should be addressed to Sheng-Fang Huang; spiculate@hotmail.com

Received 28 November 2012; Revised 8 March 2013; Accepted 10 March 2013

Academic Editor: Chung-Ming Chen

Copyright © 2013 Sheng-Fang Huang et al. This is an open access article distributed under the Creative Commons Attribution License, which permits unrestricted use, distribution, and reproduction in any medium, provided the original work is properly cited.

Bone extraction and division can enhance the accuracy of diagnoses based on whole-body bone SPECT data. This study developed a method for using conventional SPECT for automatic recognition of the vertebral column. A novel feature of the proposed approach is a novel “bone graph” image description method that represents the connectivity between these image regions to facilitate manipulation of morphological relationships in the skeleton before surgery. By tracking the paths shown on the bone graph, skeletal structures can be identified by performing morphological operations. The performance of the method was evaluated quantitatively and qualitatively by two experienced nuclear medicine physicians. Datasets for whole-body bone SPECT scans in 46 lung cancer patients with bone metastasis were obtained with Tc-99m MDP. The algorithm successfully segmented vertebrae in the thoracolumbar spine. The quantitative assessment shows that the segmentation method achieved an average TP, FP, and FN rates of 95.1%, 9.1%, and 4.9%. The qualitative evaluation shows an average acceptance rate of 83%, where the data for the acceptable and unacceptable groups had a Cronbach's alpha value of 0.718, which indicated reasonable internal consistency and reliability.

1. Introduction

In nuclear medicine, bone scintigraphy is widely used to detect bone metastases [1]. Technetium-99m methylene diphosphonate (Tc-99m MDP) scanning is the most common method of staging bone metastases and osteomyelitis in routine examinations. In a common whole-body bone scan, planar image scan protocol is usually used because it is time-saving. However, overlapping objects in a planar image may cause difficulty in interpreting images. Single photon emission computed tomography (SPECT), a functional imaging method of reconstructing skeletal objects in three-dimensional (3D) from different projection views, provides more diagnostic information compared to planar imaging [2,

3]. Vertebral SPECT is also superior for detecting metastatic foci [4].

When using SPECT for bone scan, segmentation is essential for volume rendering and for perceiving overall spatial relationships before extracting bones of interest for further analysis. After segmentation, skeletal structures are usually labeled so that abnormalities can be located automatically. However, the significant noise and relatively poor spatial resolution of SPECT often degrade nuclear imaging quality, which makes labeling difficult [5]. In whole-body bone scan images, the Tc-99m MDP uptake can also be seen in some organs. The image contains not only bone sections but also some parts of soft tissues. To ensure

adequate specificity, an automatic lesion detection algorithm is needed to distinguish soft tissues from skeletal structures. Additionally, image brightness could be irregular for different bone sections. Therefore, optimizing the global threshold for image intensity is difficult when extracting skeletal structures. Moreover, SPECT imaging provides a unique challenge in this issue because the 3D process for a SPECT image is time-consuming. Thus, an automated computer-aided detection/diagnosis (CAD) system is urgently needed to increase efficiency and effectiveness in bone metastasis screening.

So far there have been several studies proposed to solve segmentation problem in whole-body bone scan images. One of the simplest proposed solutions for solving the segmentation problem in whole-body bone scanning is binary classification based on gray level, such as thresholding or region growing. Erdi et al. proposed a semiautomated approach for quantifying the area of bone metastases [6]. After the user selects a seed point for each lesion, the procedure automatically extracts the abnormality and calculates the percentage of lesion involvement in each bone. The main contribution of this approach is saving physician's time on drawing region of interest (ROI). Yin and Chiu considered taking experts' knowledge into account to deal with segmentation problem [7]. Their approach to bone scintigraphy used a knowledge-based bone division method to detect abnormalities by performing fuzzy analysis of asymmetries in bone morphology. Although this approach eventually achieved good performance in hand and leg regions, it performed poorly when analyzing bones in the head and vertebral column. In Šajin et al., the extreme edges of the main skeletal regions were used as reference points [8]. Their study demonstrated that the obtained reference points are helpful for skeletal segmentation in bone scintigraphy. Sadik et al. proposed a procedure for building a decision-support system [9]. Abnormalities extracted according to threshold values were classified on a scale from 0.0 to 1.0 by an artificial neural network analysis of 14 clinical features. However, this approach could not detect areas with high symmetry and high uptake such as joints and vertebrae. Huang et al. proposed a CAD system for using a hybrid method of bone division to analyze planar whole-body bone images [10]. Fuzzy set histogram thresholding technique was used to differentiate bones from soft tissues. Morphological knowledge was then applied to preform skeleton segmentation. Finally, a bandwidth concept was introduced to detect hot spots. The overall sensitivity was 92.1% with 7.58 false detections per image.

In recent decades, the development of CAD systems for planar nuclear medicine imaging has steadily improved in terms of automation and sensitivity. However, fully automatic segmentation of whole-body bone SPECT scan images is still an open issue, and relevant CAD applications are quite limited in number. He et al. reported an image intelligent system that provides automatic diagnosis to process whole-body bone SPECT images [11]. The method employs optimal thresholding algorithm to extract bone regions from background and uses histogram equalization to reduce the effect caused by the high uptake of bladder. However, since the

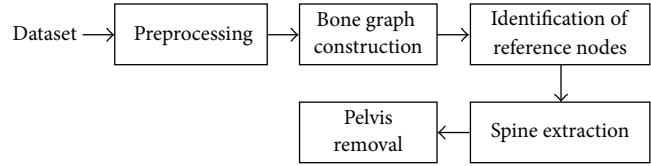


FIGURE 1: The flowchart of the proposed method.

system does not contain any function for bone division to provide skeletal information, the system cannot automatically determine the positions of abnormalities and may fail to reduce the ambiguity between bone lesions and normal parts, such as joints and kidneys. Under this consideration, our study extended a previous version of our CAD system developed in 2009 [12] and designed a 3D segmentation method for using whole-body bone SPECT images for structural analysis of human skeletal anatomy. In this paper, we focus on the techniques of spine extraction, owing to the reason that the vertebral column affects up to a third of all cancer patients and is the most frequent site of metastatic involvement of the skeleton [13]. This study developed a novel “bone graph” data structure for formulating bone segmentation problems as a graph clustering problem. The study includes quantitative and qualitative assessments to evaluate the performance. Figure 1 shows a flowchart of the proposed method.

2. Data Acquisition

The datasets were collected for 46 lung cancer patients with bone metastasis who had received Tc-99m MDP whole-body bone scans by SPECT at Buddhist Tzu Chi Hospital, Taipei Branch. The SPECT images for all patients were reviewed by a single experienced nuclear medicine physician. Patients with renal abnormalities and patients who had received surgical implants containing cement, rods, or screws were excluded from the study. A GE Infinia Hawkeye 4 gamma camera was used to acquire data in 6 degrees and with 16 seconds per step. One detector head collected data in 180 degree and another one collected data in the opposite 180 degree [14]. The SPECT imaging started at 3.5 hours after tracer injection. A full scan requires 5 sections, taking 8 minutes for each. The scan time was 40 minutes in total. The projection data were reconstructed using the GE's Evolution for bone reconstruction algorithm, where a 3D Collimator-Detector Response compensation method is used and integrated into an iterative reconstruction algorithm for SPECT images. Each dataset was saved in Interfile (Analyze 7.5) format. Image slices were included in a single image file and other information were saved in a header file. This study was reviewed and approved by the institutional review board at Tzu Chi Hospital. This Health Insurance Portability and Accountability Act-compliant single center is a retrospective study. A waiver of informed consent was obtained because the research involves no more than minimal risk and the waiver will not adversely affect the rights and welfare of the patients.

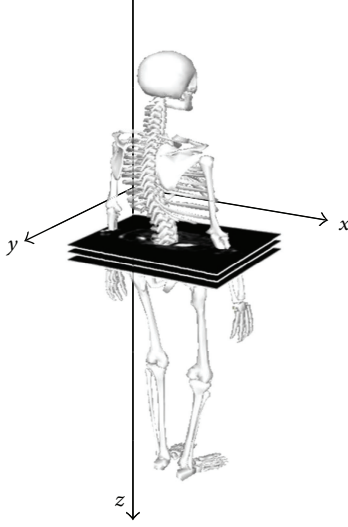


FIGURE 2: The three axes of the coordinate system defined in the proposed method.

3. Method

3.1. Preprocessing. A dataset containing whole-body bone scan SPECT images is initially converted to bitmap format images in transaxial view. Assume that the coordinate system of the images is defined as shown in Figure 2. A threshold value T is then applied to separate bone regions from soft tissues. However, the partial-volume effect (PVE) could lead to lower intensity values for voxels that only partially represent bone regions. Therefore in this study, moment-preserving thresholding is used to determine the value of T [15]. The thresholding method was computed based on the image histogram improved by using boundary characteristics, in order to avoid the interference caused by a large background area or the extremely high intensities from disease hotspots [16]. The image is then converted into a binary image, $b(x, y, z)$, where $b(x, y, z)$ equals 1 if the pixel value is larger than; otherwise, 0 is assigned. For each image slice, a connected component with gray level higher than T is defined as bone region. Each region is characterized by its shape features, including spatial center, area and bounding box, which will be used to determine the topological relationships among regions.

3.2. Design of Bone Graph Model

3.2.1. Graph Initialization. A special graph is used to describe the connectivity between bone regions so that segmentation problems could be solved with graph algorithms. This “bone graph” can be represented by $G = (V, E)$, where V denotes the node set and E denotes the edge set. The elements of V and E have the following characteristics.

- (1) Each region (connected component) in each plane is represented by a node in V .
- (2) When a plane K contains a node m , a plane L contains a node n , and $K < L$, a directed edge extending from

m to n (down-link) and a directed edge extending from n to m (up-link) are added to E if a projection of node m onto plane L overlaps with node n .

The construction of the bone graph is shown in Figure 3, where the node level is determined by the number of slices to which it belongs. The discrimination of uplink and downlink can provide a clear definition to the edge direction on the graph, which indicates a super-/subordinate relation link between two nodes. For example, a node p pointed by an uplink from a node q implies that the plane where p is located is higher than that of q . This prevents the traverse from falling into the wrong level of image plane when nodes are scanned in the upward or downward direction. Each edge is weighted in order to evaluate the correlation between neighboring nodes. If $R(i)$ is the set of projected pixels corresponding to the node i , the edge weight, w_{ij} , represents the region similarity of the node i with the node j and can be defined as follows:

$$w_{ij} = \frac{|R(i)| |R(i) \cap R(j)|}{|R(i) \cup R(j)|^2}. \quad (1)$$

Varying from 0 to 1, a significant overlap of $R(i)$ with $R(j)$ will result in a high value of w_{ij} , as shown as Figure 4.

3.2.2. Model Optimization. Given the pairwise similarity matrix $\mathbf{W} = (w_{ij})$, segmentation using the bone graph can be modeled by a graph-cut clustering framework. The similarity between two clusters C_1 and C_2 is defined as follows:

$$S(C_1, C_2) \equiv \sum_{i \in C_1} \sum_{j \in C_2} w_{ij}. \quad (2)$$

The objective of the proposed segmentation method requires an iterative process of image region decomposition and graph modification so that $S(C_1, C_2)$ is minimized to zero. The algorithm is described next.

Step 1. At the beginning, a seed node is selected into a cluster denoted by C_1 , while each of the other nodes is a cluster itself, denoted by C_i for $i > 1$:

Step 2. For all $i > 1$, if $S_{1i} = S(C_1, C_i) > 0$, the distance from C_1 to C_i is measured by the following cost function:

$$d_i = \frac{|S_{1i} - \sum_{j>1, j \neq i} S_{ij}|}{\max(S_{1i}, \sum_{j>1, j \neq i} S_{ij})}. \quad (3)$$

If $d_i < 0.5$, then C_i is combined into C_1 ; otherwise, C_i is split to create more clusters. To achieve this, some pixels are built by using morphological operations to decompose the corresponding image region into parts. The bone graph is then updated to reflect this modification.

Step 3. If $\sum_{i>1} S_{1i} = 0$, the process stops. Otherwise, it goes back to Step 2 to continue.

Figure 5 illustrates a situation that requires cluster splitting. The graph pattern shown in this figure may occur at

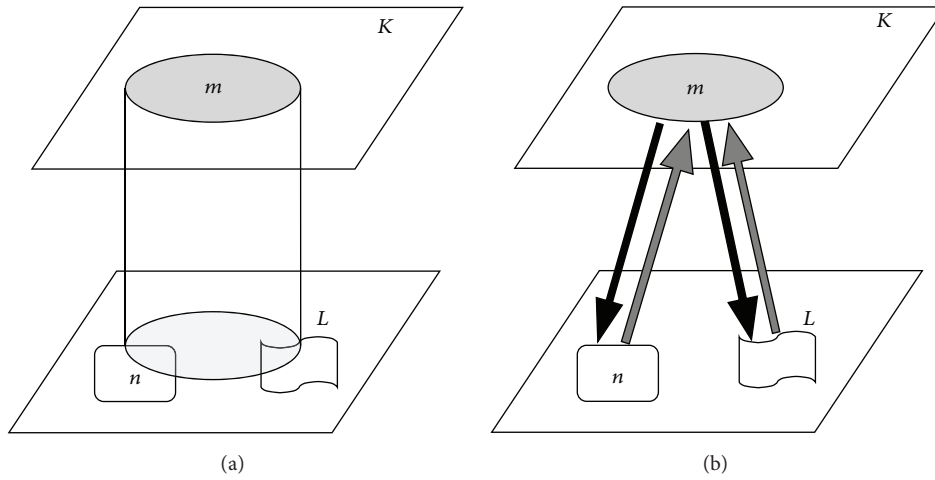


FIGURE 3: The construction of a bone graph. If the region m in the plane K overlaps the region n in the plane L , and then a downlink edge pointing from m to n and an uplink edge from n to m (uplink) are added.

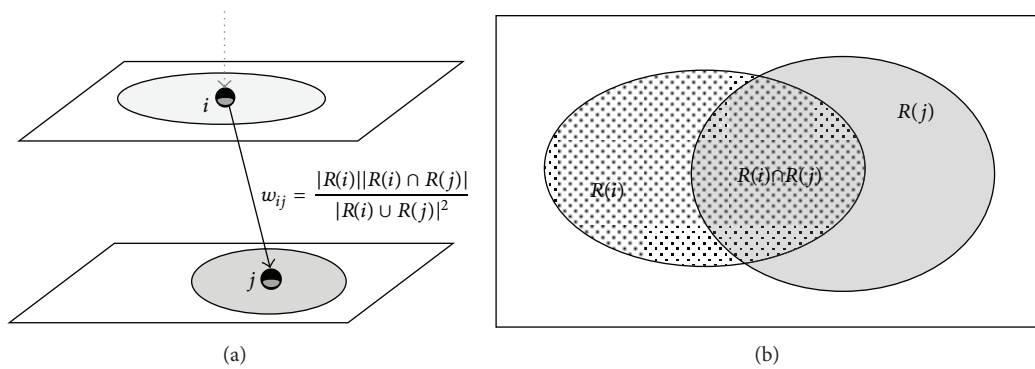


FIGURE 4: The edge weight w_{ij} is computed as the similarity evaluation between two image regions. The value is based on the fraction of how large the two regions overlap on the 2D projection plane, as shown in (b).

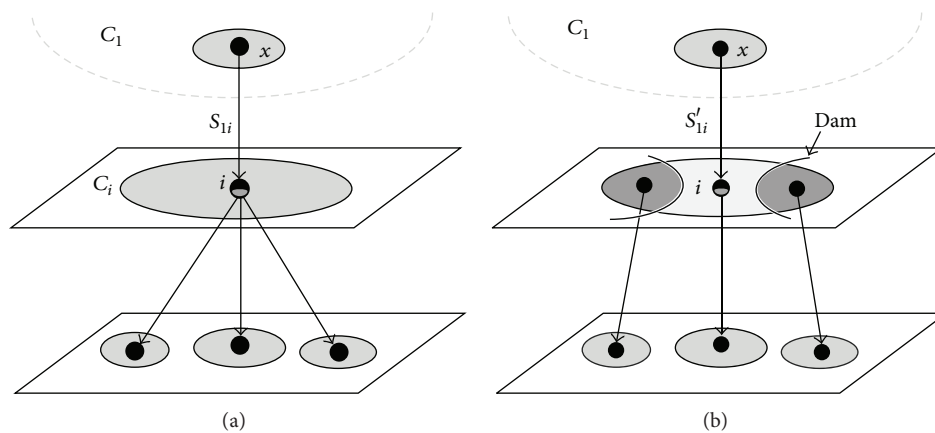


FIGURE 5: (a) The pattern represents an unbalanced cluster C_i , which usually corresponds to a branching node in the graph. (b) A cluster splitting procedure creates dam lines to separate the image region of the node i into more parts. After that, the bone graph and its corresponding clusters are updated so that the merging process can be continued.

a branching node, such as shoulders, joints, or a vertebrae nearby kidneys, which will result in irregular similarities with neighboring clusters. The distance computed by the cost function is used to evaluate this variance in order to determine whether the expansion of C_1 would be trapped into an unbalanced cluster. If so, a cluster splitting process is then performed to modify the graph topology. At the end when $\sum_{i>1} S_{1i} = 0$, the subgraph included in the cluster of C_1 is entirely isolated and disconnected to other subgraphs, where the image regions of the extracted subgraph form the final segmentation result of interest.

3.2.3. Image Decomposition and Cluster Splitting. To decompose a target region image M , a set containing n reference regions is defined as R_M , where $R_M = \{M_k \mid M_k \subseteq M \text{ and } M_x \cap M_y = \phi \text{ for } 1 \leq x, y \leq n \text{ and } x \neq y\}$. To split M , each M_k is iteratively enlarged by using morphological dilation. The dilation is restricted within the bound of M and continues until the entire area of M is filled. At each iteration, the coordinates where two dilated regions met are marked as dam points. Once this procedure completes, the dam points are removed, which therefore separates M into n subregions.

According to the algorithm in Section 3.2.2, if a clustering splitting procedure is required for C_i , we decompose the image region of C_i in order to create more clusters. Suppose that the image region of C_i is defined as M . As illustrated in Figure 5(b), if the node x in C_1 connects to the node i of C_i , then assume that $R(x)$ denotes the set of projected pixels corresponding to the node x . The set of reference regions, R_M , can be assembled by the following regions:

$$R_M = \{[R(x) \oplus B] \cap M\} \cup \{r \mid r \subseteq [M - R(x)] \otimes B\}. \quad (4)$$

The symbols \otimes and \oplus represent image morphological operators, respectively, for erosion and dilation. The term B is a 5×5 window, denoting the structuring element for the morphological operations. The image region of M is then decomposed based on R_M . Finally, the nodes and edges of the bone graph, as well as node clusters, are therefore updated according to the new topology.

3.3. Details of the Proposed Method

3.3.1. Identifying Reference Nodes. Two reference nodes are required as anatomical landmarks in the bone graph, including neck and hip-joint. To identify the reference node for neck, the top node of the graph is retrieved at first, and then the down-links are traced through each node in successive slices. For each traversed node, as the bounding box area of its corresponding region is examined, the maximum area is updated as a representative value of the cross-sectional area for head. Since the cross-sectional area of neck is relatively smaller than that of head, the reference node of neck, denoted as RP_{Neck} , is marked if its corresponding region has the bounding box with area less than a threshold. In our study, the threshold value is determined based on human anatomy as well as the physicians' recommendations, which is 40% of the maximum cross-sectional area of head.

For the reference node of hip joint, the thresholded images computed in the preprocessing section are used to

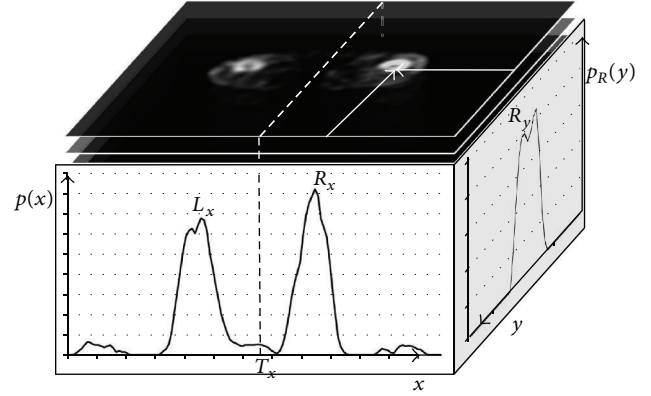


FIGURE 6: The accumulation of the horizontal counts of nonzero pixels from the bottom to the k th image plane where k is given.

identify the nodes of two legs on the bone graph. First, pixels in the last third of the binary images were scanned. The counts of nonzero pixels were then computed over the x -axis as follows:

$$p(x) = \int_{n/3}^n \int_y b(x, y, z) dy dz. \quad (5)$$

As illustrated in Figure 6, the curve of $p(x)$ has two peaks relatively corresponding to the positions of the two legs. Since the curve is highly symmetrical, the two groups can be separated by an optimal global threshold obtained by a binarization method [17]. In Figure 6, L_x and R_x indicate the coordinates with the maximum values in their respective groups on the x -axis. The ratios of nonzero pixel count over the y -axis, denoted as $p_L(y)$ and $p_R(y)$, are also recomputed. The y coordinates with the maximum values of $p_L(y)$ and $p_R(y)$ are, respectively, defined as L_y and R_y . Next, by centering on the pixels at the coordinates of (L_x, L_y) and (R_x, R_y) on each image plane, two ROIs, R_{LEFT} and R_{RIGHT} , respectively, are definable where the diameters of the ROIs were determined by the standard deviations computed from $p_L(y)$ and $p_R(y)$. The two ROIs are used to identify the leg nodes in the bone graph. For a node, if the corresponding region has the center locating within the ROI R_{LEFT} or R_{RIGHT} , the node is then marked as left or right leg node. As tracing the uplinks for these nodes in the bone graph, the tracking procedure marks the traversed nodes on the bone graph as left or right leg nodes, which are then connected to form a tracking path for each leg. The procedure eventually identifies the node joining the two paths, which indicates the location of the hip joint. The node is then marked and designated the hip-joint reference node ($RP_{\text{Hip-joint}}$).

3.3.2. Spine Extraction. Given RP_{Neck} as the initial node in C_1 , additional spine nodes are found by traversing upward and downward in the graph to optimize the clustering of bone graph model, as described in Section 3.2.2. This process measures the cost for each node connecting to C_1 . Any node satisfying the cost criterion will be marked as a spine node and joined to C_1 . Also, as C_1 expands, the image region decomposition and cluster splitting procedures are involved

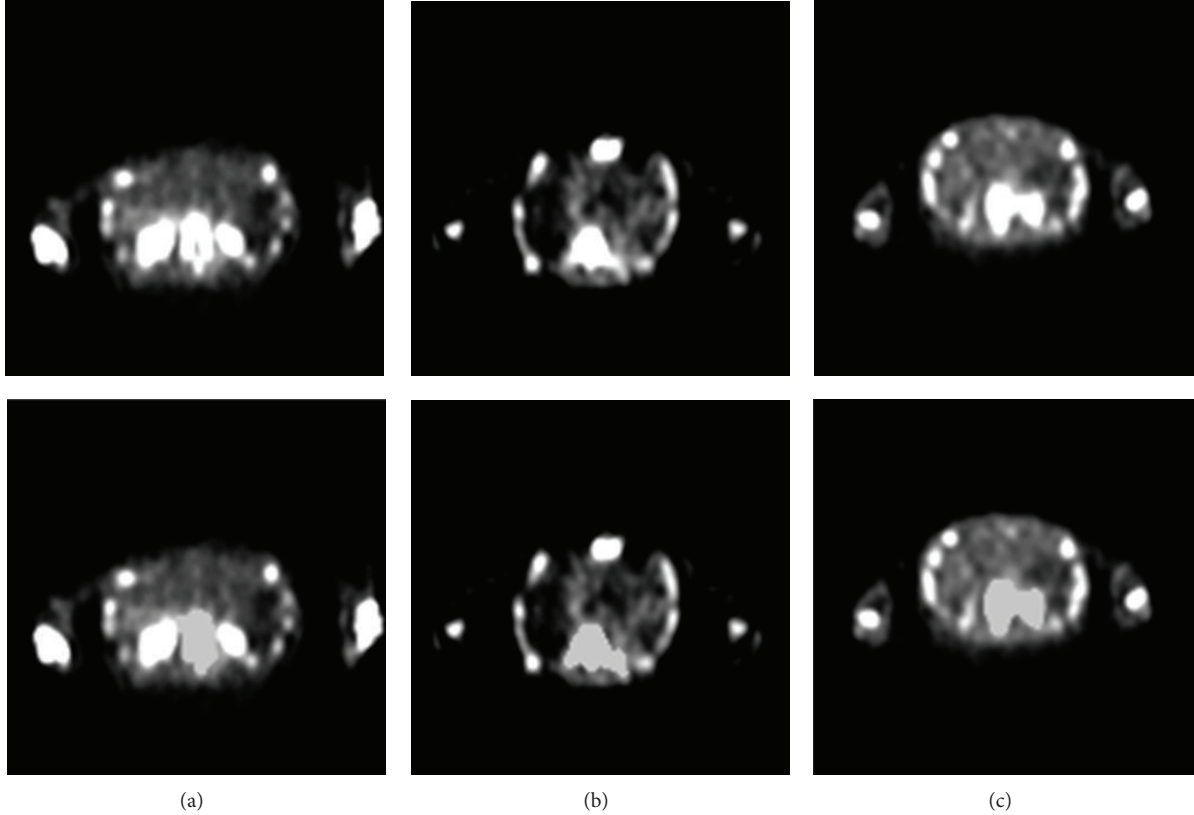


FIGURE 7: (a) and (b) show two examples of acceptable segmentation results and (c) illustrates an example of unacceptable result. The first row denotes the transaxial planes extracted from the original SPECT data, whereas the second row lists their corresponding segmentation results.

in order to disconnect the vertebral to other structures, such as rib-cage, joints, pelvis, or kidneys. The segmented image regions are then stacked into volumetric data. A morphological opening with a $3 \times 3 \times 3$ structuring element is finally applied on the 3D image to smooth the segmentation result.

3.3.3. Pelvis Removal. Residual urine activity in the bladder often produces interference in whole-body bone scan images. The bladder is close to the sacrum, and the urine activity usually has relatively higher pixel values compared to soft tissues. Therefore, the bladder may be misinterpreted as part of spine because of its location in a region connecting the vertebral column in the bone graph. Because the bladder is surrounded by the pelvis, the final step of spine segmentation is to exclude the section of pelvis to avoid containing the bladder in the final result. Two image planes are determined to evaluate the range of pelvis. First, the leftmost and rightmost coordinates on the x -axis for the regions corresponding to leg nodes are computed. Given the thresholded images as input, the pixels not within this range are excluded as background. In addition, the pixels of the regions corresponding to the nodes marked as spine or as legs are also eliminated from the images. In the image plane where the hip-joint reference node is located, the nonzero pixels are selected as initial seed points. A 3D region-growing segmentation algorithm is performed on the image stack to form a connected component for the pelvis [6]. On the z -axis, the upper and lower ends of the connected

component are marked to generate a range for representing pelvis location. In the extracted segmentation result, any pixel labeled as spine within this range is removed.

3.4. Evaluating Segmentation Result. The study includes quantitative and qualitative assessments to evaluate the performance. For the quantitative assessment, segmentation accuracy was tested by comparing the automatically extracted vertebral column images to the ground truth. Since the datasets of the study do not have corresponding CT images as gold standard, the manual segmentation was obtained by image thresholding that followed a sequence of manual adjustments to remove the structures not belonging to vertebral column, where the optimal threshold value was chosen manually for each dataset. The accuracy was measured with three different error measures: true-positive (TP) and false-positive (FP) volume fractions, which were defined as follows [18]:

$$\begin{aligned}
 \text{TP} &= \frac{\text{Volume}(A_a \cap A_m)}{\text{Volume}(A_m)}, \\
 \text{FP} &= \frac{|\text{Volume}(A_a \cup A_m) - \text{Volume}(A_m)|}{\text{Volume}(A_m)}, \\
 \text{FN} &= \frac{|\text{Volume}(A_a \cup A_m) - \text{Volume}(A_a)|}{\text{Volume}(A_m)},
 \end{aligned} \tag{6}$$

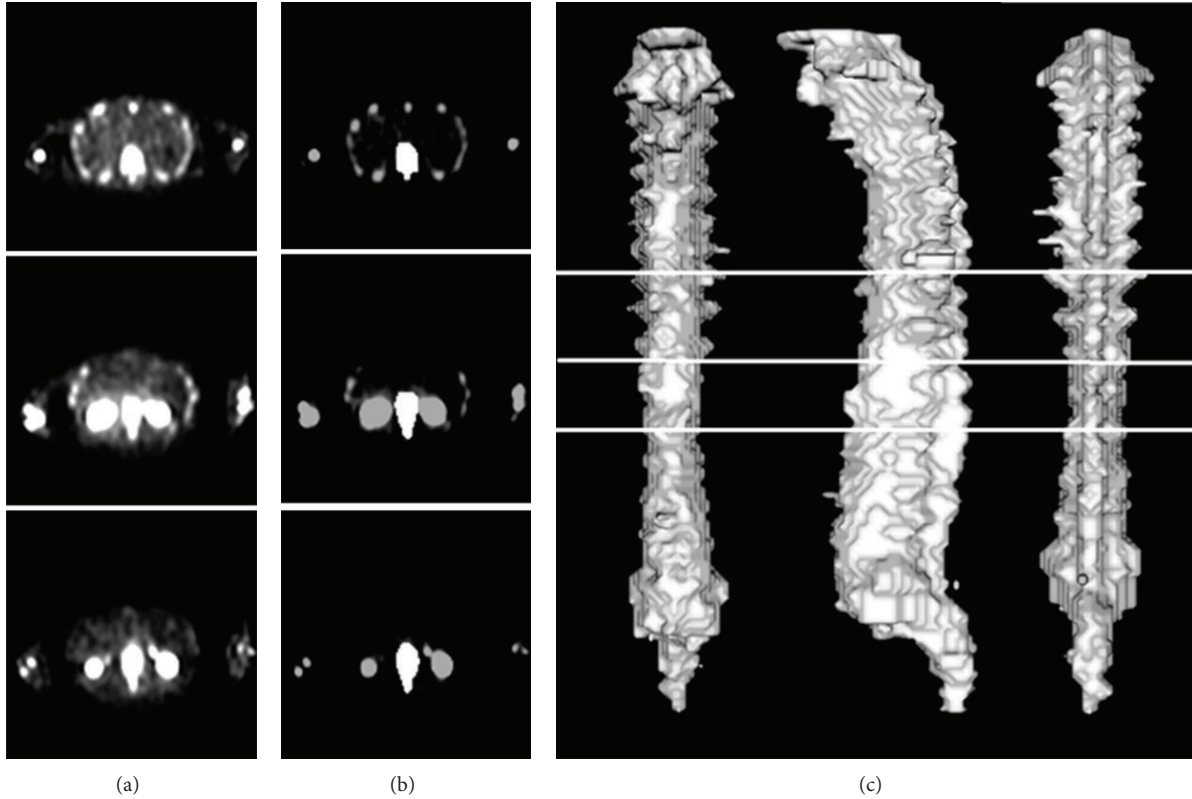


FIGURE 8: The reconstruction of the segmentation result classified as acceptable. (a) Original transaxial image plane, (b) segmented vertebral regions (white), and (c) the 3D reconstruction, where the white line denotes the height for the left three images in (a).

where the term A_m refers to the vertebral regions determined by manual segmentation and A_a are the ones extracted by the proposed method.

For the qualitative evaluation, two experienced nuclear medical physicians independently examined the segmentation results. In this test, each dataset was classified “acceptable” or “unacceptable” by a physician after comparing the original images with those obtained by the computer. A dataset is classified as acceptable if only a few slices (fewer than 10%) had computed ROIs that did not perfectly match the boundary of spine bone region and in which the segmentation area would not substantially affect the future identification of lesions and other abnormalities. Finally, unacceptable segmentation denotes an error in ROI computed for skeletal structures or other organs (e.g., the kidney or bladder) that was large enough to produce a misdiagnosis. Finally, the acceptance rate of the method was quantified by the ratios of datasets that were classified “acceptable”.

Figure 7 shows examples of segmentation results. The images in the first row denote the transaxial planes extracted from the original SPECT data, whereas the second row lists their corresponding segmentation results. The regions colored in light grey represent the segmented vertebrae regions. Figure 7(a) shows a perfect segmentation result where bone regions can be successfully extracted and fully isolated from other skeletal structures and organs. Figure 7(b) shows segmented bone regions partly covering soft tissues. These regions generally had lower intensities and were not

considered hot spots. The dataset was also classified as acceptable segmentation since the partial obstruction and reduced intensity did not affect diagnostic accuracy. However, if the segmented area overlapped kidney regions as shown in Figure 7(c), the result was then classified as unacceptable.

To test the reliability of the independent evaluations by two different physicians, Cronbach’s alpha values were computed for the two sets of grades. The Cronbach’s alpha value is a statistical measure of the correlation between two groups of observed scores, which is used to determine the internal consistency between two observers [19]. That is, expert evaluations should be considered trustworthy only if their evaluations are adequately correlated. The equation for calculating Cronbach’s alpha is

$$\alpha = \frac{k}{k-1} \left(1 - \frac{\sum_i s_i^2}{s_T^2} \right), \quad (7)$$

where k is the number of items, s_i^2 is the variance in the i th item and s_T^2 is the variance in the total score formed by summing all the items. In the study, k equals 46, which corresponds to the number of datasets. Each item was assigned a score of 0 or 1, to represent an unacceptable or acceptable segmentation result. The theoretical value of alpha value varies from zero to 1, where a higher value larger than 0.7 is desirable for an appropriate degree of reliability.

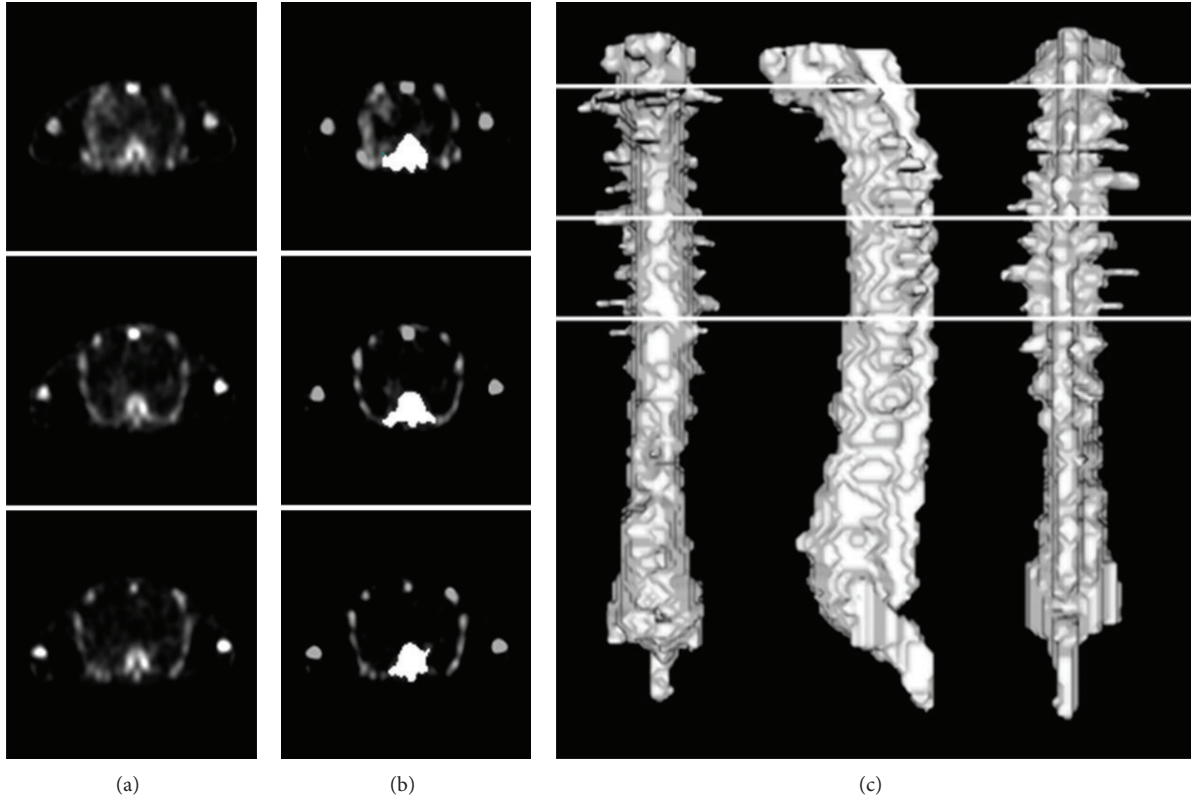


FIGURE 9: Another dataset that was also classified as acceptable. (a) Original transaxial image plane, (b) segmented vertebral regions (white), and (c) the 3D reconstruction, where the white line denotes the height for the left three images in (a).

TABLE 1: Correct acceptance rates of the method.

	Physician 1	Physician 2	Average
Acceptable	41 (89%)	35 (76%)	83%
Unacceptable	5 (11%)	11 (24%)	17%
Total	46	46	

4. Results and Discussion

The area error metrics TP and FP can quantitatively evaluate the performance of the proposed method. The average TP, FP, and FN percentages obtained by the system were 95.1%, 9.1%, and 4.9%, respectively. For the qualitative assessment, Table 1 lists the ratios for the two categories assigned by the two physicians. According to the table, 89% and 76% (average, 83%) of all images were acceptable.

Figures 8–10 show three segmentation results, which were reconstructed by surface rendering using the Visualization Toolkit (VTK). Figures 8 and 9 demonstrate acceptable segmentation results, while Figure 10 shows an erroneous outcome for those classified as unacceptable. The first column in Figures 8–10 lists three transaxial slices extracted from their original SPECT data, and their positions are given in the third column. Figures 8 and 9 show successfully extracted vertebral columns in which high-activity organs such the kidney or bladder were fully excluded (images in second column). Figure 10 shows a case in which the horizontal

boundary of one kidney is very close to the spine. The method initially grouped the bone and kidney as a single bone region, which produced errors in subsequent iterations of the segmentation procedure. The Cronbach's alpha values for the two sets of grades (0.718) exceeded 0.70, which indicated that the grades had reasonable internal consistency and reliability.

Factors that can degrade image quality and produce segmentation error [20–22] include equipment malfunctions such as those in a camera that has not been serviced regularly or the use of an inaccurate flood correction map, which can produce image noise and may cause a nonuniform appearance similar to that produced by soft-tissue uptake. Additionally, movement by the patient frequently causes blurred images, which may be misinterpreted as soft-tissue uptake. Finally, even when performed correctly, soft tissues may cause faulty uptake patterns when using the proposed method.

The degree of noise in SPECT images also varies due to the factors of different imaging protocols and reconstruction parameters and therefore could affect the accuracy of the method. So far the proposed method has only focused on how to delineate important landmarks on skeleton and extracting vertebral column from the original SPECT image. Therefore, the imaging protocol and scan time used in the study were managed to guarantee reduced noise in the image. In the proposed method, most noise in the background and soft tissues can be removed by the moment preserving method. In the future, a more complicated image filtering algorithm

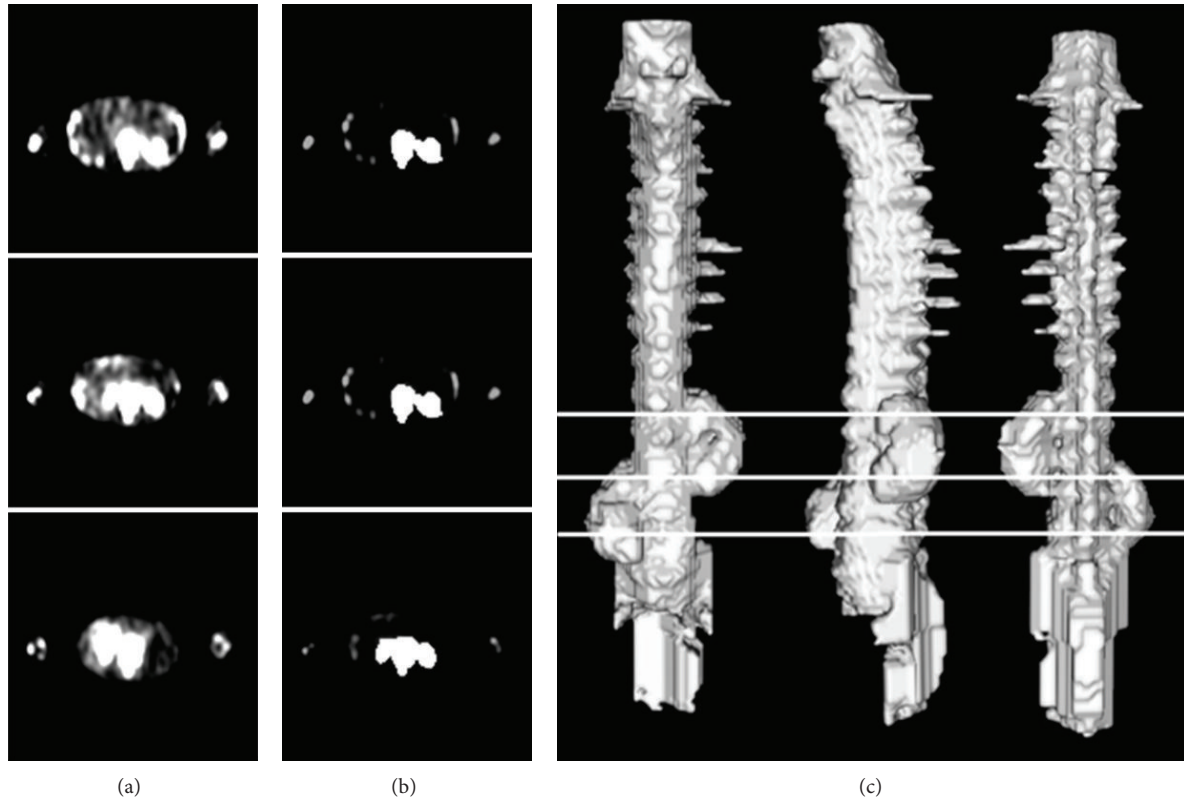


FIGURE 10: The reconstruction of the segmentation result classified as unacceptable. In this case, the kidneys are very close to the spine due to ectopia. (a) Original transaxial image plane, (b) segmented vertebral regions (white), and (c) the 3D reconstruction, where the white line denotes the height for the left three images in (a).

for noise reduction can be used in the preprocessing step if the other imaging protocols are considered. Comparison between different preprocessing algorithms and how they impact on the segmentation accuracy will also be analyzed.

5. Conclusions

Compared to planar bone scintigraphy, SPECT scan provides better contrast resolution without superposing body structures, which increases the specificity of positive scan findings and improves accuracy in locating equivocal lesions. Furthermore, an automated CAD system can effectively help doctors to identify whether a whole body bone SPECT scan is abnormal. As shown in the study of He et al. [11], bone lesions can be recognized according the morphological data of high uptake regions, but with the lack of spatial information, false-negatives may still remain due to the ambiguity of high uptake resulted by neighboring organs and skeletal joints. Combining functional data with anatomical findings should further increase its diagnostic accuracy. However, without the aid of an additional CT component, the anatomical information of bone scintigraphy acquired by SPECT is difficult to interpret due to the complexity of human skeletal structures. For conventional SPECT scan, this study developed a software solution for recognizing important anatomical landmarks on SPECT bone scintigraphy. To our knowledge, this study is the first to address this problem. The proposed “bone graph” image description method graphically depicts the

connectivity between bone regions on neighboring images so that bone specialists can graphically manipulate the morphological relationships of skeletal structures. By using the graph to characterize the images, the problem of vertebral column extraction can be solved by applying graph algorithms.

Extracting the vertebral column is a challenging task because the spine is connected to many other skeletal structures such as the skull, shoulder bones, rib cage, and pelvis. By tracking their paths with the proposed bone graph, morphological operations can be performed to isolate these parts. For each dataset, the performance of the proposed method was confirmed by independent reviews of images by two experienced nuclear medicine physicians. According to the quantitative evaluation, the segmentation method achieved a high TP rate of 95.1% and a low FN rate of 4.9%, showing that most of the ROIs obtained automatically by the proposed method have a large percentage of overlapping to the manual segmentation. The FP rate was 9.1%, which was slightly higher than the FN percentage due to the segmentation that erroneously included kidneys and other skeletal structures. The qualitative assessment shows an average acceptance rate of 83%. The Cronbach’s alpha value between the two sets of scores was 0.718, which indicated reasonable internal consistency reliability.

Although the algorithm successfully segmented vertebrae in the thoracolumbar spine, errors may occur in sections near the bladder. Because tracer not taken up by bones is excreted in the urine of a patient with normal renal function,

the bladder and kidneys are overenhanced in a whole-body bone scan image, which may complicate the segmentation of vertebrae. High bladder activity reportedly renders up to 20% of SPECT pelvis scans unusable [23]. The proposed method, however, simply used the computed reference lines to define a VOI around the pelvis to exclude the bladder. Other techniques, such as atlas-based registration scheme [24], can be adopted to improve the segmentation accuracy. Nevertheless, this method may exclude lesions near the sacrum, which would increase the false-negative rate. The recent development of integrated hybrid SPECT/CT systems, which provide functional and anatomical images in the same scanning session, could significantly improve its diagnostic capability [25]. From the perspective of image engineering, both SPECT and CT require segmentation techniques for extracting the important anatomical information to achieve a precise image fusion. This study develops an approach in delineating human anatomy using SPECT images without the aid of CT. In the future, the anatomical information extracted by using the proposed image characterization technique can be combined with image registration and fusion method in the SPECT/CT system for improving anatomic localization of a suspected site of increased radiotracer uptake at bone scanning. The result of this study can be further applied on the detection and localization of bone metastases in vertebrae. In future studies of whole-body bone division, the authors will include hot spot detection in the proposed bone graph. Partial extraction of SPECT image data will enable investigators to exclude typical hot spots such as joints. In addition, contrast enhancement or thresholding approaches can be optimized for different skeletal sections to improve irregularly distributed intensity. For classifying bone metastases, the authors will also explore methods combining texture analysis with a machine-learning algorithm. The proposed segmentation method may also be used to increase diagnostic accuracy and efficiency in an automated CAD system for quantitatively estimating bone metastases.

Acknowledgment

This work was supported by the National Science Council, Taiwan, under Grant NSC-97-2221-E-320-001-MY2.

References

- [1] M. V. Merrick, "Bone scanning," *British Journal of Radiology*, vol. 48, no. 569, pp. 327–351, 1975.
- [2] L. J. Han, T. K. Au-Yong, W. C. M. Tong, K. S. Chu, L. T. Szeto, and C. P. Wong, "Comparison of bone single-photon emission tomography and planar imaging in the detection of vertebral metastases in patients with back pain," *European Journal of Nuclear Medicine*, vol. 25, no. 6, pp. 635–638, 1998.
- [3] G. Savelli, A. Chiti, G. Grasselli, M. Maccauro, M. Rodari, and E. Bombardieri, "The role of bone SPET study in diagnosis of single vertebral metastases," *Anticancer Research*, vol. 20, no. 2B, pp. 1115–1120, 2000.
- [4] S. Kosuda, T. Kaji, H. Yokoyama et al., "Does bone SPECT actually have lower sensitivity for detecting vertebral metastasis than MRI?" *Journal of Nuclear Medicine*, vol. 37, no. 6, pp. 975–978, 1996.
- [5] J. W. Wallis and T. R. Miller, "Volume rendering in three-dimensional display of SPECT images," *Journal of Nuclear Medicine*, vol. 31, no. 8, pp. 1421–1430, 1990.
- [6] Y. E. Erdi, J. L. Humm, M. Imbriaco, H. Yeung, and S. M. Larson, "Quantitative bone metastases analysis based on image segmentation," *Journal of Nuclear Medicine*, vol. 38, no. 9, pp. 1401–1406, 1997.
- [7] T.-K. Yin and N.-T. Chiu, "A computer-aided diagnosis for locating abnormalities in bone scintigraphy by a fuzzy system with a three-step minimization approach," *IEEE Transactions on Medical Imaging*, vol. 23, no. 5, pp. 639–654, 2004.
- [8] L. Šajn, M. Kukar, I. Kononenko, and M. Milčinski, "Computerized segmentation of whole-body bone scintigrams and its use in automated diagnostics," *Computer Methods and Programs in Biomedicine*, vol. 80, no. 1, pp. 47–55, 2005.
- [9] M. Sadik, D. Jakobsson, F. Olofsson, M. Ohlsson, M. Suurkula, and L. Edenbrandt, "A new computer-based decision-support system for the interpretation of bone scans," *Nuclear Medicine Communications*, vol. 27, no. 5, pp. 417–423, 2006.
- [10] J.-Y. Huang, P.-F. Kao, and Y.-S. Chen, "A set of image processing algorithms for computer-aided diagnosis in nuclear medicine whole body bone scan images," *IEEE Transactions on Nuclear Science*, vol. 54, no. 3, pp. 514–522, 2007.
- [11] Y.-L. He, L.-F. Tian, C.-M. Zhu, P. Chen, B. Li, and Z. Y. Mao, "Development of intelligent diagnosis and report system based on whole body bone spect image," in *Proceedings of the International Conference on Machine Learning and Cybernetics (ICMLC '05)*, pp. 5437–5441, Guangzhou, China, August 2005.
- [12] S.-F. Huang, H.-Y. Chao, C.-C. Hsu, S.-F. Yang, and P.-F. Kao, "A computer-aided diagnosis system for whole body bone scan using single photon emission computed tomography," in *Proceedings of the IEEE International Symposium on Biomedical Imaging: From Nano to Macro (ISBI '09)*, pp. 542–545, Boston, Mass, USA, July 2009.
- [13] D. A. Wong, V. L. Fornasier, and I. MacNab, "Spinal metastases: the obvious, the occult, and the impostors," *Spine*, vol. 15, no. 1, pp. 1–4, 1990.
- [14] P. Reuland, W. Muller-Schauenburg, H. Kuhn, K. D. Keller, and U. Feine, "180° versus 360° rotation in skeletal SPECT," *NuclearMedizin*, vol. 27, no. 6, pp. 242–247, 1988.
- [15] W.-H. Tsai, "Moment-preserving thresholding: a new approach," *Computer Vision, Graphics, & Image Processing*, vol. 29, no. 3, pp. 377–393, 1985.
- [16] R. C. Gonzalez and R. E. Woods, *Digital Image Processing*, Prentice-Hall, Upper Saddle River, NJ, USA, 2nd edition, 2001.
- [17] P. H. Pretorius, T.-S. Pan, M. V. Narayanan, and M. A. King, "A study of the influence of local variations in myocardial thickness on SPECT perfusion imaging," *IEEE Transactions on Nuclear Science*, vol. 49, no. 5, pp. 2304–2308, 2002.
- [18] A. Madabhushi and D. N. Metaxas, "Combining low-, high-level and empirical domain knowledge for automated segmentation of ultrasonic breast lesions," *IEEE Transactions on Medical Imaging*, vol. 22, no. 2, pp. 155–169, 2003.
- [19] J. C. Nunnally, *Psychometric Theory*, McGraw Hill, New York, Ny, USA, 2nd edition, 1978.
- [20] I. Loutfi, B. D. Collier, and A. M. Mohammed, "Nonosseous abnormalities on bone scans," *Journal of Nuclear Medicine Technology*, vol. 31, no. 3, pp. 149–153, 2003.

- [21] M. K. O'Connor and B. J. Kelly, "Evaluation of techniques for the elimination of 'hot' bladder artifacts in SPECT of the pelvis," *Journal of Nuclear Medicine*, vol. 31, no. 11, pp. 1872–1875, 1990.
- [22] J. R. Kessler, R. G. Wells, and J. R. Sty, "Skeletal scintigraphy radiographic artifacts," *Clinical Nuclear Medicine*, vol. 17, no. 6, pp. 511–512, 1992.
- [23] B. D. Collier, G. F. Carrera, and R. P. Johnson, "Detection of femoral head avascular necrosis in adults by SPECT," *Journal of Nuclear Medicine*, vol. 26, no. 9, pp. 979–987, 1985.
- [24] A. Khmelinskii, H. C. Groen, M. Baiker, M. de Jong, and B. P. F. Lelieveldt, "Segmentation and visual analysis of whole-body mouse skeleton microSPECT," *PLoS One*, vol. 7, no. 11, Article ID e48976, pp. 264–271, 2012.
- [25] D. Utsunomiya, S. Shiraishi, M. Imuta et al., "Added value of SPECT/CT fusion in assessing suspected bone metastasis: comparison with scintigraphy alone and nonfused scintigraphy and CT," *Radiology*, vol. 238, no. 1, pp. 264–271, 2006.